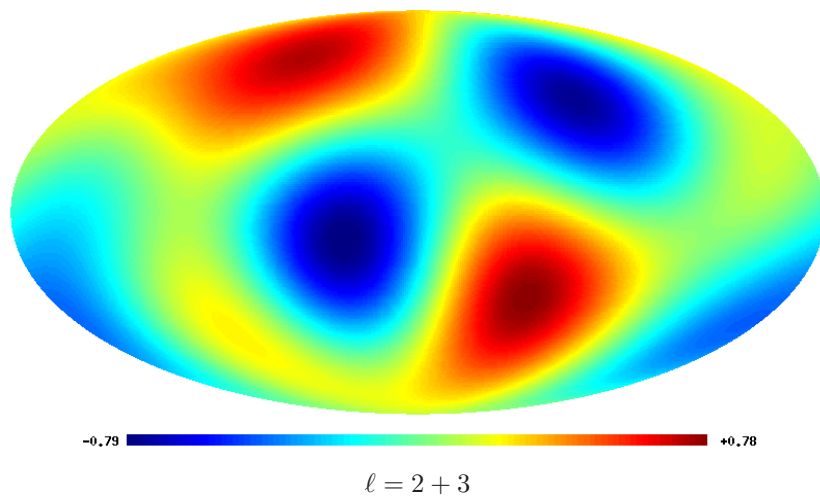


Aleksandar Rakić

On the Influence of Local Inhomogeneities on Cosmological Observables

From Galaxies to the Microwave Background



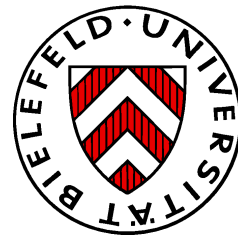
Doctoral Thesis in Theoretical Physics

On the Influence of Local Inhomogeneities on Cosmological Observables

From Galaxies to the Microwave Background

Aleksandar Rakić

Department of Physics
Bielefeld University



Bielefeld
November 2007

On the Influence of Local Inhomogeneities on Cosmological Observables

From Galaxies to the Microwave Background

DISSERTATION ZUR ERLANGUNG DES GRADES EINES DOKTORS DER
NATURWISSENSCHAFTEN (DOKTOR RERUM NATURALIUM)
AM FACHBEREICH PHYSIK DER UNIVERSITÄT BIELEFELD

VORGELEGT VON: ALEKSANDAR RAKIĆ
GEBOREN AM 28 MAI 1979 IN MENDEN

GUTACHTER UND PRÜFER - REFEREES:

PROF. DR. DOMINIK J. SCHWARZ

PROF. DR. DIETRICH BÖDEKER

PROF. DR. REINHART KÖGERLER

PROF. DR. ANDREAS HÜTTEN

ABSTRACT. Despite the good consistency of the cosmological standard model with the bulk of present observations, a number of unanticipated features have recently been detected within large-angle data of the Cosmic Microwave Background. Among these features are the anomalous alignments of the quadrupole and octopole with each other, their unexpected alignments with certain astrophysical directions (e.g. equinox, ecliptic) as well as the stubborn lack of angular autocorrelation on scales $> 60^\circ$. We pursue the idea that processes of non-linear structure formation could contribute to the large-scale anomalies via a local Rees-Sciama effect. We find that existing structures are able to produce CMB contributions up to 10^{-5} . For an axially symmetric setup we show that this effect does induce alignments, albeit not of the same form as extracted from the data, and that yet a Solar system effect seems preferred by the data. Moreover, we address the relationship between the intrinsic alignment of quadrupole and octopole on the one hand and the anomalous angular two-point correlation function on the other hand. We demonstrate the absence of any correlations between them and are able to exclude the joint case at high confidence with respect to recent data. This result enables us to put stringent constraints on any relevant model that exhibits an explicit axial symmetry.

Key words. galactic dynamics, dark matter, cosmic microwave background, large-scale structure of universe, dark energy, general relativity, cosmology

ABRISS. Trotz der guten Übereinstimmung des aktuellen kosmologischen Standardmodells mit dem Großteil der vorhandenen Daten, wurden kürzlich unerwartete Eigenschaften der kosmischen Mikrowellenhintergrundstrahlung bezüglich der größten gemessenen Winkelskalen bekannt. Diese beinhalten: die anomale Richtungskorrelation zwischen Quadrupol und Oktupol selbst, ihre unverstandene Ausrichtung bezüglich bestimmter astrophysikalischer Richtungen (z.B. Equinox, Ekliptik) als auch eine Temperatur-Zweipunktskorrelationsfunktion, die auf Winkelskalen $> 60^\circ$ unerwarteterweise verschwindet. Wir untersuchen die Möglichkeit, dass Prozesse, die der nichtlinearen Strukturbildung angehören, zu den Anomalien beitragen können, und zwar durch den lokalen Rees-Sciama Effekt. Wir finden, dass der Rees-Sciama Effekt durch tatsächlich vorhandene, sehr massive Strukturen, die Größenordnung 10^{-5} in den Temperaturanisotropien erreichen kann. Wir können zeigen, dass, im Rahmen einer axial-symmetrischen Geometrie, in der Tat bestimmte Richtungskorrelationen durch den Effekt induziert werden, diese jedoch nicht von der gleichen Form wie die in den Daten gefundenen sind. Gleichwohl wird eine Korrelation mit den Richtungen unseres Sonnensystems von den Daten bevorzugt. Außerdem untersuchen wir inwiefern zwischen der intrinsischen Ausrichtung von Quadrupol und Oktupol zueinander und der anomalen Zweipunktskorrelationsfunktion eine Abhängigkeit bestehen könnte. Wir demonstrieren, dass keinerlei Abhängigkeit zwischen diesen Anomalien besteht und wir können das kombinierte Szenario mit hoher Signifikanz ausschließen. Dadurch sind wir in der Lage, scharfe Einschränkungen anzugeben, die für alle relevanten axial-symmetrischen Modelle bindend sein müssen.

Schlagwörter. Galaxiendynamik, dunkle Materie, kosmische Mikrowellenhintergrundstrahlung, großräumige Struktur des Universums, dunkle Energie, allgemeine Relativitätstheorie, Kosmologie

BIELEFELD, DECEMBER 20, 2007

On the Influence of Local Inhomogeneities on Cosmological Observables

From Galaxies to the Microwave Background

This thesis is based upon the following publications:

► *Microwave Sky and the Local Rees-Sciama Effect*

Aleksandar Rakić, Syksy Räsänen and Dominik J. Schwarz; Mon. Not. Roy. Astron. Soc. Lett. **369**: L27–L31, 2006; astro-ph/0601445

► *Correlating Anomalies of the Microwave Sky: The Good, the Evil and the Axis*

Aleksandar Rakić and Dominik J. Schwarz; Phys. Rev. D **75**: 103002, 2007; astro-ph/0703266

► *Can Extragalactic Foregrounds Explain the Large-Angle CMB Anomalies?*

Aleksandar Rakić, Syksy Räsänen and Dominik J. Schwarz; astro-ph/0609188; to appear in the proceedings of the 11th Marcel Grossmann Meeting on general relativity

Publications in preparation:

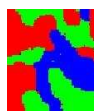
► *General Relativistic Galactic Dynamics and the Newtonian Limit of Lewis-Papapetrou Space-Times*

Aleksandar Rakić and Dominik J. Schwarz

► *Backreaction Effects on the Observer's Past Light Cone*

Thomas Buchert, Aleksandar Rakić and Dominik J. Schwarz

The work contained in this thesis is part of the research done within the International Research Training Group (GRK 881) entitled as *Quantum Fields and Strongly Interacting Matter: From Vacuum to Extreme Density and Temperature Conditions*. This graduate school is a joint project of the University of Bielefeld and the Université Paris-Sud XI (Paris VI, Paris VII, Saclay); it is funded by the German research foundation (DFG) and so was the author.



PhD thesis in theoretical physics

Author: Aleksandar Rakić

E-mail address: arakic@web.de

Typeface: Computer Modern Roman 8pt, 9pt, 10pt, 11pt, 12pt

Distribution: L^AT_EX 2_ε using A^MS^ET_EX and hyperref

Compiled on February 25, 2008 as a native dvi document

Contents

Notation	1
Preface	3
Part I. Exact Solutions as Toy Models	11
Chapter 1. The Cosmological Problem of Dark Energy	13
1.1. Facets of the Problem	14
1.2. Dark Energy and the Standard Cosmological Model	15
1.3. An Inhomogeneous Alternative?	27
Chapter 2. The Cosmological Problem of Dark Matter	45
2.1. Direct Evidence and Lensing	45
2.2. Classical Evidence from Dynamics	51
2.3. Modelling Galaxies with General Relativity	55
Part II. Axisymmetric Effects in the CMB	75
Chapter 3. On the Cosmic Microwave Background	77
3.1. Overview of Sources of CMB Anisotropy	77
3.2. Recombination	80
3.3. Observables of the CMB	85
Chapter 4. Extrinsic Alignments in the CMB	95
4.1. The Alignment Anomalies	96
4.2. Local Rees-Sciama Effect	97
4.3. Angular Power Analysis	101
4.4. Extrinsic Alignment Analysis	103
4.5. Conclusion	106
Chapter 5. Intrinsic Alignments in the CMB	109
5.1. Introduction	110
5.2. Choice of Statistic	112
5.3. Standard Model Predictions	113
5.4. Inclusion of a Preferred Axis	117
5.5. Conclusion	119
Summary and Outlook	121
Acknowledgements	123
Part III. Appendices	125
Appendix A. Critical Values of Ω_m and Ω_Λ in the FRW Model	127
Appendix B. Details of the Lemaître-Tolman-Bondi Model	131

B.1. General Spherically Symmetric Spacetime with Zero Vorticity	131
B.2. Einstein Equations of the Lemaitre-Tolman-Bondi Model	132
Appendix C. Rotating Post-Newtonian Metrics	135
C.1. Full Differential Rotation	135
C.2. Spatial Curvature Terms	135
Appendix D. Aspects of Structure Formation	137
D.1. Gravitational Instabilities and Peculiar Velocities	137
D.2. Statistical Properties of the Density Field	138
D.3. Silk Damping and Hierarchy	139
Appendix E. Thermal History in a Nutshell	143
E.1. Neutrino Decoupling	143
E.2. Electron-Positron Annihilation	144
E.3. Nucleosynthesis	145
Appendix F. Additional Plots and Results	147
Bibliography	159

Notation

Throughout this work we will use the following metric signature,

$$(-, +, +, +).$$

By small latin indices, running from 1 to 3, we denote spatial components of tensors, e.g. K_{ij} . Using small greek indices, running from 0 to 3, we denote four-dimensional components of tensors, e.g. $K_{\mu\nu}$. We make use of the Einstein summation convention.

Partial derivatives are indicated by a comma,

$$K_{\mu\nu,\lambda} \equiv \frac{\partial}{\partial x^\lambda} K_{\mu\nu}$$

and covariant derivatives by a semicolon

$$K_{\mu\nu;\lambda} \equiv \frac{\partial}{\partial x^\lambda} K_{\mu\nu} - \Gamma^\rho_{\lambda\mu} K_{\rho\nu} - \Gamma^\rho_{\lambda\nu} K_{\rho\mu}.$$

The sign conventions which we use for the cosmological constant, for the definition of the Riemann curvature tensor as well as for the other relevant quantities in the Einstein equations are given in app. B. The spatial Ricci scalar is written caligraphically throughout the text, $\mathcal{R} \equiv {}^{(3)}R^i_i$.

Vectors and vector fields are written in boldface, e.g. $\boldsymbol{\xi}$, \mathcal{L}_σ . Normal vectors are denoted by a hat, e.g. $\hat{\boldsymbol{x}}$.

We denote the symmetrisation and antisymmetrisation of tensors by

$$K_{\{\mu\nu\}} \equiv \frac{1}{2}(K_{\mu\nu} + K_{\nu\mu}), \quad K_{[\mu\nu]} \equiv \frac{1}{2}(K_{\mu\nu} - K_{\nu\mu}).$$

In chap. 2 we will deal with axisymmetric systems, and therefore the operators $\Delta^{(3)}$ and $\Delta^{(2)}$ denote the three-dimensional and two-dimensional Laplace operators in cylindrical coordinates. The use of cartesian coordinates is explicitly indicated, e.g. $\Delta_{\text{cart}}^{(3)}$.

Preface

The most fundamental cosmological observation one can think of is the darkness of our night sky. At first glance, this might appear trivial, but the appropriate question is, how is it possible that our sky is dark at night? The proper answer to it has crucial implications for cosmology. In the early days of astronomy, the common cosmological paradigm stated that the Universe was eternal, infinite and of Euclidean geometry. Following this paradigm, in 1826 Heinrich Olbers calculated the total radiation energy density of stars that would be present in such a Universe. The stars were taken as point sources with constant luminosity and their number density was also constant. The result of the calculation is astonishingly absurd: there would be an *infinite* radiation density coming from starlight. Interpreted within a static, infinite and Euclidean world model, the common fact that our night sky is dark becomes suddenly a mystery. This lack of optical background light is usually referred to as *Olbers' paradox*, but it should be mentioned that the problem was discussed already much earlier, for instance by de Cheseaux in 1744.

Within the modern standard model of cosmology, a common way of resolving Olbers' paradox lies in assuming a Big Bang and taking the cosmological expansion of spacetime into account. In a Universe that has existed for a finite amount of time, the extension of the observable part of the Universe – the horizon – is also finite, and therefore only a limited number of stars is potentially observable. In this formulation of Olbers' paradox we assumed a distribution of point sources. We could go one step further and consider the extended surfaces of the emitting stars. Then it turns out that every line of sight toward us must start at some finite surface and – within the old world view – we would inevitably be led to a sky that is, due to projected overlap, fully covered by the luminous surfaces of the stars. The brightness temperature of stars is independent of distance in the Euclidean picture, and so this formulation of Olbers' paradox states that the whole sky should be as hot as the surface of a typical star. Now the resolution of Olbers' paradox within modern cosmology becomes somewhat different. Assuming a Big Bang and continuous cosmic expansion, one can extrapolate that there indeed must have existed a common hot emission surface, namely the *surface of last scattering* at which the Universe became transparent for photons. This instant marks the birth of the Cosmic Microwave Background (CMB) radiation. Now, since last scattering occurred a long time ago – when the temperature of the Universe was around 3000K – and the Universe has expanded ever since, one can find that the CMB photons have undergone a redshifting by a factor of roughly 1100 up to day. This results in a present-day background temperature of 2.73K. In this sense, the existence of the CMB represents the resolution of Olbers' paradox: we cannot observe a 3000K hot sky, because the cosmic expansion has cooled down the primordial radiation.

Today, measurements of the tiny anisotropies in the microwave background radiation provide a cosmological probe of utmost relevance. With satellite measurements of the CMB – like the Wilkinson Microwave Anisotropy Probe (WMAP) – a considerable precision in cosmological data has been reached.

Due to its very good accordance with CMB measurements, as well as with other data sets from the observation of the large-scale structure at lower redshifts, a cosmological standard model has emerged, the inflationary Λ Cold Dark Matter model. Among the energy density ingredients of that model are the contributions of Dark Energy (76%), Dark Matter (20%) and baryonic matter (4%). Although they represent dominant contributions, the standard model is not explanatory with respect to the nature and origin of the dark components of the Universe.

Although a lot of effort is invested, and although numerous attempts to attack the problem can be found, there exists no settled explanation for the dark components of the standard model; they remain poorly understood up to day. Moreover, the current cosmological standard model is based upon a relatively simple, homogeneous and isotropic solution of the underlying general relativistic field equations, the Friedmann-Robertson-Walker spacetime. Within this model, both CMB and other data require the Universe to be spatially flat.

In chap. 1 we review the phenomenology of the current standard model of cosmology as well as its theoretical framework. We focus on the cosmological problem of Dark Energy and we explain its basic experimental evidence. The validity of the crude standard model assumptions of homogeneity and isotropy on large scales can be questioned. It is subject to current debate in how far *inhomogeneous models* can fit the available data that indicates an accelerated expansion of the Universe. The crucial difference is that inhomogeneous models are potentially able to achieve this without Dark Energy. In particular we analyse the spherically symmetric Lemaitre-Tolman-Bondi model and discuss how it may change the interpretation of supernova and CMB data. In order to use the inhomogeneous model for the CMB analysis in the later chapters, we finally present analytic calculations of the integrated Sachs-Wolfe effect in that model.

Chap. 2 deals with the cosmological problem of Dark Matter. We review present evidence for Dark Matter and focus especially on the flat galactic rotation curves. We omit discussions of particle candidates for Dark Matter and focus on an unusual approach, namely the general relativistic modelling of galaxies. Regarding rotation curves, the comparison from which Dark Matter follows in the standard picture, is always a comparison between Newtonian physics and the data. It can be questioned whether general relativistic terms really can be fully neglected. In fact, recently a general relativistic model of a galaxy has been presented (the Cooperstock-Tieu model) in which it is claimed that Dark Matter is made superfluous. Partly, chap. 2 is very technical; we carry out various analytical analyses in order to better understand the Cooperstock-Tieu model and especially its Newtonian limit.

A crucial component of the standard model is the inflationary scenario. Inflation predicts an early epoch of dramatic global expansion of spacetime and so provides the seeds for the formation of large-scale structure through a freeze-out of primordial quantum fluctuations on macroscopic scales. As a consequence, the simplest inflationary theories, predict a nearly scale-invariant power spectrum of statistically isotropic, adiabatic and gaussianly distributed primordial fluctuations.

Despite the remarkable achievements of the standard model, there are also some problems with it. When analysing WMAP data from the largest angular separation scales, several anomalies are found, which are in conflict with the prediction of statistical isotropy of the CMB.

After reviewing the basic physical mechanisms that contribute to the CMB, and discussing the underlying theoretical framework in chap. 3, we approach the problem of the large-scale CMB anomalies in chap. 4 and chap. 5. In chap. 4 our ansatz is a local Rees-Sciama effect – the non-linear analogue of the integrated Sachs-Wolfe effect. We state that the local Rees-Sciama effect of vast, yet non-virialised structures induces significant contributions to the large-scale CMB. We compute its influence on the phase anomalies with the help of a statistical analysis and find that an Rees-Sciama effect – modelled by a simply spherical overdensity – can be excluded at high confidence. In contrast to chap. 4, chap. 5 copes only with intrinsic alignments among the lowest CMB multipoles. There are two classes of anomalies, phase (directional) anomalies and angular power anomalies. We ask to what extent anomalies of the two classes are correlated with each other, because this is of importance for model building. We perform an exhaustive statistical analysis and demonstrate the absence of such correlations with high significance. Further, we find stringent constraints on any models, trying to explain the anomalies, that exhibit axial symmetry (‘Axis of Evil’).

*Der wahre Weg geht über ein Seil, das
nicht in der Höhe gespannt ist,
sondern knapp über dem Boden.
Es scheint mehr bestimmt stolpern zu
machen, als begangen zu werden.*

Franz Kafka (1883 – 1924)
*Aphorismen – Betrachtungen über Sünde, Leid,
Hoffnung und den wahren Weg, 1931*

[...] What is the significance of the vast processes it portrays? What is the meaning, if any there be which is intelligible to us, of the vast accumulations of matter which appear, on our present interpretations of space and time, to have been created only in order that they may destroy themselves? What is the relation of life to that Universe of which, if we are right, it can occupy only so small a corner? What if any is our relation to the remote nebulae, for surely there must be some more direct contact than that light can travel between them and us in a hundred million years? Do their colossal incomprehending masses come nearer to representing the main ultimate reality of the Universe, or do we? Are we merely part of the same picture as they, or is it possible that we are part of the artist? Are they perchance only a dream, while we are brain cells in the mind of the dreamer? Or is our importance measured solely by the fractions of space and time we occupy – space infinitely less than a speck of dust in a large city, and time less than one tick of a clock which has endured for ages and will tick on for ages yet to come?

Sir James Jeans (1877 – 1946)
Astronomy and Cosmogony, 1928

Part I

Exact Solutions as Toy Models

CHAPTER 1

The Cosmological Problem of Dark Energy

Why does Dark Energy seem to dominate the energy budget of the cosmos? What does this major contributor consist of at all? Why is the absolute value of the Dark Energy density so tiny as compared to the expectation from quantum theory? Undoubtedly, the challenge posed by Dark Energy is the most far-reaching of the grand open questions in modern cosmology. It is tightly related to the question of how far there is crucial physics missing in the underlying theories at the moment; an example thereof would be a unified theory of gravity and quantum fields. There is a generic relation to the very fundamental question of how the absolute zero-point energies of quanta gravitate. The notion of Dark Energy goes hand in hand with Einstein's cosmological constant Λ . On the other hand, also dynamical scalar fields – that would contribute to Λ in a time-dependent way – are considered, like for instance quintessence or moduli fields.

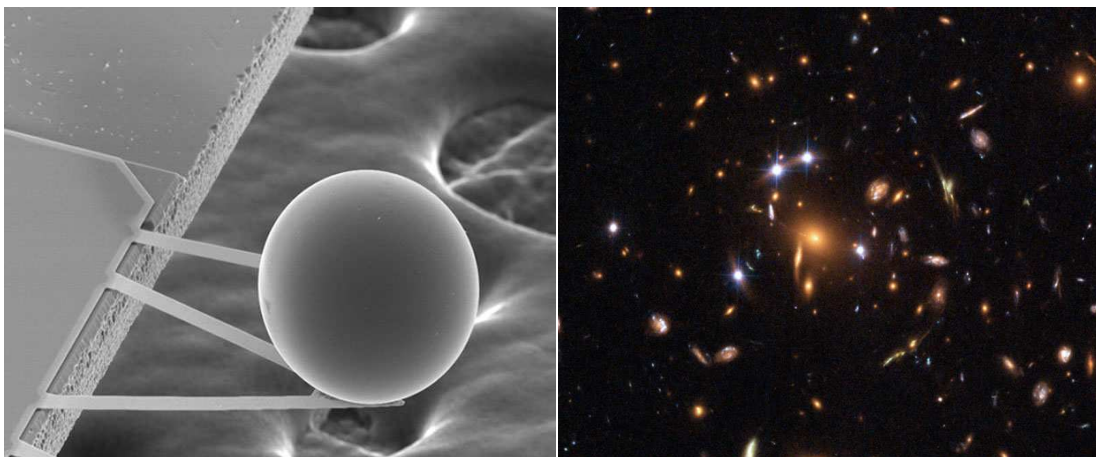


FIGURE 1.1. The influence of Dark Energy reaches from the smallest to the largest structures in the Universe. Left: microscopic image of a tiny ball ($d \simeq 10^{-1}$ mm) that is mounted at a small distance upon a smooth plate in order to measure the occurring (electromagnetic) Casimir effect. The minute Casimir force pulls the ball toward the plate because the number of vacuum fluctuation modes in the small space between ball and plate is limited, whereas the wavelengths of vacuum fluctuations occurring in the 'free space' on the opposite side of the plate can take arbitrary values. Vacuum fluctuations similar to those from the Casimir effect are associated with Dark Energy but in this case are generated by space itself. The nowadays dominant Dark Energy acts as a repulsive force on the largest scales, eventually causing the Universe to expand forever. Right: an image of the cluster of galaxies named SDSS J1004 + 4112 after its detection within the Sloan Digital Sky Survey. The cluster is around seven billion light years away ($z = 0.68$), located in the constellation of Leo Minor, and represents a beautiful sample of Large-Scale Structure. Also, due to gravitational lensing off the huge lensing mass of the cluster, arc images of more distant galaxies in the background can be seen in the image. According to observations of distant supernovae ($z \gtrsim 0.2$) the recession of galaxies is currently speeding up as due to the actual density contribution from Dark Energy. Pictures are taken from [APO].

1.1. Facets of the Problem

The famous mismatch of ~ 120 orders of magnitude that results from trying to estimate Λ from quantum field theory illustrates well the amount of our ignorance regarding the fundamental physics that may be involved. Likewise the Dark Energy which is so poorly understood does in fact constitute a whole $\sim 70\%$ of the energy density content of the Universe, which readily indicates the weight of the problem. Still, it is always adequate to carefully reconsider all assumptions that are made in order to get a physical result, especially if it is such a weighty one. In fact, the above situation results from a comparison of a large variety of astronomical tests with the cosmological standard model. Additionally, the comparison of Λ with the absolute zero-point energy takes place within quantum field theory which is at the basis of the actual standard model of elementary particle physics. We want to emphasise that the empirical basis of the cosmological standard model is far less substantial than that of the standard model of particle physics. One of the main differences is of course the inherent impossibility to do astronomical measurements in such a repeatable and controlled way as it is done in a laboratory. That is, mostly astronomers are clever spectators, waiting for the right moment of observation, but always being incapable of touching or turning the source in order to repeat their measurement. As we will see below, one of the most weighty evidence for Λ comes from such an astronomical measurement, namely the observation of distant supernovae.

Within the standard cosmological model the energy-matter content of the Universe is characterised by four dimensionless density parameters with the following normalisation:

$$(1.1) \quad \Omega_m + \Omega_r + \Omega_\Lambda + \Omega_k = 1.$$

Here, Ω_m is the density of matter involving all kinds of matter present whether dark or luminous, baryonic or non-baryonic; $\Omega_r \sim 10^{-4}$ stands for the energy present in the cosmic microwave as well as in the primordial low-mass neutrino background radiation; Ω_k stands for the energy-matter contribution associated with the curvature of space due to General Relativity and finally Ω_Λ is the contribution of Dark Energy. From measurements of e.g. the CMB it is known that the three-geometry of space is flat to a high degree of accuracy such that Ω_k can be set to zero. Also neglecting the minor contribution from Ω_r , a couple of different classes of astronomical observations suggest the so called cosmic concordance:

$$(1.2) \quad \Omega_b \simeq 0.04, \quad \Omega_{DM} \simeq 0.20, \quad \Omega_\Lambda \simeq 0.76,$$

where, according to usual notation, we split the matter density parameter Ω_m into a baryonic contribution and a contribution from Dark Matter. The issue of Dark Matter is discussed in more detail in chapter 2. But whatever the particular composition of the numerical values of the different energy-matter components, as inferred in the framework of the cosmological standard model may try to tell us, one result is particularly striking: only 4% of the whole is due to well-understood physics, i.e. to baryons. Another surprising feature of Dark Energy is known as the *coincidence problem*. It refers to the fact that the contribution of the time-independent Λ parameter, if we would measure it together with the other cosmological density parameters in the past when the universe had only around one tenth of its present size, would be only $\Omega_\Lambda \simeq 0.003$. That is, the influence of Λ , causing the expansion of the Universe to accelerate, appears to become significant at just around at the present time. It is unclarified in how far these ‘coincidences’ are reflecting some deep physical contiguity. However, it is conceivable that the cosmological constant might be a running and would approach some natural value at late times [PR03].

We consider the possibility of Λ itself being a superposition of different physical effects:

$$(1.3) \quad \Omega_\Lambda = \Omega_{\Lambda, \text{Einstein}} + \Omega_{\Lambda, \text{QF}} + \Omega_{\Lambda, \text{unknown}}.$$

The term $\Omega_{\Lambda, \text{Einstein}}$ is nothing else than the original cosmological constant as introduced by Einstein in order to maintain static cosmological solutions of his field equations; $\Omega_{\Lambda, \text{QF}}$ is a contribution from virtual particle-antiparticle fluctuations in the quantum vacuum; $\Omega_{\Lambda, \text{unknown}}$ would describe contributions from yet unknown physics like new fields or interactions. The fact

that quantum fluctuations $\Omega_{\Lambda, \text{QF}}$ really do exist is impressively demonstrated by measurements of the (electromagnetic) Casimir effect, see fig. 1.1. The Casimir effect can be measured between microscopic objects, for example small conducting plates, that are positioned at a tiny distance to each other. Whereas the quantum fluctuations of the vacuum, as predicted within quantum field theory, can populate arbitrary modes in empty space, the number of possible modes in between the microscopic objects is limited and so the energy of the system is suppressed. This results in an attractive force that is of measurable strength for e.g. the electromagnetic field and is purely due to subtle quantum effects.

The problem one naturally encounters with the contribution of Λ may be demonstrated by using the CMB as an example [PR03]. The CMB has a monopole temperature of $\simeq 2.7\text{K}$ and energy density $\Omega_{\text{CMB}} \sim 10^{-5}$ reaching its maximum at the Wien peak $\lambda \sim 2\text{mm}$. Here the photon occupation number is $\sim 1/15$. Given a certain frequency, the zero-point energy amounts to half the energy of the photon. Therefore the zero-point energy of the electromagnetic field at the Wien peak translates into a contribution of $\delta\Omega_{\Lambda, \text{CMB}} \sim 10^{-4}$ to the Dark Energy density parameter. As it will become clear from equation (1.32) the sum over wavelengths scales according to λ^{-4} and thus we would have $\delta\Omega_{\Lambda, \text{CMB}} \sim 10^{10}$ at visible wavelengths! This naive extrapolation already yields such an absurd figure. However, as was already mentioned above, it may be hypothesised [PR03] that the Dark Energy density associated with Λ is running and has reached nowadays – because Dark Energy had almost 13.4 billion years time for running by now – close to a value that would be somewhat natural, namely zero.

1.2. Dark Energy and the Standard Cosmological Model

Before we are going to discuss rather direct evidence for a recent acceleration of the cosmic expansion, we will concisely review the current standard model of cosmology. This comprises the underlying symmetries of the Friedmann-Robertson-Walker spacetime as well as the resulting general relativistic dynamics of the model. Also the basic concepts and the consequences of the standard inflationary scenario are reviewed.

In cosmology there exist several definitions of what may be attributed as an observable distance to an astronomical object. The non-trivial point is that the various distance measures give approximately the same result only for nearby objects and moreover that their measurement for distant objects is sensitive to the particular dynamics of the underlying theory. There exists recent evidence that supports the presence of Dark Energy provided by the analysis of distant supernovae. Under the assumption that supernovae of type Ia form a class of standard candles their measured brightness can be used to directly test the distance-redshift relation within different dynamical realisations of the standard model.

1.2.1. The Standard Model in a Nutshell. A very crucial statement that is made right from the beginning is that the Universe appears *isotropic* to us in a global sense when observed from earth. Second, following the *Copernican standpoint* it is assumed that an observation of the Universe made from any other galaxy should also look isotropic for the observers there. Once we accept this, the Universe must also be *homogeneous* because of its isotropy around any point. Of course, observations of our near neighbourhood do neither look homogeneous nor isotropic at first glance. In the standard model it is assumed that there is a transition from a clumpy to an approximately smooth picture at a scale of roughly 100Mpc. This implies, that when we place balls of radius 100Mpc in the Universe at random locations and we measure the mass profile within an ensemble of balls then the root mean square fluctuation of the values taken at 100Mpc is roughly equal to the mean value, such that we can regard the fluctuations at large scales as perturbations on top of the homogeneous model. On the other hand, the smaller the scale, the more non-linear are the departures of fluctuations from homogeneity. In the following we review the nice overview paper by Peebles and Ratra on Dark Energy and the standard model [PR03].

Within the framework of General Relativity, homogeneity and isotropy lead quite naturally to the expansion of the Universe. Expansion of the Universe means that the proper physical

distance D_P between two well-separated galaxies as a function of cosmic time t is

$$(1.4) \quad D_P(t) \propto a(t),$$

where a is the scale factor. But a is defined such that it is independent of the choice of galaxies we make for the comparison. Thus the expansion (1.4) preserves homogeneity and isotropy. The derivative of (1.4) gives us the proper speed

$$(1.5) \quad v_P(t) = \frac{dD_P}{dt} = H(t)D_P, \quad H(t) \equiv \frac{\dot{a}(t)}{a(t)},$$

introducing the Hubble parameter H and denoting derivatives with respect to cosmic time with a dot. The value of the Hubble parameter as measured today is a central parameter and so we give here its current measure (2007) according to [Y⁺06]

$$(1.6) \quad H_0 = 100 h \text{ km s}^{-1} \text{ Mpc}^{-1} = h (9.78 \text{ Gyr})^{-1} \quad \text{with} \quad h = 0.73_{-0.03}^{+0.04}.$$

The actual expansion of the Universe was first observed in 1929 and it is referred to as the Hubble expansion due to its discoverer [Hub29].

A law similar to (1.4) also holds for the wavelengths of light signals that are exchanged between two galaxies. The change in wavelength that a signal – a given feature in the spectrum – undergoes that has been emitted from a distant source amounts to

$$(1.7) \quad \frac{\lambda_{\text{ob}}}{\lambda_{\text{em}}} = \frac{a(t_{\text{ob}})}{a(t_{\text{em}})} \equiv 1 + z,$$

and z is called the cosmological redshift. The redshift provides the most convenient characteristic to label observations of the Universe that reach into the very far past. For example, the decoupling of matter and radiation in the young Universe which is the origin of the CMB radiation, occurred at around $z = 1088$. The Universe is ionised today; from CMB measurements one infers that reionisation took place at redshifts of around $z \simeq 10$. The galaxy cluster SDSS J1004 + 4112 shown in fig. 1.1 is observed at a redshift of around $z \simeq 0.68$. How in general the redshift is translated into distances, or vice versa, is generically depending on the parameters of the underlying general relativistic model. However, given a small redshift $z < 1$, equation (1.7) becomes Hubble's law, which then reads to lowest order: $cz = HD_C$.

The results so far have been obtained by using homogeneity and isotropy only, and represent the low-redshift limit of the standard model. However, for extrapolation to higher redshifts $z > 1$, the general relativistic formulation of the theory is to be used. The crucial assumptions of homogeneity and isotropy are reflected by the well-known Friedmann-Robertson-Walker (FRW) spacetime

$$(1.8) \quad ds^2 = -dt^2 + a^2(t) \left[\frac{1}{1 - kr^2} dr^2 + r^2 (d\theta^2 + \sin^2\theta d\varphi^2) \right].$$

Through remapping of the radial coordinate one usually normalises the spatial curvature parameter k such that it takes the values $k = 1, 0, -1$, which stand for a closed, flat or open spatial geometry of the model. The metric can be rewritten as

$$(1.9) \quad ds^2 = -dt^2 + a^2(t) [d\chi^2 + S_k^2(\chi) (d\theta^2 + \sin^2\theta d\varphi^2)],$$

by introducing the function $S_k(\chi)$ with

$$(1.10) \quad S_k(\chi) = \begin{cases} \sin\chi & \text{for } k = 1 \\ \chi & \text{for } k = 0 \\ \sinh\chi & \text{for } k = -1 \end{cases}.$$

Employing the Friedmann-Robertson-Walker metric and the assumption that on large scales the galaxies behave like the constituents of a perfect fluid, one can solve the field equations

$$(1.11) \quad G_{\mu\nu} \equiv R_{\mu\nu} - \frac{1}{2} R g_{\mu\nu} = 8\pi G [(\rho + p) u_\mu u_\nu + p g_{\mu\nu}] + \Lambda g_{\mu\nu},$$

and, denoting cosmic time derivatives with a dot, obtain the result:

$$(1.12) \quad \frac{\ddot{a}}{a} = -\frac{4}{3}\pi G(\rho + 3p) + \frac{\Lambda}{3}.$$

The covariant conservation of energy and momentum $T^{\mu\nu}{}_{;\mu} = 0$ implies then additionally

$$(1.13) \quad \dot{\rho} = -3H(\rho + p).$$

Integrating the equations (1.12) and (1.13) yields the important *Friedmann equation*

$$(1.14) \quad H^2 = \frac{8}{3}\pi G\rho - \frac{k}{a^2} + \frac{\Lambda}{3},$$

and the integration constant k is related to the present value of the spatial curvature via

$$(1.15) \quad \Omega_k = -\frac{k}{H_0^2 a_0^2}.$$

If Λ is constant, a useful way of writing the Friedmann equation is

$$(1.16) \quad H^2(z) = H_0^2 [\Omega_m(1+z)^3 + \Omega_r(1+z)^4 + \Omega_\Lambda + \Omega_k(1+z)^2],$$

and similarly one rewrites the equation (1.12)

$$(1.17) \quad \frac{\ddot{a}}{a} = -H_0^2 \left(\Omega_m \frac{(1+z)^3}{2} + \Omega_r(1+z)^4 - \Omega_\Lambda \right),$$

whereby the remaining density parameters of the standard model Ω_i are given by

$$(1.18) \quad \Omega_{m,r} = \frac{\rho_{m,r}}{\rho_{\text{crit}}}, \quad \rho_{\text{crit}} \equiv \frac{3H_0^2}{8\pi G}, \quad \Omega_\Lambda = \frac{\Lambda}{H_0^2}.$$

The use of (1.16) lies in the fact that one can immediately read off the redshift dependence of the respective components of the Friedmann model. Therein, Ω_m stands for all non-relativistic matter whose pressure we neglect ($p_m \ll \rho_m$). We see that the mass density is diluted by the expansion of the Universe as $\rho_m \propto a^{-3} \propto (1+z)^3$. Further, Ω_r stands for radiation (e.g. the CMB) as well as relativistic matter with equation of state^a $w = 1/3$, and behaves like $\rho_r \propto a^{-4} \propto (1+z)^4$ under expansion. By construction, Λ is constant for the moment, and further the density corresponding to spatial curvature (1.15) is diluted as $\rho_k \propto a^{-2} \propto (1+z)^2$.

eq. of state	density	scaling	Hubble
w	$\rho \propto a^{-3(1+w)}$	$a(t) \propto t^{\frac{2}{3(1+w)}}$	$H(t) = \frac{2}{3(1+w)} \frac{1}{t}$
radiation, $w = \frac{1}{3}$	ρa^{-4}	$a(t) \propto t^{1/2}$	$H(t) = \frac{1}{2t}$
matter, $w = 0$	ρa^{-3}	$a(t) \propto t^{2/3}$	$H(t) = \frac{2}{3t}$

TABLE 1.1. Standard solutions to the Friedmann equation for a radiation dominated and a matter dominated Universe. The FRW expressions for density, scale factor and Hubble parameter assuming a contribution with equation of state w are given in the first line. Regarding a Dark Energy contribution with $w = -1$ the density is constant and integration of the Friedmann equation yields the exponential behaviour (1.25).

Next, we want to consider the properties of Λ in further detail. As inspired by special relativity, we can make the assumption that every inertial observer should measure the same vacuum. An inertial observer is an observer who lives locally in a Minkowskian frame, that is his metric is characterised by $\eta_{\mu\nu} = \text{diag}(-1, \mathbf{1})$. Now, the form of the metric is left invariant by Lorentz transformation to some other inertial observer's frame. Because we assumed that all inertial observers should see the same vacuum, the energy-momentum tensor is

$$(1.19) \quad T_{\mu\nu}^\Lambda = \rho_\Lambda g_{\mu\nu},$$

^aIn the cosmological context the term equation of state refers to the ratio $w = p/\rho$.

with a constant vacuum energy density ρ_Λ . Thus the field equations can be written in the form

$$(1.20) \quad G_{\mu\nu} = 8\pi G(T_{\mu\nu} + \rho_\Lambda g_{\mu\nu}),$$

which reflects Einstein's original idea^b of modifying the energy-matter content of the Universe by adding a constant Λ . We see that Dark Energy behaves like an ideal fluid with negative pressure according to the equation of state

$$(1.21) \quad p_\Lambda = -\rho_\Lambda.$$

At the time Einstein thought about this modification, the Hubble recession of nebulae was not yet established; quite the contrary, a static cosmos was the state of the art, which was an extrapolation of the finding that nearby stars moved at low velocities. In order to obtain a static solution with $\ddot{a} = 0$ Einstein introduced an Ω_Λ – in modern language – to neutralise the (positive) contributions of the other ingredients of matter and radiation, c.f. (1.17). However, the balance $\ddot{a} = 0$ is not a stable one because already small perturbations to either the mean mass density or the distribution of mass will cause the Universe to contract or expand. Note that, if the density ρ_Λ is not constant in time – which is the case in many modern Dark Energy scenarios – also the Dark Energy momentum tensor would have a form that differs from (1.19), such that in the end the characteristics of the vacuum do depend on the observer's velocity.

In the context of gravitational fluid dynamics one usually distinguishes between the active and passive gravitational mass density. The active mass density ($\rho + 3p$) stands for the gravitational field that is generated by the fluid, the passive gravitational mass density ($\rho + p$) is a measure of how the fluid streaming velocity is affected by a gravitational source. Thus, in the Dark Energy model characterised by (1.19) and (1.21), the active gravitational mass density is negative (assuming a positive ρ_Λ) and if this dark component dominates the energy-momentum tensor then \ddot{a} will be positive. This reflects the fact that the expansion of the Universe accelerates. Thus one can summarise the effect of Λ in physical terms as follows: the accelerated expansion is not the result of some new force, rather it is due to the negative active gravitational mass density that we can associate with the Dark Energy. Then, considering non-relativistic movement, the relative acceleration \mathbf{g} of free falling test bodies is modified by a homogeneous active mass density due to the presence of Λ to^c

$$(1.22) \quad \frac{d^2\mathbf{r}}{dt^2} = \mathbf{g} + H_0^2\Omega_\Lambda\mathbf{r}.$$

We can already guess that the magnitude of this effect is probably small. We can estimate the size of the ratio of accelerations g_Λ/g . Let us assume that the Solar System moves in a circular orbit around the centre of the Milky Way with a circular speed of $v \simeq 220\text{km/s}$ at a radius of

^bTo be exact, this is not strictly true. Though mathematically the same, Einstein [Ein17] added the new term to the left hand side of the field equations, that is to the 'geometric side': $G_{\mu\nu} - \Lambda g_{\mu\nu} = 8\pi G T_{\mu\nu}$. Note that Einstein further motivated this modification by an analogy to Newton Gravity. Interestingly, in Newton Gravity one encounters a serious problem with a world model that is homogeneous and infinite. It was already seen by Newton himself that the gravitational potential energy of such a system diverges: the volume of a shell at distance r to $r + \delta r$ from an observer is $\delta V = 4\pi r^2 \delta r$ and with the assumption of homogeneous mass density ρ , the mass within δV amounts to $\delta M = 4\pi \rho r^2 \delta r$. Thus the gravitational potential energy according to this mass becomes $\delta U = G\delta M/r = 4\pi G\rho r \delta r$. Integrating δU we see that U diverges like r^2 when r becomes very large [Pee93]. Einstein and after him others, c.f. [PR03], suggested a cure for this situation by a modification of the Poisson equation according to $\Delta^{(3)}\phi - \lambda\phi = 4\pi G\rho$, which gives the potential of a point mass a Yukawa form $\phi \propto e^{-\sqrt{\lambda}r}$ (these solutions are also called Seeliger-Neumann solutions). Now, the modified Poisson equation allows for a homogeneous static solution $\phi = -4\pi G\rho/\lambda$. But the analogy should not be taken too seriously: note that the modified Poisson equation does not come out as a Newtonian limit from the general relativistic equation with cosmological constant. That is, Λ does not act like a long-range cutoff in gravitation, it is rather a repulsive form of energy that is in opposition to the mean gravitational attraction of matter.

^cAlso, the instability of the static Einstein solution can be seen from equation (1.22). A mass distribution can be assigned such that the right hand side of equation (1.22) vanishes but this equilibrium can then be easily destroyed by just redistributing the mass again.

$r \simeq 8\text{kpc}$. The ratio of g_Λ to the total gravitational acceleration $g = v^2/r$ is then estimated by

$$(1.23) \quad \frac{g_\Lambda}{g} = \frac{H_0^2 \Omega_\Lambda r^2}{v^2} \sim 10^{-5}.$$

This is already a small number but it becomes much smaller when the radius is reduced. Since the Sun is already located at the very outskirts of the luminous disc of the Milky Way, the possibility of detecting this effect by measuring deviations from the ordinary internal dynamics in other galaxies is not very promising. The accuracy of precision tests of gravitation on the level of our Solar System is much better. But on these scales the ratio (1.23) is of the order $g_\Lambda/g \sim 10^{-22}$. Next we want to consider a complication, namely a working model for a dynamical ρ_Λ .

The aforementioned mechanism of coupling Λ to a negative active gravitational mass density is closely related to the concept of cosmological inflation. There exists a problem that is encountered if we assume that the Universe was evolving due to a FRW solution within its entire history. Let us recall the expression for the particle horizon

$$(1.24) \quad x = \int \frac{dt}{a(t)},$$

where we assumed spatial flatness. It is a measure of the integrated coordinate displacement as a light ray moves the proper distance $dl = a(t)dx$ during the time dt . Now the point is that for vanishing Ω_Λ the integral (1.24) does converge in the past (ax is the proper radius of the particle horizon), that is our view should fall on several causally disconnected parts of the Universe. In order to make the Universe homogeneous, signals must travel between the regions that are in contact with at most the speed of light. Thus, no regions that are more than $2ax$ apart could have ever been in causal contact. Let us try an estimate: assuming that the temperature of the young Universe was $T \simeq 10^{14}\text{GeV}$ at some initial time t_{init} , we can then imagine a corresponding causally connected ball with radius $2ax$ that has expanded and today should form the border of the currently observable Universe. In our simple estimate, the temperature of the Universe has evolved from that initial epoch at $T \simeq 10^{14}\text{GeV}$ to $T_0 \simeq 2.7\text{K} \simeq 2.4 \times 10^4\text{eV}$ today, thus giving a factor of expansion of the Universe of $T/T_0 \simeq 4 \times 10^{26}$. Moreover, at the temperature $T \simeq 10^{14}\text{GeV}$, the horizon size has been $2ax \simeq 6 \times 10^{-25}\text{cm}$ at a time of $t_{\text{init}} \simeq 10^{-35}\text{s}$. Therefore the primordial causal ball would have expanded to a size of 2.4m today which is rather small for the current size of the Universe. And how can then galaxies as observed today in different directions on the sky look so similar^d to each other? The answer is provided by the statement that the expansion history of the Universe was not FRW-like for a certain time period in the young Universe. Instead one assumes a DeSitter solution with $\Lambda > 0$ and $T_{\mu\nu} = 0$ and the scale factor behaviour

$$(1.25) \quad a(t) \propto e^{H_\Lambda t},$$

with H_Λ being constant. That is, in the DeSitter model, the Universe undergoes a phase of exponential blowup and Λ becomes essential.

In the inflationary view the early universe is dominated by a large Dark Energy density ρ_Λ . Then the Dark Energy can be modelled with the help of an approximately homogeneous scalar field Φ in analogy to models known from quantum field theory. The action takes the form

$$(1.26) \quad S = \int \sqrt{-g} \left(\frac{1}{2} g^{\mu\nu} \partial_\mu \Phi \partial_\nu \Phi - V(\Phi) \right) d^4x,$$

^dOne can give another very instructive illustration of the horizon problem regarding the CMB. Using the concept of the angular diameter distance (1.38) (which is a measurable quantity) one can compute that up to the time of last scattering of the CMB photons, regions that could have had causal contact to each other, today have the size of approximately one degree on the sky. That means an image of the CMB should contain many patches of size one degree that are rather anisotropic as a whole because they never had the chance to communicate. Maps of the CMB however, show a totally different situation: the CMB appears overall isotropic to a high degree.

where g is the determinant of the metric $g = \det(g_{\mu\nu})$ and we used $\hbar = 1$. The function $V(\Phi)$ is the potential energy density and with vanishing spatial curvature we get the field equation

$$(1.27) \quad \ddot{\Phi} + 3\frac{\dot{a}}{a}\dot{\Phi} + \frac{dV(\Phi)}{d\Phi} = 0.$$

We can define the rest frame of an observer who is moving such that the Universe looks isotropic; then the energy-momentum tensor of the homogeneous field Φ is diagonal with

$$(1.28) \quad \rho_{\Phi} = \frac{1}{2}\dot{\Phi}^2 + V(\Phi) \quad \text{and} \quad p_{\Phi} = \frac{1}{2}\dot{\Phi}^2 - V(\Phi).$$

From these equations it is clear that if the scalar field varies slowly with time $\dot{\Phi}^2 \ll V$, then the equation of state of the cosmological constant can be recovered: $p_{\Phi} \simeq -\rho_{\Phi}$.

Normally it is assumed in inflationary theory that the exponential phase (1.25) lasts so long that all regions in the observable Universe have reached causal contact with each other. Eventually Φ can start to vary rapidly thus producing entropy for the Universe. This is because after a rollover phase the field falls into the potential well of the real vacuum and starts to oscillate due to its kinetic energy. The large initial vacuum energy is transformed into coherent oscillations of the field Φ and these fluctuations are damped – besides the Hubble friction $3H\dot{\Phi}$ – by particle production or the interaction of Φ with other fields, which is equivalent to a thermalisation of the field energy and entropy production. Through this so called reheating, e.g. baryons can be produced and in the end ρ_{Φ} remains small or zero. However, it is conceivable that ρ_{Φ} could have a very slow late-time behaviour, possibly slower than the evolution of the matter density. Then ρ_{Φ} will be dominant again, after a certain time and this could provide an answer to the coincidence problem. A concrete ansatz that leads to such a late time evolution of ρ_{Φ} is $V_{\kappa} = \kappa/\Phi^{\alpha}$ with a constant κ that has the dimension of $\text{mass}^{\alpha+4}$ [PR03]. We can constrain the form of the scale factor by assuming that after the inflationary phase the Universe is dominated by matter or by radiation which leads to a power law expansion behaviour of $a \propto t^n$, c.f. tab. 1.1. With this form of the scale factor we can solve the field equation (1.27) and obtain $\Phi \propto t^{2/(2+\alpha)}$. The mass density associated with the scalar field Φ behaves like $\rho_{\Phi}/\rho \propto t^{4/(2+\alpha)}$ with respect to the matter or radiation density. Thus we can recover Einstein's cosmological constant Λ from this model in the limit of $\alpha \rightarrow 0$ which corresponds to a constant ρ_{Φ} . In the case $\alpha > 0$ the field Φ can grow very large and due to $V_{\kappa} = \kappa/\Phi^{\alpha}$ the according density will go to zero, $\rho_{\Phi} \rightarrow 0$, which implies that the Universe approaches a Minkowskian state. Such a power law model with $\alpha > 0$ has two important characteristics [PR03]. First, the energy density of matter and radiation decreases more rapidly than that of the scalar field solution. This implies that it is possible to have a ρ_{Φ} that is small right after inflation (but still at high redshift) and thus does not interfere with the standard production scenario of the light elements. However, after some time ρ_{Φ} can dominate again, mimicking a cosmological constant. Second, it has been shown by Ratra and Peebles that the class of solutions $\alpha > 0$ has the attractor characteristic, that is a vast range of initial conditions eventually end up with this solution.

The inflationary scenario explains the large-scale homogeneity of the Universe today by postulating a DeSitter-like phase of exponential growth of the Universe at very early times. Moreover it provides the initial conditions for structure formation by the vast freezing of zero-point quantum field fluctuations to cosmological scales. Thus the seeds for the observed structures on cosmological scales today have originated from quantum fluctuations of the early Universe. The power spectrum of the classical density fluctuations that have been frozen out from quantum fluctuations is

$$(1.29) \quad P(k) = \langle |\delta(k, t)|^2 \rangle = Ak^n T^2(k),$$

where $\delta(k, t)$ is the Fourier transform of the density contrast, $\delta(\mathbf{x}, t) = \rho(\mathbf{x}, t)/\bar{\rho}(t) - 1$ at wavenumber k , with the mass density ρ and its mean $\bar{\rho}$. A is a constant that comes out from the concrete form of the potential V one chooses within a given inflationary model. The transfer function $T(k)$ governs how the density contrast $\delta(k, t)$ evolves under the influence of radiation

pressure and the dynamics of matter at redshifts $z \lesssim 10^4$. Now, for an inflationary expansion following an approximate DeSitter solution (1.25), the *spectral index* n will be close to unity^e. A spectrum with exactly $n = 1$ is called *Harrison-Zel'dovich power spectrum*. The striking feature of such a spectrum is that it would have equal power (amplitude) in all its modes at the time it enters Hubble horizon and is this also named *scale invariant*. Anticipating results for the Sachs-Wolfe effect from sec. 1.3.3 we can understand the notion of *scale invariance* alternatively by the following result [Lon98] for the angular scale dependence of CMB temperature fluctuations originating from an initial power spectrum proportional to k^n ,

$$(1.30) \quad \frac{\Delta T}{T} \simeq \frac{\Delta \phi}{c^2} \propto \theta^{(1-n)/2},$$

with $\Delta T/T$ being scale-free in the Harrison-Zel'dovich case $n = 1$. Note that more complicated scalar field potentials can be imagined (e.g. exponential form potentials) under which the spectral index is tilted $n \neq 1$ and can be used as an additional free parameter of the model. However, recent CMB measurements indicate that $n = 1$ is very close to the best fit^f. The initial conditions for the mass distribution in these inflationary models are provided by a single function $\delta(\mathbf{x}, t)$, which is a realisation of a *spatially random Gaussian process* since the macroscopic perturbations are frozen out from almost free and pure quantum fluctuations. This is also referred to as *adiabaticity* because such fluctuations can be understood as the result of purely adiabatic compressions and decompressions of regions of an homogeneous (post-inflationary) Universe. A consequence of the fact that the simplest inflationary models obey the above conditions is that the initial condition as described by a single function of position $\delta(\mathbf{x}, t)$ is statistically fully characterised by its power spectrum (1.29). More complicated models of inflation for instance produce fluctuations that are not exactly Gaussian or have power spectra that cannot be brought into a power law form.

Before we come to the cosmological tests of the standard model let us return to the problem of the smallness of the vacuum energy density. The zero-point energy of quantum fields contributes to the Dark Energy density. A relativistic field can be understood as a collection of quantum mechanical harmonic oscillators with all possible frequencies ω . The zero-point energy will be non-vanishing and amounts, by superposition of frequencies, to $E_0 = \sum_i \omega_i/2$, where i labels oscillators and $\hbar = 1$. We can think of the system as locked in a box of length L and we then consider the limit $L \rightarrow \infty$ under appropriate periodic boundary conditions. We then have

$$(1.31) \quad E_0 = \frac{L^3}{2} \int \frac{\omega_k}{(2\pi)^3} d^3k,$$

with the wavenumber $k = 2\pi/\lambda$. We are considering a massive bosonic field $\tilde{\Phi}$. By employing the dispersion relation $\omega_k^2 = k^2 + m^2$ and introducing a cutoff frequency $k_{\max} \gg m$ in order to make physical sense^g, we arrive at [KKZ97]

$$(1.32) \quad \rho_{\tilde{\Phi}} = \lim_{L \rightarrow \infty} \frac{E_0}{L^3} = \int_0^{k_{\max}} \frac{4\pi k^2}{(2\pi)^3} \frac{\sqrt{k^2 + m^2}}{2} dk = \frac{k_{\max}^4}{16\pi^2}.$$

^eLet us add a small note on the approximation of $n = 1$ in inflationary models. In general, it depends on the particular underlying scalar field dynamics of the model in how far scale invariance is realised. In slow roll inflation the field is initially rolling down the inflationary potential slowly and its movement is sizeably damped by the Hubble friction term $3H\dot{\Phi}$. Imagine a limit where the damping is extremely intense and the rollover becomes infinitely slow, then this would correspond to exact scale invariance $n = 1$. Consequently, a genuine inflationary prediction is $n = 1 \pm \varepsilon$ with some small ε . The (small) deviations of a particular model of inflation from exact scale invariance quantify how slow the field actually has rolled and how strongly it was damped meanwhile, see also [DS02].

^fActually, from WMAP(3yr) data alone a value of $n = 0.958 \pm 0.016$ is obtained [S+07]. Nevertheless, a running spectral index, that is an n that varies a bit with the wavenumber k of the perturbation modes, is slightly preferred by the WMAP(3yr) data.

^gNote that, as we introduce a cutoff wavenumber k_{\max} , we at the same time have to specify in what frame the cutoff is defined, thus invoking a preferred frame. This violation of Lorentz invariance poses a problem of the argument and there seems not to be a satisfactory resolution by now. In [Akh02, PR03] one can find a discussion of possible interpretations of the occurring ambiguity.

If we assume General Relativity to be valid up to, say the Planck scale and set $L_{\text{Planck}} = (8\pi G)^{-1/2} = k_{\text{max}}$ we obtain a value for the vacuum energy density of

$$(1.33) \quad \rho_{\bar{\Phi}} \sim 10^{92} \text{gcm}^{-3},$$

which is 121 orders of magnitude off the observed value of $\sim 10^{-30}$. Reducing the cutoff scale to the electroweak scale of $\sim 200\text{GeV}$ still produces a discrepancy of 54 orders of magnitude; inserting the QCD scale Λ_{QCD} as cutoff results in a mismatch of 42 orders of magnitude. These discrepancies could indicate a massive incompleteness of the current underlying physics; it is thinkable that there might be some connection between the different components in (1.3) coming from yet undiscovered physics that causes the almost complete cancellation of the seemingly uncorrelated terms in (1.3), c.f. [KKZ97].

1.2.2. Distance Measures and Dark Energy Evidence. In order to describe the current phenomenology of the standard model we first should recall the common distance measures in cosmology. We have already introduced the proper distance D_{P} through (1.4). Another natural distance is that associated with the current Hubble volume, the Hubble distance

$$(1.34) \quad D_{\text{H}} \equiv \frac{c}{H_0}.$$

Assuming continuous FRW evolution, an object that would be seen at a distance of roughly the Hubble distance is seen as it was around a Hubble time in the past. The Hubble distance represents a measure of the observable Universe, c.f. fig. 1.2.

The definition of the Hubble parameter as a function of redshift (1.16) will be very useful in the following. The constant of proportionality of the proper distance scaling (1.4) can be expressed by the comoving distance. The comoving distance along the line of sight is defined by

$$(1.35) \quad D_{\text{C}} \equiv D_{\text{H}} H_0 \int_0^z \frac{dz'}{H(z')}.$$

The comoving distance between two points that were close in redshift in the past is the distance we would measure today between the points if they were glued to the expanding background, c.f. [Hog00]. See fig. 1.2 for an illustration of proper and comoving distances and their relation to important cosmological scales like the particle horizon and the Hubble distance.

Going further, one can define a comoving distance in a lateral sense. If we measure two objects at the same redshift that are separated by an angle θ on the sky then their comoving distance is $D_{\text{TC}}\theta$ with transverse comoving distance denoted by D_{TC} and defined by

$$(1.36) \quad D_{\text{TC}} \equiv \begin{cases} D_{\text{H}}\Omega_k^{-1/2} \sinh(\Omega_k^{1/2} D_{\text{C}}/D_{\text{H}}) & \text{for } \Omega_k > 0 \\ D_{\text{C}} & \text{for } \Omega_k = 0 \\ D_{\text{H}}\Omega_k^{-1/2} \sin(\Omega_k^{1/2} D_{\text{C}}/D_{\text{H}}) & \text{for } \Omega_k < 0 \end{cases}.$$

If the cosmological constant vanishes there exists a closed solution

$$(1.37) \quad D_{\text{TC}} = 2D_{\text{H}} \frac{2 - (1-z)\Omega_{\text{m}} - (2 - \Omega_{\text{m}})(1+z\Omega_{\text{m}})^{1/2}}{(1+z)\Omega_{\text{m}}^2} \quad \text{for } \Omega_{\Lambda} = 0.$$

It can be shown that there is a correspondence between transverse comoving distance and the so called proper motion distance. The proper motion distance is defined as the ratio of transverse velocity to proper motion of an object and is measured in radians per time, c.f. [Wei72].

The ratio of the lateral physical size of an object to its angular size is an explicit observable called the *angular diameter distance*. It is very useful for cosmological measurements. Especially when considering the CMB which can be mapped onto a sphere at $z = 1088$, it is crucial to convert angular separations measured by an instrument to proper separations in the source plane. The angular diameter distance is given by

$$(1.38) \quad D_{\text{A}} \equiv \frac{D_{\text{TC}}}{1+z}.$$

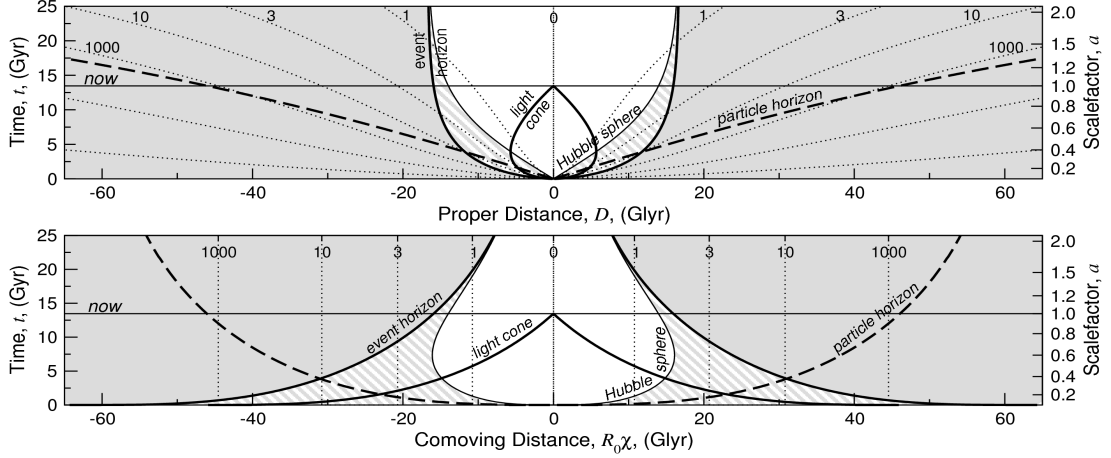


FIGURE 1.2. Spacetime diagrams of cosmological time versus proper distance (upper figure; D_P in our notation) and versus comoving distance (lower figure; D_C in our notation) within a fiducial FRW model with $(\Omega_m, \Omega_\Lambda) = (0.3, 0.7)$ and $H_0 = 70 \text{ km s}^{-1} \text{ Mpc}^{-1}$. Therein the dotted lines, that are labelled by values of redshift, represent the worldlines of comoving objects. The past *light cone* (belonging to the observer with central worldline at zero distance) enfolds all events that we are currently ($t = \text{now}$) observing. Further, there are three kinds of horizons in the figures: the *particle horizon* names the distance that light can principally have travelled from $t = 0$ until some given t , c.f. (1.24), and the redshift of objects at particle horizon becomes infinite; the *event horizon* represents the distance that light can have travelled from a given time t until $t = \infty$; the *Hubble sphere* enfolds the set of spacetime events beyond which comoving objects are receding faster than light – the Hubble sphere is not really a horizon because $z \neq \infty$ for objects at Hubble distance and moreover it is possible to see beyond it in cosmological models with $q < -1$. As can be seen from the slope of the light cone, the speed of photons relative to the observer $v_{\text{rec}} - c$ is not constant. Photons from the region of superluminal recession (hatched) can only reach us when coming to the region of subluminal recession (no shading). As can be seen in the figure, initially objects beyond the Hubble sphere have been receding from us – note the bulge of the light cone at $t \lesssim 5 \text{ Gyr}$. Note that the light cone does not hit the line $t = 0$ asymptotically; rather it reaches a finite distance of $\sim 46 \text{ Glyr}$ at $t = 0$ which is exactly the current distance to the particle horizon. Thus, the light of any objects that are currently observable to us, whose light has propagated toward us since $t = 0$, has been emitted from comoving positions around 46 Glyr (14 Gpc) away from us. Note that the aspect ratio of the figures $\sim 3/1$ reflects the ratio of the size of observable Universe to its age $\sim 46/14$. The pictures are taken from [DL03].

In contrast to several other distance measures, the angular diameter distance does not diverge for $z \rightarrow \infty$, in fact it is not a monotonic function of z ; it reaches a maximum at around $z \sim 1$. At high redshifts one can say, as a rule of thumb, that the angular diameter distance relates an angular separation of one arcsecond to a size of $\sim 5 \text{ kpc}$ [Hog00].

The *luminosity distance* measures the ratio of total bolometric (i.e. integrated over all frequency bands) luminosity L to the apparent luminosity L_A . The apparent luminosity or bolometric flux L_A is the power received per unit mirror area. The apparent luminosity of a non-moving source at some distance l in Euclidean space would be $L/(4\pi l)$. Therefore it makes sense to generalise this and define the luminosity distance as [Wei72]

$$(1.39) \quad D_L \equiv \left(\frac{L}{4\pi L_A} \right)^{1/2}.$$

However, in astronomy what is really measured is the apparent magnitude m . After fitting for the calibration factor M (absolute magnitude) one usually uses the difference of these magnitudes for analysis: the distance modulus $m - M$. The distance modulus is related to the luminosity distance through $m - M = 5 \log(D_L/1 \text{ Mpc}) + 25$, with the number 25 coming from the fact that the distance modulus is defined to vanish at 10pc. Note that due to a fundamental result – the reciprocity theorem, c.f [EvE98] – the angular diameter distance and the luminosity distance can be related directly by

$$(1.40) \quad D_L = (1 + z)^2 D_A = (1 + z) D_{TC}.$$

Based on the concept of the luminosity distance, in 1998 the first direct evidence for an apparent accelerated expansion of the Universe was published [R⁺98, P⁺99]. This was made possible by measurements of the redshift and the (luminosity) distance of supernovae. The appearance of this kind of evidence was dubbed a cosmological revolution, for it provided the first direct evidence that the Universe may recently have become dominated by some mysterious form of energy. After this discovery, measurements of the CMB and statistical analyses of galaxy-redshift surveys have confirmed the supernova findings, albeit in a more indirect way. However, the supernova measurements remain up to today the most direct means of probing a present large-scale acceleration of the Universe. What one necessarily needs in order to make reliable measurements with the help of the luminosity distance (1.39) is a *standard candle*. A standard candle would be – in a much simplified sense – something like a constant 100W light bulb. That means, if we can rely on the fact that the light bulb is standardised, i.e. it always will emit a power of 100W, then we can infer the distance to the bulb by measuring its apparent luminosity. Now, in cosmology it appeared at first not promising to think of supernovae as standard candles because their observation yields a very heterogeneous class of light curves. Originally, the classification scheme for supernovae was such that the type SNI was characterised by the lack of hydrogen features in the supernova spectrum. From 1980 on the astronomers divided the type I supernovae into two subclasses: Ia and Ib. The distinction was made due to the presence or absence of a certain silicon absorption feature at 6150Å. In the light of this reclassification a remarkable uniformity in the light curves of supernovae Ia suddenly became apparent.

But, are SNIa really standard candles in a strict sense? One speculates that SNIa originate from exploding white dwarfs. But why should the white dwarfs explode and why should this then happen at a uniform threshold? Normally, white dwarfs are produced as remnants of Sun-like stars that have used up their nuclear fuel for fusion. The only thing that saves the dwarf from further collapse is the effective pressure upheld by electron degeneracy. Now, if it happens that the white dwarf is provided with some steady stream of matter accreting onto its surface, it would accumulate mass until a common physical threshold – which is near the Chandrasekhar mass of $\simeq 1.4M_\odot$ – and then suddenly erupt within a massive thermonuclear explosion. If this scenario is true then essentially always the same physical process triggers SNIa explosions, which then would back the assumption of regarding SNIa as standard candles. Still, taking an accurate look, the uncorrected light curves of SNIa do show some offset. Their maximal luminosities exhibit a slight but obvious dispersion of roughly 0.4 magnitudes as measured in the blue band [Sch06]. One finds a strong correlation between intrinsic brightness and the shape of the respective light curves: the supernovae that have a higher maximal brightness also decrease slower (as measured from their maximum) than those with smaller maximal brightness. Moreover it turned out that supernovae that were fainter also appeared redder or were observed in highly inclined host galaxies. This effect can be attributed to an extinction in the host galaxy additional to the extinction in the Milky Way. Altogether it is possible to quantify these systematics with a phenomenological recalibration that takes care of both the maximal brightness-duration correlation and the extinction. The fundamental calibration is gauged to a sample of supernovae that were located in host galaxies to which the distances are very well known. Once the above explained correction to SNIa is applied they appear to be appropriate standard candles. The collection of a sufficient number of SNIa observations requires very careful

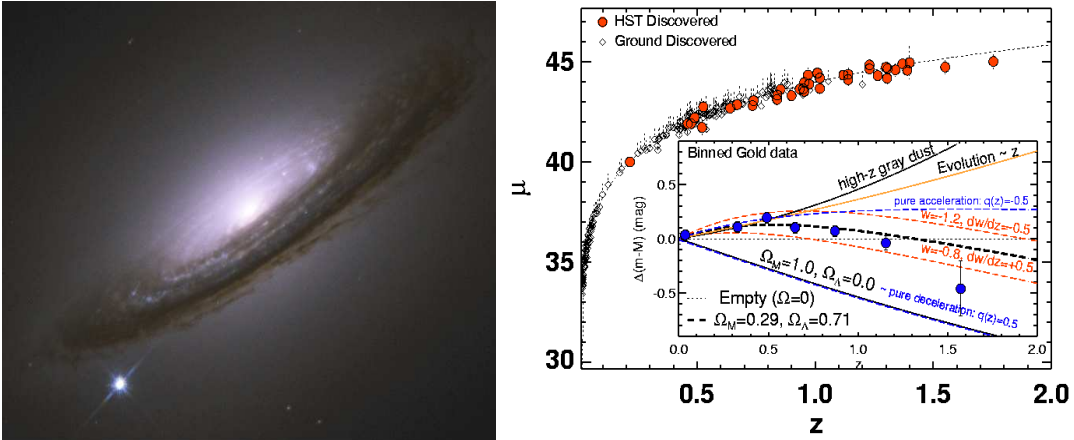


FIGURE 1.3. Supernovae of type Ia provide standard candles and measurements of far-away SNIa are sensitive to the cosmological parameters of the standard model. Left: an image of supernova 1994D that took place in the outer regions of its host galaxy NGC 4526. The supernova is of type Ia which implies that its light curve is very similar to any other supernova of the same type, irrespective of its distance or location. Combining a measurement of its luminosity distance with a measurement of the redshift of the host galaxy one can use such events to probe the Hubble law (1.41). Right: a Hubble diagram (distance modulus vs. redshift) of the 2006 Riess et al. sample [R⁺06]. The outer diagram shows the good fit of a $\Omega_{\Lambda} \simeq 0.71$, $\Omega_{\text{m}} \simeq 0.29$ standard model parametrisation. The inset is a binned residual Hubble diagram of 47 chosen (Gold Sample) SN with respect to an empty Universe $\Omega_{\text{m}} = 0 = \Omega_{\Lambda}$, being in accordance with a recent acceleration of the Universe. Note that supernovae at very high redshifts become again brighter than expected in the fiducial model, indicating the matter domination of the Universe at very early times. The pictures are taken from [APO] and [R⁺06].

logistics and search strategy: at new moon a large set of images of certain patches of the sky is made, then just at the next new moon exactly the same regions are imaged again and eventually found candidates are fastly assigned to follow-up spectroscopy.

Let us discuss how the supernova evidence can be quantified. The Hubble law corresponds to the following formula for the luminosity distance [SW07]

$$(1.41) \quad D_{\text{L}} = D_{\text{H}} \left[z + (1 - q_0) \frac{z^2}{2} + \left(-j_0 + 3q_0^2 + q_0 - 1 - \frac{k}{a_0^2} D_{\text{H}}^2 \right) \frac{z^3}{6} + \text{h.o.} \right],$$

to third order in z . One introduces the deceleration parameter and the jerk parameter

$$(1.42) \quad q = -\frac{\ddot{a}}{a} \frac{1}{H^2} \quad \text{and} \quad j = \frac{\dddot{a}}{a} \frac{1}{H^3}.$$

Note that this cosmological test is highly model-dependent. Within the standard model the deceleration parameter provides a measure for acceleration or deceleration of the cosmic expansion and the jerk parameter measures the rate of change of the latter. Thus, at high redshift potential deviations from the linear part in the Hubble law (1.41) should provide a measure of the parameters of the underlying cosmology. The predictions of different cosmological models (i.e. different parameter sets within the standard model) start to diverge at redshifts of around $z \sim 0.2$. The result of a recent measurement is shown in fig. 1.3. It is found that supernovae for^h $z \lesssim 1$ are even fainter than one would expect in an empty Universe model ($\Omega_{\text{m}} = 0 = \Omega_{\Lambda}$). The fiducial empty Universe model expands at a constant rate [$q = 0 = j$ in (1.41)]; in no other

^hNote that the Hubble law does not hold for measurements at very low redshift because here the Universe is evidently not homogeneous, see for instance fig. 1.5.

parametrisation with $\Omega_\Lambda = 0$ is the luminosity distance higher than in the empty Universe. Is it possible to increase the luminosity distance only if the Universe has expanded slower in the past than it does today, thus the cosmic expansion must have accelerated. Looking at the Einstein equation (1.12) this implies an $\Omega_\Lambda > 0$, if we believe in the very foundations of the standard model.

Moreover, supernovae at very high redshift $z \gtrsim 1$ provide additional evidence: they here appear brighter than expected in an empty Universe because at such early times the Universe was still matter dominated which is consistent with the above explained interpretation of supernovae at $z \lesssim 1$. Summarising the supernova results one can say that a recent accelerated expansion of the Universe with standard model parametrisation $\Omega_\Lambda \simeq 0.71$ and $\Omega_m \simeq 0.29$ provides an excellent fit to the available data sets.

As is indicated in fig. 1.3, nowadays the scope of experiments is not only to confirm the presence of Λ domination in recent times within the standard model, but moreover to try to measure the properties of Dark Energy for instance through its equation of state. Results of the ESSENCE supernova survey have recently been analysed especially under this viewpoint [D⁺07]. The study is done with the help of *Bayesian analysis* which is a statistical framework in which models are effectively penalised for not being economic with their parameters. The analysis unfolds tests with: Dark Energy models with variable equation of state, (flat) DGP braneworld models, Cardassian models and models of the Chaplygin gas. The result of the competition is that the most simple spatially flat Ω_Λ dominated model represents the best fit to the ESSENCE sample.

Besides the findings from supernova surveys other important cosmological probes converge to very similar results. For instance the shape of the CMB angular power spectrum is highly sensitive to the parameters of the standard cosmological model, c.f. sec. 3.3.2. Moreover, the statistical analysis of galaxy redshift surveys as well as measurements of the number density of massive galaxy clusters provide consistent results. The composition of density parameters (1.2) characterised by the domination of Dark Energy today and measured by different classes of experiments has been attributed the notion of a *cosmic concordance*. The evidence is depicted in a combined plot in fig. 1.4. Summarising, we can say that the standard model facilitates precision cosmology and that in turn the measurements a posteriori back the standard model. Recalling the main results of this section we can summarise the cornerstones of the standard model as follows:

- validity of General Relativity as the basic framework; a *homogeneous* and *isotropic* as well as *spatially flat* FRW solution models the large-scale dynamics of the Universe; a *trivial topology* of the Universe, that is the actual size of the Universe is much bigger than the observable horizon;
- *standard inflation* solves the horizon problem and it produces spatial flatness; moreover it predicts a nearly scale-invariant spectrum of *statistically isotropic*, *adiabatic* and *Gaussian random* primeval density perturbations;
- the energy content of the Universe as measured today is *dominated by Dark Energy*; a subdominant fraction is due to *Dark Matter* and only a marginal contribution is due to baryonic matter [see eqs. (1.2)]; as a consequence, the cosmological expansion undergoes a recent acceleration.

Note that (Cold) Dark Matter, to which the next chapter is devoted, is also needed in models of structure formation in order to maintain the growth of the inflationary seeds of structure within an acceptable amount of time; read app. D for more details on this issue. Of course, the standard model also unfolds a lot of physics that takes care of the production of the today observed particles in the early Universe. A detailed discussion of the model of Big Bang Nucleosynthesis and scenarios of baryogenesis as well as leptogenesis are not within the scope of this work. In the following we are going to use the terms Lambda Cold Dark Matter (Λ CDM) model or just concordance model for the current cosmological standard model described above.

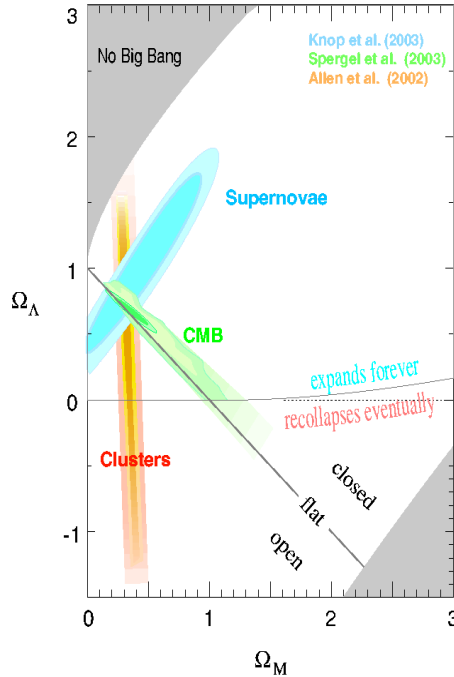


FIGURE 1.4. The cosmic concordance: roughly three thirds of the total energy-matter content of the Universe as measured today is made up of Dark Energy, the rest is mainly provided by the similarly mysterious Dark Matter. The most direct evidence for Dark Energy comes from accurate measurements of supernova Ia Hubble diagrams. Moreover, the shape of the angular power spectrum of the CMB is highly sensitive to the parameters of the cosmological standard model, and so are also analyses of the redshift evolution of the number density of galaxy clusters as well as number counts provided by galaxy redshift surveys. Due to their very different (partly orthogonal) systematics the combination of these observations constrains the cosmological parameters much better than the single experiments. The convergence of the different measurements impressively indicates self-consistency of the cosmological standard model. The picture is taken from [Lid04]; the shaded regions as well as the other critical lines are explained in more detail in app. A.

1.3. An Inhomogeneous Alternative?

The standard model prediction that the Universe is homogeneous on large scales *today* is a very bold one, likewise problematic to prove as a matter of principle. Yet, measurements of the CMB yield isotropy to a degree of 10^{-5} , albeit at a very early epoch. It requires measurements at high distances and at the same time with high statistics in order to map the Large-Scale Structure of the Universe. As observations of far-away regions show objects as they were an enormous amount of time ago in the past, it is not possible to strictly distinguish effects of evolution from spatial variations of the matter density. In other words, a probe that would strictly prove the homogeneity of our current Large-Scale neighbourhood, would ideally consist of a deep galaxy survey taken at very low redshifts. Of course, such a probe is not viable as a matter of principle because of the enormous size of the Universe. Leaving this principal objection apart, it is possible to demonstrate the approximate homogeneity of the Large-Scale Structure for instance with the luminous red galaxy catalogue ($z \sim 0.3$) of the Sloan Digital Sky Survey [HEB⁺05].

Nevertheless, homogeneity is obviously broken at small scales: catalogues within $\sim 100\text{Mpc}$ draw a complicated picture with large voids, lots of concentrated clusters of galaxies and even

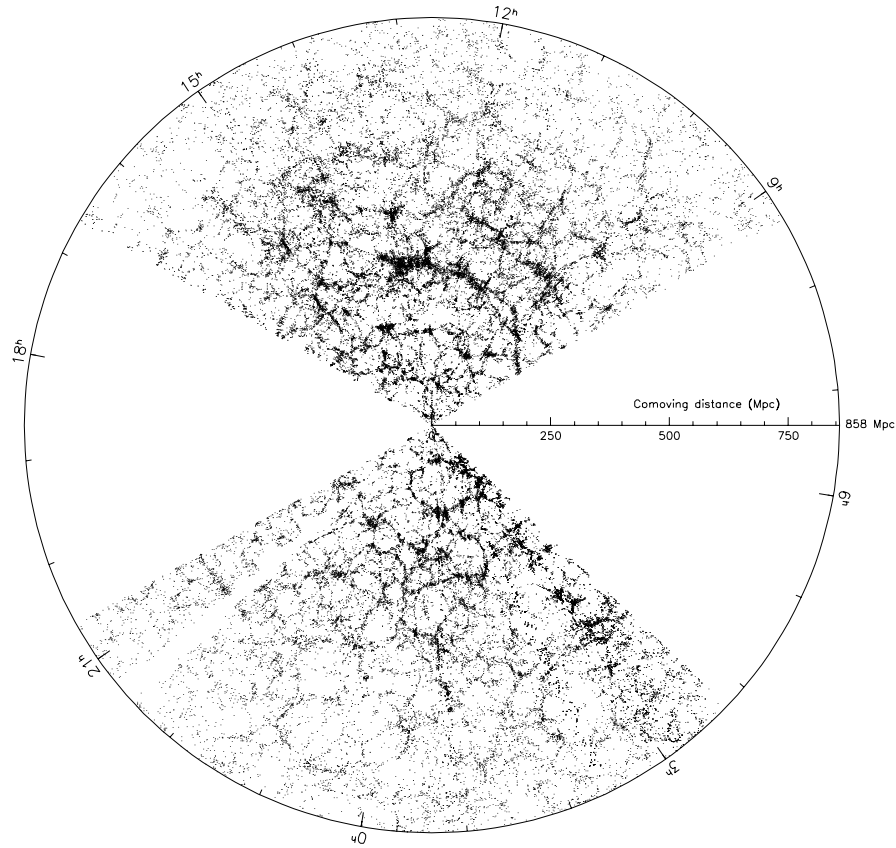


FIGURE 1.5. An SDSS image of the large-scale structure of our cosmological neighbourhood. The Sloan Digital Sky Survey is a wide-angle spectroscopic galaxy redshift survey. Shown are wedges of already considerable depth, that is up to roughly 900Mpc in comoving distance. The survey has a wedge-like structure because the optical light from far-away sources cannot penetrate through the material in the direction of our Milky Way's disc (Zone of Avoidance). All of the displayed points are galaxies taken from the main galaxy sample as well as from the bright red galaxy sample of the SDSS. Here a conformal projection is used that is shape preserving. The image uncovers an impressively sharp look on the surrounding large-scale cosmological structure. Clearly, the filament-like distribution of matter, structured like a honeycomb, is seen. As clearly, large voids in structure that often approximate spherical shape are resolved throughout the map. In the upper wedge, the largest cohesive structure ever observed by now, *the Sloan Great Wall* is clearly displayed. In equatorial coordinates this branching object stretches from 8.7h to 14h in R.A. at a median distance of around 310Mpc. The picture is taken from [G⁺05].

large accumulations thereof forming vast structures like the great wall, see fig. 1.5. Given that basic assumptions of the Λ CDM model do not hold at low redshift, naturally the call for a more complicated model arises. Interestingly, the general relativistic dynamics of even the simplest inhomogeneous models carry the possibility to eventually make Dark Energy superfluous.

1.3.1. The Lemaître-Tolman-Bondi Model. This spherically symmetric model is one of the most important known inhomogeneous working models; we follow here partly the review given in [PK06]. For general spherical coordinates, the assumption of a perfect fluid automatically implies a vanishing rotation $\omega_{\alpha\beta} = 0$, c.f. (1.50). Under this restriction, coordinates can be used that are comoving and in which there are no space-time mixing terms, and consequently the most general four-dimensional spherically symmetric spacetime can be written as

$$(1.43) \quad ds^2 = -e^C dt^2 + e^A dr^2 + R^2 (d\theta^2 + \sin^2\theta d\varphi^2),$$

where C, A and R are functions of (t, r) only and the velocity field is given by $u^\alpha = e^{-C/2} \delta^\alpha_0$. The parameter R is sometimes called the *areal radius*ⁱ. As a further simplification we consider the dynamics under purely gravitational interaction ($p = 0$). Zero pressure implies that the movement of the fluid occurs along timelike geodesics, which then leads to $C_{,r} = 0$. We can then make a coordinate transformation $t \mapsto \int e^{C/2} dt$ and achieve $C = 0$. The 1_0 field equation (see app. B) then gives

$$(1.44) \quad \frac{\partial}{\partial t} \left(e^{-A(t,r)/2} R_{,r} \right) = 0.$$

The solution with $R_{,r} = 0$ is not of interest here; however it leads to a physical solution (Datt-Ruban solution) of the Einstein-Maxwell equations associated with dust in an electromagnetic field, c.f. [PK06]. Taking $R_{,r} \neq 0$ we can directly integrate (1.44) to obtain

$$(1.45) \quad e^{A(t,r)} = \frac{R_{,r}^2}{1 + \mathcal{E}(r)}.$$

We introduce the arbitrary function $\mathcal{E}(r)$ which will be important in the following. In order to maintain the used signature we require $\mathcal{E} \geq -1$ for all r . Note that $\mathcal{E} = -1$ is not strictly excluded; if $R_{,r} = 0$ at the same point, this leads to the occurrence of a *wormhole*, c.f. [PK06]. The spherically symmetric dust solution is due to Lemaître [Lem33] and was rediscovered and rediscussed by Tolman [Tol34] and Bondi [Bon47] (LTB), it takes the final form

$$(1.46) \quad ds^2 = -dt^2 + \frac{R_{,r}^2}{1 + \mathcal{E}} dr^2 + R^2 (d\theta^2 + \sin^2\theta d\varphi^2).$$

where the functions $R(t, r)$ and $\mathcal{E}(r)$ are related to each other and to the energy density $\rho(t, r)$ and the cosmological constant Λ as follows

$$(1.47) \quad R_{,t}^2(t, r) = \frac{2m(r)}{R(t, r)} + \mathcal{E}(r) + \frac{1}{3} \Lambda R^2(t, r),$$

$$(1.48) \quad 4\pi G \rho(t, r) = \frac{m(r)_{,r}}{R^2(t, r) R(t, r)_{,r}}.$$

Therein $m(r)$ is a function that describes how much energy is present within the radius r as can be seen by integrating (1.48).

We can utilise the framework of the 3+1 split of spacetime (see 2.3.4 for an explicit discussion of the formalism) in order to deduce the interpretation of the mass function $m(r)$ and understand where it stems from. Let us note that for the given LTB metric (1.46) the shift vanishes and the lapse is equal to unity, such that the extrinsic curvature here is given by the time evolution of the three-metric $K_{ij} = -\frac{1}{2} \frac{\partial}{\partial t} g_{ij}$, yielding explicitly

$$(1.49) \quad K_{11} = -\frac{R_{,r} R_{,t,r}}{1 + \mathcal{E}}, \quad K_{22} = -R R_{,t}, \quad K_{33} = -R R_{,t} \sin^2\theta, \quad K \equiv K_i^i = -\frac{R_{,t,r}}{R_{,r}} - 2 \frac{R_{,t}}{R}.$$

For the following it is convenient to recall the standard kinematical decomposition of a three-velocity vector field. First considering Newtonian theory, the velocity gradient $v_{i,j}$ is a measure of the relative velocity of two neighbouring particles in the fluid, and can be decomposed

ⁱThis is because R plays the role of a radius in the Euclidean spherical area equation $S = 4\pi R^2$, where S stands for the area of surfaces at constant t and constant r [PK06].

into two parts: its symmetric part $v_{(i,j)} = 1/2(v_{i,j} + v_{j,i}) \equiv \theta_{ij}$ (the expansion scalar) and its antisymmetric part $v_{[i,j]} = 1/2(v_{i,j} - v_{j,i}) \equiv \omega_{ij}$ (the vorticity or rotation tensor) such that

$$(1.50) \quad v_{i,j} = v_{(i,j)} + v_{[i,j]} \equiv \theta_{ij} + \omega_{ij} \equiv \frac{1}{3}\theta\delta_{ij} + \sigma_{ij} + \omega_{ij},$$

where we additionally decomposed the symmetric part into a traceless contribution (the shear tensor σ_{ij}) and a trace part $\theta \equiv v_{i,i}$ (the expansion scalar or rate of expansion). This result from Newton Gravity can be transported one-to-one to General Relativity. In General Relativity – for vanishing shift and a lapse equal to unity, see sec. 2.3.4 – the expansion tensor is defined through $\Theta_{ij} \equiv \frac{1}{2}\frac{\partial}{\partial t}g_{ij}$ and is decomposed in an analogous way

$$(1.51) \quad \Theta_{ij} = \frac{1}{3}\theta g_{ij} + \sigma_{ij} + \omega_{ij}.$$

Recall that we work in a gauge with vanishing rotation. Next, we have computed the shear in the LTB model and get

$$(1.52) \quad \sigma_{11} = \frac{2}{3}\frac{R_{,r}^2}{1+\mathcal{E}}\left(\frac{R_{,t}}{R} - \frac{R_{,t,r}}{R_{,r}}\right), \quad \sigma_{22} = \frac{1}{3}R^2\left(\frac{R_{,t,r}}{R_{,r}} - \frac{R_{,t}}{R}\right), \quad \sigma_{33} = \frac{1}{3}R^2\sin^2\theta\left(\frac{R_{,t,r}}{R_{,r}} - \frac{R_{,t}}{R}\right).$$

Furthermore, the shear scalar reads

$$(1.53) \quad \sigma^2 \equiv \frac{1}{2}\sigma_{ij}\sigma^{ij} = \frac{1}{3}\left(\frac{R_{,t}}{R} - \frac{R_{,t,r}}{R_{,r}}\right)^2.$$

As a check, one sees directly from (1.52) that the shear is indeed traceless as it must be by construction. Now, because of the correspondence

$$(1.54) \quad K_{ij} = -\Theta_{ij},$$

we can use the decomposition (1.51) for further calculation.

Our aim was to derive the mass function $m(r)$, and for this we have to compute the field equations. In order to keep the derivation simple, we can calculate the 3 + 1 splitted field equations; to be exact only one of them, the *Hamiltonian* or *energy constraint*

$$(1.55) \quad \mathcal{R} - K_{ij}K^{ij} + K^2 = \mathcal{R} + \frac{2}{3}\theta^2 - 2\sigma^2 = 16\pi G\rho + 2\Lambda,$$

c.f. subsection 2.3.4. Here \mathcal{R} denotes the spatial Ricci scalar for which we have, in case of the LTB model,

$$(1.56) \quad \mathcal{R} = -2\left(\frac{\mathcal{E}_{,r}}{RR_{,r}} + \frac{\mathcal{E}}{R^2}\right).$$

Now the above introduced results turn useful and the energy constraint becomes

$$(1.57) \quad -\left(\frac{\mathcal{E}_{,r}}{RR_{,r}} + \frac{\mathcal{E}}{R^2}\right) + 2\frac{R_{,t}R_{,t,r}}{RR_{,r}} + \left(\frac{R_{,t}}{R}\right)^2 = 8\pi G\rho + \Lambda, \\ \text{or, with } R, R_{,r} \neq 0, \quad (\mathcal{E}R)_{,r} + (R_{,t}^2 R)_{,r} = (8\pi G\rho + \Lambda)R^2 R_{,r}.$$

We can integrate the last equation in (1.57) over r and thereby define

$$(1.58) \quad m(r) \equiv 4\pi G \int_{r_0}^r \rho R^2 R_{,r'} dr',$$

where we let R vanish at r_0 . Using this mass term, the last equation in (1.57) becomes

$$(1.59) \quad R(R_{,t}^2 - \mathcal{E}) = 2m + \frac{1}{3}R^3\Lambda,$$

which is just our equation (1.47). For this we have used the definition of the mass $m(r)$ (1.58), which measures how much mass there is within a radius r and is self-consistent with the density

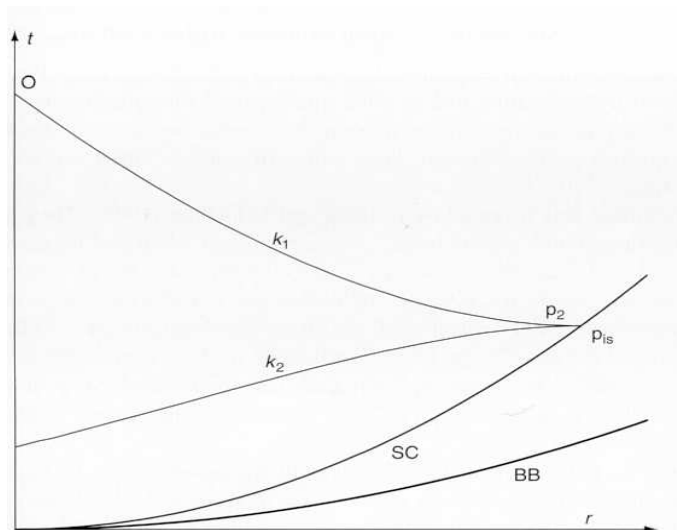


FIGURE 1.6. An LTB inspired solution to the cosmological horizon problem, c.f. [CS98, PK06]. The LTB light cone is here expressed via radial null geodesics $\theta = 0$, $\varphi = 0$ in (1.46). The figure shows the past light cones k_1 and k_2 of an observer O as well as the Big Bang (BB) and a shell crossing (SC) function of a certain class of LTB models. A shell crossing occurs where $R_{,r} = 0$ and when geodesics cross SC they must have a horizontal tangent at intersection and the LTB density becomes infinite. Below shell crossing pathologies occur – like a negative LTB density (1.48) – and thus to keep the model physical we exclude the spacetime set below SC. From the Last Scattering Surface at p_2 , which is defined as the two-sphere at temperature $T \sim 4000\text{K}$, photons can propagate toward the observer O at $(r = 0, t_0)$. The horizon problem is solved if one can show that the two-sphere of last scatter (r_2, t_2) is contained inside the future light cone of any point on the t -axis.

Assume an increasing LTB bang function $t_B(r)$ with local minimum at $r = 0$ such that there exists a shell crossing at some $t > t_B$. This curve is labelled (BB) in the figure and has in this example the form $t_B \propto r^2$. Note that here the shell crossing curve is tangent to the bang function at $r = 0$. The observer sits at O and sends a radial null geodesic k_1 – with strictly negative derivative wherever $t_{k_1}(r) > t_{SC}(r)$ – backwards in time, and it intersects with the shell crossing at a point p_{is} , having there a horizontal tangent to k_1 . We do not follow the geodesic through shell crossing because the model might become problematic there. On its way toward SC the geodesic will encounter successive surfaces of constant temperature which can also be parameterised as functions $t(r)$. Then at around $T \sim 4000\text{K}$, let us denote the last scattering by the event (r_2, t_2) , from the point p_2 on k_1 that is after t_{is} , so that $t_2 > t_{is}$ and $r_2 < r_{is}$, a second radial null geodesic k_2 is being sent backwards in time, this time towards the centre of symmetry at $r = 0$. The geodesic $t_{k_2}(r)$ will have a strictly positive derivative wherever $t_{k_2}(r) > t_{SC}(r)$. One can now show that k_2 must reach the line of $r = 0$ at a later time than the Big Bang, because of monotony. By this mechanism all regions of sky that are observable to O at present have had the possibility to causally interact with a common source in the past. As long as O can see the shell crossing set $t_{SC}(r)$ with $\partial_r t_{SC} > 0$ this mechanism resolves his horizon problem. Moreover if $\partial_r t_{SC} > 0$ for all r then this solution is a permanent one. The picture is taken from [PK06].

equation (1.48) stated before. The full Einstein equations of both the general metric (1.43) and the LTB spacetime (1.46) are given in app. B.

In the course of the derivation of (1.57) we have seen that the cases $R = 0$ and $R_{,r} = 0$ are special. As can be read off the definition (1.48), the LTB density becomes infinite at two points;

that happens just where $R = 0$ and $m_{,r} \neq 0$ as well as at $R_{,r} = 0$ and $m_{,r} \neq 0$. The $R = 0$ singularity is just the Big Bang which is compulsory for models with vanishing cosmological constant. The second singularity at $R_{,r} = 0$ is associated with a *shell crossing singularity*. Consider two points in the LTB spacetime with the same angular and time coordinates but different radial coordinates r and $r + dr$, then at a shell crossing singularity the radial geodesic distance $|g_{11}|^{1/2}dr$ between those points vanishes. This is odd because it means that two distinct shells with different spatial coordinates r coincide. Inserting the condition $R_{,r} = 0$ into components of the Riemann curvature tensor produces infinities and thus it can be shown that shell crossings are curvature singularities. Shell crossing singularities are considered less problematic than Big Bang singularities because a bundle of geodesics that is sent into a shell crossing singularity does not become degenerated (in a Big Bang singularity the bundle becomes focused onto a line or a surface), and thus physical objects are not destroyed at a shell crossing [PK06]. However, LTB shell crossings can be excluded by either requiring R to be monotonic with respect to r , or requiring that when $R_{,r}$ vanishes, $m_{,r}$ also has to vanish. On the other hand, shell crossings in LTB models pose an excellent working example of how very interesting, yet non-intuitive, curiosities can occur in general relativistic models. In the inflationary model the horizon problem was solved by imposing a phase of near exponential growth (1.25) in the early Universe^j. As is pointed out by C el erier and Schneider [CS98] an LTB model with shell crossing can be constructed to solve the horizon problem; the mechanism is sketched in fig. 1.6.

Because equation (1.47) with $\Lambda = 0$ is equivalent to the Newtonian equation of motion for objects in a Coulomb potential, we can interpret the mass mc^2/G that we defined in (1.58) as the *active gravitational mass*. This mass is the generating mass of the effective gravitational field and it is in general different from the mass one obtains by summing up all the constituent masses. In a different context we already encountered this distinction in sec. 1.2.1. In fact the active gravitational mass of a bound object could e.g. be smaller than the sum of its constituents; this is the gravitational version of the *mass defect* known from nuclear physics. In this case the mass defect equals the energy that would be needed to drag the constituents of the gravitating body apart. For the LTB model we can explicitly compare the two mass terms. Imagine an LTB sphere with radius r_1 and centre of symmetry at r_0 , then the sum of masses of the components within the sphere amounts to

$$(1.60) \quad m(r_1)_{\text{sum}} = G \int_V \rho \sqrt{-g} d^3V = 4\pi G \int_{r_0}^{r_1} \frac{\rho R^2 R_{,r}}{(1 + \mathcal{E})^{1/2}} dr,$$

whereas the active gravitational mass was given by (1.58) and is in this example

$$(1.61) \quad m(r_1) \equiv 4\pi G \int_{r_0}^{r_1} \rho R^2 R_{,r} dr.$$

Now, the function $\mathcal{E}c^2/G$ plays the role of the total energy within a shell of given radius and governs the relationship of active and summed mass in the LTB model. If $\mathcal{E} < 0$ the system is a bound one and $m_{\text{sum}} - m > 0$ is the gravitational mass defect that was already mentioned, whereas for $\mathcal{E} > 0$ the gravitational system must be unbound. In the case of $\mathcal{E} = 0$ the LTB system is said to be marginally bound.

On top of its interpretation as a total energy function, the parameter $\mathcal{E}(r)$ can also be understood by means of differential geometry. Taking sheets of constant time coordinate, one can attribute an orthonormal three-tetrad to the spatial hypersurfaces. The tetrad now provides an orthonormal basis of the three-dimensional subspaces at $t = \text{const.}$ by the forms $e^1 = dR/(1 + \mathcal{E})^{1/2}$, $e^2 = R d\theta$ and $e^3 = R \sin\theta d\varphi$. In this basis the components of the three-Riemann curvature read [PK06]

$$(1.62) \quad R_{1212} = R_{1313} = -\frac{\mathcal{E}_{,r}}{2R} \quad \text{and} \quad R_{2323} = -\frac{\mathcal{E}}{R^2}.$$

^jIt is outlined in [CS02] that the inflationary scenario rather postpones the horizon problem than solving it in a permanent manner. This is because if an observer only waits for long enough he will be able to observe regions that have not been causally connected in the early Universe.

Now the interpretation of the function \mathcal{E} as a measure of spatial curvature becomes intuitive: looking at (1.62), the curvature of the three-space becomes constant when \mathcal{E}/R^2 is also constant with respect to r . On the other hand, if $\mathcal{E} = 0$ all the hypersurfaces with $t = \text{const.}$ then are flat. Therefore we can view $-\mathcal{E}$ as a measure of the *local curvature* of spatial hypersurfaces at constant times. Local means that the LTB curvature is allowed to switch sign from one spatial region to the other. In this light, the FRW model with its global curvature parameter k can be regarded as a very simplifying one, for a locally varying curvature appears as a natural thing in LTB models and so a curvature characteristic as simple as k is only a peculiarity of the FRW models and not a generic expectation from the physical world.

It remains to discuss the Newtonian-like equation of motion (1.47) and give a solution to it. The equation can be formally integrated and the solution reads

$$(1.63) \quad \int_0^R \left(\frac{2m(r)}{R'(t,r)} + \mathcal{E}(r) + \frac{1}{3}\Lambda R'^2(t,r) \right)^{-1/2} dR' = t - t_B(r),$$

where we introduce another arbitrary function t_B which is called the *bang time function*. In the case of vanishing cosmological constant the bang time characterises the time at which the Big Bang singularity occurred. Unlike in the FRW model, the Big Bang is not a unique event anymore but in the LTB model appears to have occurred at different times for different distances from the centre of symmetry. We now assume $\Lambda = 0$ because for $\Lambda \neq 0$ one has to cope with elliptic integrals. With this simplification (1.63) can be solved parametrically as follows:

- regarding a negative \mathcal{E} (elliptic case),

$$(1.64) \quad R = -\frac{m}{\mathcal{E}}(1 - \cos\xi) \quad \text{and} \quad \xi - \sin\xi = \frac{(-\mathcal{E})^{3/2}}{m}.$$

For $0 < \xi < \pi$ the LTB model is in the expanding phase and for $\pi < \xi < 2\pi$ it is in the recollapsing phase. Assuming the former one can eliminate ξ and write [BKH05]

$$(1.65) \quad t - t_B = \frac{m}{(-\mathcal{E})^{3/2}} \left\{ \arccos\left(1 + \frac{\mathcal{E}R}{m}\right) - \left[1 - \left(1 + \frac{\mathcal{E}R}{m}\right)^2\right]^{1/2} \right\}.$$

- Regarding a vanishing \mathcal{E} (parabolic case),

$$(1.66) \quad R = \left[\frac{9}{2}m(t - t_B)^2 \right]^{1/3},$$

- and regarding a positive \mathcal{E} (hyperbolic case),

$$(1.67) \quad R = \frac{m}{\mathcal{E}}(\cosh\xi - 1) \quad \text{and} \quad \sinh\xi - \xi = \frac{\mathcal{E}^{3/2}}{m}(t - t_B),$$

or in a closed form

$$(1.68) \quad t - t_B = \frac{m}{\mathcal{E}^{3/2}} \left\{ \left[\left(1 + \frac{\mathcal{E}R}{m}\right)^2 - 1 \right]^{1/2} - \text{arcosh}\left(1 + \frac{\mathcal{E}R}{m}\right) \right\}.$$

Finally, we consider the FRW limit of the LTB model. As can be derived from the above solutions (1.64)-(1.68), the FRW case can be obtained from the LTB solution by setting

$$(1.69) \quad R = ar, \quad m = m_0 r^3, \quad \mathcal{E} = -kr^2, \quad t_B = \text{const.},$$

wherein a denotes the FRW scale factor. Inserting these conditions into e.g. the LTB metric (1.46) immediately returns the FRW spacetime (1.8). Also, inserting the conditions (1.69) into the last line of the calculation in (1.57) readily returns the Friedmann equation (1.14). However, the limit defined through the conditions (1.69) is coordinate dependent [PK06]. An invariant transfer condition is given by the requirement $\rho_{,r} = 0$ or equivalently by

$$(1.70) \quad \frac{\mathcal{E}}{m^{2/3}} = \text{const.} \quad \text{and} \quad t_B = \text{const.}$$

1.3.2. Some Applications of the LTB Model. From modern galaxy surveys it is nowadays evident that voids are basic components of the local Universe. These ubiquitous underdense regions of the Universe often approximate spherical shape. Their first prediction was independently made by Tolman [Tol34] and Sen [Sen34] in 1934. The basic statement is that FRW (and also Einstein) models show instability against processes of structure growth. The basic effect can be understood with the help of the LTB model [PK06]. Differentiating the logarithm of (1.48) with respect to time we have

$$(1.71) \quad \left[\frac{\partial^2}{\partial t^2} \ln \rho \right]_{\text{LTB}} (t_1) = \left[-2 \frac{R_{,t,t}}{R} + 2 \frac{R_{,t}^2}{R^2} - \frac{R_{,t,t,r}}{R_{,r}} + \frac{R_{,t,r}^2}{R_{,r}^2} \right]_{\text{LTB}} (t_1),$$

where an initial time t_1 is introduced at which the radial coordinates of the LTB model and of a fiducial FRW model – we want to compare with – are synchronised such that the identity $R_{\text{LTB}}(t_1, r) = r R_{\text{FRW}}(t_1)$ defines the relation between the two coordinate systems of LTB and FRW model, and we additionally let $R_{\text{LTB},t}(t_1, r) = r R_{\text{FRW},t}(t_1)$. Note that this is not yet sufficient in order to uniquely fix the LTB evolution. Because of this $R_{,t,t}$ is arbitrary and thus the densities at time t_1 are allowed to differ. What we assumed so far implies that $(R_{,t,r}/R_{,r})_{\text{LTB}}(t_1) = (R_{,r}/R)_{\text{FRW}}(t_1)$. The interpretation of these initial conditions is the following: we assume a perturbation in the initial FRW density but, since $R_{,t}$ is a measure of the expansion velocity, an unperturbed initial velocity.

Applying first (1.47) to get the derivatives $R_{,t,t}$ and $R_{,t,t,r}$ and then reapplying (1.48) yields

$$(1.72) \quad \left[\frac{\partial^2}{\partial t^2} \ln \rho \right]_{\text{LTB}} (t_1) = \left[4\pi G \rho - \Lambda + 2 \frac{R_{,t}^2}{R^2} + \frac{R_{,t,r}^2}{R_{,r}^2} \right]_{\text{LTB}} (t_1).$$

The analogue of this within the FRW model is given by

$$(1.73) \quad \left[\frac{\partial^2}{\partial t^2} \ln \rho \right]_{\text{FRW}} (t_1) = \left[4\pi G \rho - \Lambda + 3 \frac{R_{,t}^2}{R^2} \right]_{\text{FRW}} (t_1).$$

The direct comparison can be made

$$(1.74) \quad (\ln \rho_{\text{LTB}} - \ln \rho_{\text{FRW}})_{,t,t} = 4\pi G (\rho_{\text{LTB}} - \rho_{\text{FRW}}),$$

and it becomes clear that whenever there is a difference between the densities of the LTB and the FRW model, irrespective of whether they correspond to under- or overdensities, the difference would be increasing in time. In other words, an LTB model with matched initial conditions as discussed above must be fine-tuned in order not to alienate from the background model during its evolution with time.

Consequently, LTB models have been extensively studied in order to understand the details of general relativistic structure growth or formation of voids. A remarkably extensive review of such studies that is exhaustive up to 1994, has been compiled by Krasiński [Kra97]. For instance, it was demonstrated by Mészáros [M91], with the help of a particular realisation of an LTB model, that there exist initial conditions that allow for a homogeneous model in the beginning which develops a void of realistic size 10-100Mpc, surrounded by a shell crossing with an evolution time similar to the age of our Universe. Moreover, in this work it is explicitly demonstrated that perturbation theory on an LTB model is safe if the considered inhomogeneity is small enough.

Due to the standard model, the tiny CMB temperature anisotropies of order 10^{-5} that have been boosted by inflation provide the initial seeds for the growth of structure. Hellaby and Krasiński argue that density fluctuations alone are not sufficient to properly trigger the formation of structure, rather the distribution of initial velocities has to be incorporated into the theory [KH04b]. In an extended series of works the same authors have developed sophisticated algorithms which cope with the question of how an evolution between given initial and final density profiles (or velocity profiles) that are astrophysically relevant, can be achieved within an LTB model. As already mentioned, the interesting result is that models are much more sensitive

to the initial velocity profiles than to the initial density profiles regarding their evolution toward realistic present-day density profiles. A non-exhaustive list of studies following that line is given by [KH02, KH04b, KH04a, KH05, BKH05, KH06].

Usually, Black Holes are studied in the context of vacuum solutions like the Kerr spacetime (2.46) or static solutions like Schwarzschild's (2.40). In any case, such Black Holes must have existed since ever and are observed from far away (we do not consider Hawking-Penrose radiation). It has been first noted by Bondi [Bon47] that the *formation* of a Black Hole can be described by means of the LTB model; the condition is that the collapse velocity of matter must be very high. It turns out that the LTB framework is useful for gaining detailed insight into the formation process of a Black Hole; albeit it is very non-trivial to locate the event horizon because of the lack of Penrose-like null coordinates in the LTB case, c.f. [PK06]. See also [ES79, Chr84].

As was outlined in sec. 1.2.2, when interpreting the supernova Ia findings within the standard model, a present-day acceleration of the cosmic expansion involving Dark Energy is the consequence. This is not necessarily true when working in inhomogeneous cosmologies: inhomogeneous models often easily reproduce good fits to the standard cosmological observations. Nevertheless, this alone is not sufficient to supersede a working standard model; it is not unexpected that highly complicated models that involve quite a number of parameters provide a good fit. The point is that the physics of the inhomogeneous models should be understood at least as good as in the standard model and that a new model must of course provide universality. Hence, it is worthy and necessary to analyse models like the LTB solution as inhomogeneous toy-models in order to develop a feeling for non-standard model physics that might well be necessary. Therefore the current literature on inhomogeneous cosmologies and applications thereof reflects the huge amount of effort that is invested in order to test the viability of models and better understand their sometimes unusual physics. The current situation of these subjects is far from settled, the field is evolving rapidly. Thus we like to give a short overview and focus on applications of the LTB model on SNIa data and CMB data.

In order to cope with observational cosmology we need a distance measure as we have worked out in sec. 1.2.2. According to Partovi and Mashhoon [PM84] it turns out that the *luminosity distance in an LTB spacetime* takes the form

$$(1.75) \quad D_L^{\text{LTB}} = (1+z)^2 R,$$

thus being a function of the redshift and via $R(t, r)$ also of the LTB model parameters $m(r)$, $\mathcal{E}(r)$ and $t_B(r)$. Note that equation (1.75) is to be taken [PM84] at the observer's time. That the result (1.75) makes sense can be seen easily: as we have seen the LTB function R is nothing else than the angular diameter distance between an observer at arbitrary position and the LTB origin at $R = 0$; then, by use of the reciprocity theorem we readily end up with (1.75) for the LTB luminosity distance.

But how is the redshift function properly defined within the LTB model? From the LTB metric (1.46) we read off the defining differential equation of a radial null geodesic heading in the direction of the observer

$$(1.76) \quad \frac{dt}{dr} = -\frac{R(t, r)_{,r}}{\sqrt{1 + \mathcal{E}(r)}}.$$

To reduce the possible solutions to (1.76), we consider two light rays being emitted and heading in the same direction, but with a small time delay τ in between. Following [Bon47] we think of the first light ray as parametrised through $t = T(r)$ and the second through $t = T(r) + \tau(r)$. Since both light rays must obey the common geodesic equation (1.76), we have

$$(1.77) \quad \frac{dT}{dr} = -\frac{R[T(r), r]_{,r}}{\sqrt{1 + \mathcal{E}(r)}} \quad \text{and} \quad \frac{d(T + \tau)}{dr} = -\frac{R[T(r) + \tau(r), r]_{,r}}{\sqrt{1 + \mathcal{E}(r)}}.$$

For we allowed only very little time in between the two signals $\tau(r) \ll T(r)$, we can write to leading order

$$(1.78) \quad R_{,r}[T(r) + \tau(r), r] \simeq R_{,r}[T(r), r] + \tau(r) R_{,t,r}[T(r), r],$$

and insert this together with the left equation of (1.77) into the right equation of (1.77), yielding

$$(1.79) \quad \frac{d\tau}{dr} = -\tau(r) \frac{R[T(r), r]_{,t,r}}{\sqrt{1 + \mathcal{E}(r)}}.$$

We can access the redshift by comparing the period of the light wave at emission with its period at observation

$$(1.80) \quad \frac{\tau(r_{\text{ob}})}{\tau(r_{\text{em}})} \equiv 1 + z(r_{\text{em}}).$$

If we now move the sources to slightly different distances r_{em} and $r_{\text{em}} + dr$ and use this in equation (1.80) we get by differentiation

$$(1.81) \quad \frac{1}{\tau} \frac{d\tau}{dr} = -\frac{1}{1+z} \frac{dz}{dr}.$$

Inserting this in (1.79) finally gives

$$(1.82) \quad \frac{1}{1+z} \frac{dz}{dr} = \frac{R[T(r), r]_{,t,r}}{\sqrt{1 + \mathcal{E}(r)}}.$$

And with this the initial geodesic equation (1.76) becomes

$$(1.83) \quad \frac{dt}{dz} = -\frac{1}{1+z} \frac{R[T(r), r]_{,r}}{R[T(r), r]_{,t,r}}.$$

Now, we have reduced the problem to the solution of the two equations (1.82) and (1.83). Both of them are solved by radial null geodesics that span from $z(r_{\text{em}})$ to $z = 0$.

In [C00], the above equations for the luminosity distance have been solved using perturbative methods. It was found that the inhomogeneous LTB model is able to reproduce the SNIa data at least up to $z \sim 1$, without the need for Dark Energy. The issue of finding the right model to compare with the cosmological data is far from settled; rather it is the object of an increasing number of studies. From the sizeable amount of work that has been published – discussing cosmological phenomenology with the LTB model, especially with regard to supernova Ia and CMB observations – we want to give a few examples that indicate recent progress in the field. In a recent review [Enq07], Enqvist confirms the ability of LTB models to yield good fits to SNIa data and simultaneously give reasonable values for cosmological parameters. He also discusses the potential of LTB models to become more realistic competitor models, especially with regard to other (combined) datasets from CMB and Large-Scale Structure; see also [EM07]. In [MH07] McClure and Hellaby push forward the non-trivial program of extracting metric information of the Universe directly from cosmological observations. Homogeneity is not a priori assumed, so that a description is approached within the framework of an LTB model, and a numerical groundwork for detailed analysis of future combined datasets is set up. Tanimoto and Nambu [TN07] present a novel, non-parametric form of solving for the LTB areal radius. Therewith the LTB luminosity distance is calculated perturbatively, and it is claimed that dust FRW models and LTB models are indistinguishable up to second order, under a certain regularity requirement at the centre of the LTB model. For LTB relations that incorporate the perspective of off-centre observers we refer e.g. to [BMN06, HMM97]. Other useful reading on the LTB model might be [Gar06a, Bol05, INN02, Tom01].

An arrangement of several LTB spheres within one model is called an LTB Swiss-Cheese Universe [Kan69] and therein inhomogeneity is realised locally while the Swiss-Cheese remains globally homogeneous. As it is found by Biswas and Notari [BN07], the integrated effect on light propagation in LTB Swiss-Cheese models – that is, the averaged effect over several LTB patches observed from outside a patch – is small, and only within a *local setup* – that is, within a single LTB patch – the effect on the photon paths can be large. Further recommended reading on the LTB Swiss-Cheese model comprises [MKMR07, BTT07a, BTT07b, KKN⁺07].

If the LTB model is to be taken serious it should also be able to explain CMB data. This has been tested for by Alnes and Amarzguoui for an off-centred observer in an LTB underdensity

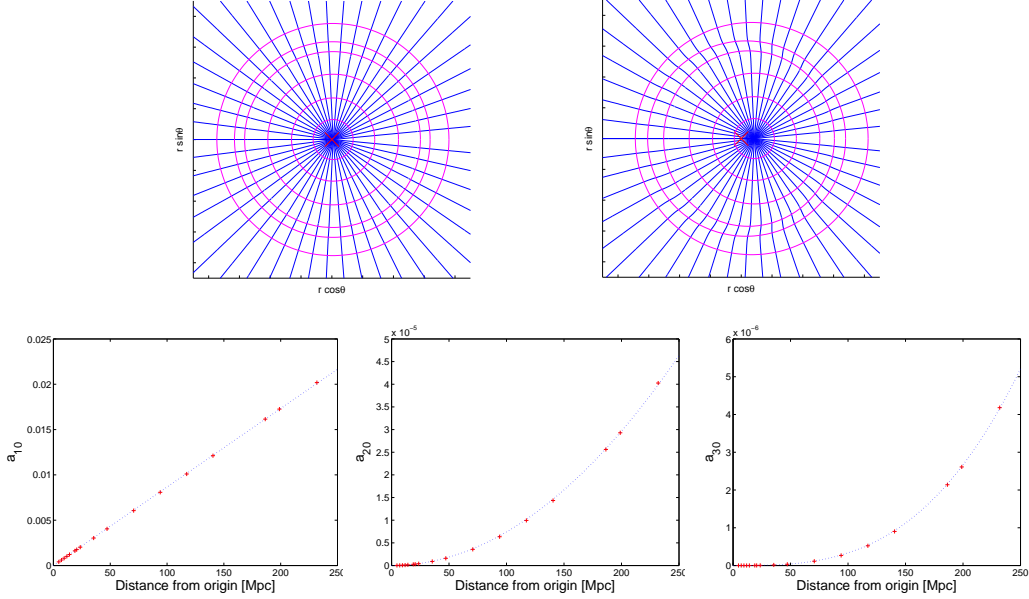


FIGURE 1.7. Main results from a qualitative CMB analysis of an LTB underdensity with off-centre observer [AA06]. Upper row: (r, θ) -geodesics (blue lines) within a certain LTB model as they converge toward an observer that is displaced a little (left: $d = 20\text{Mpc}$), and a lot (right: $d = 200\text{Mpc}$) from the origin (red cross). The red circles indicate equidistant shells that are, in terms of cosmic time, 1Gyr apart respectively. In case of the very large displacement (right) one clearly resolves the strong distortion of geodesics. This distortion is due to a strong density gradient at the transition from LTB model to a homogeneous background. Lower row: from left to right, the CMB dipole, quadrupole and octopole plotted as functions of the observer's distance to the LTB centre. Evidently, quadrupole and octopole are several orders of magnitude smaller than the dipole. An experimental bound for the dipole is 10^{-3} which immediately puts an upper limit of around 15Mpc on the allowed displacement of the observer. At such distances, the model then predicts a quadrupole and octopole that are far too small, namely of the orders 10^{-7} and 10^{-9} . Moreover, anisotropy induced by such a displacement is per construction axially symmetric and thus must be subject to the general constraints that we develop in part II. In principle it would be possible to compensate a large dipole that is due to displacement with a contrary contribution from Doppler velocity, but this movement toward the centre of the underdensity had to be put in just by hand. Pictures are taken from [AA06].

[AA07]. The authors find that, even though an LTB model is found that fits well a sample of SNIa data *and* can reproduce the location of the first peak in the CMB power spectrum, the inclusion of SNIa data does not yield compelling evidence for an LTB off-centre observation nor is it able to tightly constrain the degree of displacement with respect to the LTB centre. In [AA06] the same authors apply an off-centre analysis on CMB data alone and find the important result, that the observed CMB dipole constrains a potential off-centre displacement to be at most 15Mpc. Moreover it is found that, once the dipole is matched to data, the quadrupole and octopole resulting from the displacement are too low to be in accordance with the observed multipoles, c.f. fig. 1.7. On the other hand, Sarkar and Hunt discuss distortions in the measured CMB power spectrum known as ‘glitches’ [HS04]. A non-standard primordial spectrum is used, coming from a so-called multiple inflation scenario, to mimic the glitches and it is found that the LTB model is successful in fitting the new CMB spectrum as well as the found baryon oscillations in the galaxy two-point correlation function [c.f. app. D], and also SNIa data [HS07].

Ishak and others have recently investigated the possibility to fit SNIa data in a more complicated model, the inhomogeneous Szekeres model [Sze75]. This solution needs not to have any symmetry and can therefore be used for instance for modelling of double or triple structures. The advantage of the model lies in the fact that it is – like LTB – an exact solution from General Relativity and therefore it is not necessary to constrain the model to cases of small density contrast. The disadvantage is that the Szekeres model is very complex due to the lack of explicit symmetry. In turn, this makes the solution appear very interesting because of its potential to model the true lumpy structure of the Universe. In the coordinates used in [Bol07], the Szekeres metric takes the form

$$(1.84) \quad ds^2 = -dt^2 + \frac{(\Upsilon_{,r} - \Upsilon E_{,r} E^{-1})^2}{(\varepsilon - k)} dr^2 + \frac{\Upsilon^2}{E^2} (dp^2 + dq^2),$$

where $\Upsilon = \Upsilon(r, t)$, $\varepsilon = 1, 0, -1$ and the arbitrary function $k = k(r) \leq \varepsilon$ plays a similar role like the energy function \mathcal{E} in the LTB model. The arbitrary function $E = E(r, p, q)$ is constrained by

$$(1.85) \quad E(r, p, q) = \frac{1}{2S} (p^2 + q^2) - \frac{P}{S} p - \frac{Q}{S} q + C \quad \text{with} \quad C = \frac{P}{2S} + \frac{Q^2}{2S} + \frac{S}{2} \varepsilon,$$

with S, P, Q and C being functions of r only. The case $\varepsilon = 1$ is a special one: it allows the model to have the FRW curvature cases as can be seen from the metric (1.84). This choice is called quasispherical Szekeres model and is physically most interesting, for it is possible to have a homogeneous FRW limit at large distances from the origin. Now, Ishak et al. [IRWG07] have found that the Szekeres model fits SNIa data as good as the Λ CDM model, and moreover, that the found best-fit model yields spatial flatness at CMB-relevant scales.

There is a tight coupling of the above listed work on inhomogeneous models and the issue of *cosmological backreaction*. The backreaction – or averaging, or fitting – problem refers to the fact that, in general, the evolution of a homogeneous general relativistic model (like FRW) does not match with the averaged evolution of an inhomogeneous model (like LTB). This is a pure General Relativity problem, for the mentioned difference stems from the inherent non-linearity of the underlying theory. There are serious technical difficulties with the backreaction calculations, since: (a) in the non-perturbative case it is not clear in how far one can properly define averages of tensor quantities, albeit this seems to be under control for scalars; and (b) in the perturbative case the calculations become arbitrarily tedious with higher orders. See [Buc07] for a recent overview on non-perturbative as well as perturbative studies in backreaction. Nevertheless, see for instance [Zal04, Zal93, Par07, Beh03] for approaches toward fully covariant averaging.

1.3.3. The Integrated Sachs-Wolfe Effect in LTB Models. Here, we develop the general relativistic framework on which the analysis of the large-scale CMB anomalies in the next part of the thesis is based. Our aim is to model the effect of a local overdense structure on the CMB sky. Taking an overdensity is well motivated by local galaxy surveys that indicate the presence of very massive, non-linear structures at distances of around 100Mpc; note that the motivation will be discussed in more detail in part II. As was mentioned in sec. 1.3.2, the LTB model can describe the collapse of an overdensity or the formation of a void in an expanding universe. Moreover it has also been used to parametrise nearby inhomogeneous structure [FSSB01, HTET01]. In contrast to voids, overdense structures do not generally approximate a spherical shape, but we will use the LTB model as a first approximation to describe the local neighbourhood within approximately 100Mpc. Our picture of the local structure is therefore a spherical density concentration, with our Local Group of galaxies falling toward the centre. The setup that shall be analysed here is that of a moderate LTB perturbation on a flat FRW background. Note that this is different from models, like e.g. in [Mof05], in which it is speculated that the entire universe is spherically symmetric. Instead, we are considering the effect of local inhomogeneities that are known to exist, c.f. fig. 1.5.

The observational situation with regard to the Local Group falling towards a density concentration, known as the Great Attractor, is somewhat unclear [HSLB04, LRSH04]. Moreover,

the expected infall towards us from clusters on the other side of the centre has not been confirmed. Apparently a model with two mass concentrations provides a more satisfactory fit to the data [Mas05]. Here we will treat the overdensity as linear, so additional attractors could then be taken into account simply by adding their effect on top of the one we find. However, it is evident that linearly adding a new source of anisotropy will in general add multipole power, not reduce it, which will turn out to be a peculiar constraint to such models.

Tully points out that surveys of the local peculiar velocity field give rise to a *local velocity anomaly* [Tul88]. The anomaly manifests itself as an unexplained discontinuity in measured peculiar velocities when going from objects belonging to our local filament (Coma-Sculptor Cloud) to galaxies belonging to the adjacent structure (Leo Spur). The evacuation of the so called local void provides an important contribution to our local velocity field. The ‘observation’ of the local void is made difficult by the fact that most of it is hidden in the line of sight through the galactic disc of our Milky Way (Zone of Avoidance); and thus catalogues including that region cannot be made in the optical band. As further reading we strongly recommend [T⁺07] and [Tul07].

As we assume that the local overdensity is moderate, it is possible to linearise around the FRW model, to which the LTB model should reduce at large distances from the centre of symmetry. The transfer conditions are listed in (1.69). Assuming that the universe be spatially flat far away from the overdensity as well as $\Lambda = 0$, we have $R(t, r) = a(t)r$ and $\mathcal{E} = 0$, with a being the FRW scale factor. We use the standard normalisation $a(t_0) = 1$ today. In order to do the perturbation theory we can introduce a perturbation function $f(t, r)$ that parameterises small deviations from the FRW case. It makes sense to define the perturbation function as the deviation of physical distances in the LTB and the FRW model:

$$(1.86) \quad f(t, r) \equiv \frac{R(t, r) - R_{\text{FRW}}(t)}{R_{\text{FRW}}(t)}.$$

The constraint of smallness of perturbations can then be expressed by the requirements

$$(1.87) \quad |f(t, r)| \ll 1, \quad \frac{f_{,t}(t, r)}{H} \ll 1, \quad |rf_{,r}(t, r)| \ll 1,$$

and so the linearised LTB metric functions take the form

$$(1.88) \quad R(t, r) = ar [1 + f(t, r)] \quad \text{and} \quad \mathcal{E}(r) = (aHr)^2 [3f(t, r) + 2H^{-1}f_{,t}(t, r)],$$

where we obtained the second equation from inserting the first equation into (1.47) and making an ansatz $m(r) \propto r^3$. According to (1.48) the linearised density parameter becomes

$$(1.89) \quad \rho(t, r) = \rho_{\text{F}}(t) [1 - 3f(t, r) - rf_{,r}(t, r)],$$

with ρ_{F} denoting the FRW density that scales as $\rho_{\text{F}} \propto a^{-3}$. Inverting (1.89) we likewise obtain for the perturbation function

$$(1.90) \quad f(t, r) = -\frac{1}{r^3} \int_0^r r'^2 \delta(t, r') \mathcal{E}(r') dr' = -\frac{1}{3} \langle \delta(t, r) \rangle_r,$$

where $\delta \equiv (\rho - \rho_{\text{F}})/\rho_{\text{F}}$ stands for the *density contrast* and $\langle \delta \rangle_r$ denotes its spatial average as measured from the symmetry centre up to r . Employing these results, the perturbed LTB metric can be written in terms of the conformal time $dt = ad\eta$ as

$$(1.91) \quad ds^2 = a^2(\eta) [-d\eta^2 + (1 + 2f + 2rf_{,r} - \mathcal{E})dr^2 + (1 + 2f)r^2 d\Omega^2],$$

with the angular element $d\Omega^2 \equiv d\theta^2 + \sin^2\theta d\varphi^2$.

For an off-centre observer, CMB photons coming from different directions have travelled different routes through the local overdensity, hence producing additional anisotropy. Since the effect vanishes for an observer at the centre because of the spherical symmetry, its amplitude depends on the distance from the centre; more specifically on the ratio $\varepsilon \equiv r_0/d$, where d is the distance to the surface of last scattering. The line from the observer to the centre defines a preferred direction, so the situation becomes *axially symmetric*, and we can restrict our attention to the plane $\varphi = 0$. The geometry of the situation is sketched in fig. 1.8.

A commonly used tool of the standard model is *cosmological perturbation theory*. Considering linear perturbations around a spatially flat FRW model, the according metric takes the general form [MFB92]

$$(1.92) \quad ds^2 = a^2(\eta) \times \left\{ -(1 + 2\Phi)d\eta^2 + 2(B_{;i} - S_i)dx^i d\eta + [(1 - 2\Psi)g_{ij} + 2E_{;i;j} + F_{i;j} + F_{j;i} + h_{ij}] dx^i dx^j \right\}$$

with the potentials Φ , B , Ψ and E being the sources of scalar perturbations and S_i , F_i represent vector perturbations that satisfy $S_i^{;i} = 0 = F_i^{;i}$. Furthermore, tensor perturbations (gravitational waves) are characterised by h_{ij} with $h_i^{;i} = 0 = h_{ij}^{;j}$. As long as only Latin indices are involved the semicolon stands for covariant differentiation with respect to the three-metric g_{ij} .

Since the LTB model has vanishing vorticity, as explained in sec. 1.3.1, we can set the vector modes to zero $F_i = 0 = S_i$. Moreover, the spherical symmetry together with the requirement that perturbations do not diverge anywhere also rules out the tensor perturbations, so that $h_{ij} = 0$. Adopting spherical coordinates and comparing the remaining components of (1.91) with (1.92) enables us to solve for the metric functions (up to integration constants):

$$(1.93) \quad \Phi(t, r) = 0 = B(t, r), \quad \Psi(r) = -\frac{1}{2} \int_0^r \frac{\mathcal{E}(r')}{r'} dr',$$

$$(1.94) \quad E_{;j}^i(t, r) = \delta_{ij}^i \left[f(t, r) - \frac{1}{2} \int_0^r \frac{\mathcal{E}(r')}{r'} dr' \right] + \delta_{jr}^i \delta_{jr} \left[r f_{,r}(t, r) - \frac{1}{2} \mathcal{E}(r) \right].$$

Note that the first identity in (1.93) is a result that is equivalent to the application of the synchronous gauge, which is justified because of the zero vorticity characteristic of the LTB model. In order to obtain a formula for the CMB anisotropy, we should further follow the analogy to cosmological perturbation theory. There exists a framework which returns the temperature anisotropies for general perturbations as characterised by (1.92) that we discuss next.

A complete general relativistic treatment that describes the full evolution of CMB radiation undergoing effects of metric perturbations was first given by Sachs and Wolfe [SW67]. The hereafter named Sachs-Wolfe formula describes the transfer of the effects of a three-dimensional gravitational potential pattern on CMB photons to the two-dimensional temperature anisotropy field $\Delta T/T$ which is, in the end, the observable today.

Imagine \mathcal{P}_{ob} to be the position of an CMB observer today and let \mathbf{n} be a unit vector that points from the observer's position to the last scattering surface. Further, let \mathcal{P}_{em} denote the position of the primeval photon emission. With E_{ob} standing for the CMB photon energy received by the observer and E_{em} being the initial energy of the CMB photon emitted at some location \mathcal{P}_{em} , we are ready to formulate the ratio $E_{\text{ob}}/E_{\text{em}}$ as induced by the Sachs-Wolfe effect. In the unperturbed case one has the common result $E_{\text{ob}}^{(0)}/E_{\text{em}}^{(0)} = a(\eta_{\text{em}})/a(\eta_{\text{ob}})$; for general metric perturbations (1.92) the according relation extends to [MS98]

$$(1.95) \quad \frac{E_{\text{ob}}}{E_{\text{em}}} = \frac{a(\eta_{\text{em}})}{a(\eta_{\text{ob}})} \left\{ 1 + [\Phi + n^i(v_i + B_{;i} - S_i)](\mathcal{P}_{\text{ob}}) - [\Phi + n^i(v_i + B_{;i} - S_i)](\mathcal{P}_{\text{em}}) - \int_{\eta_{\text{em}}}^{\eta_{\text{ob}}} \left[\Phi_{,;\eta} - \Psi_{,;\eta} - 2n^i \Phi_{;i} + n^i n^j (E_{,;\eta} - B)_{;i;j} + n^i n^j (S_i + F_{i,;\eta})_{;j} + \frac{1}{2} h_{ij,\eta} n^i n^j \right] d\eta \right\},$$

taken in the frame of the three-velocities. Neglecting the vector and tensor contributions and employing the synchronous gauge, $\Phi = 0 = B$, the above relation simplifies to

$$(1.96) \quad \frac{E_{\text{ob}}}{E_{\text{em}}} = \frac{a(\eta_{\text{em}})}{a(\eta_{\text{ob}})} \left[1 + n^i v_i(\mathcal{P}_{\text{ob}}) - n^i v_i(\mathcal{P}_{\text{em}}) - \int_{\eta_{\text{em}}}^{\eta_{\text{ob}}} (-\Psi_{,;\eta} + n^i n^j E_{;i;j,\eta}) d\eta \right].$$

Therein v^i denotes the respective peculiar velocities that enter the setup; we will discuss the peculiar velocities in more detail below. The \mathbf{n} dependence enters in $E_{\text{ob}}/E_{\text{em}}$ and is fixed by the requirement that \mathcal{P}_{ob} denotes 'here and now' which is expressed as $\mathcal{P}_0(\eta_0, \mathbf{x}_0)$, and hence we everywhere replace $\mathcal{P}_{\text{em}}(\eta_{\text{em}}, \mathbf{x}_{\text{em}})$ with $\mathcal{P}_{\text{ls}}[\eta_{\text{ls}}, \mathbf{x}_0 - \mathbf{n}(\eta_{\text{ls}} - \eta_0)]$, where 'ls' indicates emission

from last scattering. Note that η_{ls} is fixed by the requirement that $z_{\text{ls}} = 1088$. Since the last scattering surface is a surface of constant radiation energy density, the density contrast of the photon fluid component δ_γ obeys the scaling [MS98]

$$(1.97) \quad a(\eta_{\text{em}}) \simeq a(\eta_{\text{ls}}) + \frac{1}{4} \delta_\gamma(\mathbf{n}) a(\eta_{\text{ls}}),$$

and we further assume a foliation such that, as seen from the hypersurface of the observer, the baryonic energy density is constant, leading to the following scaling of the density contrast of baryons

$$(1.98) \quad a(\eta_{\text{ob}}) \simeq a(\eta_0) - \frac{1}{3} \delta_b(\mathcal{P}_0) a(\eta_0).$$

Thus we can insert into the Sachs-Wolfe formula (1.96) and have

$$(1.99) \quad \frac{E_0}{E_{\text{ls}}} = \frac{a(\eta_{\text{ls}})}{a(\eta_0)} \times \left[1 + \frac{1}{4} \delta_\gamma(\mathbf{n}) - \frac{1}{3} \delta_b(\mathcal{P}_0) + n^i v_i(\mathcal{P}_0) - n^i v_i(\mathcal{P}_{\text{ls}}) - \int_{\eta_{\text{ls}}}^{\eta_0} (-\Psi_{,\eta} + n^i n^j E_{;i;j,\eta}) d\eta \right].$$

This is readily rewritten in terms of the temperature anisotropy:

$$(1.100) \quad \frac{\Delta T}{T}(\mathcal{P}_0) = \frac{\Delta T}{T}(\mathcal{P}_{\text{ls}}) + n^i v_i(\mathcal{P}_0) - n^i v_i(\mathcal{P}_{\text{ls}}) - \int_{\eta_{\text{ls}}}^{\eta_0} n^i n^j E_{;i;j,\eta} d\eta,$$

note that the Ψ term vanishes because it is a function of only r (1.93). It has to be taken into account that the overdensity is local, that is its effects vanish at the surface of emission; moreover, we transform back to cosmic time and thus finally obtain for the Sachs-Wolfe term

$$(1.101) \quad \frac{\Delta T}{T}(\mathcal{P}_0) = n^i v_i(\mathcal{P}_0) - \int_{t_{\text{ls}}}^{t_0} n^i n^j E_{;i;j,t} dt.$$

The integral is over the CMB photon path along the line of sight to the last scattering surface (i.e. rays of constant $\tilde{\theta}$ in fig. 1.8). The directional dependence is due to the unit vector n^i which points from the observer to the emission surface and hence quantifies anisotropy deviations. Therefore we should next consider the geometry of the model setup in more detail.

The geometric situation of our LTB model is shown in fig. 1.8. There are two relevant sets of unit vectors, those denoted with \mathbf{n} are pointing from the location of the observer towards the last scattering surface, whereas the vectors \mathbf{e} define the coordinate system and have their origin at the centre of the LTB overdensity. From fig. 1.8 we read off that $\Delta\theta = \tilde{\theta} - \theta$; applying the law of cosines gives

$$(1.102) \quad r_L^2 = d^2 \left[\sin^2 \tilde{\theta} + \left(\frac{r_0}{d} + \cos \tilde{\theta} \right)^2 \right].$$

Our aim is to compute the components of \mathbf{n} , thus we can start with e.g. $\mathbf{n} \cdot \mathbf{e}_r = \cos \Delta\theta$. In order to compute $\cos \Delta\theta$ we can use the projection law for inclined triangles and get, c.f. fig. 1.8

$$(1.103) \quad \begin{aligned} d &= r_L \cos \Delta\theta + r_0 \cos(\pi - \tilde{\theta}), \\ \cos \Delta\theta &= -\frac{r_0}{r_L} \cos(\pi - \tilde{\theta}) + \frac{d}{r_L} = \frac{\varepsilon \cos \tilde{\theta} + 1}{\sqrt{\sin^2 \tilde{\theta} + (\varepsilon + \cos \tilde{\theta})^2}} = \mathbf{n} \cdot \mathbf{e}_r. \end{aligned}$$

Recall the definition of the ratio $\varepsilon \equiv r_0/d$. We can utilise the fact that $\mathbf{n} = n^1 \mathbf{e}_r + n^2 \mathbf{e}_\theta + 0$ and thus obtain the remaining component of \mathbf{n}

$$(1.104) \quad n^i = (n^r, n^\theta, n^\varphi) = (1 + 2\varepsilon \cos \tilde{\theta} + \varepsilon^2)^{-1/2} (1 + \varepsilon \cos \tilde{\theta}, r^{-1} \varepsilon \sin \tilde{\theta}, 0).$$

Obviously $\tilde{\theta}$ – the angle in the observer-centred system – is the relevant angle for the CMB. There is no dependence on $\tilde{\varphi}$ due to the axial symmetry. Before we proceed and finally insert these findings into the Sachs-Wolfe formula (1.101), we will discuss an appropriate general relativistic treatment of the occurring peculiar velocities.

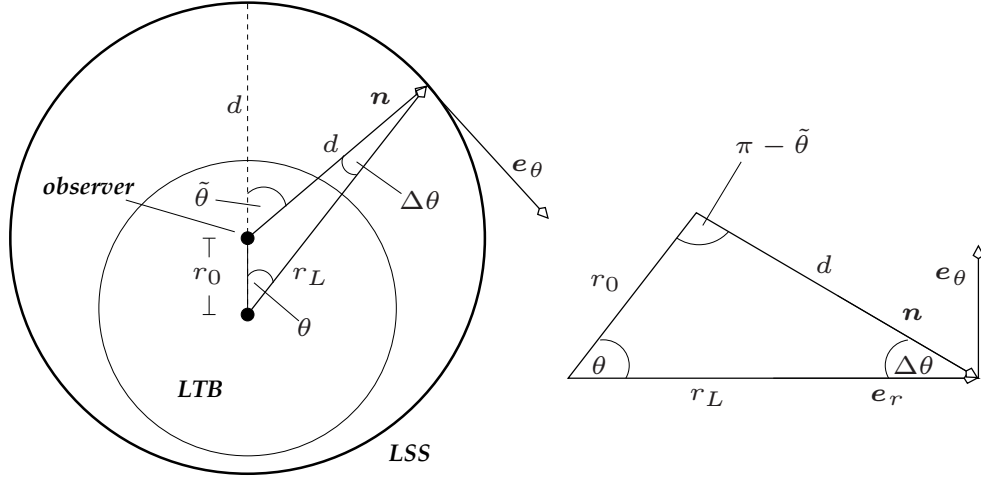


FIGURE 1.8. Schematic depiction of the LTB overdensity and its relation to the surface of last scattering. Here d is the distance between us and the last scattering surface, r_0 is the distance between our location and the centre of the overdensity and r_L is the distance from the LTB centre to the emission surface. The unit vectors of the coordinate system e^i point from the centre of the overdensity, the unit vectors n^i point from our position to the LSS. Note that the figure lies in the x - z plane.

Regarding the peculiar velocity, there are three main components contributing to the observer's motion: the overall expansion, the radial infall velocity due to the spherical overdensity and random motion associated with smaller structures. In the comoving coordinate system (1.46), the fluid velocity equals the background velocity $u^\mu = \delta^\mu_0$, so that the v_i appearing in the temperature anisotropy (1.101) pick up a contribution only from the random component. This is due to coordinate artefacts and, as is emphasised in [HPLN02, HN99], the individual terms in the temperature anisotropy are difficult to identify by physical means.

By definition, the peculiar velocity is the extra motion on top of the overall expansion of the Universe. In the present context the solution is exact, so in order to find the peculiar velocity we shall follow an unambiguous procedure presented in [Maa98, EvEM01]: we construct a physical four-velocity such that the corresponding flow is *shear-free*, and obtain the peculiar velocity as the difference between the comoving four-velocity and this (physical) shear-free flow. We start with the comoving four-velocity $u^\mu = \delta^\mu_0$ and the corresponding non-zero shear

$$(1.105) \quad \sigma_{\mu\nu} = u_{\langle\mu;\nu\rangle} \quad \text{with} \quad B_{\langle\mu\nu\rangle} = \left(q^\alpha_{(\mu} q^\beta_{\nu)} - \frac{1}{3} q^{\alpha\beta} q_{\mu\nu} \right) B_{\alpha\beta},$$

where the last equation defines the operation $\langle \cdot \rangle$ of taking the spatially projected, symmetric and traceless part of some tensor $B_{\alpha\beta}$ with the help of the according spatial projection tensor $q_{\mu\nu} \equiv g_{\mu\nu} + u_\mu u_\nu$. Working to linear order in v^μ , we now define a new velocity \tilde{u}^μ such that

$$(1.106) \quad u^\mu = \tilde{u}^\mu + v^\mu, \quad \tilde{u}^\mu v_\mu = 0, \quad \tilde{\sigma}_{\mu\nu} = 0.$$

Now we introduce the peculiar velocity v^μ and by $\tilde{\sigma}_{\mu\nu}$ we denote the shear associated with \tilde{u}^μ ,

$$(1.107) \quad \tilde{\sigma}_{\mu\nu} = \sigma_{\mu\nu} - v_{\langle\mu;\nu\rangle} = 0.$$

Given (1.105) and the linearly perturbed LTB metric (1.91) we can solve (1.107) for the peculiar velocity and obtain

$$(1.108) \quad v^\mu = \delta^\mu_r r f_{,t},$$

so that $v^2 = g_{\alpha\beta}v^\alpha v^\beta = a^2 f_{,t}^2 r^2$ and the corresponding, properly normalised spatial peculiar velocity vector becomes

$$(1.109) \quad v^i = \delta^i_r ar f_{,t}.$$

This finding is in accordance with the naive definition $v^r = R_{,t} - HR$, where H is the background Hubble parameter; note that using the physical expansion rate $\frac{1}{3}\theta = \frac{1}{3}u^\alpha_{,\alpha}$ instead of H would yield a different result. As can be read off from fig. 1.8, the observer is located on the z -axis, thus giving $\mathbf{n} \cdot \mathbf{v}(\mathcal{P}_0) = \mathbf{n} \cdot \mathbf{e}_z v^r(\mathcal{P}_0) = ar f_{,t} \cos\tilde{\theta}$. Finally, we can write the Sachs-Wolfe contribution of the linear LTB model as

$$(1.110) \quad \begin{aligned} \frac{\Delta T}{T}(\tilde{\theta}, \tilde{\varphi}) &= r_0 f_{0,t} \cos\tilde{\theta} - f_0 - r_0 f_{0,r} \frac{(1 + \varepsilon \cos\tilde{\theta})^2}{1 + 2\varepsilon \cos\tilde{\theta} + \varepsilon^2} \\ &\simeq - \left[f_0 + \left(1 - \frac{2}{3}\varepsilon^2\right) r_0 f_{0,r} \right] + \left(r_0 f_{0,t} - \frac{4}{5}\varepsilon^3 r_0 f_{0,r} \right) P_1(\cos\tilde{\theta}) - \frac{2}{3}\varepsilon^2 r_0 f_{0,r} P_2(\cos\tilde{\theta}) \\ &\quad + \frac{4}{5}\varepsilon^3 r_0 f_{0,r} P_3(\cos\tilde{\theta}) + \dots, \end{aligned}$$

and where we have expanded the temperature anisotropy in terms of the Legendre polynomials P_ℓ , as is convenient for CMB analysis. Therein f_0 stands for the perturbation function as measured today $f_0 \equiv f(t_0, r_0)$ at our position as the off-centre observers in the LTB picture. The power series structure in the parameter ε reflects the fact that here the anisotropy is due to the observer's deviation from the centre, and thus the amplitude of multipoles scales as ε^ℓ .

In principle it is possible to obtain the perturbation function f from a fit to observation data. This can be done by extending the general relativistic analysis of the peculiar velocity (1.109) in order to take into account also the effects of overall cosmic expansion as well as radial LTB infall. This can be taken care of by using a common phenomenological parametrisation of the local peculiar velocity field as measured today, see e.g. [Pan92, HSLB04]

$$(1.111) \quad v^i = \delta^i_r v_0 \frac{r}{r_0} \left(\frac{r_0^2 + c^2 r_0^2}{r^2 + c^2 r_0^2} \right)^{\frac{n+1}{2}},$$

where r_0 is again the distance from observer to the centre of the overdensity, v_0 stands for the infall velocity at the position of the observer, cr_0 parameterises the core size of the structure (the velocity peaks at $cr_0/n^{1/2}$), and the exponent n determines how fast the velocity field falls off with increasing r . Then the perturbation function $f(t, r)$ can be parametrised by means of the local velocity field using (1.109) and this can be inserted into the Sachs-Wolfe formula.

Now we can try to estimate the multipole's amplitudes from the Sachs-Wolfe expansion (1.110) as due to some very massive structure in our cosmic neighbourhood. After estimating $f_{,t} \simeq Hf$ – which is exact with a vanishing cosmological constant – we then get $f \simeq v/(arH)$. As we read off from equation (1.110), the quadrupole and the higher multipoles are proportional to the term $rf_{,r}$. Because of (1.89) we can write $rf_{,r} = \langle \delta \rangle_r - \delta$ and thus arrive at $rf_{,r} = -3f - \delta \simeq 3v/(arH) - \delta$. The magnitude of the quadrupole is $\varepsilon^2 rf_{,r}$. Let the observer be placed at $r_0 = 60\text{Mpc}$ from the origin, yielding $\varepsilon \simeq 10^{-2}$, and further assume an infall velocity of around 500km/s [KME04], we end up with $(0.25 - \delta) \times 10^{-4}$ for the quadrupole. With $\delta = 0.1$ the contribution to the quadrupole is of the same order as the intrinsic anisotropies, 10^{-5} . The contribution to the octopole is $-6\varepsilon/5$ times the one to the quadrupole, and therefore we cannot get a significant contribution to the octopole (or higher multipoles). The reason why our numerical estimate fails is rather simple: the Sachs-Wolfe theory that we developed is linear, but in order to go for a significant CMB effect we are forced to apply it to highly non-linear structures. One can see this also from the following argument. Remember the linearity conditions (1.87) and especially the time evolution constraint $f_{,t}/H \ll 1$. Now, from the definition of the perturbation function (1.86) we can readily see that, for an object like the here assumed supercluster – for instance the Great Attractor –, R is nearly constant, whereas R_{FRW} evolves at the time scale of the Hubble rate. This implies then an $f_{,t}/H$ of order unity.

Because the linearised Sachs-Wolfe calculation in our model is too naïve, we will, instead of fitting the model parameters to a local velocity input and trying to predict the temperature anisotropy, rather be interested in the general structure of the obtained solution (1.110). We will keep the coefficients in the multipole expansion open as free parameters of the particular LTB model and are going to use them in a statistical multipole analysis with regard to the excellent CMB data available. This and similar analyses are the subject of part II of this work. Summarising, let us note the main characteristic of the Sachs-Wolfe result (1.110): the *temperature anisotropies due to the LTB perturbation only contribute to the $m = 0$ components* of the multipole expansion as a consequence of the axial symmetry of the local model. In turn, any other axially symmetric structure, like e.g. a planar density field, would also be perceptible only within the $m = 0$ modes. Moreover, in the standard model the dipole is hidden in a strong signal due to peculiar motion with respect to the CMB rest frame and the quadrupole is (up to a small kinetic correction) of cosmological origin. In the LTB model a natural correlation between dipole and quadrupole arises, for they both originate from the same physical effect, thus making quadrupole-dipole alignment potentially explainable.

The Cosmological Problem of Dark Matter

Diverse physical observations support the postulation of an additional matter component, non-luminous and only interacting through gravity. The effects according to which Dark Matter might be postulated, manifest themselves on multiple physical scales. From the precise measurement of the first acoustic peaks in the CMB power spectrum, a scale of up to one degree on the microwave sky ($z_{\text{dec}} = 1088$) can be accessed. Interpreting the WMAP data within Λ CDM, it is well known that the universe appears to be spatially flat ($\Omega_k \simeq 0$) and that the matter and Dark Energy density form the cosmic concordance: $\Omega_m \simeq 0.24$ and $\Omega_\Lambda \simeq 0.76$, c.f. sec. 1.2.1.

At the same time the fraction of the matter density due to baryons as inferred from primordial nucleosynthesis and the deuterium abundance from Lyman- α systems is in good accordance with the value of $\Omega_b \simeq 0.04$ obtained from WMAP; see e.g. [PRFJ07], [WMAa]. It is noteworthy to say that these results, besides their model and prior dependencies, particularly depend on the value of the Hubble constant as measured today. Counting sources within ‘low’ redshifts ($z < 2$) yields a luminous baryon density that is only [NEFM05] $\sim 50\%$ of the cosmologically inferred value above. In the literature this is referred to as the ‘missing baryon problem’. Thus we encounter a twofold problem when trying to combine cosmic matter yields on different scales. First, the matter needed to close the universe obviously cannot be in form of baryons as the inferred value for baryons from different methods is one order of magnitude too small. Second, the upper limit for the density parameter from luminous matter as inferred from all-sky surveys reveals that at least 50% of the baryonic matter must also be dark.

Being in a somewhat more direct form, there is more evidence for Dark Matter especially on smaller scales. This we want to review in the next two sections and particular emphasis will be given to the galactic rotation curves. Herculean efforts are being made in order to find an explanation for the aforementioned Dark Matter problem(s). These range from modifications of the Einsteinian, and therewith of Newtonian gravity to extensions of the standard model of particle physics that involve new, yet undetected particles that could do the job. *However, it is important to stress that there is no a priori reason to believe that all of the missing matter problems on all of the different physical scales do have a common explanation.*

2.1. Direct Evidence and Lensing

A powerful tool for attempts of cataloguing the matter distribution of large-scale structures or intermediate-scale structures in the universe is provided by the principle of gravitational lensing. The fact that the gravitational deflection of light only depends on the effective gravitational fields deployed by the lens, and not on the particular state of the lensing matter, makes the method universal.

The phenomena of gravitational lensing split naturally into two classes: (A) strong lensing, involving rather pronounced effects like the formation of arcs, Einstein rings or multiple images of a single source as well as time delays – see for instance fig. 1.1; (B) weak lensing, not observable by eye since it is a statistical effect involving a large number of background sources that appear distorted due to large-scale foreground tidal fields.

In the following we shall discuss shortly the two different branches of gravitational lensing and then give examples of strong recent evidence for Dark Matter, where the results of weak and strong lensing are going hand in hand.

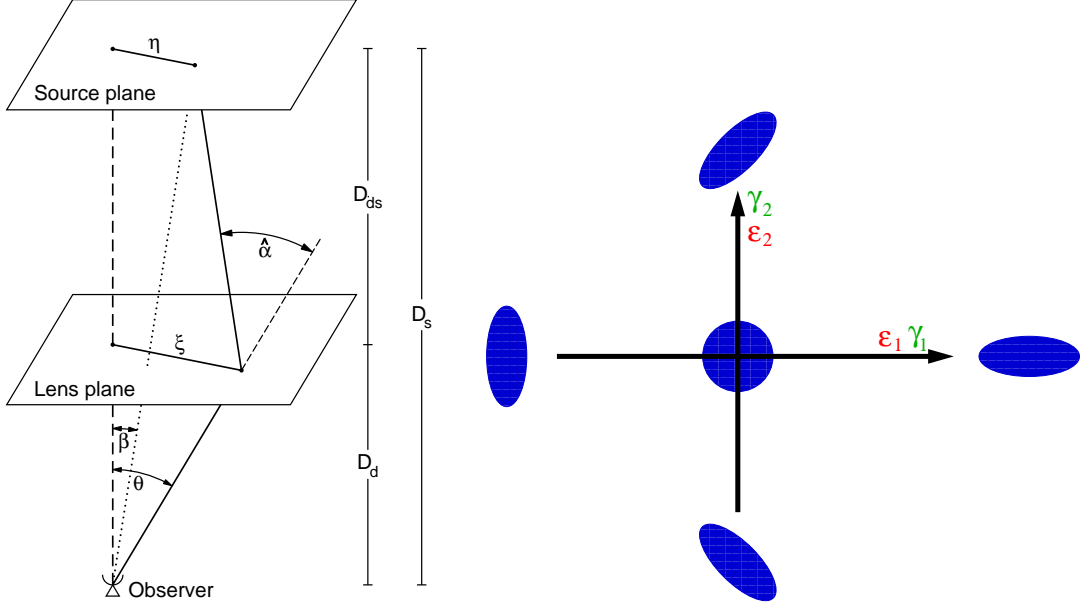


FIGURE 2.1. Geometry of strong (left) and weak (right) gravitational lensing. Left: without luminous and/or Dark Matter in the lens plane an observer sees the source under an angle β ; the presence of lensing matter changes that direction to $\hat{\alpha}$. Right: physical interpretation of the shear γ_i and ellipticity χ and ϵ . The ellipticities $\epsilon_{1,2}$ in the figure correspond to the notation χ, ϵ in the text. The shear component γ_1 is responsible for elongation (compression) along the x -axis, whereas γ_2 causes the same, just along the $x = y$ axis. Per definition, an object with vanishing ellipticity is circular (centre). The components of ellipticity χ and ϵ , defined with the help of the second brightness moments tensor, cause compressions and elongations similar to those for the shear components. Pictures are taken from [Sch03] and [Ref03].

2.1.1. Strong Gravitational Lensing. Following [Sch03] and [Sch06], we review concisely the strong lensing framework without deriving the equations. Utilising the Schwarzschild solution, the Einstein angle for a deflection off the exterior of a spherically symmetric mass M reads

$$(2.1) \quad \hat{\alpha} = \frac{2R_S}{\xi} = \frac{4GM}{c^2\xi},$$

where $2R_S$ is the Schwarzschild diameter and ξ is the impact parameter of the light ray measured in the plane of the lens, cf. fig. 2.1. This formula for ‘point mass’ deflection is valid in the weak field limit $R_S/\xi \ll 1$, or equivalently $\phi/c^2 \ll 1$ for the Newtonian gravitational potential.

In this limit, the lensing effects can be linearised, that is the (two-dimensional) Einstein angle of a complex lens can be superimposed from the deflection angles of the individual deflectors: $\hat{\alpha} = \sum_i \hat{\alpha}_i$. Within the Born approximation it is moreover assumed that the ‘lens is geometrically thin’, that is the distances between source, deflector and observer are much larger than the extent of the lensing system. This assumption is well satisfied for typical astrophysical lenses like galaxies or galaxy clusters but is not fulfilled in the case of lensing by the large-scale structure. For composed ‘thin lenses’ the deflection angle becomes

$$(2.2) \quad \hat{\alpha}(\xi) = \frac{4G}{c^2} \int d^2\xi' \int dr' \rho(\xi, r') \frac{\xi - \xi'}{|\xi - \xi'|^2} = \frac{4G}{c^2} \int d^2\xi' \Sigma(\xi') \frac{\xi - \xi'}{|\xi - \xi'|^2}.$$

The Einstein angle only depends on the surface mass density $\Sigma(\xi')$ which is the volume density after integrating out the line of sight dependence $\Sigma(\xi') \equiv \int dr_3 \rho(\xi, r_3)$. As a rule of thumb,

typical magnitudes of deflections for galaxies are $\hat{\alpha} \lesssim 1''$ and $\hat{\alpha} \lesssim 30''$ for galaxy clusters. For an illustrative example of arcs, see fig. 1.1.

Looking at fig. 2.1, we see that $\boldsymbol{\eta} = D_s \boldsymbol{\beta}$ and $\boldsymbol{\xi} = D_d \boldsymbol{\theta}$, and the lens equation can be written as:

$$(2.3) \quad \boldsymbol{\beta} = \boldsymbol{\theta} - \frac{D_{ds}}{D_s} \hat{\boldsymbol{\alpha}}(D_d \boldsymbol{\theta}) \equiv \boldsymbol{\theta} - \boldsymbol{\alpha}(\boldsymbol{\theta}),$$

with $\boldsymbol{\alpha}(\boldsymbol{\theta})$ denoting the scaled deflection angle. Note that (2.3) in general can have more than one solution corresponding to multiple imaging of the source. The dimensionless surface mass density is defined by

$$(2.4) \quad \kappa(\boldsymbol{\theta}) \equiv \frac{\Sigma(D_d \boldsymbol{\theta})}{\Sigma_{\text{crit}}}, \quad \Sigma_{\text{crit}} \equiv \frac{c^2}{4\pi G} \frac{D_s}{D_d D_{ds}} \simeq 0.35 \left(\frac{D_d D_{ds}}{D_s \text{1Gpc}} \right)^{-1} \text{g cm}^{-2}.$$

The quantity $\kappa(\boldsymbol{\theta})$ is also referred to as the convergence. The convergence may be used to infer the strength of a gravitational lens; with $\kappa \sim 1$ we characterise strong lensing and by $\kappa \ll 1$ the weak lensing regime is encountered.

The simplest models for gravitational lenses show axial symmetry, i.e. $\Sigma(\boldsymbol{\xi}) = \Sigma(\xi)$ with $\xi = |\boldsymbol{\xi}|$ being the distance to the centre of the lens. Even without detailed modelling of mass distributions it is possible to obtain a robust mass estimate for strong lensing. Because the mean surface mass density inside the Einstein radius θ_E just equals the critical surface mass density of the lens, it is

$$(2.5) \quad M(\theta_E) = \pi \Sigma_{\text{crit}} (D_d \theta_E)^2.$$

Analysing a picture of gravitational lensing that shows multiple images, the Einstein radius θ_E can be estimated from the radius of the circle that is traced by the different images. The more axisymmetric the lens system is, the better the estimate (2.5) becomes.

A common isotropic galaxy model is that of a singular isothermal sphere (SIS), c.f. [BT94]. The density profile is given by: $\rho(r) = \sigma_v^2 / 2\pi G r^2$, with σ_v being the one-dimensional velocity dispersion of stars in such a potential. Note that this model is very crude and can only be applied in a certain range of radii r : for small r the density diverges as r^{-2} and for large r the mass $M(r)$ diverges proportional to r . By integration the surface mass density is obtained: $\Sigma(\xi) = \sigma_v^2 / 2G\xi$. Finally, we arrive at a characteristic equation for the deflection angle of a galaxy-like SIS object:

$$(2.6) \quad \theta_E = 4\pi \left(\frac{\sigma_v}{c} \right)^2 \left(\frac{D_{ds}}{D_s} \right) \simeq 1''.15 \left(\frac{\sigma_v}{200 \text{ km/s}} \right)^2 \left(\frac{D_{ds}}{D_s} \right).$$

Since the separation of images is $\Delta\theta = 2\theta_E$, massive elliptical galaxies can generate separations of up to $\sim 3''$ and lighter ones as well as spiral galaxies reach $\sim 1''$.

Regarding clusters of galaxies the most simple approximative lens model is again provided by the SIS ansatz. The characteristic scale is also given by the according Einstein angle

$$(2.7) \quad \theta_E \simeq 28''.8 \left(\frac{\sigma_v}{1000 \text{ km/s}} \right)^2 \left(\frac{D_{ds}}{D_s} \right).$$

The analyses of galaxies and of clusters of galaxies with the help of strong gravitational lensing show that the masses of these lenses cannot be provided by the observable luminous matter from stars and intergalactic dust only. These findings strongly suggest that galaxies and galaxy clusters are dominated by Dark Matter.

2.1.2. Weak Gravitational Lensing. While the effects of strong gravitational lensing are rather strong and resolvable by eye, the effects of weak lensing can only be detected in a statistical sense. Due to weak lensing by dark and luminous matter in the line of sight, small distortions to the shape and orientation of background galaxies should always be present in deep astronomical images. Assuming that the intrinsic orientations (ellipticities) of the lensed

background galaxies are random, it is possible to reconstruct a map of the lensing matter in between by statistically analysing the ellipticities of an ensemble of background galaxies.

Following [Sch03], shape distortions are enfolded in the proper mapping of the lens from the plane of the source to the plane of the lens by the according Jacobi matrix

$$(2.8) \quad \mathcal{A}(\boldsymbol{\theta}) \equiv \frac{\partial \boldsymbol{\beta}}{\partial \boldsymbol{\theta}} = (1 - \kappa) \begin{pmatrix} 1 - g_1 & -g_2 \\ -g_2 & 1 + g_1 \end{pmatrix}.$$

Therein the crucial quantity is the shear $\gamma = \gamma_1 + i\gamma_2$, or similarly the reduced shear $g = g_1 + ig_2$ with $g_i = \gamma_i/(1 - \kappa)$. The physical meaning of shear and convergence κ is depicted in fig. 2.1. The mentioned mapping that describes the shape distortions of distant sources is described by the locally linearised lens equation

$$(2.9) \quad \boldsymbol{\beta} - \boldsymbol{\beta}_0 = \mathcal{A}(\boldsymbol{\theta}_0) \cdot (\boldsymbol{\theta} - \boldsymbol{\theta}_0),$$

with $\boldsymbol{\theta}_0$ being the centre of image and $\boldsymbol{\beta}_0 \equiv \boldsymbol{\beta}(\boldsymbol{\theta}_0)$. The next step is to formally define what is meant by the notion of ellipticity for arbitrary faint sources. Since the least background sources are intrinsically round, their observed ellipticity with a telescope will be an admixture of weak lensing induced shear and some initial ellipticity. In order to formally define a morphology of galaxies, one utilises the second brightness moments, which are components of a second-rank tensor that is defined upon the brightness distribution $I(\boldsymbol{\theta})$ of the image. For conciseness we do not give the explicit expressions here, the full formalism is explicitly developed for example in [Sch03]. The important point is that from the second brightness moments, two complex ellipticities χ and ϵ of the lensed source can be derived. Analogously, the ellipticities $\chi^{(s)}$ and $\epsilon^{(s)}$ can be computed from the according second brightness moments of the unlensed source. Within the standard model we make the assumption that the intrinsic orientations of the background galaxies are completely random, that is their expectation values vanish:

$$(2.10) \quad \mathbb{E}[\chi^{(s)}] = 0 = \mathbb{E}[\epsilon^{(s)}].$$

As a consequence one gets for the expectation value of ϵ after averaging

$$(2.11) \quad \mathbb{E}[\epsilon] = \begin{cases} g & \text{for } |g| \leq 1 \\ 1/g^* & \text{for } |g| > 1 \end{cases}.$$

This means that a measurement of image ellipticities directly yields an unbiased estimate of the local shear. But the estimate suffers from high noise due to the dispersion of the intrinsic ellipticities. Therefore obtaining a large enough ensemble of sources is crucial for such a shear measurement. Fortunately, this is realistic and viable: e.g. the Hubble Ultra Deep Field [HST] shows a very deep image of the sky, only $3' \times 3'$ in area, containing an impressive total number of 10^4 faint galaxies.

By the statistical effect of weak lensing it is possible to measure the coherent distortions of faint background ellipticities. The observed distortions will preferably stretch the source images in directions tangential with respect to the centre of lensing matter. Because the ellipticity that is induced by weak lensing is generically at most of the order of the initial ellipticity a high statistics is required for detection. Above it is discussed how a measurement of ellipticities can be used to get the reduced shear (2.11); but how does this translate into a matter distribution of the lensing matter in which we are finally interested? The convergence κ quantifies the increase in size of a background galaxy, independent of its shape. Within Newtonian theory the convergence plays the role of a source in the two-dimensional Poisson equation

$$(2.12) \quad \Delta^{(2)}\Psi(\boldsymbol{\theta}) = 2\kappa(\boldsymbol{\theta}),$$

where the deflection potential $\Psi(\boldsymbol{\theta})$ denotes the two-dimensional counterpart of the Newtonian potential. Thus, in Newtonian theory the convergence κ is proportional to the surface mass density of the gravitating lens, and hence producing a contour map of κ from the measured shear will trace the effective two-dimensional matter distribution. In fact, it is

$$(2.13) \quad \nabla \ln(1 - \kappa) = \frac{-1}{1 - g_1^2 - g_2^2} \begin{pmatrix} 1 - g_1 & -g_2 \\ -g_2 & 1 + g_1 \end{pmatrix} \begin{pmatrix} \partial g_1 / \partial \theta_1 + \partial g_2 / \partial \theta_2 \\ \partial g_2 / \partial \theta_1 - \partial g_1 / \partial \theta_2 \end{pmatrix}.$$

These equations can be integrated upon the two-dimensional data field and yield the final convergence map. Going a step further, in non-Newtonian gravity theories the convergence is not in a linear relation to the surface mass density anymore. However, even though within such theories an obtained κ map cannot be directly translated into a map of the two-dimensional matter distribution, the location of κ peaks will still correspond to the peak-values of the effective surface mass density, c.f. [C⁺06a]. This result is crucial for the discussion in the next subsection.

The concept of weak gravitational lensing will also be used for tomography of the large scale structure of the universe. This is a non-trivial task; there does not exist a single lens plane anymore but the complete inhomogeneous three-dimensional and very extended matter structure in the line of sight can be made responsible for distortions of faint sources. However, the method opens up a new window on a wide range of global cosmological parameters which will be accessible through completely different systematics and in a much lower redshift regime than through CMB measurements.

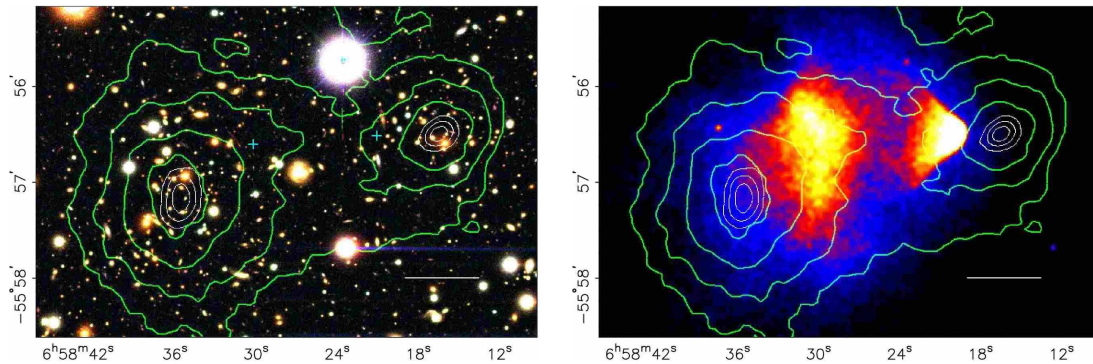


FIGURE 2.2. The ‘bullet cluster’, 3.4 billion light-years away, in optical (left) and X-ray (right) light. Left: on top of the optical image taken by the Magellan telescope the peaks in surface mass density κ [c.f. (2.13)] as reconstructed from weak lensing are shown (green contours). White contours quantify the error within the position of κ peaks: 68.3%,95.5% and 99.7% C.L. The white bar measures a distance of 200Mpc in the cluster plane. Right: an X-ray image taken by the Chandra space telescope, together with the same weak lensing reconstruction of matter density. Pictures are taken from [C⁺06a].

2.1.3. Recent Direct Evidence. Usually, lensing evidence for Dark Matter is provided by the necessity of excess gravitational potential on top of the baryonic one, in order to explain the observed phenomena. For isolated and relaxed systems, the centre of the Dark Matter potential coincides with the centre of the gravitational potential induced by the luminous matter; the luminous matter is believed to trace the (stronger) Dark Matter potential. Observing a constellation of matter, where the dark and luminous centres of mass are spatially separated, would provide eidetic and weighty evidence for Dark Matter on the scale observed. Such an observation would seriously challenge theories that invoke no Dark Matter but modifications of Newton or Einstein gravity.

Interestingly, a snapshot of the above mentioned situation might recently have been made [C⁺06a]. The object 1E0657-558 is a high-energy merger of two galaxy clusters at $z = 0.296$. In the course of the collision, the constituents of the clusters, the galaxies, behave like collisionless particles but in addition the system is interfused with intracluster relativistic plasma. This plasma behaves not collisionless at all, but undergoes massive ram pressure and this can be observed in the X-ray band. Due to the shape of the high energetic tail of one of the clusters (see fig. 2.2) the system was dubbed ‘bullet cluster’. The central regions of the two clusters coincided approximately 100 Myr ago but today the velocity of the clusters relative to each other is still ~ 4700 km/s.

Compared to the collisionless stars, the hot intracluster gas represents the dominant part of baryonic matter within the clusters. Therefore, if Dark Matter was not present in the cluster, the centre of mass of the X-ray luminous hot gas should trace the mass density of the whole system, as inferred e.g. by lensing methods. This is not in accordance with the physical observations as can be clearly seen from fig. 2.2. Imaging with optical telescopes has been used to determine a map of the surface mass density (2.13) with the help of weak gravitational lensing. At the same time images from the Chandra X-ray telescope have been made from exactly the same region of sky, showing the distribution of the hot gas only. Superimposing the images (fig. 2.2) shows that the peaks in matter density have moved in advance of the X-ray plasma which was decelerated by ram pressure. The displacement clearly indicates the presence of some form of Dark Matter which does not behave like a fluid. Constraints on the effective cross section of self-interaction of the Dark Matter can be directly obtained from this data [M⁺04]. Since the κ method only measures a two-dimensional distribution a loophole remains: in principle, it is thinkable that yet unidentified sources along the line of sight correspond to the density peaks that are detected. Nevertheless, the authors [C⁺06a] constrain the redshift interval wherein lensing sources could contribute to $0.18 \lesssim z \lesssim 0.39$. It is noteworthy to say that the data field of the bullet cluster allows for a combined analysis of weak and strong lensing methods, see [B⁺06b].

MODified Newtonian Dynamics (MOND) as invoked by Milgrom [Mil83] is based on the idea that the classical Newton force law is experimentally well tested only within Solar System scales, and hence could be modified for large scales. The TeVeS theory by Bekenstein [Bek04] comes to the same result in the weak field limit, but modifies gravity already at the level of Einstein theory by adding new vector and scalar degrees of freedom. By the observations of the bullet cluster the simplest of such models can be ruled out. However, more complicated versions of modified gravity could still be in accordance with the data, see e.g. [AFZ06] or [BM07].

Recently, a similarly impressive snapshot of Dark Matter was made using the Hubble Space Telescope (HST). The rich cluster of galaxies CL 0024+17 at $z = 0.4$ shows a ringlike structure of Dark Matter, obtained using combined strong and weak lensing methods [J⁺07b]. Fig. 2.3 shows the reconstruction of the ring of Dark Matter. The structure is thought to be the result of a high-speed collision similar to 1E0657-558, in this case occurring along the line of sight.

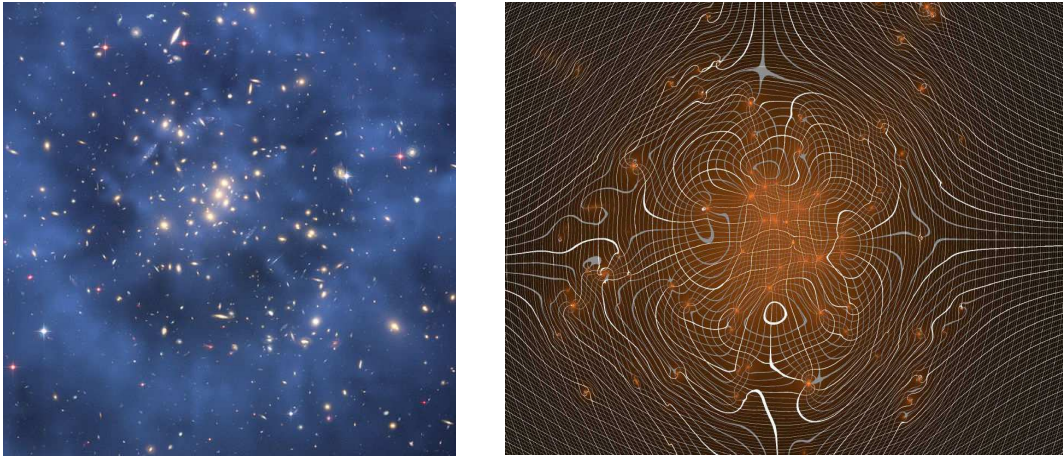


FIGURE 2.3. A ringlike structure of Dark Matter in the rich cluster CL 0024+17. Left: a reconstruction from lensing data of the Dark Matter ring is superimposed in diffuse blue upon an optical HST image. The size of the ring is $\sim 75''$ or approximately five million light-years. The ring probably originates from a massive galaxy cluster collision along the line of sight around 1-2 Gyr ago. Right: distribution of Dark Matter reconstructed from the CL 0024+17 image. A simulation of the consequences of gravitational lensing by the Dark Matter on orthogonal graph paper in the background is shown. Pictures are taken from [HST] and [LSS].

2.2. Classical Evidence from Dynamics

Historically, the first indications of Dark Matter have been observed on the scale of galaxies and galaxy clusters. In 1933 Fritz Zwicky analysed dynamical data from the Coma Cluster [Zwi33]. He found several galaxies with individual velocities that exceeded the mean cluster velocities by far. His interpretation was that these velocities provide a measure of the kinetic energy per unit mass in the cluster. After estimating the radius of the cluster he could compute the total mass of the cluster with the help of the virial theorem. Zwicky then independently estimated the mass of the cluster by counting the galaxies and using the total brightness of the galaxy cluster and found a discrepancy by a factor of 400. The observed velocities of galaxies were far too high to be bound solely by the luminous matter present. The consequence was that large, yet undetected amounts of matter had to be present in the Coma Cluster. Zwicky was the first to note this. His estimates were rather crude, but the subsequent analyses of clusters of galaxies and also of galactic systems themselves widely confirm his findings.

2.2.1. Evidence on Galactic Scales. We should begin with our galaxy, the Milky Way. Using the 21cm emission line of hydrogen HI, it is no problem to look through the interstellar gas in the direction of the centre of the Milky Way. Similarly, one makes use of the emission of the ^{12}CO gas that is present in the galactic disc. With these methods it is a straightforward measurement to obtain the circular velocities of objects that lie within the solar radius of $R_{\text{sun}} \simeq 8$ kpc using the Doppler effect. Note that our local standard of rest, the sun, is moving with a velocity of $v_{\text{sun}} \simeq 200$ km/s around the galactic centre. The result of the rotation measurement is shown in fig. 2.4. As can be seen clearly, the rotation curve shows no pronounced decrease of velocity for large radii. But the error bars are large in that region.

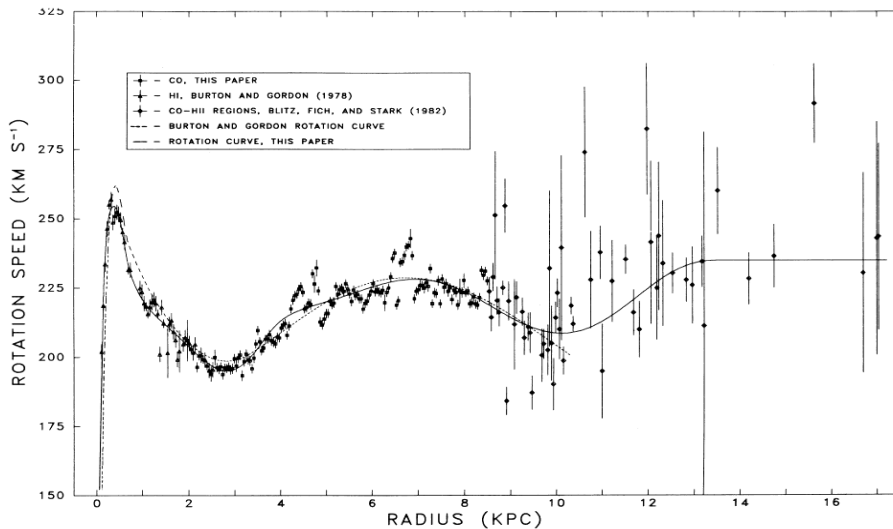


FIGURE 2.4. The rotation curve of the Milky Way. Observations make use of HI and ^{12}CO emission lines and are obtained from direct Doppler measurements of objects that lie within the solar orbit $R_{\text{sun}} \simeq 8$ kpc around the galactic centre. Orbits that have radii larger than that cannot be looked on tangentially; therefore additional distance yields are needed, leading to huge error bars in the outer regions of the curve. Picture is taken from [Cle85].

Rotation curve measurements for spirals other than the Milky Way are easier to obtain. It is possible to observe orbits tangentially and measure the Doppler effect of the rotating objects. However, correcting for the inclination of the disc is of course necessary. The rotation curves of a large number of spiral galaxies have been measured by now (fig. 2.5). Again the HI line proves

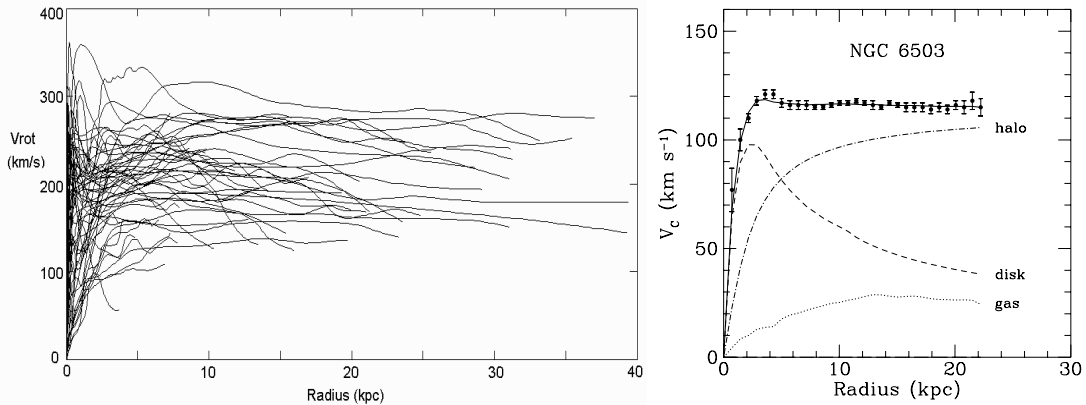


FIGURE 2.5. Left: galactic rotation curves of twenty-two spirals as inferred from H α and [NII] emission lines plotted in one figure. All the measured galaxies have either rising or flat rotation curves, which cannot be explained by luminous matter only. Right: rotation curve of the spiral galaxy NGC 6503 in Draco. The rotation velocity is decomposed into its contributions from the (luminous) galactic disc, luminous interstellar gas and the dark halo. Pictures are taken from [STT⁺98] and [BBS91].

its usefulness because one can collect the radio data within much larger radii. The finding of mostly flat rotation curves is confirmed for the different observed spirals.

A very simple calculation shows why these findings are so dramatic. We approximate the orbits of the constituents of a typical spiral galaxy as circles and get the rotation curve from the equilibrium of centripetal and gravitational force:

$$(2.14) \quad v^2(r) = \frac{GM(r)}{r},$$

where $M(r)$ is the mass within r . Further approximating the galactic bulge as a sphere with constant density, we have $M(r) = \rho \frac{4}{3} \pi r^3$. Thus in the innermost part of the galaxy, the curve should rise linearly with r and when leaving the galaxy the curve should decrease as $V(r) \propto 1/\sqrt{r}$ (Keplerian fall off). Despite the crude simplifications in this toy calculation the disagreement with experiment is dramatic.

As can be seen from fig. 2.5, in reality, rotation curves become approximately constant for large radii, which then implies $M(r) \propto r!$ Thus, enormous amounts of non-luminous matter must be made responsible for the observed curves, if Einstein gravity and therewith Newton Gravity is correct. According to (2.14) the rotation curve we expect from the luminous matter is $v_{\text{lum}}^2(r) = GM_{\text{lum}}(r)/r$ and hence the Dark Matter amounts to

$$(2.15) \quad M_{\text{dark}} = \frac{r}{G} [v^2(r) - v_{\text{lum}}^2(r)].$$

The consequence is that a halo of Dark Matter must be assumed whose mass grows linearly with radius since the density profile of the halo drops only as $1/r^2$ for large radii. As fig. 2.5 shows, measured rotation curves show no signs of decrease out to the maximally accessible radii measured with the help of 21cm emission. As a consequence the total mass of galaxies are herewith left undetermined, only a bound on the extension of a typical halo can be given: $r_{\text{halo}} \gtrsim 30$ kpc, c.f. [Sch06]. But the situation is even more disillusioning: since already the use of HI is a trick to expand the range of accessible radii, one must use something totally different in order to probe even larger scales of the halo. Satellite galaxies could be used as test bodies. However, their orbits are complicated and can only be interpreted in a statistical sense. Satellite analyses extend the typical size of halos to even $r_{\text{halo}} \gtrsim 100$ kpc, c.f. [Sch06].



FIGURE 2.6. The rare Polar Ring Galaxies can be used to study the three-dimensional shape of Dark Matter halos. A comparison of the rotation velocities within the host galaxy and the polar ring is sensitive to the geometry of the halo. Recent measurements combined with simulations suggest a flattened halo that is aligned with the polar ring [IAB⁺03]. Left: NGC 4650A, distance: 130 million light-years. Right: NGC 660, distance: 24 million light-years. Pictures are taken from [HST] and [SDS].

There are also other arguments in favour of the concept of a halo. As outlined in [BT94], stability of disc galaxies^a is a crucial issue. Normally, the evolution of disc galaxy models is highly unstable towards the formation of a dominant large bar. Although such galaxies exist, the presence of a Dark Matter halo of much larger extent than the disc is able to remove the bar instability. It is hypothesised that halos of Dark Matter could be necessary for the formation and stability of disc-like galaxies.

Polar Ring Galaxies (PRGs) are very exotic, likewise beautiful phenomena. Such non-typical galaxies are very rare occurrences; only around 150 objects have been recorded by now. Their origin is not well understood. It is hypothesised that Polar Rings develop after a merger of two galaxies, and in simulations such a behaviour could already be reproduced. PRGs often consist of a disc galaxy (host) plus a ring of interstellar gas and stars being in some inclination to the host galaxy, hence polar ring. But there are exceptions: e.g. the irregular galaxy known as Hoag's object is a PRG but its host galaxy is spherical and surrounded by an almost perfect ring. However, concerning dark halos such galaxies are important laboratories. Normally, the movement of stars via rotation curves can only be captured in one plane, as per definition only spirals can be analysed in such a way. PRGs offer the opportunity to probe the three-dimensional matter distribution of galaxies. The comparison of the perpendicular rotation curves in the respective outer regions shows that the rotation velocities in the polar plane are higher than those in the equatorial plane. By comparison with simulations, this can only be understood if the shape of the dark halo is flattened towards the polar ring [IAB⁺03]. Only if the two perpendicular rotation velocities approached equal values at large radii, the shape of the dark halo would be spherical.

Also in elliptical galaxies, a major contribution to the total mass is inferred to be dark due to dynamical considerations [KKZ97]. Rotation curves in the sense described above cannot be used for ellipticals, for the movement of stars is much more complicated. They can be characterised through an anisotropic velocity field. Assuming hydrostatic equilibrium and letting the galaxy

^aAccording to the Hubble Sequence of galaxies, disc galaxies enfold spirals as well as lenticular S0 galaxies.

be spherical [BT94] yields the Euler equation

$$(2.16) \quad \frac{dp(r)}{dr} = -\frac{GM_{\text{ellip}}(r)\rho(r)}{r^2}.$$

Therein the ideal gas law can be inserted, such that

$$(2.17) \quad M(r)_{\text{ellip}} = \frac{k_{\text{B}}T(r)r}{G\mu m_{\text{p}}} \left(-\frac{d\ln \rho(r)}{d\ln r} - \frac{d\ln T(r)}{d\ln r} \right)$$

describes the mass interior of r for an elliptical galaxy under the above assumptions. Herein μ denotes the mean molecular weight and m_{p} the proton mass. Thus, from a measurement of the temperature profile $T(r)$ and the density profile $\rho(r)$ of an elliptical galaxy, the mass within radius r can principally be obtained through (2.17), c.f. [KKZ97]. Assuming a fully ionised, optically thin medium one obtains the density profile from the luminosity profile via $L(r) \propto \rho^2(r)$. The temperature gradient is harder to get but can be obtained e.g. from CHANDRA measurements. Recent measurements confirm the presence of dark halos in elliptical galaxies, see e.g. [FBNP⁺06]. Moreover, the halo density profiles are found to approximate the Navarro-Frenk-White distribution

$$(2.18) \quad \rho(r)_{\text{dark}} = \frac{\rho_0}{\frac{r}{r_0} \left(1 + \frac{r}{r_0} \right)}.$$

Here, ρ_0 and r_0 are parameters that characterise a given halo.

2.2.2. Galaxy Clusters and the Virial Theorem. We start with the virial theorem in its tensor form

$$(2.19) \quad \frac{1}{2} \frac{d^2 I_{ij}}{dt^2} = 2K_{ij} + W_{ij}.$$

The theorem relates the moment of inertia to the kinetic and potential energy of an isolated system. Although the original version of the virial theorem is deduced from the collisionless continuum Boltzmann equation, the identity can also be proven to hold for a discrete system of say N particles; let the particles be either stars or galaxies, see e.g. [BT94]. Then I_{ij} denotes the moment of inertia tensor of the system and it reads

$$(2.20) \quad I_{ij} \equiv \sum_{\alpha=1}^N m_{\alpha} x_i^{\alpha} x_j^{\alpha},$$

where m_{α} is the mass of the object with label α . By explicitly performing the derivatives with respect to time on (2.20), one finds the expressions for the kinetic energy tensor and the potential energy tensor, i.e.

$$(2.21) \quad K_{ij} = \frac{1}{2} \sum_{\alpha=1}^N m_{\alpha} \dot{x}_i^{\alpha} \dot{x}_j^{\alpha} \quad \text{and} \quad W_{ij} = -\frac{1}{2} \sum_{\alpha, \beta=1 \wedge \alpha \neq \beta}^N Gm_{\alpha} m_{\beta} \frac{(x_i^{\alpha} - x_i^{\beta})(x_j^{\alpha} - x_j^{\beta})}{|\mathbf{x}^{\alpha} - \mathbf{x}^{\beta}|^3}.$$

Taking the trace of (2.19), gives the important scalar virial theorem:

$$(2.22) \quad \frac{1}{2} \frac{d^2 I}{dt^2} = 2K + W.$$

Under the assumption that the system is relaxed, that is the moment of inertia has become independent of time, we have $2K + W = 0$ with the traces

$$(2.23) \quad K \equiv \frac{1}{2} \sum_{\alpha=1}^N m_{\alpha} v_{\alpha}^2 \quad \text{and} \quad W \equiv -\frac{1}{2} \sum_{\alpha, \beta=1 \wedge \alpha \neq \beta}^N \frac{Gm_{\alpha} m_{\beta}}{|\mathbf{x}^{\alpha} - \mathbf{x}^{\beta}|}.$$

When the number of constituents N is not very large, the virial theorem

$$(2.24) \quad 2K + W = 0$$

will hold only for the respective time averages [BT94].

Our aim is to exploit the correlation between velocity distribution and total mass in clusters of galaxies. If we like to use the virial theorem in the form of (2.24), the galaxy cluster must be relaxed ($\ddot{I} = 0$). Therefore the question of applicability of the virial theorem (2.24) reduces to the question whether the constituents of the considered galaxy cluster did have enough time to arrive at mechanical equilibrium. The time that a typical galaxy needs in order to cross the cluster can be estimated [Sch06] from the one-dimensional velocity dispersion of the cluster $\sigma_v^{\text{cluster}}$ and its typical extension by $t_{\text{cross}} \sim R_A/\sigma_v^{\text{cluster}}$. For the typical extension one inserts the Abell radius of clusters $R_A \simeq 1.5h^{-1}\text{Mpc}$ as well as a rough value of $\sigma_v^{\text{cluster}} \simeq 1000\text{km/s}$ which finally yields $t_{\text{cross}} \sim 1.5h^{-1} \times 10^9\text{yr}$. Since this is smaller than the Hubble time, the virial theorem (2.24) for the time-averaged quantities K and W can be applied.

Following [Sch06], we proceed with defining the mass-weighted velocity dispersion and the gravitational radius

$$(2.25) \quad \langle v^2 \rangle \equiv \frac{1}{M} \sum_{\alpha=1}^N m_{\alpha} v_{\alpha}^2 \quad \text{and} \quad r_G \equiv M^2 \left(\frac{1}{2} \sum_{\alpha, \beta=1 \wedge \alpha \neq \beta}^N \frac{G m_{\alpha} m_{\beta}}{|\mathbf{x}^{\alpha} - \mathbf{x}^{\beta}|} \right)^{-1},$$

with the total mass of the cluster $M \equiv \sum_{\alpha=1}^N m_{\alpha}$. Potential and kinetic energy are then rewritten as $K = M\langle v^2 \rangle/2$ and $W = -GM^2/r_G$, and with the help of the virial theorem, a formula for the cluster mass is obtained:

$$(2.26) \quad M = \frac{r_G \langle v^2 \rangle}{G}.$$

The above mass estimate is based on the gravitational radius that involves the true distances $d^{\alpha\beta} \equiv |\mathbf{x}^{\alpha} - \mathbf{x}^{\beta}|$ in three-dimensional space. But this is not an observable, since only projections of this distance are accessible. We assume a spherical geometry and let $D^{\alpha\beta}$ denote the projected distance of two objects on the plane of the sky, then it is

$$(2.27) \quad R_G \equiv M^2 \left(\frac{1}{2} \sum_{\alpha, \beta=1 \wedge \alpha \neq \beta}^N \frac{G m_{\alpha} m_{\beta}}{D^{\alpha\beta}} \right)^{-1} \quad \text{and} \quad r_G = \frac{\pi}{2} R_G.$$

The factor of $\pi/2$ comes from the angular averaging of the projected distance. Further, it is assumed that the velocity dispersion of galaxies be isotropic: $\langle v^2 \rangle = 3\sigma_v^2$. Then, finally the cluster mass estimate amounts to

$$(2.28) \quad M = \frac{3\pi R_G \sigma_v^2}{2G} \simeq 1.1 \times 10^{15} M_{\odot} \left(\frac{\sigma_v}{1000 \text{ km/s}} \right)^2.$$

By simply taking the average $m_{\text{gal}} \equiv M/N$, we estimate the individual mass of a constituent galaxy by $m_{\text{gal}} \sim 10^{13} M_{\odot}$ which is very large. This estimate represents the main result of the virial theorem ansatz for clusters and supports the early findings using mass-to-light ratios by Zwicky.

Using the virial theorem ansatz, the matter contribution of galaxies to a typical galaxy cluster only amounts to $\sim 5\%$. Because the predominant fraction of matter of a cluster is dark, it should be questioned whether the above calculation is justified. The validity of the virial estimate can be maintained if the luminous galaxies do trace the distribution of overall matter. If the isotropy of the constituent velocity distribution is broken, or if the approximation of the system in being spherical is not valid, the above estimate becomes invalid [Sch06]. Therefore the Dark Matter evidence suggested by the virial theorem should always be taken with a pinch of salt. Moreover, observations of the hot intracluster gas yield varying fractions of this contribution to the total mass, but also here bulk Dark Matter remains necessary.

2.3. Modelling Galaxies with General Relativity

The usual framework in which we model a galactic system is Newton Gravity. This limit is commonly used for N -body simulations of galaxies but also for clusters of galaxies or even larger

structures. While General Relativity is widely accepted as the correct theory for cosmology, the Dark Matter problem has led to attempts to modify General Relativity and therewith Newton Gravity through MOND or TeVeS as sketched in sec. 2.1. Because modified gravity theories are deliberately designed to solve the Dark Matter problem raised by the observed non-Keplerian fall-off of galactic rotation curves, they pose a highly fine-tuned and a posteriori attempt. In any case, it appears adequate to modify current fundamental theories, or invent new theories, if and only if nothing else would work out. Among other outstanding problems, the need for Dark Matter has impelled the phenomenology of new fundamental theories also in particle physics. But up to day none of the candidate particles that could constitute Dark Matter has been observed directly in an experiment.

The evidence in favour of Dark Matter is manifold and appears on a vast range of physical scales. It is yet unclarified whether these effects all have the same origin. Arguably, one of the most weighty and most puzzling evidences is that of flat galactic rotation curves. In a recent work by Cooperstock and Tieu (CT) the question has been raised whether one uses the correct fiducial theory to compare with the data. Regarding a galactic system, the use of Newton Gravity appears well warranted since the fields involved are weak ($\phi_{\odot}/c^2 \lesssim 10^{-5}$) and the typical rotation velocities are small ($V_{\odot} \simeq 220$ km/s). Nevertheless, the use of the full theory of General Relativity might bring important new insights. The fields and velocities involved in a planetary two-body problem are also small but lead to the qualitatively new and peculiar effect of a different perihelion precession than that given by Newton Gravity. Also, as pointed out in [CT05a], the effects a system undergoes that is solely bound by gravity can be intrinsically non-linear, already in a stationary setup, and are thus not necessarily captured within the weak field limit.

It should be noted that the concrete model as proposed in [CT05a] has been shown to suffer from certain pathologies like singularities in the energy momentum tensor. Before we discuss this model in more detail we recall attempts of modelling a stationary and axisymmetric gravitational system within general relativity which exist since the nineteenth century. *It is astonishing to note that a simple and physically applicable answer, moreover without pathologies, to the problem of a stationary rotating and axisymmetric matter system in general relativity does not exist by now.* We conclude the section with an analysis of the Newton limit of the CT model and state that indeed a post-Newtonian model has to be invoked in order to make sense.

2.3.1. General Relativistic, Axisymmetric Systems in Equilibrium. A very important branch of exact solutions in General Relativity belong to the axisymmetric and stationary self-gravitating systems. Lots of astrophysical objects can principally be modelled with these assumptions. These could be stars, black-holes, accretion discs or galaxies; we will be especially interested in the latter. Before we can write down a general relativistic model of a galaxy, the crucial attributes of axisymmetry and stationarity should first be defined properly.

In a formal sense [Wal84], the existence of two commuting one-parameter groups of isometries that possess timelike and closed spacelike orbits respectively, is sufficient to call a spacetime stationary and axisymmetric. More explicitly, this notion can be expressed with the help of the according Killing vector fields. Killing vectors are the generators of the mentioned isometries on a manifold and can be used to characterise the symmetries of a spacetime. Consequently, the axisymmetric and stationary spacetimes will have two independent Killing fields; e.g. in Minkowski spacetime there exist ten Killing vectors (due to translation, rotation and boost).

In the following we use at least $c \equiv 1$. We will mainly follow the excellent presentation in Islam's book on rotating fields in General Relativity [Isl85]. If there exists a Killing vector field ξ , associated with a given spacetime, that is timelike everywhere, then the spacetime is called stationary. If, in turn, a manifold additionally admits a Killing vector field η that is spacelike everywhere and whose orbits are closed, then the spacetime is understood to be stationary and axisymmetric. Equivalently, using Killing's equations

$$(2.29) \quad \xi_{\mu;\nu} + \xi_{\nu;\mu} = \mathcal{L}_{\xi} g_{\mu\nu} = 0 \quad \text{and} \quad \eta_{\mu;\nu} + \eta_{\nu;\mu} = \mathcal{L}_{\eta} g_{\mu\nu} = 0,$$

one can verify that the two Killing vector fields commute everywhere on the spacetime:

$$(2.30) \quad [\xi, \eta] = 0.$$

With a semicolon we denote covariant differentiation and \mathcal{L}_σ stands for the Lie derivative along some vector field σ – we return to the Lie derivative in sec. 2.3.4. From the requirement of asymptotic flatness one can deduce the explicit form of the vectors: $\xi^\mu = \delta^\mu_0$, $\eta^\mu = \delta^\mu_2$. Once ξ and η do commute everywhere, it is possible to define coordinates t and φ according to

$$(2.31) \quad \xi = \xi^\mu \frac{\partial}{\partial x^\mu} = \frac{\partial}{\partial t} \quad \text{and} \quad \eta = \eta^\mu \frac{\partial}{\partial x^\mu} = \frac{\partial}{\partial \varphi},$$

where we use the component-free notation due the explicit form of Killing vectors. Then from Killing's equation (2.29) it follows that

$$(2.32) \quad \frac{\partial g_{\mu\nu}}{\partial t} = 0, \quad \frac{\partial g_{\mu\nu}}{\partial \varphi} = 0.$$

The remaining coordinates are called r and z and their according vector fields $\zeta = \partial/\partial r$ and $\chi = \partial/\partial z$ are each orthogonal to both ξ and η due to orthogonal transitivity [Car69]. These orthogonalities imply for instance that $g_{\mu\nu}\xi^\mu\zeta^\nu = 0$; with $\xi^\mu = \delta^\mu_0$ and $\zeta^\nu = \delta^\nu_1$, this in turn implies $g_{01} = 0$. Analogously, from $g_{\mu\nu}\xi^\mu\chi^\nu = 0$ it follows $g_{03} = 0$ and so on, such that we arrive at the general form of the metric (2.35). This derivation of the general form of axisymmetric and stationary spacetimes is rather formal. Interestingly, it is possible to deduce the result by much simpler means.

Can we interpret the above formalism in physical terms? First, let us write down the four-velocity that characterises objects undergoing stationary and purely angular movement,

$$(2.33) \quad u^0 = \frac{dt}{d\tau} = u^0(r, z), \quad u^1 = \frac{dr}{d\tau} = 0, \quad u^2 = \frac{d\varphi}{d\tau} = \frac{d\varphi}{dt} \frac{dt}{d\tau} \equiv \Omega(r, z)u^0, \quad u^3 = \frac{dz}{d\tau} = 0,$$

$$(2.34) \quad \text{where } (x^0, x^1, x^2, x^3) = (t, r, \varphi, z)$$

is the coordinate notation already introduced above and which we also use in the following. Further, τ denotes the proper time and $\Omega(r, z)$ is the (differential) angular velocity. Notably, the gravitational field produced by a rotating body according to (2.33) is neither invariant to time reversal $t \rightarrow -t$ nor is it invariant under $\varphi \rightarrow -\varphi$, for both operations are inverting the rotational sense of the object. Now, a simultaneous transformation of both $t \rightarrow -t$ and $\varphi \rightarrow -\varphi$ leaves the movement of the body unchanged. From this we can already deduce what metric components must vanish: if e.g. $g_{01} \neq 0$, then $g_{01}dt dr$ would change sign^b under the transformation $(t, \varphi) \rightarrow -(t, \varphi)$ and thus destroy invariance of the metric. Analogously, we see that any mixing terms g_{03}, g_{12}, g_{23} must vanish. Therefore the metric takes the form:

$$(2.35) \quad ds^2 = -g_{00}dt^2 + 2g_{02}dt d\varphi + g_{22}d\varphi^2 + g_{MN}dx^M dx^N,$$

where the indices M, N take the values 1 or 3. Finally, after some coordinate transformations, we arrive at the general axially symmetric and stationary spacetime as due to Lewis [Lew32] and Papapetrou [Pap66]

$$(2.36) \quad ds^2 = e^{-2U} [g_{MN}dx^M dx^N + W^2 d\varphi^2] - e^{2U} (dt + A d\varphi)^2,$$

see also [SKM⁺03]. The metric functions U, g_{MN}, W and A are free functions of r and z only, reflecting axisymmetry and stationarity. This is the spacetime that is most general under the above symmetry assumptions. Note that, with the help of $\xi^\mu = \partial x^\mu / \partial t$ and $\eta^\mu = \partial x^\mu / \partial \varphi$, it is possible to write all the metric functions from (2.36) as scalar products of the Killing fields

$$(2.37) \quad -e^{2U} = \xi^\alpha \xi_\alpha, \quad e^{-2U} W^2 - e^{2U} A^2 = \eta^\alpha \eta_\alpha, \quad -e^{2U} A = \xi^\alpha \eta_\alpha, \quad W^2 = 2 \xi_{[\alpha} \eta_{\beta]} \xi^\alpha \eta^\beta.$$

In the following we will discuss to which extent it is possible to further simplify the general metric (2.36), and also what solutions to this ansatz there might exist in General Relativity.

^bFor an axisymmetric and stationary setup all metric coefficients will be functions of r, z only, c.f. (2.32).

What we have considered so far is the geometry of axially symmetric and stationary systems, that is the left hand side of Einstein's field equations of gravity

$$(2.38) \quad R_{\mu\nu} - \frac{1}{2}Rg_{\mu\nu} = 8\pi GT_{\mu\nu},$$

with the Ricci tensor $R_{\mu\nu}$ and its trace $R \equiv g^{\mu\nu}R_{\mu\nu}$. The remaining input should come through the energy-momentum tensor $T^{\mu\nu}$, that in case of a perfect fluid takes the form

$$(2.39) \quad T^{\mu\nu} = (\rho + p)u^\mu u^\nu + pg^{\mu\nu} \quad \text{with} \quad u_\mu u^\mu = -1.$$

However, constructing solutions to the field equations is a very hard task, especially when peculiar a priori assumptions on the symmetries are imposed. The reason for this is that the field equations (2.38) are technically very complicated, they represent a coupled system of ten elliptic-hyperbolic partial differential equations.

Consequently, what is done first, is to try and find exterior (vacuum) solutions to the Einstein equations, given by $R_{\mu\nu} = 0$. In this case it is always possible to replace the metric function $W(r, z)$ in (2.36) by r [Isl85]; we will discuss this simplification, the isotropic gauge, in much detail in sec. 2.3.3.

The first solution found is a very famous one, the Schwarzschild solution

$$(2.40) \quad ds^2 = -\left(1 - \frac{2GM}{r}\right) dt^2 + \left(1 - \frac{2GM}{r}\right)^{-1} dr^2 + r^2 d\Omega^2,$$

with the angular element $d\Omega^2 = d\theta^2 + \sin^2\theta d\varphi^2$. As is well known, this solution describes the field exterior to a spherically symmetric (collapsed) star with mass M . Further, the system must be static, which is no assumption but follows from Birkhoff's theorem. The interior Schwarzschild solution also exists. It can be shown that the interior Schwarzschild solution is the only axisymmetric and static spacetime that is conformally flat [SKM⁺03].

Weyl was then the first to find a solution involving the general axisymmetric geometry. However, the Weyl solution [Wey17] is of limited physical applicability^c, since it describes the exterior solution of a system without rotation, that is an axisymmetric and static system. In this case, the general spacetime (2.36) can be simplified to

$$(2.41) \quad ds^2 = e^{-2U} [e^{2k}(dr^2 + dz^2) + r^2 d\varphi^2] - e^{2U} dt^2.$$

Another set of solutions that is physically not compelling, is the Papapetrou class [Pap53]. Yet this class of exterior solutions does not contain any solution that is asymptotically flat *and* contains a non-zero mass. Asymptotic flatness is an important physical requirement, for it enables us to check the properties of the rotating source by placing an observer who is in static Minkowski space at some asymptotic distance. We define asymptotic flatness by demanding that, at large distances from the rotating gravitational system, the spacetime shall look Minkowskian

$$(2.42) \quad ds^2 = -dt^2 + dr^2 + r^2 d\varphi^2 + dz^2.$$

This condition can be cast into one for the metric functions e^{2U} and A at spatial infinity, c.f. [Isl85] and chapt. 19 of [MTW73]

$$(2.43) \quad e^{2U} = 1 + \frac{2GM}{\sqrt{r^2 + z^2}} + \dots \quad \text{and} \quad e^{2U} A = -\frac{2GSr^2}{(r^2 + z^2)^3} + \dots,$$

where S is the total angular momentum of the source and the dots stand for higher terms that vanish towards infinity faster than the other terms. Unfortunately, the Papapetrou solutions, which would describe the exterior of an axisymmetric and stationary rotating system, always lead to a zero mass in the flat asymptotic limit.

Similarly, the class of solutions due to Lewis [Lew32] and Van Stockum [vS37] does not contain any asymptotically flat solutions. The metric here takes the form

$$(2.44) \quad ds^2 = r^{-1/2} (dr^2 + dz^2) - 2rd\varphi dt + r\Xi dt^2,$$

^cNevertheless, higher dimensional extensions of the Weyl solution are discussed as models of cosmic strings or other exotics, c.f. [ER02]

where Ξ obeys $\Delta^{(3)}\Xi = 0$. If solutions with flat limits exist, these would describe the field of a rotating body that is infinitely long and axisymmetric around the z -axis. The body does not need to be cylindrically symmetric (this would imply additional translational invariance along z) but may have a varying shape along the symmetry axis z . Cylindrically symmetric and stationary solutions represent a subclass of the Lewis and Van Stockum class [SKM⁺03].

While the Papapetrou class of solutions is rotating and has a well-defined flat limit, the mass associated must be zero. Ten years after the discovery of the Papapetrou solution, another very famous exterior solution has been found. Using Boyer-Lindquist coordinates (\hat{r}, ϑ)

$$(2.45) \quad r = (\hat{r}^2 - 2GM\hat{r} + a^2)^{1/2} \sin\vartheta, \quad z = (\hat{r} - GM) \cos\vartheta,$$

the Kerr solution [Ker63] takes the form

$$(2.46) \quad ds^2 = \left(1 - \frac{2GM\hat{r}}{\hat{r}^2 + a^2 \cos^2\vartheta}\right)^{-1} \left[(\hat{r}^2 - 2GM\hat{r} + a^2) \sin^2\vartheta d\varphi^2 + (\hat{r}^2 - 2GM\hat{r} + a^2 \cos^2\vartheta) \right. \\ \left. \times \left(d\vartheta^2 + \frac{d\hat{r}^2}{\hat{r}^2 - 2GM\hat{r} + a^2} \right) \right] - \left(1 - \frac{2GM\hat{r}}{\hat{r}^2 + a^2 \cos^2\vartheta}\right) \left(dt + \frac{2GMa\hat{r} \sin^2\vartheta d\varphi}{\hat{r}^2 - 2GM\hat{r} + a^2 \cos^2\vartheta} \right)^2.$$

Therein a carries the interpretation of an angular momentum per unit mass and M is the total mass of the rotating object. The limiting cases in the above parameterisation range from $a = GM$ (extreme Kerr limit) and $a = 0$ (Schwarzschild limit). At very large radii the Kerr metric is simplified to

$$(2.47) \quad ds^2 \simeq - \left(1 - \frac{2GM}{\hat{r}}\right) dt^2 + \left(1 - \frac{2GM}{\hat{r}}\right)^{-1} d\hat{r}^2 + \hat{r}^2 (d\vartheta^2 + \sin^2\vartheta d\varphi^2) - \frac{4Gma \sin^2\vartheta}{\hat{r}} d\varphi dt.$$

Though it is flat, with non-zero mass in the asymptotic limit, the problem is that this solution is only valid in the vacuum case too. Thus, it could still be used to model the exterior of a rotating black hole or galaxy. Up to day, no interior solution has been found that matches the above exterior Kerr solution and makes physical sense.

In the 1970s a similar class of solutions has been found by Tomimatsu and Sato [TS72]. An important characteristic of the Kerr solution is that it returns to the Schwarzschild form as soon as the rotation stops, $a = 0$. This makes sense, for deformations of a spherical rotating body are normally due to its rotation and should disappear in the static limit. However, the main difference of the Tomimatsu-Sato solution to the Kerr solution is that it does not possess such a nice static limit. Instead, the static limit coincides with the axisymmetric Weyl solution which makes the model unphysical [Isl85].

As we have seen, already the known exterior solutions are not very numerous. Furthermore, a lot of them are anyway of mathematical importance only, like e.g. the Papapetrou class of solutions. It remains to consider the right hand side of the Einstein equations (2.38) and whether there exist appropriate sources when axisymmetry and stationarity is assumed. Merging exterior and interior solutions in a proper way poses a highly non-trivial program and there do not exist many such global models. By now, the situation could be described like this: to vacuum solutions that are be physically tempting, always very exotic and sometimes unphysical sources must be assigned. In other words, quoting Hermann Bondi [BL93]:

[...] the sources suggested so far for the [Kerr] metric are not the easiest materials to buy in shops.

One of the very rare exceptions is the global Van Stockum solution [vS37]. In this solution a setup of an infinitely long, stiffly rotating dust cylinder is realised. Van Stockum was able to match smoothly the original exterior solution we discussed above, to an interior solution that he found independently. In [VW77] the complication of a non-rigid rotation within the Van Stockum class has been incorporated. According to [SKM⁺03] there does not exist any solution

at all to the problem of an axially symmetric and differentially rotating perfect fluid system with non-zero pressure up to day.

It should be noted that also the Van Stockum class of solutions is not free from shortcomings. First, as pointed out by Bonnor [Bon80], in the Van Stockum solution the matter density is growing exponentially with radial distance to the axis of symmetry as $\rho = \alpha^2 e^{\alpha^2 r^2} / (2\pi)$ where α is an arbitrary positive constant. Second, the Van Stockum class implies the existence of closed timelike curves, similar to those occurring in the Gödel solution. Notably, the closed timelike curves do not lie on geodesics, i.e. observers that undergo these orbits are necessarily accelerating. The existence of such curves is hard to reconcile with causality.

All of the above approaches are based on the philosophy that the geometric part, the metric, of a given problem is fixed first and then the solutions for the matter fields (usually a perfect fluid) are derived by solving Einstein's equations; this is the classical method. There are several groups that attack the problem the other way round. As a representative thereof, we mention here the Neugebauer and Meinel solution [NM95] where the so-called inverse (scattering) method is applied. It can be shown that the Einstein equations for the problem of an axially symmetric and stationary gravitating system are formally equivalent to the associated Ernst equation

$$(2.48) \quad \text{Re}(\mathcal{E}) \Delta^{(3)} \mathcal{E} = \Delta^{(2)} \mathcal{E}.$$

In [NM95] and succeeding works an infinitesimally thin disc of dust is presumed and explicit solutions for the complex Ernst potentials \mathcal{E} and thus to the Einstein equation are derived in terms of ultraelliptic functions as well as related theta functions. For the mathematical notions see e.g. [AS72]. Being immensely complicated, this appears to be the first formally complete solution to the problem of an axisymmetric and stationary rotating thin disc of dust within General Relativity.

2.3.2. The Cooperstock and Tieu Solution. In a recent series of works, Cooperstock and Tieu suggest a new approach to the Dark Matter problem, namely via General Relativity, see [CT05a], [CT05b] and [CT06]. Rewritten in our signature, the metric of the CT model is

$$(2.49) \quad ds^2 = e^{\nu-w} (dr^2 + udz^2) + r^2 e^{-w} d\varphi^2 - e^w (dt + Nd\varphi)^2.$$

The authors immediately set $u \equiv 1$ such that there remain only three characteristic functions to the metric ν, w and N , all being functions of only r and z .

The matter model that is used is that of uniformly rotating dust. Further, comoving coordinates are used in which an observer measures the four velocity as $u^\mu = \delta^\mu_0$. From the invariant condition $u^\mu u_\mu = g_{\mu\nu} u^\mu u^\nu = -1$ we immediately get $w = 0$. Differential rotation is established through the transformation $\varphi' \mapsto \varphi + \omega(r, z)t$ which diagonalises the metric (2.49) locally. Note the difference between w and ω . The angular velocity and the observable tangential velocity become

$$(2.50) \quad \omega = \frac{Ne^w}{r^2 e^{-w} - N^2 e^w} \simeq \frac{N}{r^2} \quad \text{and} \quad v = \omega r$$

for weak fields. Writing the field equations to order G^1 yields

$$(2.51) \quad \frac{N_{,r}^2 + N_{,z}^2}{r^2} = 8\pi G\rho \quad \text{and} \quad N_{,r,r} + N_{,z,z} - \frac{N_{,r}}{r} = 0.$$

We see that the first field equation is a non-linear one. Note that, although the field equations are expanded to order G^1 , the characteristic function N is obviously of order $G^{1/2}$ which will be important later. It is emphasised in [CT06] that the metric function N , unlike w which vanishes due to the choice of comoving coordinates, cannot be eliminated consistently. Therefore the non-linearity between N and ρ in (2.51) is understood to be characteristic to this problem. However, w would not be constant if the pressure was non-zero. On the other hand, when performing the limit of vanishing ω , N vanishes also, but since the system must remain static there will be a non-zero pressure in that case. In this case, w is not constant, quite the contrary, it would then serve the Poisson equation.

Further, CT define a quasi-potential by

$$(2.52) \quad \Phi^{\text{CT}} = \int \frac{N}{r} dr,$$

such that we have $v = \partial\Phi^{\text{CT}}/\partial r$, which together with (2.50) returns a Newtonian-like definition of the tangential velocity, c.f. [BT94]. The potential equation then becomes

$$(2.53) \quad \Delta^{(3)}\Phi^{\text{CT}} = \Phi_{,r,r}^{\text{CT}} + \Phi_{,z,z}^{\text{CT}} + \frac{\Phi_{,r}^{\text{CT}}}{r} = \frac{N_{,r}}{r} + \int \frac{N_{,z,z}}{r} dr.$$

Inserting the field equation $N_{,z,z} = N_{,r}/r - N_{,r,r}$ then yields

$$(2.54) \quad \Delta^{(3)}\Phi^{\text{CT}} = 0.$$

Hence there is a direct correspondence between the Laplace equation $\Delta^{(3)}\Phi^{\text{CT}} = 0$ and the second equation in (2.51) after defining the tangential velocity in the usual way $v = \partial\Phi^{\text{CT}}/\partial r$.

Looking at (2.51) it becomes clear that it is better to first solve for the generating potential Φ^{CT} and then, after obtaining N , to compute the density profile. This is simply because the field equation for ρ is non-linear, whereas the potential equation is linear. Thus the CT strategy is to model galactic rotation curves with the help of the potential Φ^{CT} , then readily obtain N from the fit and finally calculate the density.

The separation of variables ansatz yields a general solution to the Laplace equation in terms of Bessel functions of the first kind

$$(2.55) \quad \Phi^{\text{CT}} = \sum_n C_n e^{-k_n|z|} J_0(k_n r) \quad \text{and} \quad v = - \sum_n k_n C_n e^{-k_n|z|} J_1(k_n r),$$

where the k_n are constants that are chosen so that orthogonality of the J_0 functions is maintained; see for instance the appendix of [BT94] for useful details on the Bessel functions.

The final results applied to the Milky Way, NGC 3031, NGC 3198 and NGC 7331, fit the rotation velocities remarkably well [CT06]. The total disc mass producing the non-Keplerian behaviour is quoted to be one order of magnitude smaller [CT06] than the one suggested by typical dark halo models. It is crucial to note that a successful fit of e.g. only the rotation curves would not be surprising alone; the fact that both the rotation curve and the density profile can be reproduced realistically makes the model interesting.

In several works that criticise the CT model, it has been shown that there exist pathologies within the energy-momentum tensor or various other imponderableness. Korzyński [Kor05] argues that (A) a proper asymptotical flat limit is not contained in the CT model because of the considered gauge; and that (B) the CT model must be unrealistic because unexpected additional matter sources at $z = 0$ can be found.

To (A): Korzyński derives a general perturbative form of the field equations for dust, expanded in $G^{1/2}$ and concludes that no asymptotically flat solutions exist if the lowest expansion coefficient of the metric is $G^{1/2}$. Recall, that both N and Φ^{CT} are of order $G^{1/2}$. However, the schematic Korzyński equations look rather different to the CT equations, for Korzyński works on a Minkowskian background and spends the remaining gauge freedom to simplify the equations within the De Donder gauge^d.

To (B): While the Bondi mass and ADM^e mass can be defined for asymptotically flat exterior solutions, the Komar mass is an invariant that can be defined for any spacetime that is stationary. In that case, due to Noether's theorem, time-translation symmetry ensures that the total energy of the system is a conserved quantity. Because a well-defined zero-momentum frame is present, the invariant can be defined as the system's mass, the Komar integral [Kom58]. The Komar integral can be defined considering an analogy to the gravitational mass from Gauss' law, c.f. [Wal84]. In the presence of a timelike Killing vector field we can define the differential form

^dA frame of harmonic coordinates or De Donder gauge is reached by the requirements $g^{\alpha\beta}\Gamma_{\alpha\beta}^{\gamma} = 0$, or equivalently $\square^2 x^{\gamma} = 0$.

^eNamed after Arnowitt, Deser and Misner. For an overview on energy-momentum in General Relativity see [Sza04].

$d\xi$ and denote the associated Hodge dual by $\star d\xi$. Assuming that $\nabla_\alpha \xi_\beta = \nabla_{[\alpha} \xi_{\beta]}$, which holds because of Killing's equation (2.29), we can write the differential of the dual form as [Kor05]

$$(2.56) \quad d \star d\xi = \frac{1}{3} R^{\mu\alpha} \xi_\alpha \varepsilon_{\mu\nu\rho\sigma} dx^\nu \wedge dx^\rho \wedge dx^\sigma,$$

where $\varepsilon_{\mu\nu\rho\sigma}$ is the spacetime volume form. Inserting for the Ricci tensor and integrating over an arbitrary three-dimensional volume V yields

$$(2.57) \quad \int_{\partial V} \star d\xi = \int_V d \star d\xi = \frac{4\pi G}{3} \int_V (2T^{\alpha\mu} \xi_\alpha - T\xi^\mu) \varepsilon_{\mu\nu\rho\sigma} dx^\nu \wedge dx^\rho \wedge dx^\sigma.$$

The crucial point is that, if there was only dust matter, the limit of shrinking the integration volume to zero must also yield a zero Komar integral, that is of course because the mass inside a zero volume is zero. If, on the other hand the Komar integral (2.57) gave a non-zero value in the shrinking volume limit, we must conclude that singularities in the energy momentum tensor are present. That is exactly what happens in the case of the CT model. To see that, one can choose for the integration volume a three-dimensional finite cylinder with $r \in [0, R]$ and $z \in [-a, a]$ with a and R taking positive real values. The Komar integral can be split into three parts: top ($z = a$) and bottom ($z = -a$) circular surface parts I_t , I_b and a side surface part I_s

$$(2.58) \quad I_t + I_b + I_s = \int_0^{2\pi} d\varphi \int_0^R \frac{N}{r} \frac{\partial N}{\partial z} dr \Big|_{z=a} - \int_0^{2\pi} d\varphi \int_0^R \frac{N}{r} \frac{\partial N}{\partial z} dr \Big|_{z=-a} + I_s.$$

Now, we insert N from (2.52) according to the CT model and let the volume of the cylinder go to zero by shrinking it in the z -direction. The side surface integral indeed vanishes but the two remaining integrals neither vanish nor cancel each other:

$$(2.59) \quad r\text{-}\lim_{a \rightarrow 0} (I_t + I_b) = r\text{-}\lim_{a \rightarrow 0} 4\pi \int_0^R \frac{N}{r} \frac{\partial N}{\partial z} dr \Big|_{z=a} = 4\pi k^5 \int_0^R r J_1^2(kr) dr \neq 0.$$

Therefore there must exist an additional source of matter at $z = 0$ in the CT model and this corresponds to a singular behaviour of the energy-momentum tensor at the discontinuity.

Further criticism has been raised in the years after the publishing of the CT model. In [VL05] the properties of the CT energy-momentum have been analysed. The result reveals that the additional component in the $z = 0$ plane is due to matter with negative energy density.

On the other hand, in [Gar06b] it is argued that post-Newtonian corrections should already enfold non-linear effects if they are present and that at the same time the post-Newtonian corrections to the Newtonian equations are understood to be small in the limit of small velocities and weak fields. Therefore the author claims that there should be no difference between Newtonian and general relativistic analyses considering Dark Matter.

In [Cro06] the following inconsistency is revealed: the covariant vanishing of shear in the CT model is demonstrated and it is pointed out that this reflects rigid rotation^f which is in contradiction with the initial CT assumption of differential rotation. Further, the author of [Cro06] notes that the flat rotation curve from the CT model would imply a large transfer of inertia from the inner rotating parts of a galaxy onto the outer parts, hence flattening the rotation curve in the outer regions. Since this is unexpected from General Relativity the author speculates that the CT model might be a manifestation of an alternative theory of gravity, one that follows the Machian philosophy where large induction of inertia effects are certainly thinkable.

But there also exist claims that are supporting the model of CT. Using an exact solution and somewhat different techniques, the authors of [BG06] derive a solution similar to that of CT. They find the unexpected result that in their model the amount of necessary Dark Matter is reduced by $\sim 30\%$.

^fA result already found by Bonnor in his analysis of an infinitely long and axisymmetric dust cloud [Bon77].

2.3.3. Finding the Newtonian Counterpart to the CT Model — Part I. Our basic idea is the following: if there are valid effects from the CT model, a direct comparison with the Newtonian equations would be very interesting. To do so, we shall find the correct Newtonian limit of the CT model. But before we turn to the issue of the Newtonian limit, we should reconsider the general spacetime

$$(2.60) \quad ds^2 = e^{-2U} [g_{MN} dx^M dx^N + W^2 d\varphi^2] - e^{2U} (dt + Ad\varphi)^2.$$

Recall that M, N take values 1 or 3. But it is always possible to go to isotropic coordinates

$$(2.61) \quad g_{MN} = e^{2k} \delta_{MN},$$

without touching the generality of (2.60), c.f. [SKM⁺03]. Therefore we note a central result: *the final form of the most general axisymmetric and stationary spacetime due to Lewis and Papapetrou (LP) is*

$$(2.62) \quad ds^2 = e^{-2U} [e^{2k}(dr^2 + dz^2) + W^2 d\varphi^2] - e^{2U} (dt + Ad\varphi)^2.$$

We recall that the free metric functions U, k, W, A are all functions of only r, z .

It is possible to simplify (2.62) a bit more, but only under crucial assumptions. We will show that, if and only if the metric function W is harmonic, it can be transformed to^g $W = r$. Let us consider a complex coordinate transformation $f(r + iz) = W + iV$ introducing an additional potential V . Then we have from $\rho \equiv W(r, z)$ and $h \equiv V(r, z)$ the differentials

$$(2.63) \quad d\rho = \frac{\partial W}{\partial r} dr + \frac{\partial W}{\partial z} dz \quad \text{and} \quad dh = \frac{\partial V}{\partial r} dr + \frac{\partial V}{\partial z} dz.$$

The coordinates ρ, h are only dummies that we introduce for bookkeeping reasons. Therefore we insert into (2.62), written in terms of ρ, h , and have

$$(2.64) \quad ds^2 = e^{-2U} [e^{2\tilde{k}}(d\rho^2 + dh^2) + \rho^2 d\varphi^2] - e^{2U} (dt + Ad\varphi)^2 \longmapsto ds^2 = e^{-2U} \left\{ e^{2\tilde{k}} \times \right. \\ \times \left[\left(\frac{\partial W}{\partial r} \right)^2 dr^2 + \left(\frac{\partial W}{\partial z} \right)^2 dz^2 + 2 \frac{\partial W}{\partial r} \frac{\partial W}{\partial z} dr dz + \left(\frac{\partial V}{\partial r} \right)^2 dr^2 + \left(\frac{\partial V}{\partial z} \right)^2 dz^2 \right. \\ \left. \left. + 2 \frac{\partial V}{\partial r} \frac{\partial V}{\partial z} dr dz \right] + W^2 d\varphi^2 \right\} - e^{2U} (dt + Ad\varphi)^2.$$

Requiring formal invariance as compared to the original metric, we see that the mixing terms should vanish. That is exactly provided by the Cauchy-Riemann equations for W and V

$$(2.65) \quad \frac{\partial W}{\partial r} = \frac{\partial V}{\partial z} \quad \text{and} \quad \frac{\partial W}{\partial z} = -\frac{\partial V}{\partial r}.$$

Moreover, with the help of the Cauchy-Riemann equations, we see that the coefficients of dr^2 and dz^2 can be combined to a positive definite quantity

$$(2.66) \quad \left(\frac{\partial W}{\partial r} \right)^2 + \left(\frac{\partial V}{\partial r} \right)^2 = \left(\frac{\partial W}{\partial z} \right)^2 + \left(\frac{\partial V}{\partial z} \right)^2 \equiv \tilde{K} \geq 0,$$

such that we can combine $e^{2\tilde{k}} \tilde{K} \equiv e^{2k}$ and so obtain (2.62) via (2.64). Thus we have shown that it is possible to simplify the general LP form (2.64) by allowing $W = r$, which is only possible if the transformation f is analytic, that is W (and also V) must be a harmonic function^h, $\Delta^{(2)}W = 0$. Then, we can write down *the LP metric in isotropic coordinates (or Weyl gauge)*

$$(2.67) \quad ds^2 = e^{-2U} [e^{2k}(dr^2 + dz^2) + r^2 d\varphi^2] - e^{2U} (dt + Ad\varphi)^2.$$

^gAlso $W = 1$ is possible then, but this case is of no interest as we will see later.

^hNote that, this condition for W holds for exterior solutions that are stationary and axisymmetric [Isl85].

For comparison let us repeat the CT metric ($u = 1$),

$$(2.68) \quad \boxed{ds^2 = e^{\nu-w} (dr^2 + dz^2) + r^2 e^{-w} d\varphi^2 - e^w (dt + Nd\varphi)^2}.$$

Obviously, *the CT metric does not belong to the class of the most general stationary and axisymmetric spacetimes*; it belongs to the subclass of LP solutions in the Weyl gauge, and is therefore less general.

Now, let us try to approach the problem of finding a Newtonian counterpart to the CT model (2.68). If there are really advantages in a certain general relativistic approach then eventually we can pin the differences down by comparison to the well-known Newtonian physics.

The ‘Newton metric’, that is the metric that reproduces Newtonian physics, is given by

$$(2.69) \quad ds^2 = -(1 + 2\phi)dt^2 + dr^2 + r^2 d\varphi^2 + dz^2,$$

where $\phi(r, z)$ is the Newtonian gravitational potential. For simplicity, we start with only rigid rotation, that is

$$(2.70) \quad \varphi = \varphi' - \omega t.$$

Then the rigidly rotated Newton metric (2.69) is exactly

$$(2.71) \quad ds^2 = (dr^2 + dz^2) + \frac{1 + 2\phi}{(1 + 2\phi - \omega^2 r^2)} r^2 d\varphi^2 - (1 + 2\phi - \omega^2 r^2) \left[dt + \frac{r^2 \omega}{(1 + 2\phi - \omega^2 r^2)} d\varphi \right]^2.$$

In this form we can directly compare the metric with the LP metric in Weyl gauge (2.67), and we notice a discrepancy at linear order in ϕ , looking at the $d\varphi^2$ term. Interestingly, the rigidly rotated Newton metric (2.71) is not in accord with the isotropic form of the LP class (2.67) – as it *should* be for consistency – but it is in perfect accordance with the general form of the latter (2.62).

Now, one could speculate whether the situation might be easily cured with the help of a coordinate transformation. Above we have derived the exact conditions under which the general and the isotropic LP metric can be transformed into each other: the function W must be a harmonic function with respect to the two-dimensional Laplacian $\Delta^{(2)}W = 0$.

In the present case, of the rigidly rotating Newton metric, W is given by

$$(2.72) \quad W = r\sqrt{1 + 2\phi},$$

expanding and applying the Laplacian yields

$$(2.73) \quad \Delta^{(2)}W = r\Delta^{(3)}\phi + \phi_{,r} = 4\pi G\rho r + \phi_{,r}.$$

Note that we can use the Poisson equation because the potential is Newtonian. After repeating some facts from potential theory we will show that $\Delta^{(2)}W$ in fact does not vanish in general.

Given the general problem of solving the Laplace equation with the appropriate boundary conditions for a disc-like distribution of matter, the solution for the potential can be obtained via separation of variables, c.f. [BT94]

$$(2.74) \quad \phi(r, z) = \int_0^\infty S(k)J_0(kr)e^{-k|z|} dk.$$

A given surface mass density $\Sigma(r)$ is then characterised by the according Hankel transform

$$(2.75) \quad S(k) = -2\pi G \int_0^\infty J_0(kr)\Sigma(r)r dr.$$

Now we can use these expressions for the evaluation of (2.73).

■ Case (A) $z \neq 0$ — Outside the disc the Newtonian potential fulfils the Laplace equation, such that the expression (2.73) takes the form

$$(2.76) \quad \Delta^{(2)}W = - \int_0^\infty S(k)J_1(kr)ke^{-k|z|} dk \quad \text{at } z \neq 0,$$

which will not vanish in general. As a simple example we consider the Mestel disc model of a galaxy [Mes63]. In the Newtonian Mestel model a flat rotation curve can be reachedⁱ. The Mestel model is characterised by a surface mass density that falls off inversely with the distance

$$(2.77) \quad \Sigma(r) = \frac{\Sigma_0 r_0}{r}.$$

In a Mestel galaxy the surface density Hankel-transforms as $S(k) = -2\pi G \Sigma_0 r_0 / k$. Using this we can integrate directly and obtain

$$(2.78) \quad \Delta^{(2)}W = 2\pi G \Sigma_0 r_0 \left(\frac{1}{r} - \frac{|z|}{r\sqrt{r^2 + z^2}} \right) \quad \text{at } z \neq 0.$$

■ Case (B) $z = 0$ — We want to show that (2.73) is non-zero also here. Let us assume the contrary and see what happens. If we assume that $\Delta^{(2)}W = 0$ was true then equation (2.73) gives an identity. We integrate this identity over z for some $\varepsilon > 0$ and then revoke the operation by performing the appropriate limit

$$(2.79) \quad -4\pi G r \lim_{\varepsilon \rightarrow 0} \int_{-\varepsilon}^{\varepsilon} \delta(z) \Sigma(r) dz = \lim_{\varepsilon \rightarrow 0} \int_{-\varepsilon}^{\varepsilon} \int_0^{\infty} S(k) J_1(kr) k e^{-k|z|} dk dz.$$

Since the exponential term on the right hand side serves as a damping factor, the modulus of the integrand will reach its maximum at $z = 0$. Thus, as an upper estimate, we can set the integrand of the right hand side to be constant in z and therefore the integration and limit procedure give zero. Then, for all other z the expression will be zero more than ever and we obtain

$$(2.80) \quad 4\pi G \Sigma(r) r = 0.$$

This will not hold generally for any realistic model, hence producing a contradiction, and therefore $\Delta^{(2)}W(r, z) = 0$ is not true at the surface $z = 0$ either.

Interestingly, the pure Newton metric (2.69) cannot be made compatible with the LP metric in Weyl form and thus is also not compatible with the CT model. We should go one step further and consider the Post-Newtonian (PN) metric

$$(2.81) \quad ds^2 = -(1 + 2\phi)dt^2 + (1 - 2\psi)(dr^2 + r^2d\varphi^2 + dz^2),$$

with some additional PN potential ψ . Sometimes, this metric (with $\psi = \phi$) is referred to as the ‘Newton metric’ in the literature. The reason for this nomenclature might be that the order of magnitude of the coefficient of the spatial part $d\mathbf{x}^2$ and the order of the Newtonian correction are the same. Nevertheless, conceptually this makes an enormous difference. In classical Newton Gravity there exists no curvature of space, the three-space is always euclidian. This is exactly reflected in the Newton metric (2.69) and therefore we refer to (2.81) as the PN metric; for an extensive discussion see chapt. 39 in [MTW73].

Let us again perform the stiff rotation (2.70) on the PN metric. The result (including higher orders) is

$$(2.82) \quad \begin{aligned} ds^2 &= (1 - 2\psi)(dr^2 + dz^2) + \frac{1}{(1 + 2\phi - (1 - 2\psi)\omega^2 r^2)} r^2 d\varphi^2 \\ &- (1 + 2\phi - (1 - 2\psi)\omega^2 r^2) \left[dt + \frac{(1 - 2\psi)\omega r^2}{(1 + 2\phi - (1 - 2\psi)\omega^2 r^2)} d\varphi \right]^2. \end{aligned}$$

The comparison shows that this metric is in perfect accordance with (2.67) via

$$(2.83) \quad \begin{aligned} e^{2k} &= (1 - 2\psi)(1 + 2\phi - (1 - 2\psi)\omega^2 r^2), \quad e^{2U} = (1 + 2\phi - (1 - 2\psi)\omega^2 r^2) \\ W^2 &= r^2, \quad A = -\frac{(1 - 2\psi)\omega r^2}{(1 + 2\phi - (1 - 2\psi)\omega^2 r^2)}. \end{aligned}$$

ⁱThe flat rotation curve in the Mestel model can easily be obtained from the Hankel transform of (2.77), inserted into the formula for the rotation curve: $v^2(r) = r(\partial\phi/\partial r)_{z=0} = 2\pi G \Sigma_0 r_0$.

Thus the PN metric (2.81) belongs to the class of isotropic (Weyl) axisymmetric and stationary solutions whereas the Newton metric (2.69) does not allow for that simplification.

Our aim is to approach the CT model from the side of Newton gravity. The next step is to allow for differential rotations $\omega = \omega(r)$ in order to try to make the model stepwise more realistic. So we relax the condition of rigid rotation and consider transformations

$$(2.84) \quad \varphi = \varphi' - \omega(r)t,$$

which we apply to the PN metric and arrive at a lengthy expression:

$$(2.85) \quad \begin{aligned} ds^2 &= (1 - 2\psi)dz^2 + (1 - 2\psi)(1 + r^2\omega_{,r}^2 t^2)dr^2 + \frac{1}{(1 + 2\phi - (1 - 2\psi)\omega^2 r^2)} r^2 d\varphi^2 \\ &- (1 + 2\phi - (1 - 2\psi)\omega^2 r^2) \left[dt + \frac{(1 - 2\psi)\omega r^2}{(1 + 2\phi - (1 - 2\psi)\omega^2 r^2)} d\varphi \right]^2 \\ &+ (1 - 2\psi)2r^2\omega\omega_{,r} t dr dt - (1 - 2\psi)2r^2\omega_{,r} t dr d\varphi. \end{aligned}$$

Unfortunately, this metric exhibits direct time dependence in some coefficients – which is a coordinate artefact. Because of the stationarity constraint (2.32), the differentially rotated PN metric (2.85) only makes sense in a strictly local sense, that is within small time intervals ($r^2\omega_{,r}t \ll 1$). In other words, the coordinate transformation (2.84) is not a good transformation because it holds only as long as $\omega(r)t < 2\pi$. But there might be another problem: obviously, the rotated PN metric (2.85) is not of the same form as the LP spacetime. Fortunately, it turns out – after a somewhat tedious calculation – that it is possible to find a coordinate transformation in r using a certain function $r = g(r', \varphi, t)$. Therefore we perform the following translational transformation on the metric (2.85)

$$(2.86) \quad dr = g_{,r'} dr' + g_{,\varphi} d\varphi + g_{,t} dt.$$

We solve for the transformation parameters – letting primes away – using the LP constraints and get

$$(2.87) \quad \begin{aligned} g_{,r} &= \sqrt{\frac{1 - 2\psi}{B}}, \quad g_{,t} = \frac{(1 - 2\psi)\omega\omega_{,r} r^2 t}{B}, \quad g_{,\varphi} = \frac{(1 - 2\psi)\omega_{,r} r^2 t}{B}, \\ B &= 1 - 2\psi + (1 - 2\psi)r^2\omega_{,r}^2 t^2. \end{aligned}$$

The fully rotated PN metric (2.85) with the most general angular velocity $\omega = \omega(t, r, z)$ is a horrendous expression that is written down in components in equations (C.3) in the app. C. Before we now continue on the level of dynamical equations to pin down the difference of the two Newtonian metrics (2.69) and (2.81), of which one is compatible with the LP model and one is not, we shall recall a few facts on the 3 + 1 split of spacetime.

2.3.4. The Arnowitt-Deser-Misner split. In order to gain physical insight into complicated problems in General Relativity it is often very useful to return to a familiar foliation into separate dimensions. There exists a well-defined way how to split spacetime into space and time parts (manifolds). This formalism has been developed by Arnowitt, Deser and Misner [Arn62] and is henceforth called ADM split, see also paragraph 21.4 in [MTW73] or [Yor79]. It can be derived from the application of the proper boundary conditions on the problem of constructing a rigid ‘sandwich’ structure of a one-parameter sequence of spacelike hypersurfaces, see fig. 2.7. The application of Pythagoras’ theorem in the four-dimensional setup then directly yields the form that the metric has to attain with regard to the rigidity of such a construction:

$$(2.88) \quad ds^2 = -N^2 dt^2 + g_{ij}(dx^i + N^i dt)(dx^j + N^j dt) = -(N^2 - N_i N^i) dt^2 + 2N_i dt dx^i + g_{ij} dx^i dx^j.$$

Here g_{ij} characterises the metric of the spatial hypersurfaces.

Depending on the choice of coordinates given by (2.88) we define the ‘normal vectors’

$$(2.89) \quad n_\mu = N(-1, \mathbf{0}) \quad \text{and} \quad n^\mu = \frac{1}{N}(1, -N^i),$$

whereby we introduce the *lapse function* N and the *shift vector* N^i . For concrete calculation it is important to be aware of the fact that only the indices of n^μ are raised or lowered with the four-metric $g_{\mu\nu}$, and that to do so with the N_i one may only use the spatial metric g_{ij} . Further, it will be useful to define the following projector

$$(2.90) \quad h^\mu{}_\nu = \delta^\mu{}_\nu + n^\mu n_\nu,$$

which induces the three-metric into the hypersurfaces. Next we want to take advantage of the fact that we achieved a dimensional reduction of the hypersurfaces.

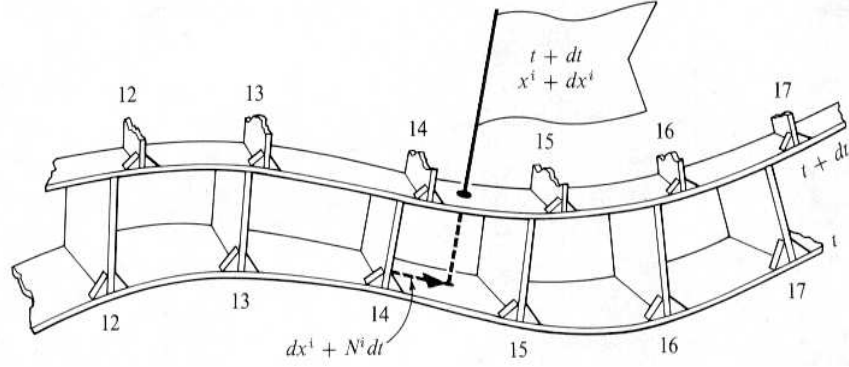


FIGURE 2.7. Illustrating the ADM split: the general relativistic spacetime is decomposed into spacelike hypersurfaces labelled with time coordinate. Two three-dimensional spacelike hypersurfaces, say at t and $t + dt$, are connected in a *rigid* way, by inserting perpendicular connectors between the slices, with tailor-made lengths and shifts, such that a stiff ‘sandwich structure’ is maintained. The connectors are given by the lapse function N (which corresponds to the choice of slicing) and the shift vector N^i (which corresponds to the choice of spatial coordinates x^i on hypersurfaces). The requirement of rigidity leads directly to the ADM metric (2.88). The picture is taken from [MTW73].

Often, the central question of general relativistic problems is that of spacetime curvature. Usually, it makes no sense to consider extrinsic curvature because it is not obvious how to assign a physical meaning to a five-dimensional manifold in which the curvature of our four-dimensional universe is measured. Therefore General Relativity is a theory of the intrinsic gravitational curvature of spacetime. When using the ADM framework it suddenly makes sense to consider extrinsic curvature, i.e. the spatial curvature of the foliated hypersurfaces with respect to the usual four-dimensional general relativistic spacetime. The extrinsic curvature is defined as

$$(2.91) \quad K_{ij} \equiv -h^\mu{}_i h^\nu{}_j n_{i;j},$$

which, in case of time-independence of the metric g_{ij} , can be written in the common form

$$(2.92) \quad K_{ij} \equiv \frac{1}{2N} (N_{i;j} + N_{j;i} - 2\Gamma^\ell{}_{ij} N_\ell).$$

The definition of K_{ij} can be understood more deeply when trying to derive it from a fundamental principle, namely the Lie derivative. Loosely spoken, the Lie derivative is something like a generalised directional derivative. The extrinsic curvature can be interpreted as the difference that occurs during a parallel transport of a normal vector on the spatial hypersurface with respect to the embedding (four-dimensional) space

$$(2.93) \quad -2K_{ij} = \mathcal{L}_n g_{ij}.$$

The extrinsic curvature is nothing else than the Lie derivative of the three-metric g_{ij} in the direction of the four-vector n^μ . Interestingly, the original definition of the Lie derivative for

four-dimensional quantities is formulated only by applying partial derivatives

$$(2.94) \quad \mathcal{L}_{\mathbf{a}}g_{\mu\nu} \equiv g_{\mu\nu,\lambda}a^\lambda + g_{\mu\rho}a^\rho{}_{,\nu} + g_{\kappa\nu}a^\kappa{}_{,\mu},$$

with respect to some four-direction \mathbf{a} . This is the Lie derivative as it is defined. It represents a derivative of a four-tensor ($g_{\mu\nu}$) in direction of a four-vector field a^μ . We have to apply this to the problem (2.93) where we are looking for the Lie derivative of a three-tensor g_{ij} along the four-vector field n^μ . The ansatz gives

$$(2.95) \quad \begin{aligned} \mathcal{L}_{\mathbf{n}}g_{ij} &= g_{ij,0}n^0 + g_{ij,k}n^k + g_{i\ell}n^\ell{}_{,j} + g_{sj}n^s{}_{,i} \\ &= \frac{1}{N} (g_{ij,0} - N_{i,j} - N_{j,i} + g_{i\ell,j}N^\ell + g_{sj,i}N^s - g_{ij,k}N^k) \\ &= \frac{1}{N} \left\{ g_{ij,0} - N_{i,j} - N_{j,i} + 2 \left[\frac{1}{2}g^{\ell p} (g_{ip,j} + g_{pj,i} - g_{ij,p}) N_\ell \right] \right\} \\ &= \frac{1}{N} \left[\partial_t g_{ij} - \underbrace{(N_{i;j} + N_{j;i})}_{\mathcal{L}_{\mathbf{N}}g_{ij}} \right] = -2K_{ij}, \end{aligned}$$

and thus we have derived the evolution equation of the spatial metric (2.92).

Now we are prepared to write down the full set of ADM equations [Buc01] that govern the dynamics of the 3+1 system – assuming a vanishing cosmological constant –

[Hamiltonian or Energy Constraint]

$$(2.96) \quad \mathcal{R} - K^i{}_j K^j{}_i + K^2 = 16\pi G E \quad \text{with} \quad E \equiv T_{\mu\nu}n^\mu n^\nu,$$

[Momentum Constraints]

$$(2.97) \quad K^j{}_{i;j} - K_{;i} = 8\pi G J_i \quad \text{with} \quad J_i \equiv -T_{\mu\nu}n^\mu h^\nu{}_i,$$

[Evolution Equation for the Metric]

$$(2.98) \quad \frac{1}{N}g_{ij,0} = -2K_{ij} + \frac{1}{N}(N_{i;j} + N_{j;i}),$$

[Evolution Equation for the Extrinsic Curvature]

(2.99)

$$\frac{1}{N}K^i{}_{j,0} = \mathcal{R}^i{}_j + K K^i{}_j - \frac{1}{N}N^{;i}{}_{;j} + \frac{1}{N}(K^i{}_k N^k{}_{;j} - K^k{}_j N^i{}_{;k} N^k K^i{}_{j;k}) - 8\pi G \left[S^i{}_j + \frac{1}{2}\delta^i{}_j(E - S) \right],$$

with $S_{ij} \equiv T_{\mu\nu}h^\mu{}_i h^\nu{}_j$, and the according trace equations,

[Evolution Equation for the Extrinsic Curvature (Trace)]

$$(2.100) \quad \frac{1}{N}K_{,0} = \mathcal{R} + K^2 - 4\pi G(3E - S) - \frac{1}{N}N^{;k}{}_{;k} + \frac{1}{N}N^k K_{;k},$$

[Evolution Equation for the Metric (Trace)]

$$(2.101) \quad \frac{1}{N}g_{,0} = 2g \left(-K + \frac{1}{N}N^k{}_{;k} \right) \quad \text{with} \quad g \equiv \det(g_{ij}).$$

2.3.5. Finding the Newtonian Counterpart to the CT Model — Part II. Applying the ADM split to the rotating Newton metric should yield the equations of movement, and on this level the differences between Newtonian and CT model might become transparent. Let us approach the problem in steps and thus first start with the static post-Newtonian metric before we include more and more complications.

■ Setup (1) static Newton model — In what follows we will always use the linearised Newtonian metrics and further approximations will be stated explicitly. We use the more general PN metrics and specialise to the Newton metric by setting $\psi = 0$ where it is apposite. The warm-up exercise is going to be the simple static PN metric in cartesian coordinates

$$(2.102) \quad ds^2 = -(1 + 2\phi)dt^2 + (1 - 2\psi)(dx^2 + dy^2 + dz^2),$$

with $\phi = \phi(x, y, z)$ and $\psi = \psi(x, y, z)$. We read off the ADM-relevant expressions and note

$$(2.103) \quad N^i = 0 = N_i, \quad N^2 = (1 + 2\phi), \quad g_{ij} = (1 - 2\psi)\delta^{ij}, \quad g^{ij} = \frac{1}{1 - 2\psi}\delta^{ij}.$$

In three dimensions there are 15 non-vanishing components of the Christoffel symbol, they are listed in app. C under equations (C.5). Since the shift vanishes completely and the induced metric does not depend on time, then the extrinsic curvature also vanishes due to (2.92),

$$(2.104) \quad K_{ik} = 0, \quad K = 0,$$

and the trace being denoted with $K \equiv K_i^i$. Further, the non-vanishing components of the three-dimensional Ricci tensor are computed and listed in the app. C under (C.6). The final result for the three-Ricci scalar is

$$(2.105) \quad \mathcal{R} = \frac{4}{(1 - 2\psi)^2} \Delta_{\text{cart}}^{(3)} \psi + \frac{6}{(1 - 2\psi)^3} (\nabla_{\text{cart}}^{(3)} \psi)^2 \simeq 4\Delta_{\text{cart}}^{(3)} \psi,$$

where D_{cart} stands for the according operators in cartesian coordinates. This result is consistent with the one resulting from the well known first-order formula in the Newtonian case [Sch85]

$$(2.106) \quad R_{ijkl} = \delta_{ik}\psi_{,jl} + \delta_{jl}\psi_{,ik} - \delta_{il}\psi_{,jk} - \delta_{jk}\psi_{,il}.$$

As a matter model of the galaxy we choose dust, implying that the energy-momentum tensor is that of a perfect fluid with vanishing pressure, $T_{\mu\nu} = \rho u_\mu u_\nu$ where u^μ is the four-velocity of a comoving observer. Note that in this setup it is not possible to simply set $u^\mu = n^\mu$, like it is done usually – because that would exclude to treat rotation. In case of the static Newton metric, the normals are $n_\mu = N(-1, \mathbf{0})$ and $n^\mu = 1/N(1, \mathbf{0})$. Therefore the E function – which is the energy density seen by the fiducial ADM observer – in the ADM formalism becomes

$$(2.107) \quad E = T_{\mu\nu} n^\mu n^\nu = \rho N^2 (u^0)^2 = \rho \frac{1}{N^2} (u_0)^2.$$

Similarly, we can evaluate the Poynting vector J_i in this case

$$(2.108) \quad J_i = -T_{\mu\nu} n^\mu h^\nu_i = \rho N u^0 u_i.$$

The calculation of the full divergence of the lapse function yields

$$(2.109) \quad \begin{aligned} N^{;k}_{;k} &= \frac{1}{\sqrt{1+2\phi}} \frac{1}{(1-2\psi)} \Delta_{\text{cart}}^{(3)} \phi - \frac{1}{\sqrt{1+2\phi}} \frac{1}{(1-2\psi)^2} \left(\nabla_{\text{cart}}^{(3)} \phi \right) \cdot \left(\nabla_{\text{cart}}^{(3)} \psi \right) \\ &- 2 \frac{1}{(1+2\phi)} \frac{1}{(1-2\psi)} \left(\nabla_{\text{cart}}^{(3)} \phi \right)^2 \simeq \Delta_{\text{cart}}^{(3)} \phi, \end{aligned}$$

as well as $N^{;i}_{;j} \simeq \phi_{,ij}$ for $i \neq j$. In the end the ADM equations become

$$(2.110) \quad \begin{aligned} \mathcal{R} &= 16\pi G E, \quad E = \rho N^2 (u^0)^2, && \text{(Hamilton constraint)} \\ J_i &= \rho N u^0 u_i = 0, && \text{(momentum constraint)} \\ 0 &= R^i_j - \frac{1}{N} N^{;i}_{;j} - 8\pi G \left[S^i_j + \frac{1}{2} \delta^i_j (E - S) \right], && \text{(evolution, non-trace)} \\ 0 &= \mathcal{R} - \frac{1}{N} N^{;k}_{;k} - 4\pi G (3E - S), && \text{(evolution, trace)} \end{aligned}$$

with the stress tensor $S_{ij} = \rho u_i u_j$. Next we analyse the two cases of the classical Newton metric and the PN metric.

◆ Case (A) $\psi = 0$ and $\phi \neq 0$ (classical Newton metric) — Since ψ vanishes, it follows directly that $\mathcal{R} = 0$, and thus from the Hamilton constraint with vanishing E , we have $\rho = 0 \vee u^0 = 0$ which is equally absurd. If we assume $\rho \neq 0$, the momentum constraint is satisfied and $u_i \neq 0$ is possible. So by now we have

$$(2.111) \quad u^0 = 0, \quad u_i \neq 0, \quad \rho \neq 0.$$

The trace of the evolution equation yields a Poisson-like equation

$$(2.112) \quad \Delta_{\text{cart}}^{(3)} \phi = 4\pi G S = 4\pi G \rho u^i u_i$$

and the non-trace part of the evolution equation yields

$$(2.113) \quad \phi_{,i,j} = -8\pi GS^i_j = -8\pi G\rho u^i u_j.$$

On the other hand, we could choose $\rho = 0$ which implies $u^0 \neq 0$, and this leads to $\Delta_{\text{cart}}^{(3)}\phi = 0$ and $\phi_{,i,j} = 0$ which is the case of a test particle – consistent but not very useful.

Astonishingly, the classical Newton solution does not make sense in the ADM split. Either $u^0 = 0$ or $\rho = 0$ must be accepted but both results are unphysical. We assume that here the PN terms are necessary in order to make sense out of the ADM split and therefore proceed with the following case.

◆ Case (B) $\psi = \phi \neq 0$ (simplest PN metric) — Note that, taking $\psi = \phi \neq 0$ right from the beginning is justified because the ansatz $\phi \neq 0$, $\psi \neq 0$ but $\phi \neq \psi$, will require $\phi = \psi$ for consistency, as we will see now. The Hamilton constraint returns us a reasonable Poisson equation right away,

$$(2.114) \quad \Delta_{\text{cart}}^{(3)}\psi = 4\pi G\rho N^2 (u^0)^2$$

But with $u^0 \neq 0$ and $\rho \neq 0$ the momentum constraint gives $u^i = 0$ and therewith a vanishing stress tensor. Consistency is indicated by the trace part of the evolution equation, it returns the same Poisson equation (2.114), only with the requirement $\psi = \phi$. The non-trace equations give only trivial identities with the same requirement. Therefore it is concluded that in order to make sense out of the ADM split, already at the level of a static setup (in combination with dust matter), the classical Newton metric makes no sense whereas the PN metric does.

■ Setup (2) rigidly rotated Newton model — A rigid rotation according to (2.70) with an constant angular velocity ω can be described with the following exact PN spacetime

$$(2.115) \quad ds^2 = [(1 - 2\psi)\omega^2 r^2 - (1 + 2\psi)]dt^2 + (1 - 2\psi)(dr^2 + dz^2) + (1 - 2\psi)r^2 d\varphi^2 - (1 - 2\psi)2r^2\omega d\varphi dt.$$

Now a non-vanishing shift is present. Interestingly, also here the extrinsic curvature vanishes exactly,

$$(2.116) \quad K_{ik} = 0, \quad K = 0.$$

The non-vanishing quantities, relevant for the ADM split, are to exact order:

$$(2.117) \quad \begin{aligned} N_\varphi &= -(1 - 2\psi)\omega r^2, & N^\varphi &= -\omega, & N^2 &= (1 + 2\psi), & g_{11} &= g_{33} = (1 - 2\psi), \\ g_{22} &= (1 - 2\psi)r^2, & g^{11} &= g^{33} = 1/(1 - 2\psi), & g_{22} &= 1/[(1 - 2\psi)r^2]. \end{aligned}$$

Note that, because we use the exact metric (2.115), the quantity N^2 is exact as it stands; the additional contribution in the time-time part of the metric cancels out in the calculation of the lapse function. The computations of the connection and the Riemann tensor are tedious and have been carried out partly with help of the computer. We give the explicit expressions in app. C. We are able to reproduce the result (2.105) in cylindrical coordinates

$$(2.118) \quad \mathcal{R} = \frac{4}{(1 - 2\psi)^2} \Delta^{(3)}\psi + \frac{6}{(1 - 2\psi)^3} (\psi_{,r}^2 + \psi_{,z}^2) \simeq 4\Delta^{(3)}\psi.$$

The form of Hamilton and momentum constraint as well as of the trace evolution equation are the same as in (2.110). Only the forms of the non-trace parts are different and they read

$$(2.119) \quad \begin{aligned} R^i_j &= \frac{1}{N} N^i_{;j} + 8\pi GS^i_j, & (\text{evolution, } i \neq j) \\ S^1_2 &= \rho u^1 u_2 = 0, \\ \overbrace{R^1_3 - \frac{1}{N} N^1_{;2}}^{\equiv C} &= 8\pi GS^1_3, \\ S^2_3 &= \rho u^2 u_3 = 0. \end{aligned}$$

◆ Case (A) $\psi = 0$ and $\phi \neq 0$ (classical Newton metric) — The same chain of conclusions as in the case of the static setup above, leads via $\mathcal{R} = 0$, $E = 0$ to $\rho = 0 \vee u^0 = 0$ which is

unphysical. We still choose $\rho \neq 0$ to see what happens. The momentum constraint is fulfilled and leaves $u^i \neq 0$ possible. To leading order, the trace of the evolution equation gives a Poisson-like equation similar to (2.112). Looking at the non-trace parts of the evolution equation, the third equation in (2.119) depends on the combination C . Within the classical Newton limit C becomes equal to $-\phi_{,1,3}$, as we have calculated. Thus we have

$$(2.120) \quad \begin{aligned} S^1_2 &= \rho u^1 u_2 = 0, \\ -\phi_{,1,3} &= 8\pi G S^1_3 = 8\pi G \rho u^1 u_3, \\ S^2_3 &= \rho u^2 u_3 = 0. \end{aligned}$$

Apart from $u^i = 0$ two other solutions are also possible: (1) $u^2 = 0$ but $u^1, u^3 \neq 0$ and hence $S \neq 0$, and (2) $u^1, u^3 = 0$ leading to $\phi_{,1,3} = 0$ but $u^2 \neq 0$ as well as $S \neq 0$ are possible. Of course, also other solutions are thinkable, e.g. such with no matter ($\rho = 0$) but none of these makes much physical sense, just as in the static case above.

◆ Case (B) $\psi = \phi \neq 0$ (simplest PN metric) — In analogy to the static case, the momentum and Hamilton constraints together require $u_i = 0$, in order not to have an empty Poisson equation ($\rho, u^0 \neq 0$). Therewith the stress tensor and its trace vanish. From the trace of the evolution equation, the Poisson equation can be reobtained like before. The non-trace equations do not give new information since $C = 0$ in the linearised case and this is then just consistent with the vanishing of u_i . Altogether, although $\rho \neq 0$ and $u^0 \neq 0$ are possible, the equations do not allow any motion.

■ Setup (3) differentially rotated Newton model — Finally, in this model we can hope for a non-vanishing extrinsic curvature and some non-trivial properties. The *linearised* differentially rotating post-Newtonian metric takes the form

$$(2.121) \quad ds^2 = -(1+2\phi)dt^2 + (1-2\psi)(dr^2 + dz^2) + (1-2\psi)r^2 d\varphi^2 - (1-2\psi)2r^2 \Omega d\varphi dt,$$

with the potentials being functions of r and z only: $\phi = \phi(r, z)$, $\psi = \psi(r, z)$, $\Omega = \Omega(r, z)$. Recall that the metric is only valid in a strictly local sense. Shift and lapse function become

$$(2.122) \quad N_\varphi = -(1-2\psi)\Omega r^2, \quad N^\varphi = -\Omega, \quad N^2 = (1+2\phi) + (1-2\psi)\Omega^2 r^2.$$

The spatial metric stays the same as before. The extrinsic curvature has vanishing diagonal components, such that $K = 0$, and we have the following non-vanishing and exact off-diagonal components

$$(2.123) \quad K^1_2 = -\frac{1}{2N}\Omega_{,r}r^2, \quad K^2_1 = -\frac{1}{2N}\Omega_{,r}, \quad K^2_3 = -\frac{1}{2N}\Omega_{,z}, \quad K^3_2 = -\frac{1}{2N}\Omega_{,z}r^2.$$

We employ dust, that is $p = 0$ and $T_{\mu\nu} = \rho u_\mu u_\nu$, and so we also have the following, like above,

$$(2.124) \quad E = \rho(Nu^0)^2, \quad S_{ij} = \rho u_i u_j, \quad J_i = -T_{\mu\nu} n^\mu h^\nu_i.$$

Then, the ADM equations become, for the differentially rotating case up to all orders,

$$(Hamiltonian constraint) \quad \mathcal{R} - K^i_j K^j_i + K^2 = 16\pi G E,$$

$$(2.125) \quad \frac{4}{(1-2\psi)^2} \Delta^{(3)}\psi + \frac{6}{(1-2\psi)^3} (\psi^2_{,r} + \psi^2_{,z}) - \frac{1}{4} \frac{1}{N^2} r^2 (\Omega^2_{,r} + \Omega^2_{,z}) = 16\pi G \rho (Nu^0)^2.$$

$$(Momentum constraints) \quad K^j_{i;j} - K_{;i} = 8\pi G J_i,$$

$$8\pi G J_1 = 8\pi G \rho N u^0 u_1 = 0,$$

$$8\pi G J_2 = 8\pi G \rho N u^0 u_2 =$$

$$\frac{r^2}{2N} \left(\Omega_{,r,r} + \frac{3}{r} \Omega_{,r} + \Omega_{,z,z} \right) - \frac{r^2}{2N^2} (N_{,r} \Omega_{,r} + N_{,z} \Omega_{,z}) + \frac{r}{2N} \frac{1}{(1-2\psi)} (\psi_{,r} \Omega_{,r} + \psi_{,z} \Omega_{,z}),$$

$$8\pi G J_3 = 8\pi G \rho N u^0 u_3 = 0.$$

$$(2.126)$$

$$\begin{aligned}
(\text{Evolution, } i \neq j) \quad & 8\pi GS^i_j = R^i_j + KK^i_j - \frac{1}{N}N^i_{;j} + \frac{1}{N}(K^i_k N^k_{;j} - K^k_j N^i_{;k} N^k K^i_{j;k}), \\
8\pi GS^1_2 &= 8\pi G\rho u^1 u_2 = 0, \\
8\pi GS^1_3 &= 8\pi G\rho u^1 u_3 = \\
& \frac{1}{(1-2\psi)^3} (3\psi_{,r}\psi_{,z} + (1-2\psi)\psi_{,r,z}) - \frac{1}{N} \frac{1}{(1-2\psi)^2} (\psi_{,r}N_{,z} - \psi_{,z}N_{,r} + (1-2\psi)N_{,r,z}) + \frac{1}{2} \frac{1}{N} r^2 \Omega_{,r} \Omega_{,z}, \\
8\pi GS^2_3 &= 8\pi G\rho u^2 u_3 = 0.
\end{aligned} \tag{2.127}$$

$$(\text{Evolution, } i = j) \quad \mathcal{R} = 4\pi G(3E - S) + \frac{1}{N}N^i{}^k{}_{;k},$$

with the relevant derivatives of the lapse function being

$$\begin{aligned}
N_{,r,z} &= \frac{1}{N^3} \left\{ \underline{\phi_{,z}} + r^2 \Omega [(1-2\psi)\Omega_{,z} - \Omega\psi_{,z}] [-\underline{\phi_{,r}} - r\Omega[(1-2\psi)(\Omega + r\Omega_{,r}) - r\Omega\psi_{,r}]] \right\} \\
&+ \frac{1}{N} \left\{ \underline{\phi_{,r,z}} + r \{ (1-2\psi)r\Omega_{,r}\Omega_{,z} - \Omega[2r\psi_{,z}\Omega_{,r} - 2\Omega_{,z}(1-2\psi - r\psi_{,r}) - r(1-2\psi)\Omega_{,r,z}] \right. \\
&\left. - \Omega^2(2\psi_{,z} + r\psi_{,r,z}) \right\} \stackrel{LO}{\simeq} \underline{\phi_{,r,z}} - \underline{\phi_{,r}}\phi_{,z}, \\
N_{,r} &= \frac{1}{N} \left\{ \underline{\phi_{,r}} + r\Omega[(1-2\psi)(\Omega + r\Omega_{,r}) - r\Omega\psi_{,r}] \right\} \stackrel{LO}{\simeq} \underline{\phi_{,r}}, \\
N_{,z} &= \frac{1}{N} \left\{ \underline{\phi_{,z}} + r^2 \Omega [(1-2\psi)\Omega_{,z} - \Omega\psi_{,z}] \right\} \stackrel{LO}{\simeq} \underline{\phi_{,z}}.
\end{aligned} \tag{2.128}$$

And the full divergence of the lapse function is given by

$$\begin{aligned}
N^i{}^k{}_{;k} &= \frac{1}{N} \frac{1}{(1-2\psi)^2} \left\{ -\psi_{,z} \{ \underline{\phi_{,r}} + r^2 \Omega [(1-2\psi)\Omega_{,z} - \Omega\psi_{,z}] \right. \\
&+ (1-2\psi) \left\{ \underline{\phi_{,z,z}} + r^2 \{ (1-2\psi)\Omega_{,z}^2 - 4\Omega\Omega_{,z}\psi_{,z} + \Omega[(1-2\psi)\Omega_{,z,z} - \Omega\psi_{,z,z}] \} \right. \\
&+ \left[(1-2\psi) \frac{1}{r} - \psi_{,r} \right] \left\{ \underline{\phi_{,r}} + r\Omega[(1-2\psi)(\Omega + r\Omega_{,r}) - r\Omega\psi_{,r}] \right\} \\
&+ (1-2\psi) \frac{1}{N^2} \left\{ \{ \underline{\phi_{,r}} + r\Omega[(1-2\psi)(\Omega + r\Omega_{,r}) - r\Omega\psi_{,r}] \}^2 - \{ \underline{\phi_{,z}} + r^2 \Omega [(1-2\psi)\Omega_{,z} - \Omega\psi_{,z}] \}^2 \right\} \\
&+ (1-2\psi) \left\{ r^2 (1-2\psi)\Omega_{,r}^2 + r\Omega[4\Omega_{,r}(1-2\psi - r\psi_{,r}) + r(1-2\psi)\Omega_{,r,r}] + \underline{\phi_{,r,r}} \right. \\
&\left. \left. + \Omega^2 [(1-2\psi) - 4r\psi_{,r} - r^2\psi_{,r,r}] \right\} \right\} \stackrel{LO}{\simeq} \Delta^{(3)}\phi.
\end{aligned} \tag{2.129}$$

For the sake of clarity the linear order terms are underlined in the above expressions. We can learn from the $(^1_3)$ -equation of (2.127) that $\phi = \psi$ is only allowed if $\Omega_{,r} = 0$ or $\Omega_{,z} = 0$. We now attempt to solve the ADM equations for the first-order case.

◆ Case (A) $\psi = 0$ and $\phi \neq 0$ (classical Newton metric) — Let us approximate the above solutions by just taking the linear orders and for convenience let us assume that $\Omega = \Omega(r)$ only. Then, in case we want to have $\rho \neq 0$, the Hamilton constraint requires the unphysical equation $u^0 = 0$. The momentum constraint yields the equation

$$(2.130) \quad 3r\Omega_{,r} + r^2\Omega_{,r,r} = 0.$$

The evolution equation for $i = j$ gives a Poisson-like equation $\Delta^{(3)}\phi = 4\pi GS$ and the $i \neq j$ equations read

$$(2.131) \quad S^1_2 = \rho u^1 u_2 = 0, \quad S^2_3 = \rho u^2 u_3 = 0, \quad -\phi_{,1,3} = 8\pi G\rho u^1 u_3.$$

The equations are exactly the same as in the rigidly rotating case above, with one exception the differential equation for Ω that came out of the momentum constraint (2.130). Here we are again left with unphysical requirements like $\rho = 0 \vee u^0 = 0$ that make the right hand side of (2.130) zero, and we can say that at most the test particle scenario with $u^0 \neq 0$ and $\rho = 0$ is viable.

◆ Case (B) $\psi = \phi \neq 0$ (simplest PN metric) — Here the setting appears at first also very similar to the rigidly rotated case. But there is the subtle feature in that we have non-vanishing mixing components g_{02} and g^{02} , which has the consequence that for instance u_2 can vanish but u^2 can be non-zero, as we will see in the following. First, we note that we can have an appropriate Poisson equation,

$$(2.132) \quad \Delta^{(3)}\phi = 4\pi GE = 4\pi G\rho(Nu^0)^2,$$

with both $\rho \neq 0$ and $u^0 \neq 0$. The momentum constraint requires both $u_1 = 0$ and $u_3 = 0$ which does imply $u^1 = 0$ and $u^3 = 0$, but also the novel relation

$$(2.133) \quad -\frac{1}{2}r^2\Delta^{(3)}\Omega(r) - r\Omega_{,r}(r) = \rho Nu^0 u_2.$$

Inserting the Poisson equation into the $i = j$ -part of the evolution equation returns $S = 0$ for consistency with the Poisson equation. The $i \neq j$ evolution equation gives to linear order

$$(2.134) \quad S^1_2 = \rho u^1 u_2 = 0, \quad S^2_3 = \rho u^2 u_3 = 0, \quad S^1_3 = \rho u^1 u_3 = 0.$$

This, together with $S = 0$, implies that $u^2 u_2 = 0$. But this alone is no problem because of the mentioned non-diagonality of the four-metric. To linear order we can compute

$$(2.135) \quad u_2 = g_{\mu 2} u^\mu = g_{02} u^0 + g_{22} u^2 = -(1 - 2\phi)\Omega r^2 u^0 + (1 - 2\phi)r^2 u^2 \simeq -\Omega r^2 u^0 + r^2 u^2.$$

So the requirement $u^2 u_2 = 0$ allows for a solution $u_2 = 0 \wedge u^2 = \Omega u^0$ which is consistent with our initial assumptions on rotating axisymmetric and stationary systems (2.33). Further, from the momentum constraint (2.133) we obtain a homogeneous differential equation for Ω , that is

$$(2.136) \quad r^2 \Omega_{,r,r} + 3r \Omega_{,r} = 0.$$

Note that this is the same equation that we have already seen in the preceding case (A), namely (2.130); but there we had the unwanted additional constraints $\rho = 0$ or $u^0 = 0$. Now, (2.136) is readily solved, yielding

$$(2.137) \quad \Omega(r) = \frac{1}{r^2} C_1 + C_2,$$

with arbitrary real constants C_1, C_2 . If $C_1 = 0$ then we obtain the limit of rigid rotation $\Omega(r) = C_2 = \omega$. If $C_2 = 0$ we obtain the rotation curve of the problem

$$(2.138) \quad C_1 = r \underbrace{r\Omega(r)}_{=v(r)} = v(r)r \equiv L_0,$$

and so C_1 can be identified as the total angular momentum of the system. However, there is a problem with this equation because the obtained rotation curve falls off as $1/r$ and not as $1/\sqrt{r}$ which is the classical Newtonian result. Therefore the linear approximations must be to naïve. In deriving the approximate results for the differentially rotating case we made a linear ansatz for the metric (2.121). The actual corresponding ADM equations are given to exact order but due to their complexity we made linear approximations while evaluating them. We therefore conjecture that the correct evaluation should enfold the full differentially rotated PN metric (C.3), including quadratic orders, as an ansatz. This introduces numerous additional components to the extrinsic curvature, because additional mixing terms have to be included at second order.

Let us summarise some basic points in brief:

- Up to day, there does not exist an applicable general relativistic solution which could help to realistically model a galactic system.

- Cooperstock and Tieu have recently proposed such a solution, but it has been argued from various directions that their solution incorporates unphysical features. It remains an open point whether the CT solution could provide an effective or approximate model in restricted cases, and to which extent the breakdown of its Newtonian limit might indicate its usefulness or its difficulties.
- We have shown that the CT solution does not belong to the class of the most general axially symmetric and stationary solutions, the Lewis-Papapetrou class. Therefore the CT solution is less general and this restriction might be a reason for the problems of the model.
- In the same line we found the surprising fact that the Newtonian metric is not appropriate for a weak field limit of the CT theory; the incorporation of a post-Newtonian potential is necessary to make physical sense.
- We applied the full machinery of the ADM formalism to the problem and we derived the exact 3 + 1-equations of motion for the static and for the rigidly rotated PN metric as well as approximate results for the differentially rotated case. We found that it is necessary to go to full quadratic order in the potentials of the differentially rotated PN metric to obtain a viable Newtonian limit, which is not presented here due to ‘finite time effects’.

Part II

Axisymmetric Effects in the CMB

On the Cosmic Microwave Background

Currently, measurements of the CMB provide one of the most important means toward high-precision evaluation of cosmological models, particularly the standard Λ CDM model. In this chapter we attempt to give a compilation of the main physical mechanisms that contribute to the CMB radiation. In some detail, we will outline the decoupling of the CMB photons from matter in the early Universe, as triggered by the process of recombination. Furthermore, we review and partly derive the standard statistical framework whose equations form the language in which modern CMB surveys are analysed and discussed. In particular, the CMB angular power spectrum poses a central observable of the field and we discuss measurements of it, as well as the explicit assumptions that go into the analysis.

3.1. Overview of Sources of CMB Anisotropy

A remarkable feature of the CMB is that is overall isotropic to a first approximation. This is only surpassed by the even more remarkable feature that tiny, yet predictable anisotropies exist. The conditions of the early Universe as well as much of the global physics that has taken place before decoupling are mirrored in these anisotropies. Physically, it is convenient to divide anisotropies into two classes: (a) primary ones, which enfold all possible sources of initial anisotropy imposed on the photon field at around the time of last scattering, triggered by gravitational or plasma physics; (b) secondary ones, these comprise a conglomeration of all significant effects the CMB photon can undergo on its long travel towards us along the line of sight. Basic primary anisotropies [Sch06] can occur as a consequence of the following physical effects:

- Due to inflation there are inhomogeneities in the primordial density field, and these force the photons on the surface of last scattering to work against deeper potential wells here and less deep ones there. In addition to the resulting redshift, there occurs a gravitative time delay for the photons. This means that, e.g. the energy loss of a photon climbing out of a deep potential well will be partly compensated by the effect that it also undergoes its last scattering a bit earlier because of a gravitational time shift. Within a full general relativistic treatment these two effects always occur together naturally and are covered by the theory of the *Sachs-Wolfe effect*.
- The initial inhomogeneities in the primordial density field would translate into perturbations in the according peculiar velocity field, c.f. app. D. Therefore, the electrons that are mainly responsible for photon scattering, do not solely follow the global expansion of spacetime but they are also subject to the induced peculiar velocities. This is the source for a frequency-shifting effect on the primeval photons: as the peculiar velocity field arises, the electrons that trace the field are subjected to a Doppler motion at the moment the primordial photons undergo last scattering off them. If, for instance, the Doppler motion in a certain region of the decoupling plasma happens to be directed away from the future observers position, then the Doppler effect will take a bit of the photon's energy away, resulting in additional redshifting in that direction.
- Before *recombination*, the primordial plasma is a tightly coupled baryon-photon fluid. The coupling is due to the free electrons that effectively glue the two fields through Thomson scattering with the photons and Coulomb scattering with the baryons. Dark

Matter (c.f. chap. 2) is attributed a crucial role also at the early epochs of the Universe. In regions where there is a condensation of Dark Matter, the density of baryons would also be higher. More exactly, before recombination and on super-Hubble scales, the distribution of Dark Matter is well traced by the distribution of the baryons. But on sub-Hubble scales the effective pressure that is produced by the baryon-photon fluid becomes sensible and important. With the gravitational pull from Dark Matter as the driving force, and the pressure of the baryon-photon plasma as the restoring force, the baryons undergo acoustic oscillations^a. The baryon oscillations correspond to elongations and compressions in the baryon fluid which, in the adiabatic case, cause the oscillating region to become colder during elongation and hotter during compression. Now, before recombination, photons are tightly coupled to the baryons, forming a baryon-photon fluid and therefore the adiabatic perturbations are imposed on the photons too; this makes the photons accordingly hotter if they last-scatter from a region of adiabatic compression and cooler if last-scattered from a region of adiabatic elongation. At recombination this effect of the baryon environment on the photons in the pre-recombination phase suddenly freezes, becomes visible and contributes additional CMB anisotropy.

- But the coupling of photons and baryons is not exact. Rather, the photons do have a finite mean free path which leads to photon dissipation on small scales. On these scales the restoring force, which was provided by the pressure support, on the baryon oscillations disappears and the fluctuations are effectively washed-out. This damping mechanism, due to photon dissipation because of the finite shear viscosity and heat conductivity of the fluid, is referred to as *Silk damping*. Due to Silk damping, on all scales smaller than roughly $\sim 5'$, there remain only tiny fluctuations. A more detailed estimate on the effective scale of Silk damping can be found in app. D.3.

Let us shortly summarise. As primary CMB anisotropies we so far have: the Sachs-Wolfe effect; frozen Doppler velocities and adiabatic baryon oscillations. But also damping of fluctuations occurs, namely through the process of Silk damping. Of course, the first three of these mechanisms are not independent of each other.

Let us add a comment explaining why the oscillations in the baryon-photon plasma are possible. After matter-radiation equality – which is at around $z_{\text{eq}} \simeq 23900\Omega_{\text{m}}h^2$ – the overall energy density of matter exceeds that of radiation. But when looking only at the baryon-photon fluid, the radiation energy density is the dominant component in this fluid and so we can treat it as a relativistic fluid. That implies that the sound speed is around $c_s \simeq \sqrt{p/\rho} \simeq c/\sqrt{3}$ and so the large pressure in the fluid makes oscillations possible. As mentioned, the gravitative force due to the Dark Matter provides the driving force and the baryon-photon pressure gives rise to a restoring force in the oscillator. The adiabatic oscillations translate into temperature anisotropies which are observable on the microwave sky today. But there is a natural size limit for the oscillations. Since the speed of sound is around $c_s \simeq c/\sqrt{3}$, there exists a maximal wavelength, the *sound horizon*, which possibly could have been covered by an acoustic perturbation up to the time of last scattering:

$$(3.1) \quad \lambda_{\text{SH}} \simeq t_{\text{rec}}c_s = r_{\text{H}}(t_{\text{rec}})/\sqrt{3} \sim 1^\circ.$$

^aLet us comment on the *growth* of the baryon perturbations. Still during the radiation dominated epoch, there would be a moment when the baryonic and Dark Matter perturbations enter the horizon. Then, on the smaller (causal) scales the pressure support stops the baryon perturbations from growing further, so that the Dark Matter perturbations can go ahead of the baryonic ones. That is, for subhorizon modes the growth of perturbations is in competition with the effective pressure from the baryon-photon fluid and is eventually compensated. At the same time, Dark Matter is not strongly coupled to photons and grows untroubled from matter-radiation equality, a_{eq} , on. One can estimate [Pad02] that the Dark Matter perturbations have the chance to grow by a factor of $\gtrsim 20$ in the period $a_{\text{eq}} < a < a_{\text{dec}}$ while the baryonic perturbations are tamed during that phase. However, after recombination the photons are no longer strongly coupled to the baryons and become free-streaming. This, after some time, unlocks the growth of baryon fluctuations, being driven by the Dark Matter perturbations, and eventually catching up with the latter.

As we will see, this scale corresponds to the first acoustic peak in the angular power spectrum of the CMB and is a directly measurable cosmological observable.

Next we continue with a list of sources [Sch06] that are important for secondary CMB anisotropies:

- Due to the lack of an absorption threshold in the Lyman- α spectra of very distant quasars up to $z \simeq 6$ – together with constraints on the baryon abundance from primordial nucleosynthesis – it is concluded that the intergalactic medium in the Universe today is highly ionised. Recent CMB analyses set reionisation at around $z \sim 10$ and so from this epoch on, there must be free electrons present in the extragalactic medium^b. Then CMB photons can again scatter off these electrons via Thomson scattering. Because the CMB is isotropic around any scattering centre, the rescattered CMB radiation that we would measure, does not contain information on the primordial temperature anisotropies anymore. Rather these photons represent an additional component with random directional origin, i.e. an isotropic background to the CMB with a mean temperature that equals the CMB mean temperature. The result is a decrease in the temperature anisotropies by the fraction of photons that undergo such late Thomson scattering.
- While the photons are on their long travel through the Universe, toward the measuring instrument today, the surrounding large-scale structure is in a process of dramatic gravitative evolution. This evolution is due to the vast processes of structure formation, c.f. app. D. As a consequence, the gravitational potentials that the photons are traversing are not stationary. This environment will induce a net effect on the photons because of the large scale of the gravitative effects. Let us explain this in more detail. Imagine two CMB photons, coming from two different directions to us. The first photon, say from direction \mathbf{n}_1 , would travel through a gravitational potential, and the second one, say from direction \mathbf{n}_2 would travel undisturbedly. Now, assume that the potential wells in the line of sight were stationary, then there would be no difference in frequency of the two photons. That is because the net effect of the potential is zero for the first photon, for it loses exactly the same energy while climbing up the potential well it has gained before while falling into it. This is not true anymore in case of a potential that varies at time scales comparable to the traversing time of the photon. Exactly such a setup is realised during structure formation – and as we will see below this is also likely to happen at low redshifts – and so additional anisotropy is induced to the CMB. This is called the *Rees-Sciama effect*. In the case of an Einstein-DeSitter Universe, one can show that the peculiar gravitational potentials are constant with time and no Rees-Sciama effect occurs. Notably, in other cosmological models this effect exists and cannot be neglected. Often, the conglomeration of any linear gravitative effects a CMB photon can undergo after recombination on the line of sight, are summed under the notion *integrated Sachs-Wolfe effect*.
- Due to the gravitational lensing of CMB photons from the cosmological field of density perturbations, there will be a directional distortion in the line of sight to the last

^bFrom observations we know that the gas in the intergalactic medium is highly ionised at low redshifts. Let us explain this finding in further detail. Assume this was not so, assume the intergalactic hydrogen would be neutral. Then we could never observe ultraviolet radiation from far-away sources; this is because due to continuous redshifting, at least somewhere in the line of sight, the photons would reach a wavelength of $\lambda_{\text{Ly}\alpha} \simeq 1216\text{\AA}$ and would be absorbed by the neutral hydrogen with a high probability. The probability is high because the cross section for photoionisation of neutral hydrogen is significantly high for photons with wavelengths near the Lyman- α line. This is called the Gunn-Peterson test. In fact there exist sources (quasars) at $z \gtrsim 6$ from which we can even see light from the blue side of the spectrum with respect to the Lyman- α line. Therefore the Universe must have become reionised somewhere between $z \sim 1100$ and $z \sim 6$. The times between last scattering and reionisation are sometimes called the ‘Dark Ages’ and it is speculated that reionisation was made possible by the very first generation of stars or active galactic nuclei. Direct measurements of the Gunn-Peterson trough for objects $z > 6$ are subject to current debate. However, recent WMAP measurements [S⁺07] of the CMB suggest that reionisation occurred at a redshift of $z_{\text{reion}} = 11.3$.

scattering surface. Without that effect, an angular separation of θ would correspond – due to the angular diameter distance (1.38) – to a distance of $D_A(z_{\text{rec}})\theta$ at the surface of last scattering. Taking the lensing distortion into account, this angular distance will be slightly different. This effect results in an effective smearing of the temperature fluctuations, observable on small scales in the correlation function of the CMB anisotropies.

- If CMB photons happen to go through a galaxy cluster in the line of sight, in which there is a very hot (ultrarelativistic) intra-cluster medium, they can undergo inverse Compton scattering. This is the *Sunyaev-Zel'dovich effect*. In such directions there will be a distortion in the frequency of the CMB photons in so far as they would gain some energy on average through the scattering off the very energetic electrons in the galaxy cluster medium. In fact, the CMB intensity shows a decrease in the low energy part and an increase on the higher energy side of the spectrum. Therefore, when observed at a frequency interval that is large enough, the Sunyaev-Zel'dovich effect is well distinguishable in the CMB data.

3.2. Recombination

Recombination is a somewhat misleading term. At recombination the primordial plasma has cooled down so far that neutral atoms could be formed. In the Big Bang picture the temperature of the Universe goes as $T(z) \propto (1+z)$, and so, before the time of recombination there was no possibility for stable neutral atoms to be present; the Universe was fully ionised ever before. The term ‘recombination’ can be understood merely in a historical sense: it refers to the process of recombination in HII regions, c.f. [Pea99]. HII regions are high-temperature regions containing hydrogen – and also helium – and can be found in the vicinity of stars. In a continuous process, the hydrogen first becomes fully ionised by the ultraviolet radiation from the stars, after which the electrons and the ions find each other again, emitting recombination radiation, before they become photoionised once more and so on. Below we present a description following Schneider [Sch06] and Peacock [Pea99].

Because of the very hot and dense environment, the formation of nuclei is possible within stars. Similarly, there should be a period in the early Universe where nuclei were formed for the first time; this is described within the model of *Big Bang Nucleosynthesis* (BBN). BBN ends at a temperature of around $T \sim 8 \times 10^8 \text{K}$, or approximately after three minutes. After BBN the particle content of the Universe is basically given by electrons, protons, helium nuclei and traces of other light elements, neutrinos, photons and possibly the particles that form Dark Matter, the Weakly Interacting Massive Particles (WIMPs). Apart from the WIMPs and the neutrinos, all particles have roughly the same temperature; this is because of the relatively strong interaction of the photons with the charged particles, and so a kind of thermal bath is realised.

Before the instant of equality at $z_{\text{eq}} \simeq 23900\Omega_m h^2$, the energy density and therewith the rate of expansion of the Universe are dominated by the radiation, that is by the photons and the neutrinos. After equality, the matter – we approximate it as dust – starts to dominate the energy density and the expansion rate of the Universe. In the Friedmann equation (1.16), this implies that the first term becomes dominant and we can make the crude simplification $H^2 \simeq H_0^2 \Omega_m a^{-3}$. From tab. 1.1 we already know the solution to this differential equation; for matter domination the scaling is

$$(3.2) \quad a(t) = \left(\frac{3}{2} \Omega_m^{1/2} H_0 t \right)^{2/3} \quad \text{within} \quad a_{\text{eq}} \ll a \ll 1.$$

This scale behaviour is valid as long as either the curvature term or the cosmological constant is dominant.

As the Universe expands further, after equality there will be a period when the free electrons can combine with the ions to form neutral atoms. But, of course, there is a competing process to this, namely the photoionisation of neutral atoms through high-energy photons. Also, there

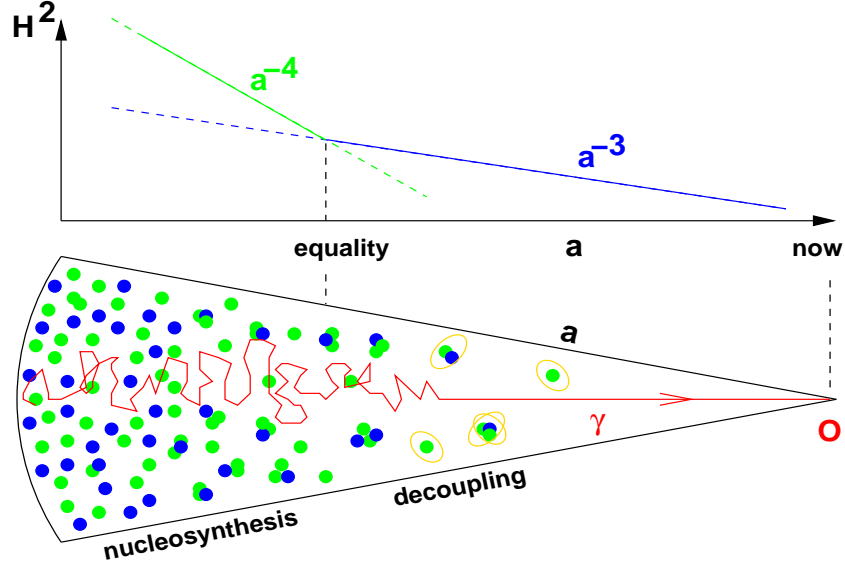


FIGURE 3.1. Schematic depiction of matter and radiation decoupling. The decoupling is no instantaneous process. Before recombination, baryons and photons form a tightly coupled fluid in which acoustic oscillations take place. Some time after the radiation and matter equality at around $z_{\text{eq}} \simeq 3000$, the recombination of electrons and ions – as described in detail in the text – sets in. At around $z_{\text{rec}} \simeq 1088$ the baryon-photon fluid becomes transparent for the first time. This gives rise to a last scattering surface from which on photons are free-streaming, and we are able to observe a snapshot of this primeval decoupling today – which itself has a finite thickness of around $z \simeq 60$. The picture is taken from [Les04].

is another competing ionisation process due to collisions. But this can be neglected because the ratio of baryons to photons η is very small, namely only of the order 10^{-8} , see also app. E on BBN. Note that the temperature of the Universe has to drop to a value well below the ionisation temperature if neutral atoms are to be formed efficiently. The reason for this is that, yet at the ionisation temperature there are photons in the Wien tail of the Planck spectrum that are energetic enough to break the formed atoms via photoionisation. Since there are so many more photons than baryons the Wien tail is still populated densely, making the effect significant. As is well known, the energy needed for ionisation of hydrogen is $\chi \simeq 13.6\text{eV}$, corresponding to a temperature of $\sim 10^5\text{K}$ (recall, $1\text{eV} \simeq 1.161 \times 10^4 k_{\text{B}}\text{K}$). Now, the fractional ionisation is the ratio

$$(3.3) \quad x \equiv \frac{\text{number density of free electrons}}{\text{total number density of protons}} .$$

Because of the above mentioned stubborn photoionisation from photons in the tail of the Planck distribution, the temperature of the Universe has to drop to a value of $T \sim 3000\text{K}$ before the fractional ionisation significantly drops below one. For instance, at temperatures $T > 10^4\text{K}$, the fractional ionisation is still roughly equal to one, implying that nearly all electrons are free. At a redshift of around $z \sim 1300$, a significant deviation of x from unity can develop.

It would be good to have a robust, quantitative estimate on when recombination has begun. As a first step we consider Saha theory, from which the following ionisation formula stems

$$(3.4) \quad \frac{1-x}{x^2} \simeq 3.84\eta \left(\frac{k_{\text{B}}T}{m_e c^2} \right)^{3/2} e^{\chi/(k_{\text{B}}T)} .$$

The Saha equation is a thermodynamic equilibrium equation and it describes the behaviour of the ionisation fraction as a function of temperature. Plotting the function reveals that the ionisation shows a rather sharp decrease, going from unity to nearly zero in a temperature

interval of around 2500K- 5000K [Nar02]. That is, if the Saha theory is all we need to describe the recombination, the cosmos would become *transparent* at these temperatures, since the main scattering partners, the free electrons, are ‘removed’ from the primordial plasma.

However, there is a loophole in the above argument. As we will see, once the process of recombination has started, the assumption of thermodynamic equilibrium becomes invalid rather fast. Consider a recombination directly to the ground state of the hydrogen, then a photon with energy $h\nu > \chi$ is emitted. Such photons are of course problematic for the recombination since they can reionise other hydrogen atoms. In fact, they do reionise other atoms with a high probability because of the large cross section of the photoionisation process. Hence, for every recombination there is a reionisation, such that the net effect is zero. Recombination shall happen stepwise: first a recombination into an excited state, whereupon the atom undergoes successive radiative processes and eventually arrives at its ground state. But there is a problem also with this picture. For every such stepwise recombination there will be an emission of a Lyman- α photon from the last step of the process, the transition from the first excited state to the ground state $2P \rightarrow 1S$ with $\lambda = 1216\text{\AA}$. The resulting Lyman- α photon would immediately lift an atom in its ground state to its first excited state. Since for this atom the ionisation energy is not χ but only $\chi/4$ and because there are much more photons with energies of $\chi/4$ than there are with χ , such atoms can be reionised even easier, which actually also happens. One can say that recombination radiation leads to small distortions in the Planck spectrum which in turn makes the recombination more difficult; the recombination suppresses itself through the above processes. Nevertheless, in gas clouds or HII regions, recombination can still happen in this way, since the unwanted Lyman- α photons dissipate because of the finite extent of the regions. Recombination in an infinite Universe seems much more problematic.

So it seems that recombination might not be possible at all! How can we circumvent this absurd finding? There is only one way out: in the end it turns out that recombination can indeed occur, namely via the scarce process of two-photon emission. Although the two-photon decay happens 10^8 times rarer than the direct Lyman- α transition, this process finally succeeds in transferring the ionisation energy into photons with wavelengths $\lambda > \lambda_{\text{Ly}\alpha}$, and so the produced radiation does not have enough energy to eventually excite an atom from the ground state. In fact, the transition $2S \rightarrow 1S$ is strictly forbidden at first order in perturbation theory. But with the emission of a pair of photons, angular momentum and energy can be conserved. Being of second order, the process is very slow – with a lifetime of around $\simeq 0.1\text{s}$ – so that the recombination is also slowed down as it has to pass this bottleneck. Therefore the actual rate at which recombination happens is completely different from the prediction of the equilibrium (Saha) theory.

Let us consider a much simplified model, a world where the hydrogen atom has only the two levels $1S$ and $2S$. We can just ignore any chain of recombination that reaches the ground state because the produced photons will cause reionisation elsewhere and the net effect is zero. Because of the above, we shall focus on recombinations into the $2S$ state. Some of the atoms in that state would undergo two-photon decay before they become excited again. Then the rate of change of the ionisation fraction follows

$$(3.5) \quad \frac{d(n_{\text{p}}x)}{dt} = -R(n_{\text{p}}x)^2 \frac{\Gamma_{2\gamma}}{\Gamma_{2\gamma} + \Gamma_{\text{up}}(T)},$$

with n_{p} being the number density of protons, $R \simeq 3 \times 10^{-17} T^{-1/2} \text{m}^3 \text{s}^{-1}$ the so called recombination coefficient, the two-photon decay rate $\Gamma_{2\gamma}$ and the ‘upward transition rate’ $\Gamma_{\text{up}}(T)$ of transitions from the $2S$ level upwards due to stimulated emission. In our simplified picture recombination is a two-body process after which excited states remain, which subsequently undergo a decay cascade until the $2S$ level is reached. Then, starting from the $2S$ level, there will not only be downward decay but also stimulated upward transition. These two transitions are in a competition whose outcome will fix the effective number of downward transitions which is the relevant one for recombination. Peebles [Pee93] offers a more detailed treatment in which the depopulation of ground states by inverse two-photon absorption or the redshifting of the

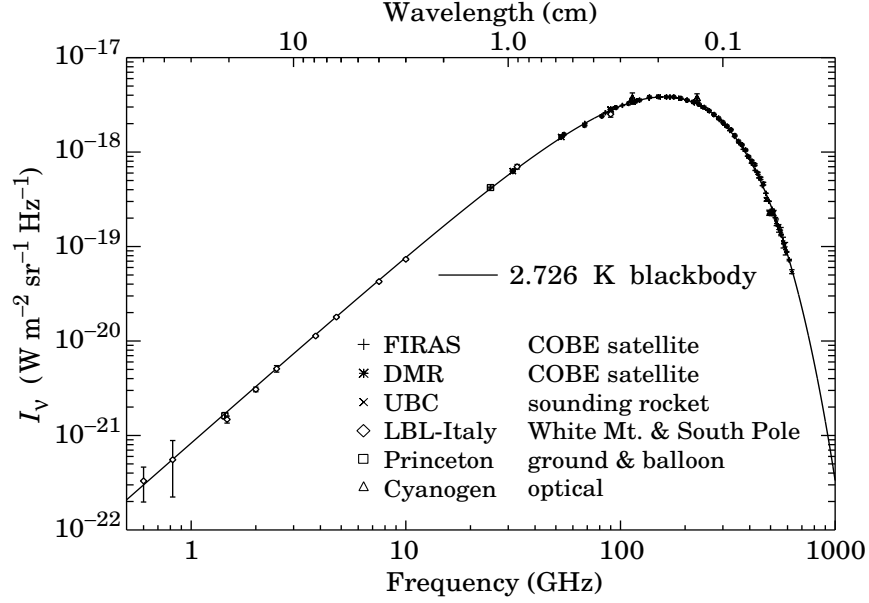


FIGURE 3.2. Spectral distribution of the CMB plotted as intensity vs. wavelength. The data points lie perfectly on a black body spectrum peaking at around 160GHz. Besides data from the COBE mission [MCC⁺94], there is also data shown from a rocket experiment (UBC Rocket) [GHW90], ground based experiments (LBL/Italy) [SBL91], (Princeton) [SJWW95] as well as spectroscopy of the rotational excitation of cyanogen [RM95]. Picture is taken from [Smo97].

Lyman- α radiation by cosmic expansion is also taken into account. However, as long as we look at relevant redshifts of 10-1000, these effects shall not significantly affect the basic results of our simplified consideration. Note that the rate equation (3.5) obeys a simple scaling. The right hand side involves Γ_{up} and R , both are functions of only temperature (redshift). Hence, parameter dependence is only carried by n_p^2 which scales as $(\Omega_b h^2)^2$ on the right hand side, and accordingly the scaling is proportional to $\Omega_b h^2$ on the right hand side. It is convenient to express things in terms of redshift, and so we can use the following transformation valid for matter domination and at large redshifts:

$$(3.6) \quad \frac{dt}{dz} \simeq -3.09 \times 10^{17} (\Omega_m h^2)^{-1/2} z^{-5/2} s,$$

Combining this with the aforementioned, we obtain a scaling law for the fractional ionisation:

$$(3.7) \quad x(z) \propto \frac{(\Omega_m h^2)^{1/2}}{\Omega_b h^2}.$$

Note that this scaling is completely different as the one obtained from Saha theory.

In order to solve the rate equation we consider late times; that is we restrict to times when the Universe has cooled so far that we can neglect excited transition of the 2S states. The rate equation then becomes

$$(3.8) \quad \frac{d \ln x}{d \ln z} \simeq 60 x z \frac{\Omega_b h^2}{(\Omega_m h^2)^{1/2}}.$$

Recall that for this equation we have neglected the cosmic expansion and so the equation is not valid anymore when the left hand side becomes less than unity.

Now, one can include all relevant effects and solve for the ionisation fraction in the redshift interval interesting for recombination, $800 \lesssim z \lesssim 1200$. It is found that the ionisation fraction

may be well approximated by the criterion [JW85]

$$(3.9) \quad x(z) \simeq 2.4 \times 10^{-3} \frac{(\Omega_m h^2)^{1/2}}{\Omega_b h^2} \left(\frac{z}{1000} \right)^{12.75}.$$

From (3.9) we can learn that the ionisation fraction has a very strong redshift dependence; that is, the redshift changes over a rather small interval while the ionisation fraction changes drastically: from $x = 1$ (complete ionisation) down to $x \sim 10^{-4}$ (nearly complete recombination). The fact that the ionisation does not go to exactly zero reflects the influence of cosmic expansion that we neglected before. At small values of the ionisation fraction the rate of recombination drops below the rate of expansion of the Universe: then it happens that some ions do not have enough time to find themselves a partner electron to recombine with before the density of the Universe becomes too much diluted. Plugging (3.9) into the formula for the *optical depth* as due to Thomson scattering, one obtains the important result

$$(3.10) \quad \tau(z) \equiv \int n_e x \sigma_T dl \simeq 0.37 \left(\frac{z}{1000} \right)^{14.25},$$

where we integrated over the proper distance l along the line of sight. The remarkable point is that in the expression for the optical depth, the cosmological parameter dependence cancels out. The reason for that is the scaling of the fractional ionisation (3.9) that came out of the rate equation. Again, τ is very sensitive to changes in z and so the last scattering shell is a rather sharp transition. The distribution function $e^{-\tau} d\tau/dz$ for the last scattering redshift can be expressed by a Gaussian with mean $z \simeq 1088$ and a standard deviation $z \simeq 60$. This is the reason why we observe a very uniform primordial radiation from an almost synchronous emission surface ('snapshot') in the early Universe: the *last scattering surface*. The redshifting during the billions of years the photons have travelled since then has brought the CMB radiation into the microwave band, where it was first observed by Penzias and Wilson in 1965 [PW65].

The spectrum of the CMB radiation is a Planck spectrum. In fact, its spectrum was first accurately measured by the Far Infrared Absolute Spectrophotometer (FIRAS) mounted on the Cosmic Background Explorer COBE satellite [MCC⁺94], and is the best black body spectrum ever obtained from a real measurement, see fig. 3.2. Let us shortly derive how an initial Planck spectrum for the primordial radiation keeps its form during the evolution of the Universe. Consider a Planck spectrum of photons at an initial temperature T_0 at time t_0 , then the function

$$(3.11) \quad B_\nu(T_0) = \frac{2h\nu^3}{c^2} \frac{1}{e^{h\nu/(k_B T_0)} - 1}$$

measures the black body surface brightness; here h is of course the Planck constant, not to be confused with the normalised Hubble parameter. The surface brightness is the luminosity that goes through a unit area during a unit time interval, per unit solid angle and unit frequency interval. Then the number density of photons in a frequency range between ν and $\nu + d\nu$ is given by

$$(3.12) \quad \frac{dN_\nu}{d\nu} = \frac{4\pi}{hc} \frac{B_\nu}{\nu} = \frac{8\pi\nu^2}{c^3} \frac{1}{e^{h\nu/(k_B T_0)} - 1}.$$

Now let us consider an instant $t_1 > t_0$, in which the Universe would have expanded by the factor $a(t_1)/a(t_0)$ and an observer sees the initial photon redshifted by the factor $1+z = a(t_1)/a(t_0)$. Accordingly, an initial frequency interval $d\nu$ is being redshifted to $d\nu' = d\nu/(1+z)$. Since we are within matter domination, the number density of photons is diluted with a^{-3} (c.f. tab. 1.1) and so $dN'_{\nu'} = dN_\nu/(1+z)^3$. Therefore, the number density of photons in the frequency range between ν' and $\nu' + d\nu'$ becomes

$$(3.13) \quad \frac{dN'_{\nu'}}{d\nu'} = \frac{dN_\nu/(1+z)^3}{d\nu/(1+z)} = \frac{8\pi}{c^3} \frac{1}{(1+z)^2} \frac{(1+z)^2 \nu'^2}{e^{h\nu'(1+z)/(k_B T_0)} - 1} = \frac{8\pi\nu'^2}{c^3} \frac{1}{e^{h\nu'/(k_B T_1)} - 1},$$

and so the form of the Planck distribution is left invariant under global expansion; only the temperature T_0 is replaced by the redshifted temperature $T_1 = T_0(1+z)$. Thus, since we

observe the spectrum of the CMB to be the one of a black body today, we can extrapolate that it has had this form – up to distortions due to additional physics – ever since last scattering.

Note that, although there is a very small offset between the instant of *recombination* and the eventual effective *decoupling* of the primordial photons, we are using z_{rec} throughout this work to denote the instant of last scattering.

3.3. Observables of the CMB

In the course of sec. 3.1 we got to know the basic mechanisms that are responsible for the CMB anisotropy. The next question is, how the main physical effects translate into quantifiable observables. In sec. 1.3.3, we have anticipated a basic part of the answer: the (integrated) Sachs-Wolfe effect. The Sachs-Wolfe formula parameterises the influence of the most important primary and secondary sources of the CMB temperature anisotropy $\Delta T/T$, which is a physical observable accessible through differential measurements. What remains to be done is to find a statistical framework of the temperature anisotropies that is convenient and suitable for the comparison of theory and experiment. In order to do this accurately, one must cope with the fact that the approximation of the matter-photon medium as a perfect fluid breaks down after recombination. An adequate treatment then involves the solution of the corresponding kinetic equation, the full Boltzmann equation for the photon distribution function. Seljak and Zaldarriaga [SZ96] have developed a publicly available FORTRAN code, called CMBFAST [CMB], that can be used for state-of-the-art computation. Here we restrict ourselves to a basic understanding of the CMB power spectrum and its use for phenomenology. However, see for instance [HS95] for an exhaustive discussion.

3.3.1. Fourier Analysis of the Temperature Power Spectrum. How can we relate the three-dimensional density perturbations from inflation to the two-dimensional temperature field that we observe in the CMB? The density perturbations – see also app. D – are characterised by their power spectrum $P(k)$ from equation (1.29). Sometimes the power spectrum is expressed as [Pea99]

$$(3.14) \quad \Delta^2(k) \equiv \frac{V}{(2\pi)^3} 4\pi k^3 P(k),$$

for a given volume V . The quantity $\Delta^2(k)$ is dimensionless and has the interpretation of the variance of perturbations per interval of $\ln k$; that is, $\Delta^2(k) = \langle \delta^2 \rangle_{\ln k} \propto k^3 P(k)$. For instance if we had $\Delta^2(k) = 1$ this would mean that, per logarithmic k interval, there are density perturbations of order unity. Here, we consider a simplified Fourier analysis following [Pea99]. The simplification is provided by the assumption of local thermodynamic equilibrium of the primeval photons as well as the assumption of spatial flatness – this will be a good approximation for intermediate scales.

Given an observed intensity I_ν , the *brightness temperature* is the temperature a black body would need to have in order to radiate that intensity. Therefore one can invert the Rayleigh-Jeans law to define the brightness temperature as

$$(3.15) \quad T_B \equiv \frac{I_\nu c^2}{2k_B \nu^2}.$$

Now, we can think of the measured CMB as a two-dimensional random field of anisotropies in the brightness temperature. Consider a patch of the two-dimensional CMB sky of side L , but being small enough to be flat. It is useful to introduce the Fourier transform of the fractional temperature differences,

$$(3.16) \quad \frac{\Delta T}{T}(\mathbf{X}) = \frac{L^2}{(2\pi)^2} \int T_K e^{-i\mathbf{K}\cdot\mathbf{X}} d^2 K \quad \text{and} \quad T_K(\mathbf{K}) = \frac{1}{L^2} \int \frac{\Delta T}{T}(\mathbf{X}) e^{i\mathbf{K}\cdot\mathbf{X}} d^2 X.$$

Here, by \mathbf{K} and \mathbf{X} we denote two-dimensional vectors of position and wavenumber respectively, and moreover the *temperature anisotropy* $\Delta T/T$ is a central quantity of CMB analysis, being defined as $\Delta T/T \equiv (T(\theta, \phi) - T_0)/T_0$ with the *monopole background temperature* T_0 .

In analogy to the treatment of the three-dimensional density perturbations, we can write down a dimensionless power spectrum of the temperature fluctuations in two dimensions

$$(3.17) \quad \mathcal{T}_{2D}^2 \equiv \frac{L^2}{(2\pi)^2} 2\pi K^2 |T_K|^2.$$

Similar to (3.14), but now in two-dimensions, this is a measure of the variance in the fractional temperature differences of the CMB, coming from modes of unit length in $\ln K$. In fact, the Fourier transform of the temperature power spectrum yields the two-point correlation function

$$(3.18) \quad C(\theta)_{2D} \equiv \int \mathcal{T}_{2D}^2(K) \frac{J_0(K\theta)}{K} dK,$$

which is the observable we were looking for. J_0 denotes the Bessel function; it enters the formula via the angular part of the Fourier integration.

We can reconstruct the two-dimensional temperature fluctuation field from the actual three-dimensional one by integrating over the optical depth at last scattering and over the wavenumber,

$$(3.19) \quad \frac{\Delta T}{T} = \frac{V}{(2\pi)^3} \int \int T_k^{3D} e^{-i\mathbf{k}\cdot\mathbf{r}} d^3k e^{-\tau} d\tau.$$

The optical depth expression can be approximated by a Gaussian with

$$(3.20) \quad e^{-\tau} d\tau \propto e^{-(r-r_{\text{rec}})/(2\sigma_r^2)} dr,$$

and r being the comoving radius. This means that the central distance to the last scattering shell is given by r_{rec} , which in turn can be approximated by the Hubble radius because of the high redshift of the last scattering shell. Above, we already used an estimate for the thickness of the last scattering shell of $z \simeq 70$. In fact one can show [Pea99] that the thickness can be expressed as

$$(3.21) \quad \sigma_r \simeq \frac{7\text{Mpc}}{(\Omega h^2)^{1/2}}.$$

Applying an analogous definition to the spatial temperature power spectrum as in the two-dimensional case, we can write

$$(3.22) \quad \mathcal{T}_{3D}^2 \equiv \frac{V}{(2\pi)^3} K^2 |T_K|^2.$$

By equating the respective two-dimensional and three-dimensional two-point functions, one obtains the final projection formula [Pea99]

$$(3.23) \quad \mathcal{T}_{2D}^2 = K^2 \int_0^\infty \mathcal{T}_{3D}^2 [(K^2 + w^2)^{1/2}] e^{-w^2\sigma_r^2} \frac{dw}{(K^2 + w^2)^{3/2}}.$$

This projection formula finally represents the relation between the two-dimensional and three-dimensional temperature power spectra. The two-dimensional power spectrum receives contributions from all the three-dimensional modes with wavenumbers smaller than K , the other modes are integrated out. Therefore, what the projection effectively does is smearing. Through smearing one gets the two-dimensional temperature spectrum from the three-dimensional one. Any feature present at a certain scale in the spatial field can be found at the very same scale in the projected spectrum. Also note that, as long as \mathcal{T}_{3D}^2 is not a very strongly increasing function, the damping term will cause the integral to be dominated by the contribution around $w = 0$. If this is not the case, the finite thickness σ_r becomes relevant.

In sec. 3.1 we discussed various sources of CMB anisotropy. Now we need some quantitative expressions for the anisotropy contributions. We consider only some of them in order to obtain a first picture of the standard interpretation within synchronous and comoving gauge.

- Sachs-Wolfe source – Perturbations in the primordial density field cause anisotropy via: (a) additional redshifting of the photons that are climbing out of potential wells, (b) time dilation of photons because of the gravitative perturbations. The full general

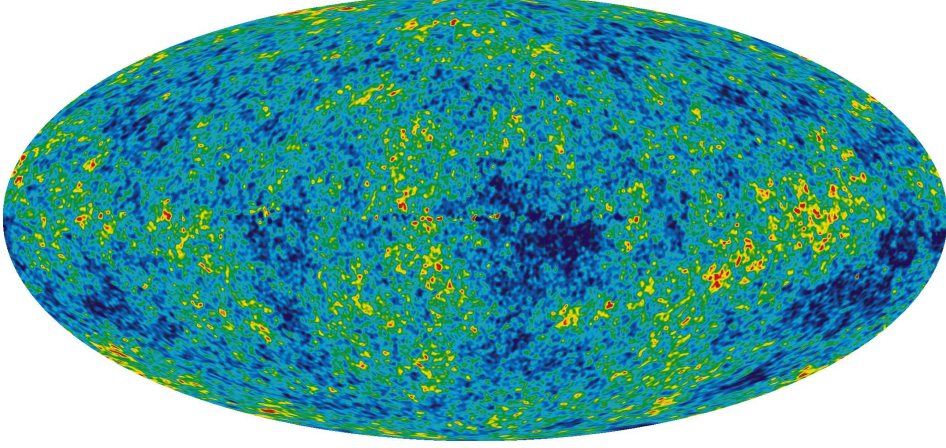


FIGURE 3.3. A Mollweide map of the intrinsic CMB temperature anisotropies [$\mathcal{O}(10^{-5})$] as derived from three years of WMAP mission data. Here, red colours indicate warmer spots and blue colours indicate colder regions. A superposition technique – the Internal Linear Combination (ILC) – has been applied to the raw data in order to subtract astrophysical foregrounds. The ILC method introduces free coefficients that are fitted in order to find a maximally clean map, with the constraints that the variance of the resulting map is minimised and, at the same time, the amplitude of the signal is preserved. Other (more obvious) cleaning has to be done in addition: removing the dipole contribution fig. 3.4 and the large Milky Way contamination, c.f. fig. 4.4 – a slice of $\sim 30^\circ$ is cut away to both sides of the equator and is to be reconstructed properly. Provided the cleaning techniques work at the required accuracy, the residual tiny anisotropies are of cosmological origin; they represent a snapshot of the primeval quantum fluctuations frozen out in the early Universe. The picture is taken from [WMAa].

relativistic perturbation calculation reveals that the net result is exactly one third of the Newtonian expression, that is

$$(3.24) \quad \left(\frac{\Delta T}{T}\right)^{\text{SW}} = \frac{\Delta\phi}{3c^2}.$$

The factor of 1/3 is non-intuitive; it can be shown [HPLN02] that it is a peculiar prediction from GR, and cannot be obtained from any kind of Newtonian reasoning. Moreover, the factor is unique also concerning the physical setting (standard model plus adiabatic perturbations). In particular, taking an isocurvature setting, the resulting Sachs Wolfe contribution is $\Delta T/T = 2\Delta\phi$. The corresponding Fourier-expanded expression is

$$(3.25) \quad T_k^{\text{SW}} = -\frac{\Omega(1+z_{\text{rec}})}{2} \left(\frac{H_0}{c}\right)^2 \frac{\delta_k(z_{\text{rec}})}{k^2}.$$

- Doppler velocity – The electrons, off which the photons last scatter, are subject to induced peculiar velocity, which results in an additional frequency-shift. The resulting anisotropy is given by

$$(3.26) \quad \left(\frac{\Delta T}{T}\right)^{\text{DV}} = \frac{\delta\mathbf{v} \cdot \hat{\mathbf{r}}}{c},$$

and the according result in Fourier space is

$$(3.27) \quad T_k^{\text{DV}} = -i[\Omega(1+z_{\text{rec}})]^{1/2} \left(\frac{H_0}{c}\right) \frac{\delta_k(z_{\text{rec}})}{k} \hat{\mathbf{k}} \cdot \hat{\mathbf{r}}.$$

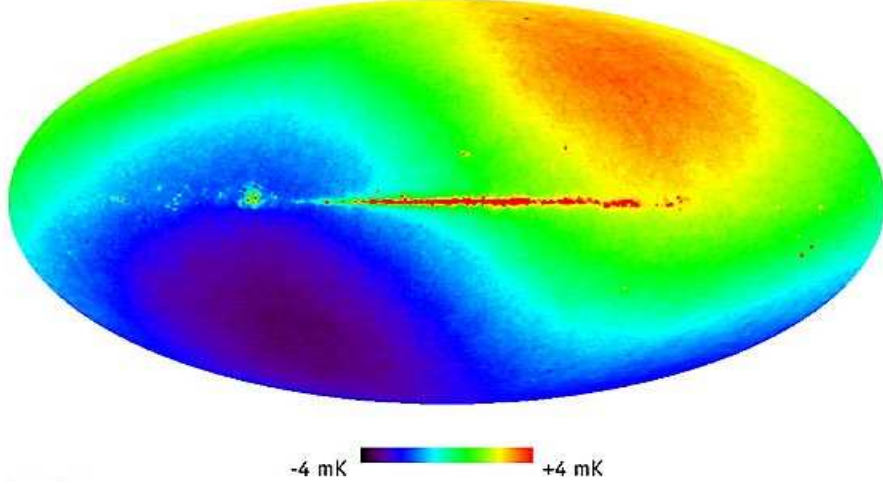


FIGURE 3.4. The uncorrected dipole as measured with COBE shown in Mollweide projection. This distribution is interpreted as being the result of the Doppler effect induced by our local motion against the CMB rest frame. Our velocity vector is the end result of a superposition of various peculiar velocities up to the last scattering surface; its magnitude is $\simeq 370\text{km/s}$. The temperature excess arising from the dipole is $\simeq 3.3\text{mK}$ and can be used for calibration. The picture is taken from [WMAb].

- Adiabatic source – Because of their tight coupling before recombination, any adiabatic perturbations in the matter-radiation density are likewise imprinted on the photons too, resulting in additional anisotropy. The respective formulae read

$$(3.28) \quad \left(\frac{\Delta T}{T}\right)^{\text{AS}} = -\frac{\delta z}{1+z} = \frac{\delta\rho}{\rho} \quad \text{and} \quad T_k^{\text{AS}} = \frac{\delta_k(z_{\text{rec}})}{3}.$$

- Isocurvature source – As opposed to the adiabatic perturbations, the isocurvature perturbations allow the entropy to vary. In the adiabatic scenario all the different energy species undergo a common density perturbation. Isocurvature perturbations are defined as an initial condition, which states that there do not exist any deviations in total energy density from the background at the initial time. Therefore the curvature is spatially constant and so the name becomes clear. A formal means to define an isocurvature setting is given by $\tilde{\Phi} \rightarrow 0$ while $t \rightarrow 0$ [MFB92]. Here $\tilde{\Phi}$ is the gauge invariant version of the metric perturbation in (1.92). The gauge invariant Bardeen potentials $\tilde{\Phi}$ and $\tilde{\Psi}$ are constructed from (1.92) as follows

$$(3.29) \quad \tilde{\Phi} \equiv \Phi + \frac{1}{a}[(B - E_{,\eta})a]_{,\eta} \quad , \quad \tilde{\Psi} \equiv \Psi - \frac{a_{,\eta}}{a}(B - E_{,\eta}),$$

where η denotes conformal time as usual. An example of an isocurvature setting would be to initially distribute different species – like baryons and photons – inhomogeneously but adjust the total energy density in a homogeneous way. As it is pointed out in [MFB92], isocurvature modes are predicted by some axion models, models with topological defects (e.g. cosmic strings) or some exotic inflationary models. Experimentally, isocurvature modes cannot be excluded fully, but stringent bounds on such admixtures can be given, especially concerning the cross-correlation of CMB and large-scale structure, as well as from the CMB alone, as is shown in [KS07] or [Tro07]. However, we will omit this component in our discussion.

Including these sources of anisotropy, the three-dimensional temperature power spectrum is given by [Pea99]

$$(3.30) \quad \mathcal{T}_{3D}^2 = \left[(f_{AS} + f_{SW})^2(k) + f_{DV}^2(k)(\hat{\mathbf{k}} \cdot \hat{\mathbf{r}})^2 \right] \Delta_k^2(z_{\text{rec}}),$$

with the dimensionless factors f parameterising the different sources as

$$(3.31) \quad f_{SW} \equiv -\frac{2}{(kD_{\text{H}}^{\text{rec}})^2}, \quad f_{DV} \equiv \frac{2}{kD_{\text{H}}^{\text{rec}}}, \quad f_{AS} \equiv \frac{1}{3}.$$

Here $D_{\text{H}}^{\text{rec}}$ denotes the Hubble horizon scale at last scattering

$$(3.32) \quad D_{\text{H}}^{\text{rec}} \equiv \frac{2c}{\Omega_{\text{m}}^{1/2} H_0} (1 + z_{\text{rec}})^{-1/2} \simeq 184(\Omega h^2)^{-1/2} \text{Mpc}.$$

Equation (3.30) provides the final answer to the question of this subsection. It relates the three-dimensional temperature power spectrum to the three-dimensional matter power spectrum. The two-dimensional temperature power spectrum is connected to the three-dimensional one via the projection (3.23). The analysis is done in Fourier space. The three basic sources of CMB anisotropy we considered here become significant on different scales. Since the comoving Hubble scale amounts roughly to $\sim 300 \text{Mpc}$ at last scattering, we can learn from (3.30) that the Sachs-Wolfe term is vital at wavelengths larger than $\sim 300 \text{Mpc}$. Going to smaller scales, first the Doppler term becomes dominant, and eventually the adiabatic fluctuations take over at small scales.

3.3.2. The CMB Angular Power Spectrum. The preceding formalism relies on the assumption of flatness; both flatness of the three-space of the Universe and flatness of the considered patches of the CMB. For several reasons, the simplified treatment breaks down, as being too naïve, both on the smallest and the largest CMB scales. Here, we want to shortly review the modern standard toolkit for an adequate statistical comparison of CMB measurements with theory, following [Lon98] and [CHSS07].

The information we receive in form of CMB photons from the epoch of decoupling, is a temperature field distributed on the inner surface of our last scattering sphere. From quantum mechanics, it is known that the appropriate machinery for expanding physical functions that live on a sphere is provided by the analysis of spherical harmonics. The spherical harmonics provide the correct basis in which we can attempt to expand temperature anisotropy recorded over the whole CMB sky. We can write

$$(3.33) \quad \frac{\Delta T}{T}(\theta, \phi) = \sum_{\ell=0}^{\infty} \sum_{m=-\ell}^{m=\ell} a_{\ell m} Y_{\ell m}(\theta, \phi),$$

with expansion coefficients $a_{\ell m}$, containing all the physics, and the spherical harmonics $Y_{\ell m}(\theta, \phi)$. For the latter, we note the following normalisation involving the associated Legendre polynomials

$$(3.34) \quad Y_{\ell m}(\theta, \phi) = \left[\frac{2\ell + 1}{4\pi} \frac{(\ell - |m|)!}{(\ell + |m|)!} \right]^{1/2} P_{\ell m}(\cos\theta) e^{im\phi} \times \begin{cases} (-1)^m & \text{for } m \geq 0 \\ 1 & \text{for } m < 0 \end{cases}.$$

The (associated) Legendre polynomials can be found tabulated, for instance in [AS72]. According to this normalisation, the spherical harmonics are a set of orthonormal basis elements with

$$(3.35) \quad \int Y_{\ell m}^* Y_{\ell' m'} d\Omega = \delta_{\ell\ell'} \delta_{mm'},$$

where the $\delta_{\ell m}$ is just the Kronecker delta and $d\Omega$ stands for the full element of solid angle. Hence it is possible to reconstruct the coefficients $a_{\ell m}$ by inversion,

$$(3.36) \quad a_{\ell m} = \int \frac{\Delta T}{T}(\theta, \phi) Y_{\ell m}^* d\Omega.$$

It is very useful to understand how the multipole power in a spherical harmonic of multipole ℓ relates to the according portion of angular power at a scale θ . Longair [Lon98] argues that the roots of $\text{Re}(Y_{\ell m})$ and $\text{Im}(Y_{\ell m})$ provide a lattice structure on the sky that divides the field into approximately rectangular patches. When looking at that sky from low latitude (θ), the minimal sides of the patches are well approximated by π/ℓ . On the other hand, when departing from low latitude – moving to the poles – the roots of the azimuthal parts $\sin m\phi$ and $\cos m\phi$ cluster more and more close to each other. But this is compensated by the associated Legendre Polynomials, since they approach zero in these regions. Together, this leads to the remarkable fact that to every spherical harmonic a unique angular resolution can be attributed

$$(3.37) \quad \theta \simeq \frac{\pi}{\ell}.$$

Now we come to the issue of Gaussianity. We discussed above, that the standard inflationary model predicts fluctuations that are – among other requirements – purely Gaussian. This is because, in the inflationary view, the initial perturbations in the density of the early Universe are provided by pure quantum fluctuations which are frozen out. With Gaussianity, it is meant that the phases of the waves that constitute the harmonic decomposition (3.33), are purely random. The assumption of Gaussianity leads to a couple of appealing simplifications. Nevertheless, there are models that predict non-Gaussian features in the CMB. Such are for instance models with topological defects like cosmic strings or cosmic textures as well as complicated inflation models.

Assuming Gaussianity of the CMB fluctuations implies that fluctuations are superimposed from waves with random phases. Therefore *each* of the expansion coefficients in (3.33) provides an estimate of the amplitude contained in the considered fluctuation mode. Because there are $(2\ell + 1)$ coefficients $a_{\ell m}$ per multipole ℓ , one obtains an ensemble of amplitude estimates over which we can simply average, if we further assume the *statistical isotropy* of the temperature anisotropy field. Statistical isotropy implies that the power spectrum is circular symmetric around any point on the sky and consequently we can construct a well-defined estimator for the power of a multipole by taking the mean of $a_{\ell m} a_{\ell m}^*$ and performing an all-sky average,

$$(3.38) \quad C_\ell = \frac{1}{2\ell + 1} \sum_m a_{\ell m} a_{\ell m}^*.$$

The bulk of current CMB analyses is well consistent with Gaussian temperature anisotropies; the quantities that are found suitable for probing non-Gaussianity, as predicted by some non-standard models, are the bispectrum (three-point correlation function of the $a_{\ell m}$), trispectrum, analyses of the Minkowski functionals as well as other machinery, see e.g. [S⁺07, C⁺06b] as some representative studies. From the side of model-building, non-Gaussian features appear rather naturally in the predictions of more involved models, like multi-field inflation. It is speculated that non-Gaussianity may be detectable with future experiments that reach higher accuracy. The according theoretical tools for analysis do exist already, see e.g. [FS07]. However, it should be noted that there are studies that claim to have detected departure from Gaussianity [BTV07]. Moreover, we note that – only in case of statistical isotropy of the microwave sky – we can write the ensemble average over the product of spherical harmonic coefficients as [CHSS07]

$$(3.39) \quad \langle a_{\ell m}^* a_{\ell' m'} \rangle = C_\ell \delta_{\ell\ell'} \delta_{mm'}.$$

As for the point with statistical isotropy, the whole next two chapters of this thesis will be concerned with the analysis of existing evidence – the so called low- ℓ CMB anomalies – indicating violation of statistical isotropy on the largest angular scales in the CMB.

Let us proceed further with the standard statistical framework of temperature anisotropies. The approach we pursued above was to first define the angular power spectrum of fluctuations (3.38), which represents, in case of Gaussianity and statistical isotropy, a *complete* statistical description of CMB anisotropy [Lon98]. An equivalent approach is to start with the definition

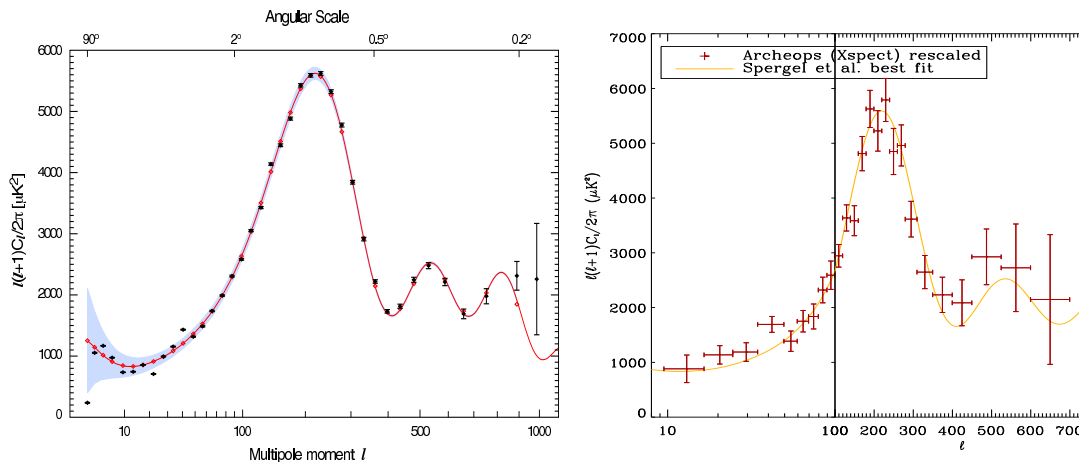


FIGURE 3.5. The temperature power spectrum of the CMB (3.38) against angular scale from two different experiments. Left: the binend measurement of the angular power spectrum from three years of WMAP data. The red curve is the Λ CDM best fit and the bluish region indicates cosmic variance. Right: power spectrum from ARCHEOPS, a balloon borne experiment that took data at around 40km in altitude. The data points have been rescaled ($\times 1.07$) for comparison with the WMAP(1yr) standard model fit. We choose to show the ARCHEOPS data because of its different systematics; also, by comparing the error bars, one gets a feeling for the high quality of the WMAP data. The angular power spectrum is the main observable from the CMB; it is very sensitive to the parameters of the cosmological model one compares with. Figures are taken from [WMAa] and [T⁺05].

of the *two-point correlation function* or *autocorrelation function*,

$$(3.40) \quad C(\theta) = \left\langle \frac{\Delta T}{T}(\hat{e}_1) \frac{\Delta T}{T}(\hat{e}_2) \right\rangle.$$

Here, \hat{e}_i are unit vectors and $\langle \cdot \rangle$ denotes an ensemble average performed over *all* pairs of directions that have an angular separation of θ . Making use of the addition theorem for the spherical harmonics

$$(3.41) \quad \sum_{\ell, m} Y_{\ell m}^*(\hat{e}_1) Y_{\ell m}(\hat{e}_2) = \sum_{\ell} \frac{2\ell + 1}{4\pi} P_{\ell}(\cos\theta),$$

introducing the Legendre polynomials $P_{\ell}(\cos\theta)$, we find that the autocorrelation function can be written as an Legendre expansion in terms of the *angular power spectrum*

$$(3.42) \quad C(\theta) = \frac{1}{4\pi} \sum_{\ell} (2\ell + 1) C_{\ell} P_{\ell}(\cos\theta).$$

Conversely, we can write the angular power spectrum in terms of the two-point function

$$(3.43) \quad C_{\ell} = 2\pi \int_{-1}^1 C(\theta) P_{\ell}(\cos\theta) d\cos\theta.$$

Usually, it is said [Lon98] that it is a matter of taste whether to use the two-point function (3.40) or the angular power spectrum (3.38) for analysis. Although the angular power spectrum is the most popular way of presenting the CMB results in the literature, we will see in chap. 5 that, when trying to detect potential deviations from statistical isotropy, an analysis of the autocorrelation function may provide additional insights. Moreover, it is outlined in [CHSS07] that, in the case of statistical anisotropy, both $C(\theta)$ and C_{ℓ} turn to be inappropriate concepts for a proper statistical description of temperature anisotropies measured. More complicated statistics – undemanding with respect to statistical isotropy – are then torpedoed by the fact

that we can only observe one single realisation of the CMB, namely our sky. We proceed with a discussion of measurement of the power spectrum and their relation to the standard model.

The measurement of the angular power spectrum allows precision tests of the standard model of cosmology. We show the measured as well as the best fit angular power spectra of two experiments, WMAP and the balloon borne experiment ARCHEOPS, in fig. 3.5. The CMB angular power spectrum can be roughly divided into three regions in angular scale: (a) for $\ell \lesssim 100$ the spectrum is flat (Sachs-Wolfe plateau) and the Sachs-Wolfe effect is dominant, a result we already anticipated in the course of the Fourier analysis in sec. 3.3.1, represented by equation (3.31); within $100 \lesssim \ell \lesssim 2000$ one clearly sees the acoustic oscillations of the primordial plasma ball; at small angular scales $\ell \gtrsim 2000$ the Silk damping makes the curve decrease steeply. The power spectrum is very sensitive to the density parameters of the cosmological model. A change in curvature, i.e. in the total density parameter Ω , strongly affects the power spectrum on all three scale regions. Tuning of the cosmological constant – at a fixed curvature parameter – only affects the large scales; this is because in the standard model it is believed that the integrated Sachs-Wolfe effect vanishes when Λ is zero. A change in baryon or matter density will shift the amplitudes as well as the positions of the acoustic peaks.

Let us note some technical points. In the plots for the angular power spectrum fig. 3.5, there is a quantity $\propto \ell(\ell+1)C_\ell$ on the y -axis. This rises the question of the normalisation of the power spectrum. One can work out [Lon98] the angular power spectrum that results from a general power law input for the density power spectrum $P(k) = Ak^n$, c.f. equation (1.29),

$$(3.44) \quad C_\ell \propto A 2^n \pi^2 \frac{\Gamma(3-n)\Gamma(\ell + \frac{n-1}{2})}{\Gamma^2(\frac{4-n}{2})\Gamma(\ell + \frac{5-n}{2})},$$

where we neglect the transfer function for the moment, for clarity. Here Γ denotes the common gamma function. Now, when we plug in the condition for a Harrison-Zel'dovich spectrum ($n = 1$) – which is suggested by many models – we get

$$(3.45) \quad C_\ell \propto \frac{A}{\ell(\ell+1)},$$

and so in the combination $\ell(\ell+1)C_\ell$ the angular dependence is cancelled out. Another point is that of the *cosmic variance* which is plotted as the blue region in the WMAP angular power spectrum in fig. 3.5. From the figure it appears that this uncertainty becomes most important for the largest angular scales. This can be understood by the following consideration. Each measurement of C_ℓ is distributed like a χ^2 having $(2\ell+1)$ degrees of freedom respectively. Therefore at largest angular scales one has only very few independent estimates of a sample of C_ℓ . Let N be the number of independent estimates of C_ℓ then the precision of the measured value for C_ℓ is limited by $N^{-1/2}$. Thus we can write the cosmic variance as

$$(3.46) \quad \sigma_{\text{CV}}^2 = \frac{2}{2\ell+1} C_\ell.$$

What is actually measured by an differential CMB experiment like WMAP, is a time-ordered data stream of the coefficients $a_{\ell m}$. Because the CMB signal we observe is an admixture of cosmological contributions and various effects that photons undergo on the line of sight – like scattering off foreground sources and many others – there are a lot of complicated cleaning algorithms applied to the raw data, see [H⁺07, J⁺07a] for details. For instance, the strong dipole signal, whose origin is thought of being due to our superimposed peculiar motion with respect to the CMB rest frame, has to be subtracted. See fig. 3.4 for a map of the WMAP dipole signal. After the application of various filtering methods the primordial CMB anisotropies can be made visible at good accuracy, see fig. 3.3. This picture is a result of the superposition of many higher multipoles. Let us finally note the main characteristics of the lowest multipoles (largest angular scales):

- The octopole ($\ell = 3$) – As computed from the three-year WMAP ILC map using a Maximum Likelihood Estimate (MLE), the octopole amounts to $(\Delta T/T)_3 \simeq 32.4\mu\text{K}$; the errors are largely cosmic variance dominated and can be found in [H⁺07].
- The quadrupole ($\ell = 2$) – According to one-year WMAP data, the quadrupole as extracted from the ILC map amounts to $(\Delta T/T)_2 \simeq 14\mu\text{K}$, with errors found in [H⁺03]. According to three-year data, the quadrupole amounts to $(\Delta T/T)_2 \simeq 15.4\mu\text{K}$. The increase from one to three-year data is mainly do to a new ILC bias correction; for details and errors see [H⁺07]. Our motion with respect to the CMB rest frame does not only affect the dipole, but also the quadrupole. The effect is of second order in $\beta \equiv v/c \sim 10^{-3}$ and gives rise to a kinetic quadrupole correction of around $1.2\mu\text{K}$.
- The dipole ($\ell = 1$) – The dipole signal is the strongest anisotropic CMB signal. Its amplitude is measured by WMAP(3yr) as $(\Delta T/T)_1 \simeq (3.358 \pm 0.017)\text{mK}$. It is interpreted as the result of the observer’s motion with respect to the CMB last scattering surface. The resulting velocity vector points to $(l \simeq 263.86^\circ \pm 0.04^\circ, b \simeq 48.24^\circ \pm 0.10^\circ)$ in galactic coordinates. As a reference we quote here the preprint of [H⁺07]. For a Mollweide map of the COBE dipole see fig. 3.4.
- The monopole ($\ell = 0$) – The monopole is not a temperature anisotropy and is thus not accessible to differential measurements like the WMAP. Therefore the best current value of the monopole background temperature comes from the FIRAS instrument of the COBE satellite, being $T_0 \simeq (2.725 \pm 0.001)\text{K}$. The spectrum of the monopole radiation follows almost perfectly that of a black body radiator, c.f. fig. 3.2.

Extrinsic Alignments in the CMB

Although the cosmological standard model is in good accordance with the data, there have been found a couple of issues concerning the CMB that cannot be explained by the standard Λ CDM paradigm. In particular, the microwave sky shows unexpected features at the largest angular scales, and among them are strange alignments of the dipole, quadrupole and octopole. Here, we pursue the idea that processes of structure formation could be responsible for the large-scale anomalies via a local Rees-Sciama effect. The application of this mechanism to the CMB anomalies is a novel idea, for usually only the (linear) integrated Sachs-Wolfe effect is taken into account in the course of standard model CMB analysis. Motivated by recent X-ray cluster studies, we investigate the possibility that local structures at the $100h^{-1}\text{Mpc}$ scale could be responsible for the observed correlations. These structures give rise to a local Rees-Sciama contribution to the microwave sky that may amount to $\Delta T/T \sim 10^{-5}$ at the largest angular scales. We model the local structure by a spherical overdensity (Lemaître-Tolman-Bondi model) and assume that the Local Group is falling toward the centre. We superimpose the local Rees-Sciama effect on a statistically isotropic, gaussian sky. Indeed, we find alignments among the low multipoles, but a closer look reveals that they do not agree with the type of correlations revealed by the WMAP data.

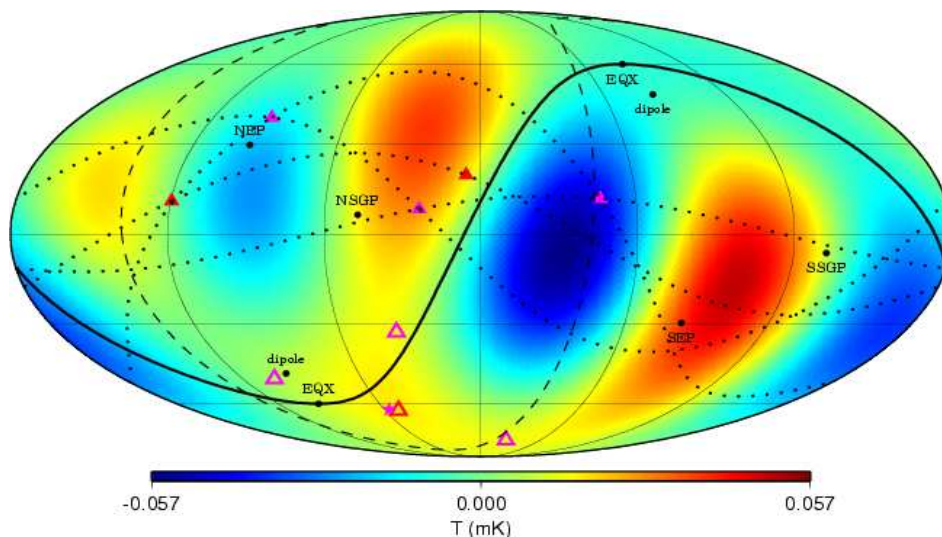


FIGURE 4.1. A Mollweide projection of the superimposed ($\ell = 2 + 3$) map from WMAP(3yr) ILC. The quadrupole vectors are shown as solid red triangles and the octopole vectors are plotted as solid magenta triangles. The according normal vectors (cross products) are shown as open triangles with the respective colour. The solid line indicates the ecliptic, the dashed line is the supergalactic plane and the dotted lines are the great circles connecting multipole vectors. The magenta star indicates the direction of maximal angular momentum dispersion for $\ell = 3$. One sees e.g. that the multipole normals are aligned with the ecliptic, or that the ecliptic plane carefully follows a zero of the temperature map. The various found alignments are described in the text, their significance is given in tab. 4.1. The figure is taken from [CHSS07].

TABLE 4.1. The significance of alignments of quadrupole and octopole with given directions as compared to WMAP(1yr) (upper row) and WMAP(3yr) (lower row), c.f. [CHSS06] and [CHSS07]. The comparison is made with respect to a sample of 10^5 fiducial standard model Monte Carlos respectively. The values have been obtained by comparison to different foreground-cleaned maps, like the ILC and others, and the most conservative figure is always quoted. Except for the case with the ecliptic, the anomalous alignments remain unchanged from one-year to three-year data. The alignment with the supergalactic plane remains in any way inconclusive.

dipole	ecliptic	galactic poles	equinox	supergalactic	$\ell = 2$ with $\ell = 3$
> 99.7 C.L.	> 98 C.L.	> 99 C.L.	> 99.8 C.L.	> 85 C.L.	99.4 – 99.6 C.L.
> 99.7 C.L.	> 96 C.L.	> 99 C.L.	> 99.8 C.L.	> 85 C.L.	99.6 C.L.

4.1. The Alignment Anomalies

The microwave sky has presented some surprises at the largest angular scales. The Wilkinson Microwave Anisotropy Probe confirmed the vanishing of the angular two-point correlation function above 60° [B⁺03b], a result first obtained by the Cosmic Background Explorer’s Differential Microwave Radiometer (COBE-DMR) experiment [HBB⁺96], and not expected within the standard model. In terms of the angular power spectrum this implies that the quadrupole and octopole are below the theoretical expectation. We will analyse and discuss the issue of the anomalous lack of two-point angular correlation in more detail in **CHAP**.

Moreover, the analysis of foreground-cleaned full-sky maps [B⁺03a, TdOCH03, EBGL04] has revealed further surprises. There are a couple of surprising anomalies concerning the phases the low multipoles. It was pointed out by [dOCTZH04] that the octopole seems to be planar – all minima and maxima are close to a great circle on the sky – and the planes of the octopole and the quadrupole are closely aligned. Eriksen et al. [EHB⁺04] showed that the northern galactic hemisphere lacks power compared with the southern hemisphere.

In order to be able to make distinct statements with respect to a phase analysis of multipoles we make use of the *multipole vector formalism* [CHS04]. With the help of the multipole vectors we achieve a demixing of the directional (phase) information and the amplitude of a multipole, as compared to the classical approach via spherical harmonics. By means of multipole vectors, Schwarz et al. [SSH04] showed that the quadrupole and octopole are correlated with each other as well as with the orientation and motion of the Solar system. The latter is highly surprising because the CMB signal is of cosmological origin. In particular, the four cross products of the quadrupole and octopole vectors are unexpectedly close to the ecliptic [$> 98\%$ Confidence Level (C.L.)] as well as to the equinox and microwave dipole (both $> 99.7\%$ C.L.) with respect to an analysis of one-year WMAP data [CHSS06]. Moreover, from the combined full sky map of $\ell = 2 + 3$ one infers that the octopole is quite planar and that the ecliptic strongly follows a zero line of the map, leaving the two strongest extrema in the southern hemisphere and the two weakest in the northern hemisphere, see fig. 4.1. Based on the additional alignment of a nodal line with the ecliptic and the ecliptic north-south asymmetry of the quadrupole plus octopole map, Copi et al. [CHSS06] argued that the correlation with the ecliptic is unlikely at the $> 99.9\%$ C.L. The significances of the above alignments are summarised in tab. 4.1; we see that the significance of the anomalies stays the same with respect to one-year and three-year WMAP data – with the exception of the ecliptic alignment. In this chapter we will be interested mainly in the alignments of quadrupole and octopole with external astrophysical directions, henceforth *extrinsic alignments*.

The apparent correlation with the Solar system is not understood by now. It is possible that some yet unknown dust cloud or other absorbing object in our vicinity disturbs the cosmological CMB signal. In fact, Dikarev et al. [DPS⁺07] recently studied the influence of known dust objects in our vicinity on the CMB anomalies and could exclude such an explanation of the

phenomenon. In contrast to an unknown Solar system effect, it also seems possible that the large-scale anomalies are due to a physical correlation with the dipole, in which case the correlation with the ecliptic and the equinox would be due to the accidental closeness of the dipole and the equinox.

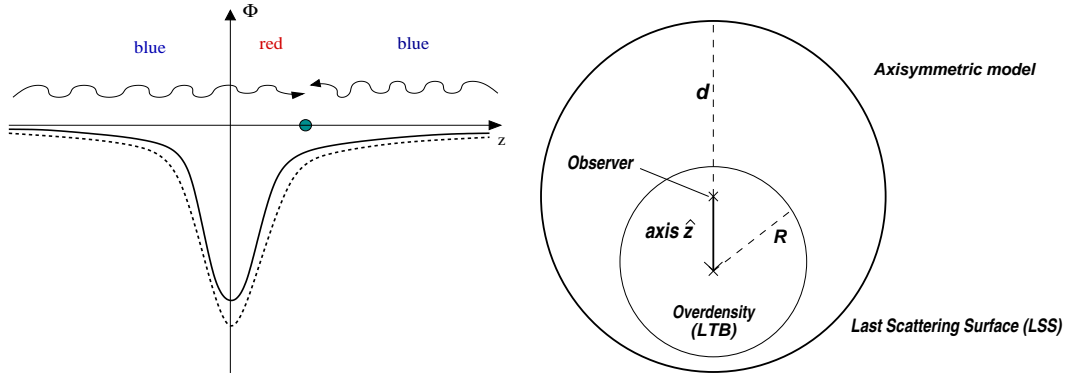


FIGURE 4.2. Left: a sketch of the Rees-Sciama effect from an overdensity that is still forming. Consider a photon crossing such a vast supercluster. If its traversing time is, at least, of the order of the evolution time scale of the supercluster, then the photon does not gain exactly the same energy when falling downhill in the potential as it loses when escaping from it; there will be a net effect in redshift for the photon in the end. Also it is possible that the cluster itself, or the bulk of (dark) matter in the cluster, shows a significant motion across the line of sight, which also produces a time-varying gravitational potential along the photon's path. This effect is called the moving cluster of galaxies effect or moving halo effect, c.f. [BG83], [TL95]. Right: a schematic depiction of the geometry of our model. The local overdensity is modelled by an LTB solution. We are located off-centre in this setup and since the structure is evolving, due to the Rees-Sciama effect, there will be additional CMB anisotropy.

4.2. Local Rees-Sciama Effect

The Rees-Sciama effect belongs to the class of secondary CMB anisotropies discussed in sec. 3.1. It originates from the fact that the CMB photons can pass through vast processes of structure growth on their way to the observer. Considering a static gravitational potential, the net effect on CMB photons passing through it would be zero. This is, because the energy that photons gain by their infall into the structure's potential is exactly compensated when they escape from it. But in the case of an evolving gravitational potential the net effect is non-zero, if the photon's traversing time is at least of comparable duration as the overall evolving time of the gravitational potential. This is actually the case for vast extragalactic superclusters that are in the non-linear regime of evolution. This effect applied to evolving voids produces a net blueshift, and when applied to still-forming overdensities it yields a net redshift. Occurring within the regime of *linear structure growth* this effect known as the *integrated Sachs-Wolfe effect* and when occurring in the epoch of *non-linear structure formation* it is called *the Rees-Sciama effect*. See fig. 4.2 for an crude illustration. In sec. 1.3.3 we have derived the mathematical machinery of the Rees-Sciama effect, which formally comes out from the integrated Sachs-Wolfe formula. In this chapter we are going to make use of these results and apply further analysis.

Here we will explore the possibility that the effect of local non-linear structures on the CMB, the local Rees-Sciama effect [RS68], could induce a correlation between the dipole and higher multipoles. In the non-linear regime of structure formation the gravitational potential changes with time, and photons climb out of a potential well slightly different from the one they fell into. As the CMB dipole is considered to be due to our motion with respect to the CMB rest frame, and this motion is due to the gravitational pull of local structures, these structures

TABLE 4.2. Directions of local motion with respect to the CMB rest frame. The estimated error for the corrected local group’s direction of [PK98](PK) is 14° , and is 5% for their velocities.

Direction	Galactic coordinates	v [km/s]
WMAP(1yr) dipole velocity [B ⁺ 03b]	$l = 263^\circ 85 \pm 0^\circ 10$ $b = 48^\circ 25 \pm 0^\circ 04$	(368±2)
local group velocity [KLS ⁺ 93]	$l = 276^\circ \pm 3^\circ$ $b = 30^\circ \pm 3^\circ$	(627±22)
Virgo infall of local group [PK98]	$l = 283^\circ 92$ $b = 74^\circ 51$	170
Virgo corrected local group velocity [PK98]	$l = 276^\circ$ $b = 16^\circ$	510
Shapley concentration [ETJ ⁺ 97]	$l = 306^\circ 44$ $b = 29^\circ 71$	-

are a natural candidate for contributions to the higher multipoles correlated with the dipole. For earlier work on connection of local structures with the low-multipole anomalies, see for instance [Tom05a, Val05, Tom05b, CS05, Man05]. The Rees-Sciama effect of distant clusters was estimated to be at most 10^{-6} in a matter-dominated Universe by Seljak [Sel96], one order of magnitude below the intrinsic CMB anisotropy. The effect of local large structures has been estimated to be at most 10^{-6} using the Swiss Cheese model [MS90] and, more reliably, using the LTB model, which is the general spherically symmetric dust solution of the Einstein equation [Pan92, AFMS93, FSA94]. For an overview and further references we recommend [Kra97].

At the time these studies were made, it was generally thought that the dipole is mostly due to the infall of the local group of galaxies towards the Great Attractor [LFB⁺88, Dre88], a density concentration located $40\text{-}60h^{-1}\text{Mpc}$ from us, with a subdominant component due to the nearby Virgo cluster, about $10h^{-1}\text{Mpc}$ away. Recent observations of X-ray clusters suggest instead that there is a major contribution to the dipole from the Shapley supercluster and other density concentrations at a distance of around $130\text{-}180h^{-1}\text{Mpc}$ [KME04, HSLB04, LRSH04, KE06]. The Shapley supercluster, c.f. fig. 4.2, is a massive concentration centred around the object A3558. It alone has a density contrast of ≈ 5 over a $30h^{-1}\text{Mpc}$ region [PQC⁺06], which is 2-3 times the size of the core (of similar density) in the Great Attractor models.

The further away and the more extended the source is, the bigger is the impact on the quadrupole and octopole – for a fixed effect on the dipole – so it is plausible that the Shapley concentration would induce anisotropies at the 10^{-5} level. This would be consistent with the early estimate for an Shapley Supercluster-like object in [MS90] and the approximate scaling suggested by Panek [Pan92], which we discuss next.

The CMB anisotropy produced by a spherical superstructure can be estimated by the integral of the gravitational potential perturbation $\phi \simeq \delta M/d$ along the path of the photon, that is

$$(4.1) \quad \left(\frac{\Delta T(\theta, \varphi)}{T} \right)_{\text{RS}} \simeq \phi v_c,$$

where d is the physical size of the structure, δM is the mass excess and v_c the evolution velocity. Since we are interested in an overdensity we take a collapsing structure. Further following Panek [Pan92], we approximate the evolution time of the structure t_c by the matter crossing time d/v_c , note $c = 1 = G$. Moreover, we estimate the typical collapse velocity from the energy balance

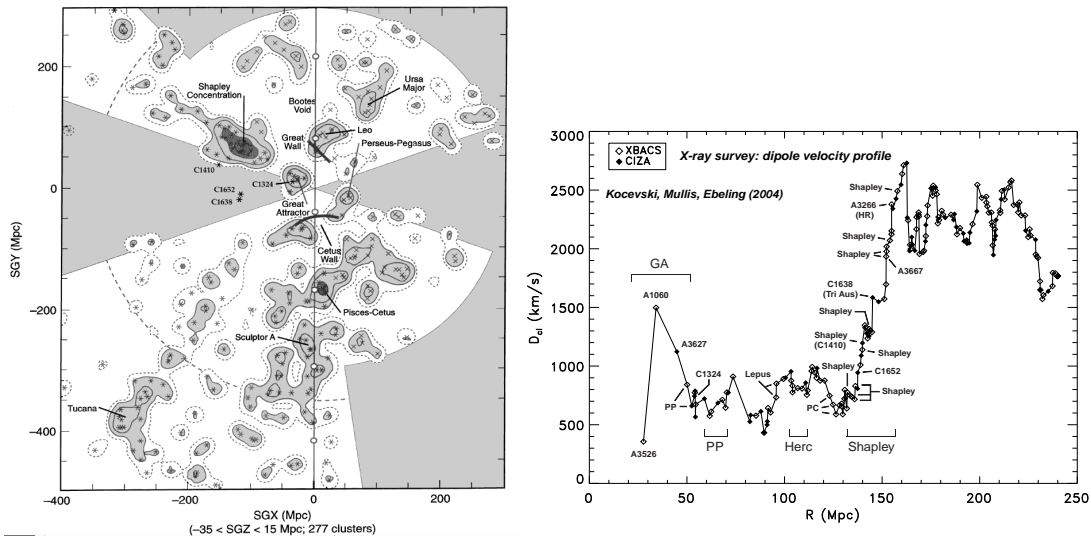


FIGURE 4.3. Left: A projection of the intermediate-scale structure in our neighbourhood to the supergalactic $x - y$ plane. The contours indicate density according to $(1, 3, 0.5) \times 10^{-3}$ clusters Mpc^{-2} respectively. The Shapley concentration represents the most massive structure in the shown distance range. One can clearly see the zone of avoidance, from which optical data cannot be taken. Right: dipole profile as derived from recent X-ray galaxy surveys. The Shapley supercluster dominantly contributes to the dipole between $\sim 100\text{Mpc}$ and $\sim 200\text{Mpc}$. The pictures are taken from [TSVZ92] and [KME04].

condition and have $v_c^2 \simeq \phi$, which leads us to

$$(4.2) \quad \left(\frac{\Delta T(\theta, \varphi)}{T} \right)_{\text{RS}} \sim \phi^{3/2} \sim \left(\frac{\delta M}{d} \right)^{3/2}.$$

We are going to model the non-linear structure by a spherically symmetric LTB model embedded in a flat ($\Omega = 1$) Friedmann-Robertson-Walker Universe. Substituting the expression for the mass excess within this model [Pan92] we obtain the *Panek scaling*

$$(4.3) \quad \left(\frac{\Delta T(\theta, \varphi)}{T} \right)_{\text{RS}} \sim \left(\frac{\delta \rho}{\rho} \right)^{3/2} \left(\frac{d}{t} \right)^3.$$

We repeat, t is the cosmic time at which the CMB photons crossed the structure, d is its physical size and $\delta \rho / \rho$ its density contrast. Inserting the characteristics of the Shapley supercluster, we see that indeed a CMB anisotropy of 10^{-5} due to a local Rees-Sciama effect is reasonable.

For a large angular scale of the source – local and nearby structures – this induces contributions to the low- ℓ multipoles, especially the dipole, quadrupole and octopole. This, in turn, could include a non-Doppler contribution to the dipole. This would imply a change of a few percent in the inferred dipole velocity, which might also explain some of the CMB anomalies [FGM⁺06]. The Shapley concentration is a non-linear structure, and the amplitude of the induced anisotropies cannot be reliably calculated in linear perturbation theory. According to a comparison of linear and exact calculations for Great Attractor-like objects with the LTB model in [FSA94], linear theory is reliable at distances comparable to the Hubble scale, but fails for structures within $1000h^{-1}\text{Mpc}$ or so.

The advantage of the spherical symmetry of the LTB model is that it allows exact calculations for non-linear objects; the drawback is that the observed non-linear objects such as the Great Attractor and the Shapley concentration do not appear to be spherically symmetric. However, we can expect the result to be correct within an order of magnitude, and the core of

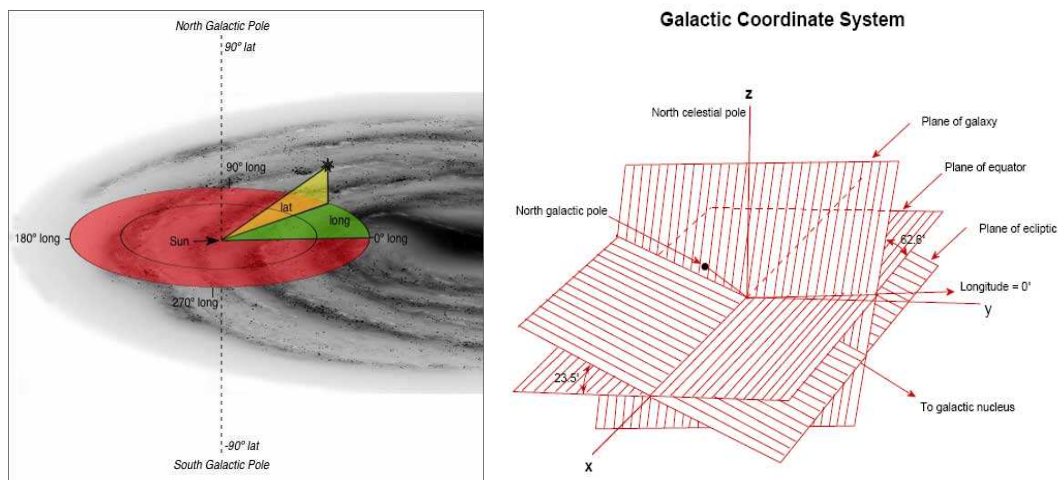


FIGURE 4.5. Left: the galactic coordinate system. The galactic coordinate system is defined as being parallel with the plane of the Milky Way and centred on the sun. So the equator in galactic coordinates (red circle, 0° galactic latitude) lies in the plane of our galaxy. The galactic latitude b is the angle above or below this plane (yellow angle) and the galactic longitude l (green angle) is measured from 0° to 360° , counter clockwise with respect to the north galactic pole. 0° of galactic longitude is arbitrarily defined as the direction pointing to the galactic centre (Sagittarius). Sometimes, in astronomy the equatorial coordinate system is used. Right: the relation of the galactic coordinate system to the equatorial coordinate system. The latter is defined through the plane of the Earth's equator. Important reference directions on the sky that we use here are, in galactic coordinates: the north ecliptic pole $(l, b) \simeq (96.4^\circ, 29.8^\circ)$, the equinox $(l, b) \simeq (276.3^\circ, 60.2^\circ)$ and the north galactic pole $(l, b) = (0^\circ, 90^\circ)$. Pictures are taken from [Ast] and [Org].

CMB. Second, the environment will affect the evolution of the intrinsic anisotropies – as the homogeneous background space does, by changing the angular diameter distance. The complete calculation taking into account both of these effects would be to study the evolution of the CMB anisotropies as they travel across the density field using perturbation theory on the LTB background. As in earlier treatments, we neglect the second effect and simply add the anisotropy generated by the LTB model on top of the intrinsic contribution. It is possible that this treatment misses some effects of processing the anisotropies already present. In particular, simply linearly adding a new source of anisotropy will in general add multipole power, not reduce it, while a proper analysis of the processing of the intrinsic anisotropies could lead to a multiplicative modification of the amplitudes of the low multipoles, as mentioned in [GHHC05].

It has been suggested that spherically symmetric inhomogeneities of the order of horizon size or larger would contribute to the low CMB multipoles [DZS78, RT81, PP90, LP96]; it was claimed in [Mof05] that this could explain the observed preferred axis. Leaving aside the issue that assuming spherical symmetry for the entire Universe seems questionable, the observational signature on the low multipoles is identical to that from the LTB model used to describe local structures, possibly apart from the amplitude.

4.3. Angular Power Analysis

First we address the question how the cosmic microwave sky is affected by the local Rees-Sciama effect. We are going to study how maps of the CMB are affected by the anisotropy induced by additional axisymmetric contributions $a_{\ell 0}^{\text{axial}}$ on the largest angular scales by using Monte Carlo methods.

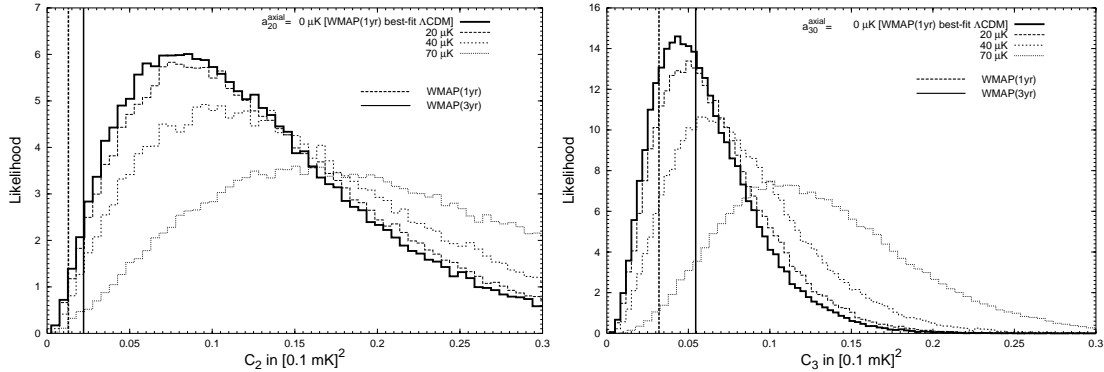


FIGURE 4.6. Likelihood of quadrupole and octopole power for increased axial contributions. Vertical lines denote experimental data: WMAP(1yr) cut-sky and WMAP(3yr) maximum likelihood estimate. Considering the quadrupole adding *any* multipole power was excluded at $> 99\%$ C.L. with respect to WMAP(1yr) but it is possible to add up to $60\mu\text{K}$ within the same exclusion level with respect to the WMAP(3yr) value. Adding $80\mu\text{K}$ ($100\mu\text{K}$) to the quadrupole leads to an exclusion of 99.7% C.L. (99.9% C.L.). The octopole is more resistant against axial contaminations as it is possible to add a whole $100\mu\text{K}$ before reaching the same exclusion level with respect to the updated WMAP data.

We saw in sec. 3.3.2 that the angular power spectrum in terms of the coefficients $a_{\ell m}$ can be expressed as

$$(4.4) \quad C_\ell = \frac{1}{2\ell + 1} \sum_{m=-\ell}^{\ell} |a_{\ell m}|^2.$$

As predicted by the standard perception of inflationary cosmology, the primordial perturbations are believed to follow a gaussian statistic. Deviations from this would be hard to reconcile with the standard inflationary paradigm. Therefore, the complex coefficients $a_{\ell m} = a_{\ell m}^{\text{Re}} + i a_{\ell m}^{\text{Im}}$ are expected to be gaussianly distributed with zero mean and variance given by the angular power C_ℓ , according to

$$(4.5) \quad f(a_{\ell 0}) = \frac{1}{\sqrt{2\pi C_\ell}} \exp\left(-\frac{(a_{\ell 0}^{\text{Re}})^2}{2C_\ell}\right) \quad \text{and} \quad f(a_{\ell m}^{\text{Re,Im}}) = \frac{1}{\sqrt{\pi C_\ell}} \exp\left(-\frac{(a_{\ell m}^{\text{Re,Im}})^2}{C_\ell}\right).$$

Therefore, in the standard model, the coefficients $a_{\ell m}$ are fully characterised by their angular power, for which we use the values from the best fit ΛCDM temperature spectrum to the WMAP data. In our axisymmetric model, we parameterise the effect of a local structure by adding axial contributions $a_{\ell 0}^{\text{axial}}$ to the quadrupole and octopole. It is obvious that the additive mechanism cannot make the power deficit anomaly disappear. For the statistical analysis we generate 10^5 Monte Carlo realisations of the quadrupole and the octopole. In the following we describe the results of our Monte Carlo analysis for the angular power (4.4) with respect to one-year as well as three-year WMAP data.

4.3.1. WMAP(1yr) Angular Power. Considering one-year data, the values of C_2 and C_3 determined from the WMAP cut-sky [H⁺03], the so called TOH map [TdOCH03], the Lagrange ILC map [EBGL04] and the ILC map [B⁺03a] are listed in tab. 4.3. The extracted quadrupoles have been Doppler-corrected as described in [SSHC04], except for the cut-sky value. The values of C_2 and C_3 from the full-sky maps are significantly larger than the cut-sky values.

In fig. F.1 we show how the C_2 and C_3 histograms compare with the one-year data as $a_{\ell 0}^{\text{axial}}$ is increased. For $a_{\ell 0}^{\text{axial}} = 40\mu\text{K}$, the number of Monte Carlo hits that are consistent with the WMAP cut-sky data is smaller by a factor of ~ 2 for both C_2 and C_3 as compared

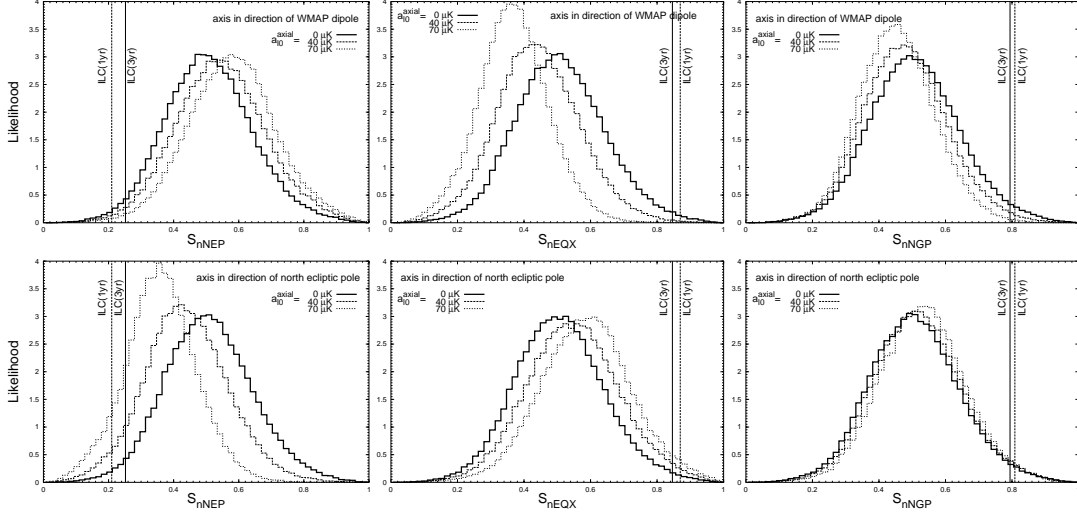


FIGURE 4.7. WMAP one- and three-year ILC maps compared to the likelihood of an alignment (4.7) of quadrupole and octopole normals with astrophysical directions [north ecliptic pole (NEP), equinox (EQX) and north galactic pole (NGP) in columns], for two orthogonal realisations of the preferred direction \hat{z} (WMAP dipole, NEP in rows). The bold histograms represent statistically isotropic and gaussian skies as predicted by the Λ CDM model. Increasing the axial contribution makes the anomalies worse for \hat{z} being aligned with the WMAP dipole, but with the exclusions being less significant for the ILC(3yr) than for the ILC(1yr). At the same time a Solar system effect is preferred by the data. The number of Monte Carlo realisations per test is always 10^5 .

with the fiducial CMB sky. For $a_{20}^{\text{axial}} = 70 \mu\text{K}$, the number of consistent Monte Carlo hits for $C_2(C_3)$ is reduced by a factor of $\sim 5(15)$ compared with the standard CMB sky. Note that adding *any* power to the theoretically expected quadrupole is excluded at the $> 99\%$ C.L. level from the cut-sky analysis, but for the octopole the same exclusion level is not reached until $a_{30}^{\text{axial}} = 80\mu\text{K}$. Further, adding $50\mu\text{K}$ ($100\mu\text{K}$) to the quadrupole leads to an exclusion of 99.6% C.L. (99.9% C.L.). In fig. 4.6 we show a comparison of one- and three-year data.

4.3.2. WMAP(3yr) Angular Power. In fig. 4.6 we show how the histograms for the quadrupole and octopole power compare with the measured values from WMAP(1yr,3yr). Considering the WMAP(1yr) cut-sky, adding *any* power to the quadrupole was already excluded at $> 99\%$ C.L. whereas the WMAP(3yr) data allows for adding up to $a_{20}^{\text{axial}} = 60\mu\text{K}$ in order to reach the same exclusion level. The octopole is quite robust against axial contaminations as it lies better on the fit: in order to reach the same exclusion level of $> 99\%$ C.L. it is necessary to add $a_{30}^{\text{axial}} = 80\mu\text{K}$ with respect to the WMAP(1yr) cut-sky and a whole $a_{30}^{\text{axial}} = 100\mu\text{K}$ with respect to the WMAP(3yr) value. Adding a moderate axial contribution of $a_{\ell 0}^{\text{axial}} = 40\mu\text{K}$ leads to an approximate bisection of the number of consistent Monte Carlo hits regarding WMAP(1yr) data (excluded at 99.5% C.L for C_2 and 91.5% C.L for C_3), where for the updated cut-sky a contribution of $a_{\ell 0}^{\text{axial}} = 40\mu\text{K}$ can be excluded at $> 98\%$ C.L. for C_2 and only at $\sim 71\%$ C.L for the octopole.

4.4. Extrinsic Alignment Analysis

Now we ask what kind of directional patterns the contribution $a_{\ell 0}^{\text{axial}}$ induces on the CMB sky. In the multipole vector representation [CHS04] any real multipole T_ℓ on a sphere

can be expressed with ℓ unit vectors $\hat{\mathbf{v}}^{(\ell,i)}$ and one scalar $A^{(\ell)}$ as

$$(4.6) \quad T_\ell(\theta, \varphi) = \sum_{m=-\ell}^{\ell} a_{\ell m} Y_{\ell m}(\theta, \varphi) \simeq A^{(\ell)} \prod_{i=1}^{\ell} \hat{\mathbf{v}}^{(\ell,i)} \cdot \hat{\mathbf{e}}(\theta, \varphi),$$

where $\hat{\mathbf{e}}(\theta, \varphi) = (\sin \theta \cos \varphi, \sin \theta \sin \varphi, \cos \theta)$ is a radial unit vector. Note that the right hand side of equation (4.6) contains contributions with ‘angular momentum’ $\ell-2, \ell-4, \dots$. The uniqueness of the multipole vectors is ensured by removing these terms by taking the appropriate traceless symmetric combination; for details see [CHS04]. Because the signs of all the multipole vectors can be absorbed into the quantity $A^{(\ell)}$, their signs are unphysical and so one is free to choose the hemisphere of each vector. Also note that the multipole vectors are independent of the angular power. With the decomposition (4.6) we achieved a unique factorisation of a multipole into a scalar part $A^{(\ell)}$, which measures its total power, and ℓ unit vectors $\hat{\mathbf{v}}^{(\ell,i)}$ that contain all the phase information.

Now it is necessary to define a suitable statistic to cope with the information from the multipole vectors. Introducing the $\ell(\ell-1)/2$ oriented areas $\mathbf{n}^{(\ell,i,j)} \equiv \hat{\mathbf{v}}^{(\ell,i)} \times \hat{\mathbf{v}}^{(\ell,j)} / |\hat{\mathbf{v}}^{(\ell,i)} \times \hat{\mathbf{v}}^{(\ell,j)}|$, we are ready to define a statistic in order to probe alignment of the normals $\mathbf{n}^{(\ell,i,j)}$ with a given physical direction $\hat{\mathbf{x}}$ [SSHC04],

$$(4.7) \quad S_{\mathbf{n}\mathbf{x}} \equiv \frac{1}{4} \sum_{\ell=2,3} \sum_{i<j} |\mathbf{n}^{(\ell,i,j)} \cdot \hat{\mathbf{x}}|.$$

This statistic is a sum over all dot products for a given $\hat{\mathbf{x}}$, so it does not imply any ordering between the terms and is a unique and compact quantity. For computing the multipole vectors we use the method introduced by [CHS04]. For mathematical details of the multipole vector formalism we refer to e.g. [Fis07].

As the contribution of the structure described by the LTB model, we add to the quadrupole and the octopole a component, denoted by $a_{\ell 0}^{\text{axial}}$, which is a pure $m=0$ mode with respect to a given physical direction $\hat{\mathbf{z}}$. For the direction $\hat{\mathbf{x}}$ we want to insert the relevant astrophysical directions which give rise to alignment, like the direction of the ecliptic plane, the equinox etc. But there is a catch. Once we rotate the $\hat{\mathbf{z}}$ axis of our initial coordinate system into the direction of the preferred axis of our model, the directions on the sky, like north ecliptic pole etc., have to be recalculated in that frame. This can be done in terms of Wigner rotation matrices [CHSS06]. Written as vectors, the coefficients \mathbf{a}'_ℓ transform under rotations as $\mathbf{a}'_\ell = \mathcal{D}^\dagger \mathbf{a}_\ell$, where the vector notation means that \mathbf{a}_ℓ is a vector of the ℓ -th multipole coefficient with $(2\ell+1)$ entries and \mathcal{D} denoting the rotation. The rotations can be parameterised in terms of the so called Euler angles α, β, γ and are given in matrix form by [CHSS06]

$$(4.8) \quad \begin{aligned} D_{m'm}^{(\ell)}(\alpha, \beta, \gamma) &= e^{im'\gamma} d_{m'}^{(\ell)} e^{im\alpha} \quad \text{with} \\ d_{m'm}^{(\ell)} &= \sum_k \frac{(-1)^{\ell-m'-k} [(\ell+m')!(\ell-m')!(\ell+m')!(\ell-m')!]^{1/2}}{k!(l-m'-k)!(l-m-k)!(m+m'+k)!} \\ &\times \left(\cos \frac{\beta}{2} \right)^{2k+m'+m} \left(\sin \frac{\beta}{2} \right)^{2\ell-2k-m'-m}. \end{aligned}$$

We have carried out the rotations with the help of a `MATHEMATICA` routine. Next, let us review our results of the Monte Carlo analysis for the alignment statistic (4.7) with respect to astrophysical directions.

4.4.1. WMAP(1yr) Alignment. We look for alignment with three different directions $\hat{\mathbf{x}}$: the north ecliptic pole, the equinox and the north galactic pole. The first two are preferred directions in the Solar system and the last defines the plane of the dominant foreground. The observed S -values from the different CMB maps are given in tab. 4.3. The results of the correlation analysis are shown in the appendix as fig. F.2, fig. F.3 and fig. F.4. By chance the CMB

dipole and equinox lie very close to each other, so an alignment test with the dipole will give results very similar to the one with the equinox.

In fig. F.2 the preferred axis \hat{z} is chosen to be the measured WMAP(1yr) dipole [B⁺03b]. We perform alignment tests (4.7) with respect to the three test directions \hat{x} . For all three tests the anomaly gets clearly worse, that is the axial mechanism drives the histograms away from the data. Next, instead of using the motion of the local group with respect to the CMB rest frame [KLS⁺93] as the test direction, we take the velocity of the local group when corrected for Virgocentric motion [PK98], since this differs more from the WMAP dipole. The results are shown in fig. F.3. The situation for the alignment with the equinox is again worse, but there is not much effect on the ecliptic alignment. For the alignment with the galactic plane, the axial contribution makes an apparent galactic correlation more probable, i.e. there is a certain probability of overestimating the galactic foreground. For both test directions by now, the alignment with the equinox gets worse. For example, in the direction of the Virgo-corrected local group motion an exclusion of $\sim 99.9\%$ C.L. for $a_{\ell 0}^{\text{axial}} = 50\mu\text{K}$ can be given with respect to all three cleaned maps. Note that adding *any* multipole power in this test can already be excluded at the $\geq 99.4\%$ C.L.

As a complementary test we show the alignment likelihood with regard to an orthogonal test direction, namely the north ecliptic pole, in fig. F.4. An ecliptic extra contribution in the CMB would indeed induce an alignment of normal vectors similar to the observed one. In particular, for $a_{\ell 0}^{\text{axial}} = 50\mu\text{K}$, the probability of finding an alignment with the north ecliptic pole itself becomes roughly 5%, and the probability for the equinox alignment rises to 1%.

TABLE 4.3. Tests applied to various cleaned maps, as defined in equation (4.7), for one- and three-year data, as well as the values for angular power (4.4). Foreground-cleaned maps: TOH(1yr) is due to [TdOCH03], LILC (1yr) to [EBGL04], the ILC maps to [H⁺03, H⁺07] and the Maximum Likelihood Estimate (MLE) for low multipoles to [H⁺07]. All one-year quadrupoles except the cut-sky value have been Doppler-corrected.

	cut sky (1yr)	TOH(1yr)	LILC(1yr)	ILC(1yr)	ILC(3yr)	MLE(3yr)
C_2	$129\mu\text{K}^2$	$203\mu\text{K}^2$	$352\mu\text{K}^2$	$196\mu\text{K}^2$	$261\mu\text{K}^2$	$221\mu\text{K}^2$
C_3	$320\mu\text{K}^2$	$454\mu\text{K}^2$	$571\mu\text{K}^2$	$552\mu\text{K}^2$	$550\mu\text{K}^2$	$545\mu\text{K}^2$
$S_{n\text{NEP}}$	-	0.194	0.193	0.210	0.252	-
$S_{n\text{EQX}}$	-	0.886	0.866	0.870	0.846	-
$S_{n\text{NGP}}$	-	0.803	0.803	0.810	0.794	-

4.4.2. WMAP(3yr) Alignment. Similarly, we test for alignment with the three generic directions \hat{x} : north ecliptic pole, equinox and north galactic pole. The results of the correlation analysis are shown in fig. 4.7: in the first row the preferred direction \hat{z} coincides with the direction of local motion, the dipole. Here the anomaly becomes worse when increasing the amplitude of the axial contribution. But for $\hat{x} = \text{NEP}$ the exclusion becomes somewhat milder going from one-year to three-year data; e.g. $a_{\ell 0}^{\text{axial}} = 40\mu\text{K}$ leads to an exclusion of 99.2% C.L. for ILC(1yr) but only 98.2% C.L. for the updated ILC map. Finding an alignment with the equinox though is strongly excluded at $> 99.2\%$ C.L., even with an vanishing axial contribution for both one- and three-year data. For instance, for $\hat{x} = \text{EQX}$ adding a contribution of $a_{\ell 0}^{\text{axial}} = 20\mu\text{K}$ ($a_{\ell 0}^{\text{axial}} = 70\mu\text{K}$) leads to an exclusion level of 99.4% C.L. (99.9% C.L.) with respect to three-year data. Similarly to above, a Solar system effect is preferred by the data. For example, an alignment with the ecliptic itself ($\hat{x} = \text{NEP}$) may only be excluded at the level of 92.3% C.L. after adding an axial contribution of $a_{\ell 0}^{\text{axial}} = 40\mu\text{K}$. For the same axial contribution, the alignment with the equinox becomes less anomalous as 99.2% C.L. \rightarrow 98.2% C.L.

4.5. Conclusion

Besides the anomalous intrinsic alignment of the CMB quadrupole and octopole with each other and the lack two-point angular correlation on the largest angular scales, there are a number of mysterious alignments with astrophysical directions concerning the lowest multipoles in the WMAP data. These anomalies are present both in the one-year and in the three-year WMAP data, c.f. tab. 4.1, and could not be satisfactorily explained by now.

Here we presented an analysis that seeks to take the influence of non-linear structure formation on the CMB photons into account. Such an effect is well motivated by present data on the large-scale structure. Recent astrophysical data cataloguing our neighbourhood in the X-ray band [KME04, KE06, HSLB04, LRSH04] point us to the existence of massive non-linear structures, like the Shapley concentration, at distances of around $100h^{-1}\text{Mpc}$. Besides its significant contribution to the dipole velocity profile, c.f. fig. 4.3, such a structure is able to induce anisotropies of order 10^{-5} via its Rees-Sciama effect.

Regarding CMB modes, the spherical symmetry of the LTB model, which we use to approximate the local superstructure, reduces to an axial symmetry along the line connecting our position and the centre of the overdensity, where we locate for instance the Shapley supercluster, c.f. fig. 4.2 (right figure). Consequently, under this assumption we should observe an axisymmetric effect on the microwave sky. The preferred axis \hat{z} has been taken to point in the direction of the CMB dipole, c.f. fig. 4.7 and fig. F.2 and the Virgo-corrected local group's flow vector, see fig. F.3. Thereby we have added the axisymmetric contribution to a statistically isotropic gaussian random map (ΛCDM standard model prediction) and compared it by means of the S -statistic with WMAP measurements. The additional zonal harmonics have been added with increasing strength, see fig. 4.8 or figs. F.5-F.7 for full-sky maps of the Rees-Sciama effect. When gauging the preferred axis to the direction of local motion (WMAP dipole), the consistency of the data with theory becomes even worse, albeit with slightly less significance with respect to three-year WMAP data. In particular, in case of $\hat{z} = \text{dipole}$, an axial contribution of $a_{\ell 0}^{\text{axial}} = 60\mu\text{K}$ led to an exclusion level of 99.4% C.L. with respect to one-year data, but can 'only' be excluded at 98.7% C.L. within the updated maps. However, in case of the alignment test with the equinox, the significance of the anomalous alignment remains nearly unchanged when comparing with one- and three-year data. On the other hand an orthogonally directed (Solar system) effect would largely increase the consistency with the data for both one-year and three-year data sets: for instance, 97% C.L. \rightarrow 83% C.L. with respect to WMAP(3yr) data after adding an axial contribution of $a_{\ell 0}^{\text{axial}} = 70\mu\text{K}$.

Here we studied additive axial effects because they are well motivated. However, from our analysis it is not excluded that there could be a multiplicative axisymmetric effect, coming from some unknown non-linear source. Note that our analysis applies likewise to any other effect which gives an *axisymmetric* addition to the statistically isotropic and gaussian random sky.

4.5.1. Alternative Proposals. The existence of the CMB anomalies support the conclusion that either the Universe as seen by WMAP is not statistically isotropic on largest scales, or that the observed features are due to unexpected foregrounds, hidden systematics or new physics challenging the standard cosmological model. Diverse attempts for explanation can be found in the literature: considering anisotropic or inhomogeneous models [Bianchi family or (LTB) models] [GHS07, JBE⁺06, AA06, Mof05, Tom05b, RRS06b], Solar system foreground [Fri05, DPS⁺07], lensing of the CMB [Val05] and moving foregrounds [CS05], Sunyaev-Zel'dovich effect [AS03, AJW06, HBM⁺05] and Rees-Sciama effect [IS07, IS06, MDW⁺07, RRS06b, RRS06a], considering a non-trivial topology of the Universe [LWR⁺03, SKCSS07, ALST07], considering modifications and refinements of the standard simplest scenario of inflation [BdVS06, CCT06, CPKL03, FRV04, GH04, WNL⁺07] and even considering possible phenomenology of loop quantum gravity [HW04, TSM04].

This list is not meant to be exhaustive. Let us pick two models out that appear particularly interesting from our point of view. First, also considering extended local foregrounds Abramo

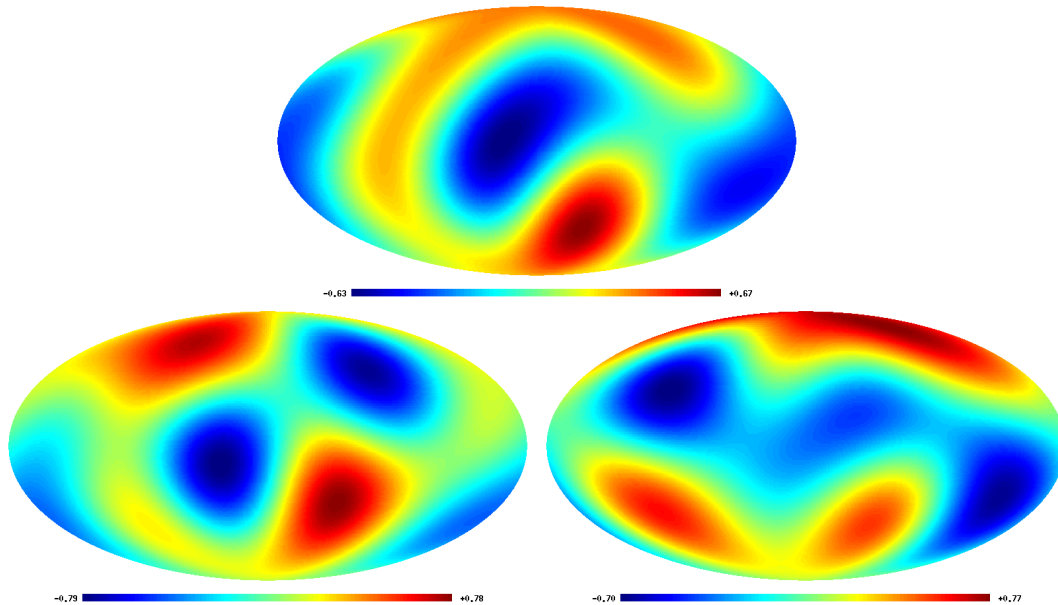


FIGURE 4.8. Full-sky Mollweide maps ($\ell = 2 + 3$) of the Rees-Sciama effect on the quadrupole and octopole. Upper map: a random realisation of an statistically isotropic and Gaussian quadrupole plus octopole. Lower left map: an axial effect – which could e.g. be due to the local Rees-Sciama effect of a spherical overdensity – of magnitude $a_{20}^{\text{axial}} = a_{30}^{\text{axial}} = 70\mu\text{K}$ is imposed on the random map, with the preferred axis of the model \hat{z} pointing in the direction of the dipole (upper right quadrant); for this model direction the alignment anomalies become worse when adding an axial effect, c.f. fig. 4.7. For an illustration of galactic coordinates and relevant directions see fig. 4.5. Lower right map: adding the same contribution, now with the preferred axis being in direction of the north ecliptic pole, in which case the Monte Carlo analysis showed that alignments become less anomalous, c.f. fig. 4.7. The colour legends are in units of 0.1mK. For map-making we made use of the publicly available GLESP package [D⁺03]. Additional maps are given in app. F.

et al. proposed [AS03, AJW06] that a cold spot in the direction of the local Supercluster could account for the cross alignments of quadrupole and octopole. The cold spot would be realised by the (thermal) Sunyaev Zel’dovich^a effect of CMB photons scattering off the hot intracluster gas. However, the values for the characteristics of the Sunyaev-Zel’dovich foreground (gas temperature, density) that are required to explain the cross-alignment are at most marginally consistent with astrophysical X-ray data.

Second, Silk and Inoue [IS06] suggested a certain geometrical pattern of two identical voids to account for the cross alignment as well as for the octopole planarity via the Rees-Sciama effect of this underdense structure. But extrinsic alignments remain unexplained in this model.

^aIn sec. 3.1 we have already mentioned this astrophysical effect. Let us shortly give some details here. CMB photons can undergo inverse Compton scattering off hot gas electrons in galaxy clusters and so get shifted to the Wien regime of the spectrum. Therefore, when looking at the CMB sky in the Rayleigh-Jeans band, there appears a lack of microwave photons at the position of the hot intracluster gas. The spectral distortion is given by [SZ70]

$$(4.9) \quad \left(\frac{\Delta T}{T}\right)_{\text{SZ}} = \left(x \frac{e^x + 1}{e^x - 1} - 4\right) y, \quad x \equiv \frac{h\nu}{k_B T}, \quad y \equiv \int n_e \frac{k_B T_e}{m_e c^2} \sigma_T dl,$$

where y is the integrated gas pressure along the line of sight, T_e is the temperature of the hot cluster electrons and σ_T is the Thomson cross section. Because the effect is independent of redshift, it can be used to detect hot galaxy clusters up to very high redshifts $z \sim 2$ within future CMB surveys [B⁺06a], as well as for an independent yield of the Hubble constant, for the basic principle see [KKZ97]. For a review see e.g. [CHR02].

However, this approach requires a high degree of fine-tuning in the geometrical setup of the voids that are placed on the sky. The actual data on the large-scale structure of the Universe do not support such a setup.

Each of the latter approaches alone is not fully satisfactory. A more realistic approach concerning extragalactic foregrounds should take both the Rees-Sciama effect and the Sunyaev-Zel'dovich effect into account. Moreover, since the local Rees-Sciama effect can contribute up to 10^{-5} to the temperature anisotropies on large angular scales, a detailed study is important for cross-correlating CMB data (including upcoming PLANCK data) with astrophysical observations on the local large-scale structure.

Intrinsic Alignments in the CMB

Now we want to focus on the intrinsic quadrupole-octopole alignment, which is independent of external directions, as well as its relation to the anomalous features in the measured CMB temperature autocorrelation function. As was mentioned, at the largest angular scales – corresponding to the multipole moments $\ell = 2$ and $\ell = 3$ – the presence of a number of unexpected features has been confirmed by the latest CMB measurements. Among these are the anomalous alignment of the quadrupole and octopole with each other as well as the stubborn lack of angular correlation on scales $> 60^\circ$. Here we search for correlations between these two phenomena and demonstrate their absence. A Monte Carlo likelihood analysis confirms previous studies in the literature and shows that the joint likelihood of both anomalies is incompatible with the best-fit Λ CDM model at $> 99.95\%$ C.L. Extending also to some higher multipoles, a common special direction has been identified and has been dubbed in the literature the ‘Axis of Evil’. In the seek for an explanation of the anomalies, several studies invoke effects that exhibit an axial symmetry. We find that this interpretation of the ‘Axis of Evil’ is inconsistent with three-year data from the WMAP. More precisely, the data require a preferred plane, whereupon the axis is just the normal direction. Rotational symmetry within that plane is ruled out at high confidence.

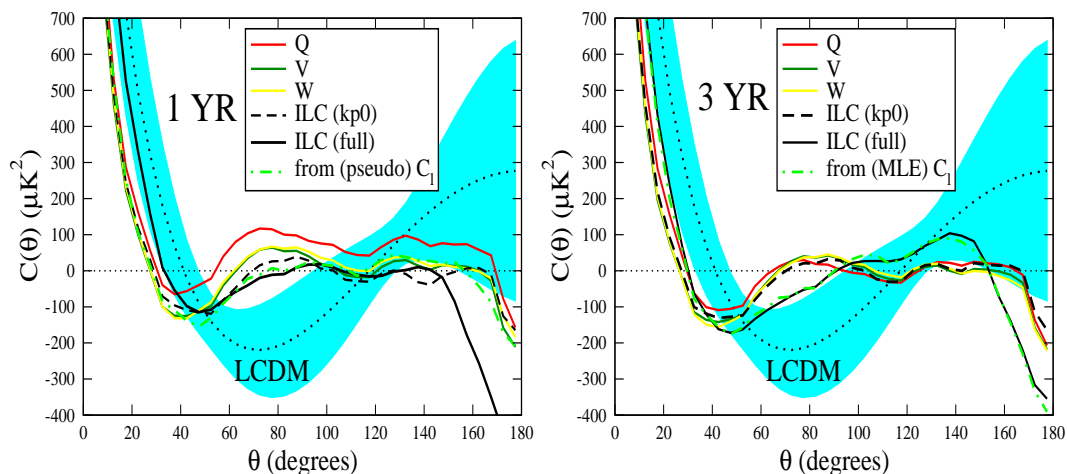


FIGURE 5.1. The temperature autocorrelation (3.40) versus angular separation scale, from WMAP(1yr) (left) and WMAP(3yr) (right) data. Kp0-masked maps from three different frequency bands Q (41GHz), V (61GHz) and W (94GHz) are shown, as well as the cut and uncut ILC maps, and the Maximum Likelihood Estimate for the smallest multipoles. None of the almost vanishing ($60^\circ \lesssim \theta \lesssim 170^\circ$) cut-sky wavebands matches the reconstructed full-sky and neither one of the latter matches the prediction of the best-fit model. The anomaly appears even more pronounced in the three-year data than in the one-year data. Figures are taken from [CHSS07].

5.1. Introduction

With the emergence of more and more precise and detailed cosmological observations, the inflationary Λ CDM model remains to provide a surprisingly good fit to the bulk of cosmological data. Thereby, the most precise and distinguished lever arm is provided by measurements of the microwave background radiation. The standard inflationary model predicts approximately scale-invariant, statistically isotropic and Gaussian temperature fluctuations on the surface of last scattering and is fully consistent with the data, c.f. sec. 1.2.2. But after the release of three years of mission data from the WMAP satellite [J⁺07a, H⁺07, P⁺07, WMAa] there remain at least open questions and at most serious challenges upon the inflationary Λ CDM model of cosmology.

Based on the high precision measurements of WMAP, a couple of anomalies on the microwave sky have been identified. These anomalies manifest themselves at the largest angular scales, mainly among the quadrupole and octopole – the dipole is overwhelmingly dominated by our local motion with respect to the CMB – but also extending to somewhat higher multipoles. The corresponding anomalies may be divided into two types:

- First, and already seen by the COBE-DMR instrument [HBB⁺96] and confirmed by the first-year analysis of the WMAP team [S⁺03], there is a lack of angular two-point correlation on scales between 60° and 170° in all wavebands. In [CHSS07] the angular two-point correlation function of the three-year WMAP measurements has been computed. Going from COBE-DMR to WMAP(3yr) the lack of correlation persists and moreover it has been outlined [CHSS07] that among the two-point angular correlation functions none of the almost vanishing cut-sky wavebands matches the reconstructed full sky and neither one of the latter matches the prediction of the best-fit Λ CDM model. This disagreement has been shown to be even more distinctive in the WMAP(3yr) data than in the WMAP(1yr) data and is found to be unexpected at 99% C.L. with respect to the three-year Internal Linear Combination [ILC(3yr)] cut-sky. Recently, it has been shown [Haj07] that indeed quadrupole and octopole are responsible for the lack of correlation and that most of the large-scale angular power comes from two distinct regions within the galactic plane (only 9% of the sky).
- Second, there exist anomalies concerning the phase relationships of the quadrupole and octopole. As we have discussed in the previous chapter, there are a number of remarkable alignment anomalies found [dOCT06, SSHC04], e.g. an unexpected alignment of the quadrupole and octopole with the dipole and with the equinox at 99.7% C.L. and 99.8% C.L., respectively [CHSS07]. In contrast to such *extrinsic* alignments, that is alignments of the low multipoles with some physical direction or plane, like the dipole or the ecliptic (discussed in the previous chapter), the *intrinsic* alignment between quadrupole and octopole does not know about external directions. In this chapter, we address the intrinsic alignment of quadrupole and octopole with each other, which from the ILC(3yr) map is found to be anomalous at the 99.6% C.L. with respect to the expectation for an statistically isotropic and Gaussian sky [CHSS07].

Both types of CMB phenomena challenge the statement of statistical isotropy of the CMB sky at largest angular scales. Here we want to study the relation between the lack of angular correlation and the intrinsic alignment of quadrupole and octopole.

In [LM05] it has been shown that intrinsic alignments among multipole moments extend also to higher moments and it has been proposed that the strange alignments at large angular scales involve a preferred direction, called the ‘Axis of Evil’. This axis points approximately towards $(l, b) \simeq (-100^\circ, 60^\circ)$ and is identified as the direction where several low multipoles ($\ell = 2 - 5$) are dominated by one m -mode when the multipole frame is rotated into the direction of the axis. Recently, in [LM07] the analysis of the ‘Axis of Evil’ has been redone in the light of the WMAP(3yr) with the use of Bayesian techniques [MS07]. It was argued [dOCT06] that the ‘Axis of Evil’ is rather robust against foreground contaminations and galactic cuts. A recent

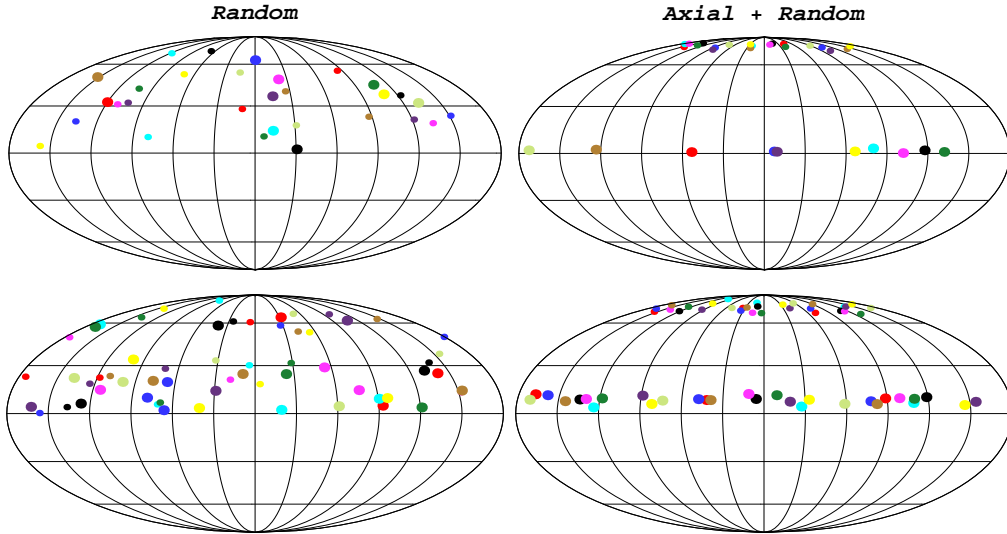


FIGURE 5.2. Mollweide projection of the sky with quadrupole (upper row) and octopole (lower row) multipole vectors [equation (5.5)]. The mesh consists of steps in 30° . Displayed are ten pairs of quadrupole vectors (small dots) and their ten area vectors [equation (5.6) (big dots)] as well as ten triples of octopole vectors (small dots) and their area vectors (big dots); togetherness is indicated by colour. The arbitrary sign of the vectors has been used to gauge them all to the northern hemisphere. The statistically isotropic and Gaussian case (left column) is broken by the imprint of a strong axial effect $a_{\ell 0} = 1000\mu\text{K}$ (right column) whereupon multipole vectors move to the pole and area vectors move to the equatorial plane. The onset of the shown separation of multipole vectors and cross products can already be observed at moderate axial contributions of $a_{\ell 0} \sim 100\mu\text{K}$, c.f. fig. F.11.

[RLLA07] cross-correlation analysis of CMB data and galaxy survey data shows no evidence for an ‘Axis of Evil’ in the observed large-scale structure. In contrast, recently an opposite claim has been put forward [Lon07], where it was claimed that an analysis of SDSS data gives rise to a preferred axis in the Universe.

Motivated by these observed CMB anomalies, several mechanisms based on some axisymmetric effect have been proposed, although the operational definition of the ‘Axis of Evil’ [LM05, LM07] does not necessarily imply the existence of such a strong symmetry. Among the various effects that have been suggested to possibly introduce a preferred axis into cosmology are: a spontaneous breaking of statistical isotropy [GHH05], parity violation in general relativity [Ale06], anisotropic perturbations of dark energy [KM06, BM06], residual large-scale anisotropies after inflation [CCT06, GCP06], or a primordial preferred direction [ACW07]. At the same time, it has been studied [RRS06b, IS06] how the local Rees-Sciama effect of an extended foreground, non-linear in density contrast, affects the low multipole moments of the CMB via its time-varying gravitational potential, see the previous chapter. In a scenario with a single overdensity the coefficients of the spherical harmonic decomposition, the $a_{\ell m}$, become modified by only *zonal harmonics*, i.e. $m = 0$ modes. This is equivalent to an axial effect along the line connecting our position with the centre of the source.

In fact, the observed pattern in the CMB for quadrupole and octopole is a nearly pure $a_{\ell\ell}$ mode respectively; as seen in a frame where the z -axis equals the normal of the plane defined by the two quadrupole multipole vectors [CHSS06]. In [CHSS07] it has already been argued, that foreground mechanisms originating from a relatively small patch of the sky would mainly excite zonal modes. Moreover all additive effects where extra contributions are added on top of

the primordial fluctuations would have difficulties explaining the low multipole power at large scales without a chance cancellation.

It is important to study how the inclusion of a preferred axis compares with the intrinsic multipole anomalies at largest scales. Our analysis is restricted to axisymmetric effects on top of the primordial fluctuations from standard inflation, thus secondary or systematic effects. We are going to quantify how poorly an axisymmetric effect at low multipoles of whatever origin matches the three year-data of WMAP. Further, we will demonstrate that there is no correlation between the two types of intrinsic low- ℓ anomalies: the two-point correlation deficit and intrinsic alignment; and that there remains none even when a preferred axis is introduced to the problem.

5.2. Choice of Statistic

A common observable is the multipole power. According to the standard perception of inflationary cosmology, the CMB fluctuations are believed to follow a Gaussian statistic and to be distributed in a statistically isotropic way. The notion of statistical isotropy means that the expectation value of pairs of coefficients $\langle a_{\ell' m'}^* a_{\ell m} \rangle$ is proportional to $\delta_{\ell' \ell} \delta_{m' m}$, c.f. (3.39). The proportionality constant measuring the expectation value of the multipole on the full sky is commonly estimated by C_ℓ , c.f. sec. 3.3.2. The angular power can also be written as

$$(5.1) \quad C_\ell \equiv \frac{1}{2\ell + 1} \sum_{m=-\ell}^{\ell} |a_{\ell m}|^2 = \frac{1}{2\ell + 1} \int d\Omega T_\ell^2(\theta, \varphi),$$

with T_ℓ being the ℓ -th multipole of the CMB temperature anisotropy. It can be expanded with the help of spherical harmonics as: $T_\ell = \sum_m a_{\ell m} Y_{\ell m}$. Note that, since we consider multipole moments that are real, the $a_{\ell m}$ must fulfil the additional condition: $a_{\ell m}^* = (-1)^m a_{\ell -m}$. Using the estimator (5.1) the angular two-point correlation function is given by

$$(5.2) \quad C(\theta) = \frac{1}{4\pi} \sum_{\ell=0}^{\infty} (2\ell + 1) C_\ell P_\ell(\cos \theta),$$

where the P_ℓ are the Legendre Polynomials of ℓ -th order.

Besides of the multipole power itself, it is useful to introduce an all-sky quantity that embraces all scales. As inspired by the $S_{1/2}$ statistic, presented in [S⁺03] for measuring the lack of angular power at scales larger than 60° , we use here an analogous all-sky statistic [CHSS07]

$$(5.3) \quad S_{\text{full}} \equiv \int_{-1}^1 C^2(\theta) d(\cos \theta).$$

It is a measure of the total power squared on the full-sky. In contrast to the $S_{1/2}$ statistic [S⁺03], the S_{full} statistic does not contain any a priori knowledge on the variation of the two point angular correlation (5.2) for angles $> 60^\circ$. Here we are considering especially the large angular scales but we are not interested in the monopole and dipole and thus arrive at

$$(5.4) \quad S_{\text{full}}^{\text{trunc}} = \frac{1}{8\pi^2} (5C_2^2 + 7C_3^2).$$

Of course, all multipoles have to be considered for the full-sky statistic (5.3) but we can use the truncated part (5.4), because here the anomalies are most pronounced and we want to check for the interplay of this part of the full-sky power statistic with the other (phase) anomalies within quadrupole and octopole. This part is then simply to be added to the rest of the sum of (squared) multipole power in (5.3), recovering the expression for the full-sky.

Next we turn to the statistics involving the phase relationships of multipoles. We use the concept of Maxwell's multipole vectors [Max79] in order to probe statistical isotropy, since this representation proved to be useful for analyses of geometric alignments and special directions on the CMB sky. Normally the CMB data is decomposed into spherical harmonics and the

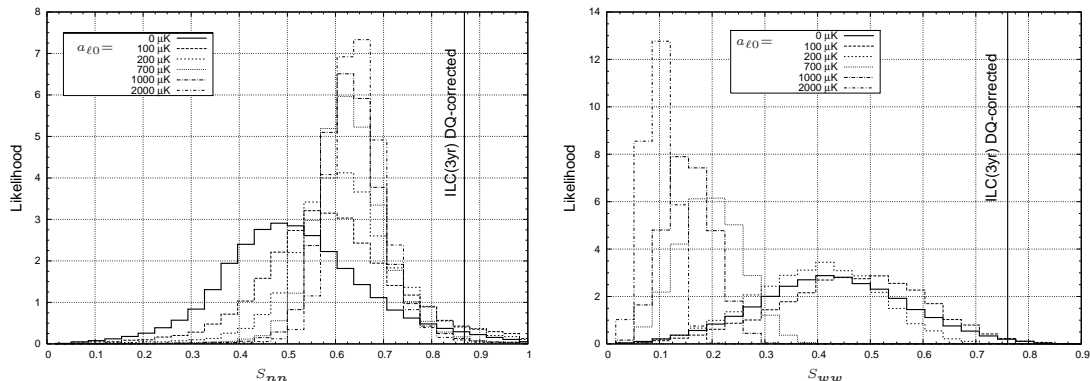


FIGURE 5.3. Evolution of the Monte Carlo likelihood of the alignment statistics S_{nn} (5.7) and S_{ww} (5.8). The effect of an axis in the CMB is modeled via increasing additional zonal harmonics with coefficients $a_{\ell 0}$. At $a_{\ell 0} = 1000 \mu\text{K}$ the multipoles become purely zonal in good approximation. Regarding WMAP's ILC(3yr) map S_{nn} is unexpected at 98.3% C.L. and S_{ww} is odd at 99.5% C.L. with respect to the statistically isotropic and Gaussian sky (bold histograms). The best improvement is reached for both statistics at roughly $a_{\ell 0} = 100 \mu\text{K}$.

coefficients $a_{\ell m}$ containing the physics. Alternatively, with the use of the multipole vectors formalism we can expand any real temperature multipole function on a sphere into

$$(5.5) \quad T_{\ell}(\theta, \varphi) = \sum_{m=-\ell}^{\ell} a_{\ell m} Y_{\ell m}(\theta, \varphi) = A^{(\ell)} \left[\prod_{i=1}^{\ell} \left(\hat{\mathbf{v}}^{(\ell, i)} \cdot \hat{\mathbf{e}}(\theta, \varphi) \right) - \mathcal{L}_{\ell}(\theta, \varphi) \right],$$

and $\hat{\mathbf{e}}$ is a radial unit vector, just like in (4.6). The ‘angular momentum’ residuals are subtracted with the help of the term $\mathcal{L}_{\ell}(\theta, \varphi)$. We choose the sign of the multipole vectors so that they all point to the northern hemisphere.

In order to disclose correlations among the multipole vectors we first consider for each ℓ the $\ell(\ell-1)/2$ independent *oriented areas* built from the cross products

$$(5.6) \quad \mathbf{w}^{(\ell; i, j)} \equiv \pm \hat{\mathbf{v}}^{(\ell, i)} \times \hat{\mathbf{v}}^{(\ell, j)},$$

whereof we will also use the normalised vectors $\mathbf{n}^{(\ell; i, j)} \equiv \mathbf{w}^{(\ell; i, j)} / |\mathbf{w}^{(\ell; i, j)}|$. Now, in [SSH04] and subsequent works, the dot products of the area vectors have proven to be a handy expression in order to quantify alignments of the multipole vectors among each other and also with external directions (which we do not consider here). The following measure, as stated in [Wee04], and used in [SSH04, CHSS06, CHSS07] serves as a natural choice of a statistic in order to quantify the intrinsic alignment of quadrupole and octopole oriented areas:

$$(5.7) \quad S_{ww} \equiv \frac{1}{3} \sum_{i < j} \left| \mathbf{w}^{(2; 1, 2)} \cdot \mathbf{w}^{(3; i, j)} \right|.$$

Note that we consider only the very largest scales, i.e. we use the statistic only for $\ell = 2, 3$. Analogously, a statistic involving the normalised area vectors is given by:

$$(5.8) \quad S_{nn} \equiv \frac{1}{3} \sum_{i < j} \left| \mathbf{n}^{(2; 1, 2)} \cdot \mathbf{n}^{(3; i, j)} \right|.$$

5.3. Standard Model Predictions

Standard inflationary ΛCDM cosmology requires the CMB anisotropies to be Gaussian and statistically isotropic. For the subsequent analysis we have produced Monte Carlo realisations of the harmonic coefficients $a_{\ell m}$ following the underlying ΛCDM theory. From [CHS04] an algorithm is available which we use to obtain Monte Carlo multipole vectors from the coefficients.

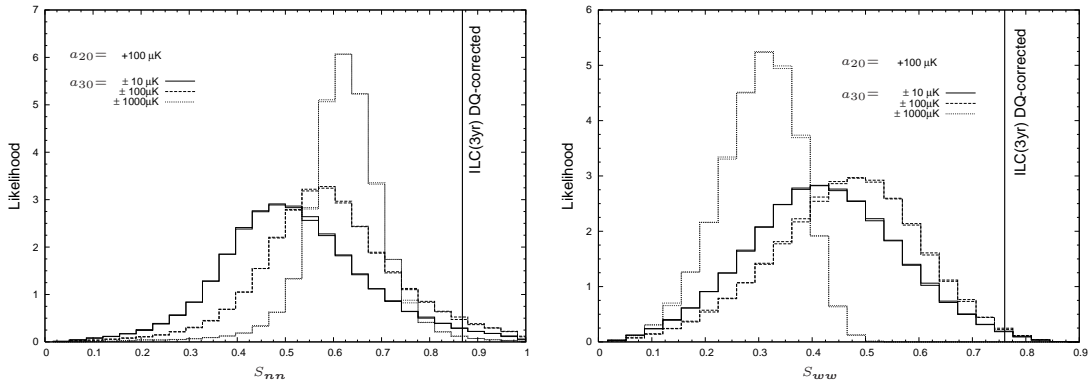


FIGURE 5.4. The sign of additional axial contributions $a_{\ell 0}$ has no physical effect on the statistics S_{nn} and S_{ww} . For the quadrupole this follows from the symmetry of the Legendre Polynomial P_2 [see equation (5.13)]. The quadrupole contribution is kept fixed at $a_{20} = 100\mu\text{K}$ while the axial contribution to the octopole is varied both in magnitude and in sign. Respective pairs of $\pm a_{30}$ histograms lie virtually on each other and their statistics are thus indistinguishable. The reference histograms following from the axially unmodified ΛCDM model (bold histograms in fig. 5.3 lie nearly on top of the displayed $a_{20} = 100\mu\text{K}$ and $a_{30} = \pm 10\mu\text{K}$ cases, and are thus not shown.

Mollweide maps of a sample of random Gaussian and statistically isotropic quadrupole and octopole vectors as well as their normals are given in fig. 5.2 (left column).

Concerning the question of correlations between the multipole power and the alignment of multipole vectors, it appears natural to expect that there is none. That is because we invoked Gaussian random and statistically isotropic skies, leading to multipole vectors (5.5) independent of the multipole power (5.1). This assumption needs to be tested and quantified.

Nevertheless, a small correlation could be expected from the following reason: Considering only multipoles up to some limiting power, the resulting probability density distribution for the $a_{\ell m}$ must be non-Gaussian. In fact, this restriction leads to a negative kurtosis for the $a_{\ell m}$ distribution (the skewness vanishes). Having that in mind, it appears suddenly unclear whether the naive expectation of vanishing correlation of power with intrinsic alignment will hold. Below we substantiate the absence of correlations by means of a Monte Carlo analysis.

Let us first look at the alignment anomalies. In fig. 5.3 the likelihood of the quadrupole and octopole alignment statistics S_{ww} and S_{nn} is shown. The predictions of the standard inflationary ΛCDM model are shown as the bold histograms respectively (= vanishing axial contamination). According to the three-year ILC map from WMAP [WMAa] we get the following measured values for the alignment statistics:

$$S_{nn}^{\text{ILC}(3\text{yr})} = 0.8682 \quad \text{and} \quad S_{ww}^{\text{ILC}(3\text{yr})} = 0.7604,$$

when [CHSS07] corrected for the Doppler-quadrupole. The total number of Monte Carlos we produced per sample is $N = 10^5$. We infer that the unmodified inflationary ΛCDM prediction is unexpected at 98.3% C.L. with the S_{nn} statistic and unexpected at 99.5% C.L.^a with respect to the S_{ww} statistic.

Next we consider the cross-correlation between the intrinsic phase anomalies and the multipole power (5.1) within the low- ℓ . For this we chose those $a_{\ell m}$ that allow for say the lowest possible 5% in the left tail of the distributions for C_2 and C_3 that follow from statistical isotropy, Gaussianity and the ΛCDM best-fit to the WMAP data. Then we compute the expression S_{ww} for the selected $a_{\ell m}$ and compare it to the according ILC(3yr) value. As expected, no correlation

^aThe value quoted above was [CHSS07] 99.6% C.L. The small difference is due to the incorporation of the WMAP pixel noise in the Monte Carlo analysis in [CHSS07].

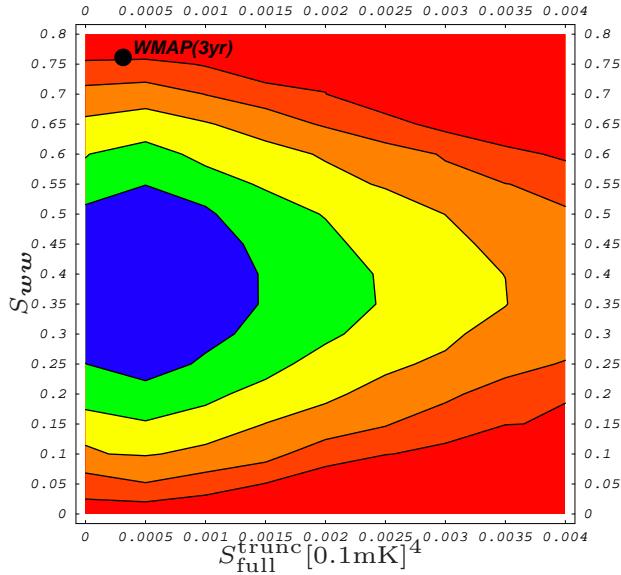


FIGURE 5.5. Contour of the scatter of intrinsic alignment (5.7) versus full-sky power squared (5.4). The shape can be understood from the folding of the two respective distributions. The total number of Monte Carlo points is $N = 10^5$. The measured data point from WMAP three-year data is included. The maximum of likelihood requires S_{ww} far smaller than obtained from ILC(3yr). Consistency with the data can be excluded at 99.95% C.L. Contours correspond to lines of $1/2^n$ times the maximal likelihood, with $n = 1, \dots, 5$.

is found, that is neither the shape nor the expectation value of the alignment statistic is shifted. We find the same also for the combination of the lowest allowed 5% in C_2 and the highest 5% from the right tail of the distribution of C_3 and the remaining two possible combinations thereof. As we do not find any correlations, we can conclude that the S_{ww} and S_{nn} statistics are not sensitive to the non-Gaussianity induced by the restriction to low multipole power.

Moreover, we probe the opposite direction by tagging those $a_{\ell m}$ that lie in the allowed right tail of the S_{ww} distribution with respect to $S_{ww}^{\text{ILC}(3\text{yr})}$. The distribution of the multipole power for C_2 and C_3 made of these $a_{\ell m}$ remains unchanged. The latter finding confirms that multipole power and the shape of multipoles (phases) are uncorrelated.

Using Equation (5.4), the [WMAa] Maximum Likelihood Estimate (MLE) from the WMAP ILC(3yr) map for the angular power spectrum yields $S_{\text{full}}^{\text{trunc,MLE}} = 29431 \mu\text{K}^4$. Compared to the value of $136670 \mu\text{K}^4$ from the ΛCDM best-fit to WMAP(3yr) data, this is not significantly unexpected, with an exclusion level of only 92.1% C.L.

Now we want to check for correlations between the all-sky multipole power and the multipole alignment. As for reasons explained in the next section we prefer the S_{ww} statistic to S_{nn} in the following correlation analysis. In Figure 5.5 the scatter plot of S_{ww} against $S_{\text{full}}^{\text{trunc}}$ is shown. The form of the contour can be understood as just the folding of the χ^2 -like form of the distribution for $S_{\text{full}}^{\text{trunc}}$ with the gaussian-like form of the S_{ww} distribution. At first glance we see from Figure 5.5 that the MLE from WMAP(3yr) $S_{\text{full}}^{\text{trunc,MLE}} = 29431 \mu\text{K}^4$ requires the alignment statistic to be of middle values (around 0.4), which is inconsistent with the respective measured anomalous value from ILC(3yr). Moreover the lack of any linear behaviour in the contour suggests that there is no correlation between the two statistics.

Given that no correlation is present between S_{ww} and $S_{\text{full}}^{\text{trunc}}$, we would expect that the joint probability that both power and alignment are in accordance with data factorises according to:

$$(5.9) \quad p(S_{\text{full}}^{\text{trunc}} \leq \text{data} \wedge S_{ww} \geq \text{data}) = p_1(S_{\text{full}}^{\text{trunc}} \leq \text{data}) p_2(S_{ww} \geq \text{data}).$$

But in reality we can only access finite statistical samples of these quantities and the factorisation will not be exact. However, we want to will check the validity of (5.9) within our statistical ensemble. When using the full sample with $N = 10^5$ respectively we obtain a *joint likelihood* of $p \simeq 0.05\%$. The error Δ of the factorisation, which we define as the difference between the left hand side in (5.9) and the right hand side, is of the order $\mathcal{O}(10^{-5})$, that is of the order of the Monte Carlo noise. In order to track the evolution of the error Δ we also compute the joint likelihood (5.9) for smaller subsamples; see tab. 5.3. Reducing N to $N = 10^4$ we obtain an even smaller joint likelihood of $p = 0.02\%$ but with an error that is of the same magnitude. With $N = 10^3$ we do not have a single hit for the joint Monte Carlos leading to $p = 0\%$ with the same error as in the $N = 10^4$ case of $\Delta = 0.02\%$. Note that just one Monte Carlo hit in favour of the joint case would raise the error here to $\Delta = 0.08\%$. In the end, the convergence of the joint likelihood appears to be very slow with respect to the sample size N .

Furthermore we are interested in the stability of the results for Δ with respect to changes in the measured data. For this we choose the WMAP(1yr) values:

$$(5.10) \quad S_{\text{full}}^{\text{trunc,pseudo-}C_\ell} = 10154 \mu\text{K}^4 \quad \text{and} \quad S_{\text{ww}}^{\text{ILC}(1\text{yr})} = 0.7731.$$

We use a sample of the full size $N = 10^5$ and obtain a joint likelihood with respect to the one-year data of $p = 0.001\%$ with an error $\Delta = 0.002\%$. That is, with respect to one-year data both the joint likelihood and its error are of the order of the Monte Carlo noise. From the WMAP(1yr) data alone we could exclude the joint case (5.9) rather conservatively at 99.99% C.L. This appears to be a stronger exclusion than the one from three-year data. But we do not bother much about the difference because of the different estimators that have been used by the WMAP team for the angular power spectrum (pseudo- C_ℓ vs. MLE) [WMAa].

sample size N	joint p	error Δ
100000	0.048%	0.008%
100000 ^b	0.001%	0.002%
10000	0.02%	0.02%
1000	0%	0.02%

TABLE 5.1. Joint likelihoods (5.9) for $S_{\text{full}}^{\text{trunc}}$ and S_{ww} being in accordance with data simultaneously. The experimental values refer to WMAP's ILC(3yr) map [WMAa] except for the second row. The error Δ of the factorisation in equation (5.9) is the difference between left hand side and right hand side in that equation.

We quote here the most conservative result, namely the full sample joint likelihood case for S_{ww} and $S_{\text{full}}^{\text{trunc}}$ with respect to the WMAP(3yr) data. Therefore we can exclude that case at $> 99.95\%$ C.L. with an error in the third digit after the comma lying within the Monte Carlo error of the used sample ($N = 10^5$).

Finally we attempt to analyse the correlation of the all-sky power statistic $S_{\text{full}}^{\text{trunc}}$ and the intrinsic multipole alignment S_{ww} by quantitative means. It is well known from statistics, that when checking a finite two-dimensional sample for correlations, the *empiric covariance*

$$(5.11) \quad \text{cov}[S_{\text{full}}^{\text{trunc}}, S_{\text{ww}}] \equiv \frac{1}{N-1} \sum_{i=1}^N (S_{\text{full},i}^{\text{trunc}} - \bar{S}_{\text{full}}^{\text{trunc}}) (S_{\text{ww},i} - \bar{S}_{\text{ww}})$$

is a crucial quantity. The bar stands for the mean of a variable. As the covariance is a scale dependent measure, i.e. depending on the magnitudes of the sample values $S_{\text{ww},i}$ and $S_{\text{full},i}^{\text{trunc}}$, the dimensionless Bravais-Pearson coefficient or *empirical correlation coefficient* is the better expression to use:

$$(5.12) \quad \rho_{S_{\text{full}}^{\text{trunc}}, S_{\text{ww}}} \equiv \frac{\text{cov}[S_{\text{full}}^{\text{trunc}}, S_{\text{ww}}]}{\sqrt{\text{cov}[S_{\text{full}}^{\text{trunc}}, S_{\text{full}}^{\text{trunc}}] \text{cov}[S_{\text{ww}}, S_{\text{ww}}]}}.$$

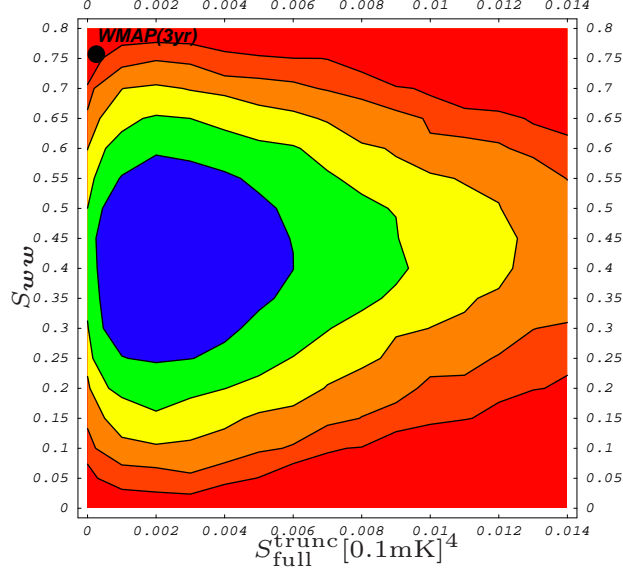


FIGURE 5.6. Scatter contour of pairs of S_{ww} and $S_{\text{full}}^{\text{trunc}}$ after an axial modification of $a_{\ell 0} = 70\mu\text{K}$ has been applied; this is the contribution involving maximal improvement in S_{ww} (see fig. 5.3). The total number of Monte Carlo pairs is $N = 10^5$. Note that the horizontal axis now runs from zero to $1.4 \times 10^{-6} \text{mK}^4$, whereas in fig. 5.5 the maximal displayed value is $4 \times 10^{-7} \text{mK}^4$. The inclusion of a preferred axis leaves all-sky multipole power and intrinsic alignment totally uncorrelated and inconsistent with the WMAP(3yr) data. Contour lines are defined as in fig. 5.5.

Finally, employing the WMAP(3yr) data we obtain an empirical correlation coefficient of

$$\rho_{S_{\text{full}}^{\text{trunc}}, S_{ww}} = -0.0027,$$

with respect to the full sample $N = 10^5$, which indeed indicates *only marginal correlation*.

5.4. Inclusion of a Preferred Axis

Now we ask what happens when introducing axial contributions on top of a statistically isotropic and gaussian microwave sky. The presence of a preferred direction with axisymmetry in the CMB will exclusively excite the zonal modes in case the axis is collinear to the z -axis. Here we do not bother about external directions since the internal alignments are independent of these. Therefore such an axis will manifest itself through additional contributions $a_{\ell 0}$. We are considering the quadrupole and the octopole and the question arises, in how far the sign of the axial contributions $\pm a_{\ell 0}$ plays a role. The coefficients $a_{\ell m}$ can be reconstructed from

$$(5.13) \quad a_{\ell m} = \int \frac{\Delta T}{T}(\theta, \varphi) Y_{\ell m}^* d\Omega.$$

Obviously, within the quadrupole the sign of $\pm a_{20}$ is irrelevant because of the symmetry of the Legendre Polynomial P_2 with respect to $\theta = 90^\circ$. The Legendre Polynomial P_3 however is antisymmetric with respect to $\theta = 90^\circ$. Therefore the relevance of the sign of the octopole contributions a_{30} has to be clarified. Consequently we have chosen a fixed value for the axial quadrupole contribution a_{20} and have then varied the according octopole contribution in sign and in magnitude. The results are displayed in fig. 5.4. Apparently the S_{nn} and S_{ww} statistics that are important here, do not distinguish between the sign of the applied axial effect. Therefore we need not to bother about the signs of the $a_{\ell 0}$ and let them henceforth be positive.

In Figure 5.3 the evolution of the S_{ww} and S_{nn} statistics with respect to increasing axial contributions is displayed in terms of likelihood histograms:

Let us first look at the evolution of the S_{nn} statistic. This expression measures the average $|\cos|$ of the angles between the quadrupole oriented area and the octopole areas. The pure Monte Carlo peaks at 0.5 reflecting the fact that the average distance of four isotropically distributed vectors on a half-sphere from each other is 60° in the case of statistical isotropy. It is a half-sphere because the signs of the multipole vectors are arbitrary and so we choose them all to point to the northern hemisphere. When increasing the contribution of the axial effect the multipoles become increasingly zonal and arrive at being purely zonal in a good approximation at values of $a_{\ell 0} = 1000\mu\text{K}$. On the level of the multipole vectors this means that their cross products all move to the equatorial plane (see fig. 5.2). That is the reason why the histogram in fig. 5.3 (left) moves to the right when we increase the axial effect, because now isotropy is broken from the half-sphere to the half-circle making the S_{nn} histogram peak sharper at higher values. The measured value from the ILC(3yr) map of $S_{nn}^{\text{ILC}(3\text{yr})} = 0.868$ is anomalous at 98.3% C.L. with respect to the pure Monte Carlo (bold histogram in fig. 5.3 which stands for the statistically isotropic and gaussian model). By adding axial contribution the maximal improvement is reached at $a_{\ell 0} = 100\mu\text{K}$ where the ILC(3yr) becomes unexpected at 96.7% C.L. Further enhancement of the axial effect makes the S_{nn} statistic more and more narrow around an expectation value < 0.7 . This makes it impossible to remove the anomaly in the S_{nn} cross-alignment with respect to the ILC(3yr) experimental value only by increasing the axial contribution to high enough values.

On the other hand the S_{ww} statistic additionally measures the modulus of the sin of the angles between the multipole vectors themselves. As can be seen from fig. 5.2 multipole vectors are all moving toward the north pole clustering more and more as the axial contribution is enhanced. The S_{ww} statistic measures the average of the modulus of the products of the sin of angles between quadrupole vectors, octopole vectors and the cos of the angle between the area vectors. Therefore on top of the information already contained in S_{nn} the S_{ww} statistic is able to go to zero for highest zonal contamination as the closeness of the multipole vectors in that case dampens the product of sines and cosines quadratically to arbitrary small values. Thus we find that S_{ww} is the more convenient statistic for further analyses, as it does contain more information than the S_{nn} statistic and additionally shows a simple and clear asymptotic behaviour. In the case of this statistic the anomaly is significant at 99.5% C.L. with respect to $S_{ww}^{\text{ILC}(3\text{yr})} = 0.7604$. Similarly to before the maximal improvement is reached with an axial contribution of $a_{\ell 0} = 70\mu\text{K}$, which degrades the anomaly in S_{ww} to 99.2% C.L.

Now we return to the correlation analysis of the alignment with the pure multipole power C_ℓ . When introducing an axial effect, say $a_{\ell 0} = 100\mu\text{K}$, we improve the fit to the S_{ww} statistic, but interestingly the multipole power anomaly becomes much more pronounced. This behaviour is expected [RRS06b, RRS06a] for the C_ℓ -distribution (being a modified χ^2 -distribution) when the axial contribution is enhanced, but it is unexpected that exactly the same happens for a multipole power distribution ‘that knows of the intrinsic alignment of quadrupole and octopole’. This indicates that there is no correlation at all between multipole power and the phase alignment even when they are tuned to each other.

Proceeding with the analysis of correlations between alignment and the full-sky power statistic, again we try to provoke correlation with the help of axial symmetry in the CMB. In fact we apply an axial effect of the ideal magnitude ($a_{\ell 0} = 70\mu\text{K}$) in order to achieve larger values in S_{ww} . The negative result is shown in fig. 5.6: as $S_{\text{full}}^{\text{trunc}}$ is a linear combination of squared C_ℓ distributions it is a sharply peaked χ^2 -like distribution being very sensitive to axial contributions. Therefore the contour in fig. 5.7 is fairly shifted to the right (to higher values in $S_{\text{full}}^{\text{trunc}}$) and broadened with respect to the axially unmodified case, obviating any correlation with the intrinsic alignment. The shape of the overall contour is roughly left invariant by the scale shift in $S_{\text{full}}^{\text{trunc}}$.

The fig. 5.7 illustrates the pure zonal case. Here a whole $a_{\ell 0} = 1000\mu\text{K}$ has been induced into the multipole vectors. Again, due to the sensitivity of $S_{\text{full}}^{\text{trunc}}$ to axial contamination this pushes the allowed region in the scatter plot to very high values in full-sky power squared, degenerating

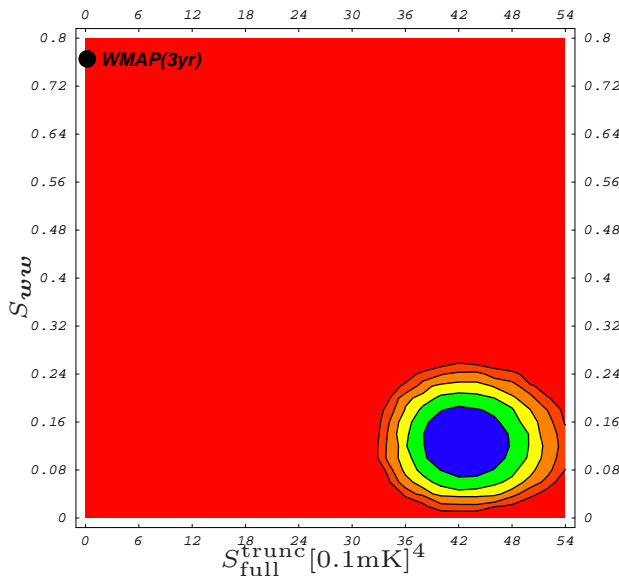


FIGURE 5.7. Contour plot of the scatter of pairs $(S_{ww}, S_{\text{full}}^{\text{trunc}})$ after a strong axial contingent of $a_{\ell 0} = 1000\mu\text{K}$ is induced to the multipole vectors (see also fig. 5.2 and fig. 5.3). The total number of Monte Carlo pairs is $N = 10^5$. The all-sky power statistic reacts heavily as the scale on the $S_{\text{full}}^{\text{trunc}}$ -axis is shifted by four orders of magnitude with respect to the case of $a_{\ell 0} = 70\mu\text{K}$ (fig. 5.6). The likelihood maximum departs very articulately from the WMAP(3yr) data. The contour lines are defined like in fig. 5.5.

the contour to a ‘small’ area far away from the measured three-year WMAP values. No change in correlation is observable.

Obviously, no coupling of the multipole power statistic and the intrinsic alignment can be driven in favour of the anomalous experimental CMB data by an additional axisymmetric effect on top of the primordial fluctuations.

5.5. Conclusion

We have shown that a literal interpretation of the ‘Axis of Evil’ as an axisymmetric effect is highly incompatible with the observed microwave sky at the largest angular scales. The formalism of multipole vectors was used to separate directional information from the absolute power of multipoles on the CMB sky. Considered were two choices of statistic, measuring the intrinsic cross-alignment between the quadrupole and octopole: the S_{nn} and the S_{ww} statistic. We confirm that the S_{ww} statistic contains more information on the multipoles and that it has more discriminative power as an axial effect is included. The presence of an axial symmetry in the CMB would excite zonal modes which are, in the frame of the axis, additional $a_{\ell 0}$ contributions in the language of the harmonic decomposition. Both statistics (S_{nn} and S_{ww}) reach slightly better agreement with the measured values from the ILC(3yr) map at amplitudes of roughly $a_{\ell 0} = 100\mu\text{K}$. Further enhancement of the axial effect only reduces consistency with WMAP(3yr) data.

Especially we have assayed in what way the alignment anomaly between quadrupole and octopole can affect the respective multipole power. We made several tests where we identified and selected the ‘anomalous $a_{\ell m}$ ’ that are still consistent with data and checked whether the resulting distribution from these $a_{\ell m}$ for either power or alignment shows any change with respect to the unbiased case. For the all-sky multipole power we make use of the statistic $S_{\text{full}}^{\text{trunc}}$. We demonstrated that the correlation between $S_{\text{full}}^{\text{trunc}}$ and intrinsic alignment is at most marginal –

correlation coefficient of -0.0027 . Thus a factorisation of the probability for the joint case into a product of the respective probabilities is allowed, c.f. (5.9).

We argued that the combined case of the measured all-sky power and the quadrupole-octopole alignment is anomalous at $> 99.95\%$ C.L. with respect to the WMAP three-year data. The correlation picture leaves no space for an axisymmetric effect in the large-angle CMB.

These findings complement our previous studies from chap. 4 of the interplay of an axisymmetric effect and the extrinsic CMB anomalies (correlation with the motion and orientation of the Solar system [SSHC04]). In that work it was suggested that an axisymmetric effect might help to explain a Solar system alignment. Finally, this study rules out that possibility.

But there is a loophole. Here and in chap. 4 we only considered *additive* modifications of the $a_{\ell m}$. Still, a preferred axis could also induce *multiplicative* modifications in all $a_{\ell m}$, see e.g. [GHHC05]. This could avoid the problem of additional multipole power. However, multiplicative effects could only be achieved by non-linear physics, like systematics of the measurement or the map making process.

A modelling that would be able to consistently remove both the power and the intrinsic alignment problem for low- ℓ must mobilise a more complex pattern of modifications than the one induced by an axisymmetric effect. As already indicated by e.g. the odd extrinsic alignment with the ecliptic, c.f. tab. 4.1, *the CMB anomalies do rather require a special plane than a preferred axis*. The so called ‘Axis of Evil’ appears as just the normal vector of that plane, but no axial symmetry is present within that plane.

Summary and Outlook

In this thesis I have addressed current open questions of the cosmological standard model. I would like to close the scientific part of this work with a concise summary of the main issues that have been covered here, as well as some remarks with regard to future interesting work.

The Issue of Dark Energy. In chap. 1 we have discussed the main observational evidence in favour of the cosmological constant Λ . In particular, we have seen that observations of distant supernovae of type Ia support an accelerated expansion of the Universe. Additionally, the supernova data shows that this acceleration has set in at redshifts of order unity, that is in cosmological terms ‘recently’. This is referred to as the coincidence problem. Together with the CMB measurements and galaxy redshift surveys, the experimental findings form the cosmic concordance.

In chap. 1 we have also seen that the supernova data can potentially be explained within inhomogeneous models (LTB model, Szekeres model) without invoking Dark Energy. Also, the additional inclusion of CMB data has been carried out successfully by some groups. The methods we have used in chap. 1 to carry out analytic calculations in the LTB model can also be used in the context of cosmological backreaction. Cosmological backreaction is an conservative attempt to solve the Dark Energy problem, for it does not invoke any new fields or interactions. It is known that backreaction is indeed able to mimic Λ , but the actual magnitude of the effect is yet undetermined and subject to current debate. On the one hand the non-perturbative approach via the Buchert equations shows a lack of suitable observables, and on the other hand the perturbative approach, which deals with observables, becomes technically immensely complicated with higher orders. However, see [LS07] for an attempt of synthesis.

Addressing these problems, Thomas Buchert (Université Lyon 1), Dominik Schwarz and I have begun a project in which we are examining the effects of general relativistic averaging – carried out on the backward light cone of the observer – on the common cosmological distance measures, which are, the angular diameter distance and the luminosity distance. This is an ongoing work and its results are too preliminary to be written down in this thesis yet.

The Issue of Dark Matter. We have seen in chap. 2 that the evidence for Dark Matter is manifold. However, it should be emphasised that there is no a priori reason to believe that all of the missing matter problems on all of the different physical scales must have a common explanation.

The most important evidence comes from a simple astrophysical test, the galactic rotation curve. A fully general relativistic galaxy model has been proposed by Cooperstock and Tieu recently, and it was shown that this model can explain the observed flat rotation curves without any Dark Matter. It is claimed by CT that Newtonian models cannot reproduce certain intrinsically non-linear terms within the CT model, which shall appear already in the stationary and axisymmetric setup.

Nevertheless, it has been argued from various directions that the CT model gives rise to unphysical features. It is an open question whether the CT solution could provide an effective model, and to which extent the breakdown of its Newtonian limit might indicate its usefulness or its difficulties.

In chap. 2 we have shown that the CT solution does not belong to the class of the most general axisymmetric and stationary solutions. Therefore the CT solution is less general and this restriction might be a reason for the problems of the model.

Moreover, we found the surprising fact that the classical Newtonian metric is not appropriate for a weak field limit of the CT theory, because the incorporation of a post-Newtonian potential is necessary to make physical sense.

We then concerned ourselves with the analysis of rotating (Post-) Newtonian spacetimes in order to find a simplified model. We applied the full machinery of the ADM formalism to the problem and we derived the exact 3 + 1-equations of motion for the static and for the rigidly rotated Post-Newtonian metric as well as approximate results for the differentially rotated case. We found that it is necessary to go to full quadratic order in the potentials of the differentially rotated PN metric to obtain a viable Newtonian limit, which will be done in the near future.

The Issue of the CMB Anomalies. The one-year CMB data taken by the WMAP exhibits several unanticipated features, especially within the smallest multipole moments (quadrupole and octopole). These findings have been widely confirmed after the WMAP three-year data release. The features are referred to as ‘anomalous’ because they contradict the predictions made by the standard inflationary Λ CDM model – especially the statistical isotropy. In chap. 4 and chap. 5 we have presented the various shapings of the anomalies in much detail. The odd features are present both in the CMB autocorrelation function $C(\theta)$ and in the phase relationships of the quadrupole and octopole.

In chap. 4 we focused on the anomalous alignments of the lowest multipoles with external (astrophysical) directions, like the CMB dipole or the characteristic directions of our Solar system. Inspired by the correlation with the dipole, we ask how extended extragalactic foregrounds would influence the CMB sky via the Rees-Sciama effect. The overdense structure responsible for the effect was modelled by a spherically symmetric LTB solution. We then made use of the analytic calculation of the Rees-Sciama effect – presented in chap. 1 – indicating that only the zonal CMB modes are modified by the effect (axisymmetry).

We have found that massive non-linear structures like the Shapley concentration (roughly 100Mpc away) are able to produce CMB contributions of up to 10^{-5} . For the axially symmetric setup we have shown that this effect does induce alignments, albeit not of the same form as extracted from WMAP, and that still rather a Solar system effect is preferred by the data.

The intrinsic alignment of the quadrupole and octopole, as well its relation to the anomalous lack of angular two-point correlation in the WMAP data was the subject of chap. 5. After carrying out a Monte Carlo cross-correlation analysis we could demonstrate the absence of correlations between the two sorts of anomalies. Based on this we were able to show that the combined case of the measured autocorrelation and the quadrupole-octopole alignment is anomalous at $> 99.95\%$ C.L. with respect to the WMAP three-year data.

The correlation picture leaves no space for an literal interpretation of the ‘Axis of Evil’ as an axisymmetric effect. As we pointed out in chap. 5 there are several models with a preferred axis in the literature which seek to provide an explanation for some of the anomalies. Our result enables us to put *stringent constraints on any model that exhibits an axial symmetry*.

But there is still a loophole for axial models. In this work we have considered *additive* modifications of the $a_{\ell m}$. Still, a preferred axis could also induce *multiplicative* modifications in all $a_{\ell m}$, see [GHHC05]. This could avoid the problem of additional multipole power. However, multiplicative effects could only be achieved by non-linear physics. In principle it is possible to get such a non-linear effect from the spectral distortion arising from the possible interaction of the CMB photons with small objects in the Kuiper Belt, the so called Trans-Neptunian objects, c.f. [BBS07]. This is a promising idea to pursue in the near future.

Moreover, I think that it is fruitful to carry out a similar Rees-Sciama analysis within the more complicated Szekeres model, c.f. sec. 1.3.2, because much more non-trivial symmetries can be expected there.

Acknowledgements

I come to a part that is easily written – for it reflects my very gratefulness. Dealing with the manifold physics that cosmology is ready to offer to the interested mind was not always easy and in the least cases perception occurred quickly. Still, the feeling, the evergrowing construct of knowledge gives to us, the view on its increasing elegance and purity as it seems to mimic nature, can only be shared by those who were ready to walk that path for a time. It would not have been possible to spend the enormous amount of time and effort for studying the physics that I admire so much without a number of people, whom to address here is a pleasure for me.

I hardly can imagine a better advisor than Dominik Schwarz. I hope that I succeed in writing a few lines of acknowledgement that are neither arbitrary nor standard. Finding an PhD advisor more willing to help, more offering guidance and being more motivating than Dominik, would be, to my opinion, very hard. For very numerous occasions I had the opportunity to absorb the remarkable flow of knowledge as well as the important subtle insights that he was always ready to offer without compromise. Besides being a mentor, he is a most pleasant research colleague from whom I could not only learn a whole lot of physics, but also how to approach it and how to take another perspective. I am grateful to him, for always finding some time for my questions, despite of his increasingly full time-table; and if it was only a few minutes in the elevator, clarifying my requests. And, what is most important to me, I want to thank Domink for giving me a chance.

Meinen Eltern gebührt mehr Dank als ich hier zum Ausdruck bringen könnte. Nichts von dem hier wäre möglich gewesen ohne den Zuspruch und die moralische Unterstützung, die sie mir jederzeit haben zuteil werden lassen.

I am grateful to Thomas Buchert and Syksy Räsänen for collaborating with me and sharing their ideas. Also, I thank them very much for supporting my job applications.

I want to thank Prof. Dietrich Bödeker for being a referee of this thesis. Also, I like to thank Prof. Reinhart Kögerler for being ‘Prüfungsvorsitzender’, and I am likewise grateful to Prof. Andreas Hütten for joining the group of referees.

I very much thank Florian Kühnel, Marina Seikel and Maik Stuke for proofreading parts of this thesis. Also, I am thankful to Benjamin Jurke for providing me a template of the underlying Latex. I am deeply indebted to Jan van der Heide for his heroic efforts in proofreading and his attempts to improve my English.

It is a pleasure to thank the members of the Bielefeld cosmology group for the nice working atmosphere we have shared and for always being open to lively and fruitful discussion.

I am grateful to the members of the Bielefeld theory department for the fantastic time in Bielefeld. To my experience, the social bonds within the Bielefeld group are unparalleled. Especially, I want to thank the people that (almost all) have already left the Bielefeld group some time ago, but with whom I shared a marvellous time, e.g. within our ‘extraordinary seminars’, and for many other occasions. In particular, it is a pleasure for me to mention: Matthias Döring, the crazy and ingenious Jörg Erdmann, André Fischer, Lars Fromme, Jan van der Heide, Kay Hübner, Jack Liddle, Kai Matzutt, Michael Seniuch, Stanislav Shcheredin, Wolfgang Söldner, Tim Stockamp, Christian Torrero and Sönke Wissel.

Finally, I want to thank the members of our football group for the many hot and intense battles that we fought and for the great time we shared. Especially, I like to mention Hans Pollpeter and Jan Schmalhorst who helped me with the organisation.

Part III

Appendices

APPENDIX A

Critical Values of Ω_m and Ω_Λ in the FRW Model

Here we give a discussion of the various, partly exotic, solutions that are possible within an FRW model with non-vanishing cosmological constant. The presentation partly refers to [FI86].

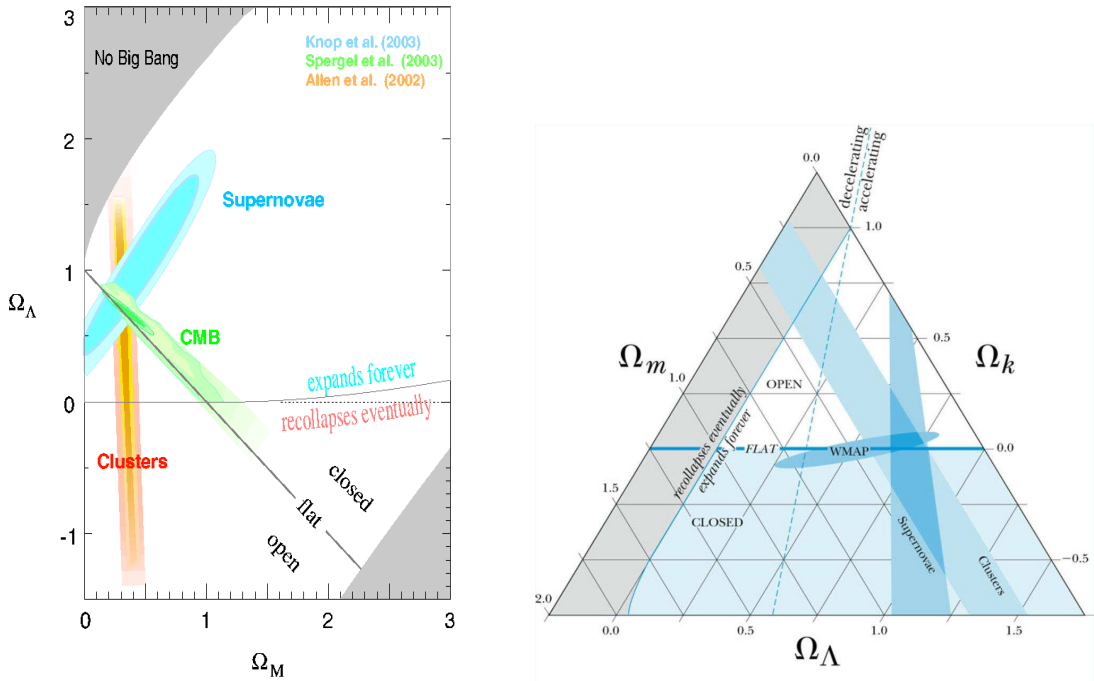


FIGURE A.1. Left: the cosmic concordance plot from fig. 1.4 has critical lines. For instance, there is a borderline formed by the *coasting* (sometimes also called *loitering* or *hesitating*) cosmologies that separates FRW models with a Big Bang from such without Big Bang in the upper left corner of the figure. Moreover there is an ‘expansion/recollapse’ borderline in the middle of the diagram. The derivation of the critical curves is given in the text. In the lower right corner of the figure there is another shaded region. This parameter region is falsified for it implies solutions where the Universe is younger than the oldest stars $t_0 \lesssim 9.6$ Gyr (with any $H_0 \gtrsim 50$ km s $^{-1}$ Mpc $^{-1}$ [P⁺98]). Right: an alternative way of plotting the concordance results in the form of a ‘cosmic triangle’. Pictures are taken from [Lid04] and [Gfr].

First, the line of geometrically closed, open or flat in the above fig. A.1 simply refers to the respective choice of k . The dynamics of the FRW model is governed by the Friedmann equation (1.14). Writing the Friedmann equation *today*, when the radiation is no more dominant, we have

$$(A.1) \quad \frac{k}{H_0^2 a_0^2} = \Omega_m + \Omega_\Lambda - 1,$$

such that we can read off the curvature lines in fig. A.1 by

$$(A.2) \quad \begin{aligned} \Omega_m + \Omega_\Lambda > 1 &\rightarrow k > 0, & \text{spatially closed} \\ \Omega_m + \Omega_\Lambda = 1 &\rightarrow k = 0, & \text{spatially flat} \\ \Omega_m + \Omega_\Lambda < 1 &\rightarrow k < 0, & \text{spatially open.} \end{aligned}$$

Next we consider the line of ‘acceleration/deceleration’ (see the cosmic triangle). Using dimensionless variables $R = a/a_0$ and $\tau = H_0 t$ we can write the Friedmann equation, after a bit of algebra, as follows

$$(A.3) \quad R_{,\tau}^2 = 1 + \Omega_m (R^{-1} - 1) + \Omega_\Lambda (R^2 - 1).$$

The deceleration parameter was defined in (1.42) and takes *today* the value

$$(A.4) \quad q_0 = - \left(\frac{a\ddot{a}}{\dot{a}^2} \right) \Big|_0,$$

where dots indicate differentiation with respect to cosmic time. Differentiation of equation (A.3) further gives

$$(A.5) \quad \frac{1}{H^2} \left(2 \frac{a\ddot{a}}{a_0^2} \right) = -\Omega_m \left(\frac{a_0 \dot{a}}{a^2} \right) + \Omega_\Lambda \left(2 \frac{a\dot{a}}{a_0^2} \right),$$

so that taking the equation today yields

$$(A.6) \quad q_0 = \frac{1}{2} \Omega_m - \Omega_\Lambda.$$

Thus, with $q_0 = 0$ we just get the dividing line $2\Omega_\Lambda = \Omega_m$ as indicated in the figure.

The critical lines of Λ are more interesting. For very high and positive values of Λ the Universe would lose its Big Bang in the past. The borderline for this is given by the class of Eddington-Lemaître models; in these models one employs a value for Λ that is slightly higher than Λ_{stat} which is in turn defined by the static (Einstein) limit: $\Lambda_{\text{stat}} \equiv 1/a_{\text{stat}}^2$. In the Eddington-Lemaître model the Universe rapidly expands from $a = 0$ (Big Bang) on and reaches a turning point near $a = a_{\text{stat}}$, where it mimics the Einstein model for an arbitrarily long time before it erupts again, now expanding to infinity; at the time of invention of the Eddington-Lemaître model it was hoped that the quasistatic feature in the model may provide time for structure formation, c.f. [Nar02]. The ‘Big Bang/no Big Bang’ borderline models are thus asymptotic to the Einstein model in their (infinite) past. Then models with $\Lambda < \Lambda_{\text{stat}}$ do have a Big Bang in the past, whereas models with $\Lambda > \Lambda_{\text{stat}}$ are collapsing from some infinite radius to a finite minimal scale where they turn around and reexpand again to infinity – this behaviour is also referred to as *catenary* or *bounce*. Analytic formulas for the according critical lines of Λ are readily obtainable. Besides the critical line of ‘Big Bang/no Big Bang’ we will also get a solution for models that are quasistatic in their infinite future and they form the ‘recollapse eventually/expand forever’ borderline in the figure. Models that are to be asymptotically equal to a static Einstein solution must obey the equation

$$(A.7) \quad \frac{K_0}{R_{\text{stat}}^2} = \Lambda_{\text{stat}} = \frac{3}{2} \underbrace{\left(\frac{8\pi G}{3} \rho \right)}_{\equiv C} \frac{1}{R_{\text{stat}}^3} \quad \text{with} \quad R_{\text{stat}} \equiv \frac{a_{\text{stat}}}{a_0},$$

where K_0 is the Gauss curvature $K_0 \equiv k/a_0^2$ and we used the rescaling $R \equiv a/a_0$ so that $R_0 = 1$ today. In fact, the static model conditions (A.7) are two separate equations so that we can eliminate R_{stat} and solve for the critical Lambda value

$$(A.8) \quad \Lambda_{\text{stat}} = \frac{4}{9} K_0^3 C^{-2} \quad \text{and} \quad C = \Omega_m H_0^2.$$

On the other hand we have from the Friedmann equation, as evaluated today,

$$(A.9) \quad K_0 = H_0^2 (\Omega_m + \Omega_\Lambda - 1).$$

We now can insert this into (A.8) and bring the result to a form convenient for the following steps,

$$(A.10) \quad \frac{\Lambda_{\text{stat}}}{12\Omega_m H_0^2} = \frac{1}{27} (\Omega_m + \Omega_\Lambda - 1)^3 \frac{1}{\Omega_m^3}.$$

It is useful to define the following function

$$(A.11) \quad x \equiv \left(\frac{\Lambda_{\text{stat}}}{12\Omega_m H_0^2} \right)^{1/3} = \left(\frac{\Omega_\Lambda}{4\Omega_m} \right)^{1/3},$$

such that we can rewrite equation (A.10)

$$(A.12) \quad x^3 = \left[\frac{1}{3} (1 - \Omega_m^{-1} + 4x^3) \right]^3.$$

Now, taking the three-root is unique and we get

$$(A.13) \quad x^3 - \frac{3}{4}x + \frac{1}{4} \frac{\Omega_m - 1}{\Omega_m} = 0,$$

a dimensionless inhomogeneous cubic equation. One possibility of solving (A.13) is to use the method by Cardano and Tartaglia: first, the ‘discriminant’ is given by

$$(A.14) \quad \Delta \equiv \alpha^{-2} (\beta^2 + 4\gamma^3) = \frac{1}{16} (1 - 2\Omega_m) \frac{1}{\Omega_m^2},$$

and moreover we define

$$(A.15) \quad p \equiv \frac{1}{2} \left[-\beta + (\beta^2 + 4\gamma^3)^{1/3} \right] = \frac{1}{2} \left[\frac{1}{4} (1 - \Omega_m) \Omega_m^{-1} + \Delta^{1/2} \right],$$

with the identities $\alpha = 1$, $-\beta = 1/4(1 - \Omega_m)\Omega_m^{-1}$ and $\gamma = -1/4$. The solutions are formulated for x , but our aim was to convert these to solutions for Ω_m and Ω_Λ . Consequently we are here interested only in the positive and real roots of the cubic equation and with these constraints the trigonometric form of solution [Tur52] is more convenient than the above form. The borderline of models that expand to infinity to those that recollapse is given by the solutions that are quasistatic in the infinite future. For universes that are to expand to infinity we get the following trigonometric solution

$$(A.16) \quad \Omega_\Lambda \geq \begin{cases} 0 & \text{for } 0 \leq \Omega_m \leq 1 \\ 4\Omega_m \left\{ \cos \left[\frac{1}{3} \arccos \left(\frac{1-\Omega_m}{\Omega_m} \right) + \frac{4\pi}{3} \right] \right\}^3 & \text{for } \Omega_m > 1 \end{cases}.$$

The critical line of Big Bang/no Big Bang is characterised by those models that have been quasistatic in the infinite past. Models without an initial singularity are characterised by

$$(A.17) \quad \Omega_\Lambda \geq \begin{cases} 4\Omega_m \left\{ \cos \left[\frac{1}{3} \arccos \left(\frac{1-\Omega_m}{\Omega_m} \right) \right] \right\}^3 & \text{for } \Omega_m > \frac{1}{2} \\ 4\Omega_m \left\{ \cosh \left[\frac{1}{3} \operatorname{arccosh} \left(\frac{1-\Omega_m}{\Omega_m} \right) \right] \right\}^3 & \text{for } \Omega_m < \frac{1}{2} \end{cases}.$$

Note that the join at $\Omega_m = \frac{1}{2}$ is perfectly analytic. The need for two formulas to represent a single function is an artefact of solving cubic equations as it is discussed by [Tur52]: ‘From a real cubic, three real roots cannot be extracted by Cardano’s formula without a circuitous passage into, and out of, the domain of complex numbers’.

APPENDIX B

Details of the Lemaître-Tolman-Bondi Model

Here the field equations for the LTB model and for its more general progenitor model are given. First let us recall the Einstein field equations of gravity with cosmological constant ($c \equiv 1$)

$$(B.1) \quad R_{\alpha\beta} - \frac{1}{2}Rg_{\alpha\beta} + \Lambda g_{\alpha\beta} = 8\pi GT_{\alpha\beta}.$$

The definition that is used throughout this work for the energy momentum tensor is the one from (2.39)

$$(B.2) \quad T^{\alpha\beta} = (\rho + p)u^\alpha u^\beta + pg^{\alpha\beta} \quad \text{with} \quad u^\alpha u_\alpha = -1,$$

The used metric signature is $(-, +, +, +)$ which here corresponds to $T^{\alpha\beta} = \text{diag}(\rho, p, p, p)$ but $T^\alpha_\beta = \text{diag}(-\rho, p, p, p)$. The combination $G_{\alpha\beta} \equiv R_{\alpha\beta} - \frac{1}{2}Rg_{\alpha\beta}$ is referred to as the Einstein tensor. Given a spacetime representation $g_{\mu\nu}$ the Christoffel symbols are calculated via

$$(B.3) \quad \Gamma^\alpha_{\beta\gamma} \equiv \frac{1}{2}g^{\alpha\delta}(g_{\beta\delta,\gamma} + g_{\gamma\delta,\beta} - g_{\beta\gamma,\delta}).$$

The Riemann curvature tensor can be expressed in coordinate notation as

$$(B.4) \quad R^\alpha_{\beta\gamma\delta} \equiv \Gamma^\alpha_{\beta\delta,\gamma} - \Gamma^\alpha_{\beta\gamma,\delta} + \Gamma^\epsilon_{\beta\delta}\Gamma^\alpha_{\epsilon\gamma} - \Gamma^\zeta_{\beta\gamma}\Gamma^\alpha_{\zeta\delta}.$$

The Ricci tensor is defined as the trace of the Riemann tensor

$$(B.5) \quad R_{\beta\delta} \equiv R^\alpha_{\beta\alpha\delta},$$

and taking the trace of the Ricci tensor we define the Ricci scalar

$$(B.6) \quad R \equiv R^\delta_\delta.$$

The respective quantities in their three-dimensional versions are defined analogously; in the above relations one only changes greek to latin indices. The spatial Ricci scalar is written in caligraphics ${}^{(3)}R \equiv \mathcal{R}$. The following results refer to [PK06] and [Bon47] as well as to my own calculations.

B.1. General Spherically Symmetric Spacetime with Zero Vorticity

We first discuss a more general case than the LTB solution from which the LTB model originates. When the matter model is that of a perfect fluid, the vorticity vanishes for spherically symmetric spacetimes. The synchronous gauge is then justified and the metric takes the general form (1.43)

$$(B.7) \quad ds^2 = -e^C dt^2 + e^A dr^2 + R^2 (d\theta^2 + \sin^2\theta d\varphi^2).$$

Note that there may be an ambiguity with the term ‘synchronous gauge’ which is sometimes used differently in the literature. What we mean here (following [PK06]), is that there are no mixing terms in the metric. Further, the metric coefficients C, A and R are functions of (r, t) only. The four-velocity field takes the form

$$(B.8) \quad u^\alpha = e^{-C/2}.$$

Then the field equations read

$$(B.9) \quad G^0_0 = \frac{1}{R^2} + e^{-C} \left(\frac{R_{,t}^2}{R^2} + \frac{A_{,t}R_{,t}}{R} \right) - e^{-A} \left(2\frac{R_{,r,r}}{R} + \frac{R_{,r}^2}{R^2} - \frac{A_{,r}R_{,r}}{R} \right) = 8\pi G\rho + \Lambda,$$

$$(B.10) \quad G^1_1 = \frac{1}{R^2} + e^{-C} \left(2\frac{R_{,t,t}}{R} + \frac{R_{,t}^2}{R^2} - \frac{C_{,t}R_{,t}}{R} \right) - e^{-A} \left(\frac{R_{,r}^2}{R^2} + \frac{C_{,r}R_{,r}}{R} \right) = -8\pi Gp + \Lambda,$$

$$(B.11) \quad G^2_2 = G^3_3 = \frac{1}{4} e^{-C} \left[4\frac{R_{,t,t}}{R} + 2\frac{R_{,t}(A_{,t} - C_{,t})}{R} + 2A_{,t,t} + A_{,t}^2 - C_{,t}A_{,t} \right] - \frac{1}{4} e^{-A} \left[4\frac{R_{,r,r}}{R} + 2\frac{R_{,r}(C_{,r} - A_{,r})}{R} + 2C_{,r,r} + C_{,r}^2 - C_{,r}A_{,r} \right] = -8\pi Gp + \Lambda,$$

$$(B.12) \quad G^1_0 = e^{-A} \left[2\frac{R_{,t,r}}{R} - \frac{A_{,t}R_{,r}}{R} - \frac{R_{,t}C_{,r}}{R} \right] = 0.$$

In this general case also a mass term can be assigned. Multiplying (B.9) by $R^2R_{,r}$ and applying (B.12) we end up with

$$(B.13) \quad \frac{\partial}{\partial r} \left(R + e^{-C}RR_{,t}^2 - e^{-A}RR_{,r}^2 - \frac{1}{3}\Lambda R^3 \right) = 8\pi G\rho R^2R_{,r}.$$

Analogously, we can multiply (B.10) by $R^2R_{,t}$ and get

$$(B.14) \quad \frac{\partial}{\partial t} \left(R + e^{-C}RR_{,t}^2 - e^{-A}RR_{,r}^2 - \frac{1}{3}\Lambda R^3 \right) = -8\pi GpR^2R_{,t}.$$

Now, a look at (B.13) suggests that it makes sense to define the term in the brackets as a mass

$$(B.15) \quad m(r) \equiv \frac{1}{2} \left(R + e^{-C}RR_{,t}^2 - e^{-A}RR_{,r}^2 - \frac{1}{3}\Lambda R^3 \right),$$

such that (B.13) upon integration yields

$$(B.16) \quad m(r) = 4\pi G \int_{r_0}^r \rho R^2 R_{,r'} dr'.$$

Therein we take the r_0 such that it coincides with $R = 0$. The second equation (B.14) can then be interpreted as an energy conservation, where the work done by volume change equals the rate of change of mass. As a simple example one could consider a spherical body, e.g. a star modelled with the above equations. At the surface of the star the pressure is zero and thus the conservation equation (B.14) says $m_{,t} = 0$, i.e. the total stellar mass remains constant with time for a star that is surrounded by vacuum.

B.2. Einstein Equations of the Lemaître-Tolman-Bondi Model

Under the assumption of zero pressure (i.e. dust) C can be transformed away $C = 0$ and solving the off-diagonal Einstein equation (B.12) which can be written also in the form of (1.44) determines the form of e^A (1.45) up to an arbitrary function $\mathcal{E}(r)$. Thus the metric takes the LTb form

$$(B.17) \quad ds^2 = -dt^2 + \frac{R_{,r}^2}{1 + \mathcal{E}} dr^2 + R^2(d\theta^2 + \sin^2\theta d\varphi^2).$$

The according non-vanishing Christoffel symbols read

$$\begin{aligned}
\Gamma^1_{01} &= \frac{R_{,t,r}}{R_r}, & \Gamma^2_{02} = \Gamma^3_{03} &= \frac{R_{,t}}{R}, & \Gamma^0_{11} &= \frac{R_{,r}R_{,t,r}}{1+\mathcal{E}}, & \Gamma^0_{22} &= RR_{,t}, \\
\Gamma^0_{33} &= RR_{,t} \sin^2\theta, & \Gamma^1_{11} &= \frac{R_{,r,r}}{R_r} \frac{\mathcal{E}_{,r}}{2(1+\mathcal{E})}, & \Gamma^2_{12} = \Gamma^3_{13} &= \frac{R_{,t}}{R}, \\
\Gamma^1_{22} &= -\frac{R}{R_r}(1+\mathcal{E}), & \Gamma^1_{33} &= -\frac{R}{R_t}(1+\mathcal{E}) \sin^2\theta, & \Gamma^2_{33} &= -\sin\theta \cos\theta, \\
\Gamma^3_{23} &= \cot\theta.
\end{aligned}
\tag{B.18}$$

The Riemann curvature tensor takes the form

$$R = 2\frac{R_{,t,t,r}}{R_r} + 4\frac{R_{,t,t}}{R} + 2\frac{2R_{,t}R_{,t,r} - \mathcal{E}_{,r}}{RR_{,r}} + 2\frac{R_{,t}^2 - \mathcal{E}}{R^2},
\tag{B.19}$$

and the non-vanishing components of the Ricci tensor are

$$\begin{aligned}
R^0_0 &= \frac{R_{,t,t,r}}{R_r} + 2\frac{R_{,t,t}}{R}, & R^1_1 &= \frac{R_{,t,t,r}}{R_r} + \frac{2R_{,t}R_{,t,r}}{RR_{,r}} - \frac{\mathcal{E}_{,r}}{RR_{,r}}, \\
R^2_2 = R^3_3 &= \frac{R_{,t}^2}{R^2} + \frac{R_{,t,t}}{R} - \frac{\mathcal{E}}{R^2} + \frac{R_{,t}R_{,t,r}}{RR_{,r}} - \frac{\mathcal{E}_{,r}}{2RR_{,r}}.
\end{aligned}
\tag{B.20}$$

The Einstein equations of the LTB model read

$$G^0_0 = \frac{R_{,t}^2 - \mathcal{E}}{R^2} + \frac{2R_{,t,r}R_{,t} - \mathcal{E}_{,r}}{RR_{,r}} = 8\pi G\rho + \Lambda,
\tag{B.21}$$

$$G^1_1 = 2\frac{R_{,t,t}}{R} + \frac{R_{,t}^2 - \mathcal{E}}{R^2} = -8\pi Gp + \Lambda,
\tag{B.22}$$

$$G^2_2 = G^3_3 = \frac{R_{,t,t,r}}{R_r} + \frac{R_{,t,t}}{R} + \frac{1}{2} \frac{2R_{,t,r}R_{,t} - \mathcal{E}_{,r}}{RR_{,r}} = -8\pi Gp + \Lambda.
\tag{B.23}$$

When using these results, please take care of the sign convention for the Einstein equations, energy momentum tensor, Riemann tensor and so forth that has been used here. The consistency of the signs can be checked by performing the FRW limit on the LTB equations.

Rotating Post-Newtonian Metrics

C.1. Full Differential Rotation

We apply the following transformation involving full differential rotation,

$$(C.1) \quad \varphi = \varphi' - \omega(t, r, z)t$$

on the following Post-Newtonian metric

$$(C.2) \quad ds^2 = -(1 + 2\phi)dt^2 + (1 - 2\psi)(dr^2 + r^2d\varphi^2 + dz^2).$$

In component notation the transformed spacetime then reads

$$(C.3) \quad \begin{aligned} g_{tt} &= -(1 + 2\phi) + (1 - 2\psi)(\omega + \omega_{,tt})^2 r^2, & g_{tr} &= (1 - 2\psi)2tr^2(\omega + \omega_{,tt})\omega_{,rt}, \\ g_{t\varphi} &= -(1 - 2\psi)2r^2(\omega + \omega_{,tt}), & g_{tz} &= (1 - 2\psi)2r^2(\omega + \omega_{,tt})\omega_{,zt}, \\ g_{rr} &= (1 - 2\psi)(1 + r^2\omega_{,r}^2 t^2), & g_{r\varphi} &= -(1 - 2\psi)2r^2\omega_{,rt}, \\ g_{rz} &= (1 - 2\psi)2r^2\omega_{,r}\omega_{,zt}^2, & g_{\varphi\varphi} &= (1 - 2\psi)r^2, \\ g_{\varphi z} &= -(1 - 2\psi)2r^2\omega_{,zt}, & g_{zz} &= (1 - 2\psi)(1 + r^2\omega_{,z}^2 t^2). \end{aligned}$$

C.2. Spatial Curvature Terms

C.2.1. Static Newton Metric. From the non-rotating PN metric in *cartesian* coordinates

$$(C.4) \quad ds^2 = -(1 + 2\phi)dt^2 + (1 - 2\psi)(dx^2 + dy^2 + dz^2),$$

we have computed – using the notation $(1, 2, 3) \hat{=}(x, y, z)$ – the following non-zero components of the *spatial Christoffel symbols*

$$(C.5) \quad \begin{aligned} \Gamma^1_{11} &= -\frac{\psi_{,x}}{1 - 2\psi}, & \Gamma^1_{22} &= \frac{\psi_{,x}}{1 - 2\psi}, & \Gamma^1_{33} &= \frac{\psi_{,x}}{1 - 2\psi}, & \Gamma^1_{12} &= -\frac{\psi_{,y}}{1 - 2\psi}, \\ \Gamma^1_{13} &= -\frac{\psi_{,z}}{1 - 2\psi}, & \Gamma^2_{22} &= -\frac{\psi_{,y}}{1 - 2\psi}, & \Gamma^2_{11} &= \frac{\psi_{,y}}{1 - 2\psi}, & \Gamma^2_{33} &= \frac{\psi_{,y}}{1 - 2\psi}, \\ \Gamma^2_{12} &= -\frac{\psi_{,x}}{1 - 2\psi}, & \Gamma^2_{23} &= -\frac{\psi_{,z}}{1 - 2\psi}, & \Gamma^3_{33} &= -\frac{\psi_{,z}}{1 - 2\psi}, & \Gamma^3_{22} &= \frac{\psi_{,z}}{1 - 2\psi}, \\ \Gamma^3_{11} &= \frac{\psi_{,z}}{1 - 2\psi}, & \Gamma^3_{32} &= -\frac{\psi_{,y}}{1 - 2\psi}, & \Gamma^3_{31} &= -\frac{\psi_{,x}}{1 - 2\psi}. \end{aligned}$$

For the three-dimensional Ricci tensor we get the following non-vanishing components

$$(C.6) \quad \begin{aligned} R_{11} &= 2\frac{\psi_{,x,x}}{1 - 2\psi} + \frac{\psi_{,y,y}}{1 - 2\psi} + \frac{\psi_{,z,z}}{1 - 2\psi} + 4\left(\frac{\psi_{,x}}{1 - 2\psi}\right)^2 + \left(\frac{\psi_{,y}}{1 - 2\psi}\right)^2 + \left(\frac{\psi_{,z}}{1 - 2\psi}\right)^2, \\ R_{22} &= \frac{\psi_{,x,x}}{1 - 2\psi} + 2\frac{\psi_{,y,y}}{1 - 2\psi} + \frac{\psi_{,z,z}}{1 - 2\psi} + \left(\frac{\psi_{,x}}{1 - 2\psi}\right)^2 + 4\left(\frac{\psi_{,y}}{1 - 2\psi}\right)^2 + \left(\frac{\psi_{,z}}{1 - 2\psi}\right)^2, \\ R_{33} &= \frac{\psi_{,x,x}}{1 - 2\psi} + \frac{\psi_{,y,y}}{1 - 2\psi} + 2\frac{\psi_{,z,z}}{1 - 2\psi} + \left(\frac{\psi_{,x}}{1 - 2\psi}\right)^2 + \left(\frac{\psi_{,y}}{1 - 2\psi}\right)^2 + 4\left(\frac{\psi_{,z}}{1 - 2\psi}\right)^2, \\ R^i_k &= \frac{\psi_{,i,k}}{(1 + 2\psi)^2} + 3\frac{\psi_{,i}\psi_{,k}}{(1 + 2\psi)^3} \simeq \psi_{,i,k} \quad \text{for } i \neq k. \end{aligned}$$

Therefore the spatial Ricci scalar becomes

$$(C.7) \quad \mathcal{R} = \frac{4}{(1-2\psi)^2} \Delta_{\text{cart}}^{(3)} \psi + \frac{6}{(1-2\psi)^3} (\nabla_{\text{cart}}^{(3)} \psi)^2 \simeq 4\Delta_{\text{cart}}^{(3)} \psi.$$

C.2.2. Rotating PN Metrics. Let us consider the constantly rotating ($\omega = \text{const.}$) Post-Newtonian metric to exact order,

$$(C.8) \quad ds^2 = [(1-2\psi)\omega^2 r^2 - (1+2\phi)]dt^2 + (1-2\psi)(dr^2 + dz^2) + (1-2\psi)r^2 d\varphi^2 - (1-2\psi)2r^2 \omega d\varphi dt,$$

where we switch to the cylindrical coordinate notation $(1, 2, 3) \hat{=} (r, \varphi, z)$. In this case the non-vanishing components of the affine connection read

$$(C.9) \quad \begin{aligned} \Gamma^1_{11} &= -\frac{\psi_{,r}}{1-2\psi}, & \Gamma^1_{13} &= \frac{\psi_{,z}}{1-2\psi}, & \Gamma^1_{22} &= -\frac{r(1-2\psi-r\psi_{,r})}{1-2\psi}, & \Gamma^1_{33} &= \frac{\psi_{,r}}{1-2\psi}, \\ \Gamma^2_{21} &= \frac{1-2\psi-r\psi_{,r}}{r(1-2\psi)}, & \Gamma^2_{23} &= -\frac{\psi_{,z}}{1-2\psi}, & \Gamma^3_{11} &= \frac{\psi_{,z}}{1-2\psi}, & \Gamma^3_{13} &= -\frac{\psi_{,r}}{1-2\psi}, \\ \Gamma^3_{22} &= \frac{r^2\psi_{,z}}{1-2\psi}, & \Gamma^3_{33} &= -\frac{\psi_{,z}}{1-2\psi}. \end{aligned}$$

The spatial Ricci scalar in cylindrical coordinates then reads

$$(C.10) \quad \mathcal{R} = \frac{4}{(1-2\psi)^2} \Delta^{(3)} \psi + \frac{6}{(1-2\psi)^3} (\psi_r^2 + \psi_z^2) \simeq 4\Delta^{(3)} \psi.$$

When considering differentially rotating PN metrics with $\Omega = \Omega(r)$ or $\Omega = \Omega(r, z)$, in the linearised case, there are no mixing terms in the purely spatial metric; there is only time-space mixing. Note that the case $\Omega = \Omega(r)$ is not written down in sec. 2.3.5, but we have done the calculation. Moreover, the spatial metric is independent of the angular velocity in the linear case, and therefore the above non-vanishing components of the affine connection (C.9) can be used for calculation in both the two rotating cases $\Omega = \Omega(r)$ and $\Omega = \Omega(r, z)$ with linear metric ansatz, as well as in the case of rigid rotation $\omega = \text{const.}$

In the case of the simple differentially rotating ($\Omega = \Omega(r)$) linear PN metric,

$$(C.11) \quad ds^2 = -(1+2\phi)dt^2 + (1-2\psi)(dr^2 + dz^2) + (1-2\psi)r^2 d\varphi^2 - (1-2\psi)2r^2 \Omega(r) d\varphi dt$$

we have calculated also the four-dimensional connection components. They read:

$$(C.12) \quad \begin{aligned} \Gamma^0_{01} &= \frac{\phi_{,r}}{1+2\phi}, & \Gamma^0_{03} &= \frac{\phi_{,z}}{1+2\phi}, & \Gamma^0_{12} &= \frac{1}{2}r^2 \Omega_{,r}, & \Gamma^0_{30} &= \frac{\phi_{,z}}{1+2\phi}, \\ \Gamma^1_{00} &= -\frac{\phi_{,r}}{1+2\phi}, & \Gamma^1_{02} &= \frac{1}{2}r^2 \Omega_{,r} + \Omega r, & \Gamma^1_{11} &= -\frac{\psi_{,r}}{1-2\psi}, & \Gamma^1_{13} &= -\frac{\psi_{,z}}{1-2\psi}, \\ \Gamma^1_{22} &= -r(1-r\psi_{,r}), & \Gamma^1_{33} &= \frac{\psi_{,r}}{1-2\psi}, & \Gamma^2_{01} &= -\frac{1}{2}\Omega_{,r} - \frac{1}{r}\Omega, & \Gamma^2_{12} &= \frac{1}{r} - \psi_{,r}, \\ \Gamma^2_{23} &= -\frac{\psi_{,z}}{1-2\psi}, & \Gamma^3_{00} &= \frac{\phi_{,z}}{1-2\psi}, & \Gamma^3_{11} &= \frac{\psi_{,z}}{1-2\psi}, & \Gamma^3_{13} &= -\frac{\psi_{,r}}{1-2\psi}, \\ \Gamma^3_{22} &= \frac{r^2\psi_{,z}}{1-2\psi}, & \Gamma^3_{33} &= -\frac{\psi_{,z}}{1-2\psi}. \end{aligned}$$

The according inverse four-dimensional metric has the linearised components:

$$(C.13) \quad g^{00} = -\frac{1}{1+2\phi}, \quad g^{02} = -\frac{\Omega}{1+2\phi}, \quad g^{11} = \frac{1}{1+2\psi}, \quad g^{22} = \frac{1}{r^2(1+2\psi)}, \quad g^{33} = \frac{1}{1+2\psi}.$$

Aspects of Structure Formation

Here we concisely review the basic concepts of structure growth within linear Newtonian theory. We want to emphasise the limits of the below outlined concepts: the Newtonian linear perturbation theory breaks down at latest for non-linear structures, that is for structures with density contrast of order unity as well as for fluctuations at length scales that come close to the horizon scale. First, we review the theory of peculiar velocities and the underlying (Newtonian) hydrodynamical equations. We also attach a concise treatment of dissipative (Silk) damping of baryonic oscillations before recombination. In the following we closely relate to the description given in [Sch06] and [Lon98].

D.1. Gravitational Instabilities and Peculiar Velocities

Let us denote the peculiar velocity with \mathbf{u} , it is per construction the velocity on top of the Hubble flow

$$(D.1) \quad \mathbf{v}(\mathbf{r}, t) = H(a)\mathbf{r} + \mathbf{u}(\mathbf{r}/a, t) .$$

The initial density inhomogeneities are small – they correspond to CMB anisotropies $\mathcal{O}(10^{-5})$ – and so are the resulting initial peculiar velocities. However, the inhomogeneities in density today are not small, their evolution enfolds a growing mode. This can be physically understood by simple means: through self-gravitation the initial density seeds have condensated more and more throughout the ages ever since inflation. The linearised treatment of gravitational instability within a Newtonian hydrodynamic framework implies the solution of the continuity equation, the Euler equation and the Poisson equation. When looked at in a comoving frame ($\mathbf{r} = a\mathbf{x}$), these equations read in order of appearance

$$(D.2) \quad \frac{\partial \rho}{\partial t} + 3H(a)\rho + \frac{1}{a}\nabla \cdot (\rho\mathbf{u}) = 0$$

$$(D.3) \quad \frac{\partial \mathbf{u}}{\partial t} + \frac{1}{a}(\mathbf{u} \cdot \nabla)\mathbf{u} + H(a)\mathbf{u} = -\frac{1}{a\bar{\rho}}\nabla p - \frac{1}{a}\nabla\phi ,$$

$$(D.4) \quad \Delta\phi(\mathbf{x}, t) = 4\pi G a^2(t)\bar{\rho}(t)\delta(\mathbf{x}, t) .$$

The *density contrast* is a crucial quantity we have already encountered in sec. 1.3.3, here given by

$$(D.5) \quad \delta(\mathbf{x}, t) \equiv \frac{\rho(\mathbf{x}, t) - \bar{\rho}(t)}{\bar{\rho}(t)} .$$

Being interested in small deviations from the homogeneous evolution $\delta = 0 = u^i$ one can linearise the above set of hydrodynamical equations and, after eliminating ϕ and \mathbf{u} among the equations, one ends up with a second-order equation for the density contrast

$$(D.6) \quad \frac{\partial^2 \delta}{\partial t^2} + 2H(a)\frac{\partial \delta}{\partial t} = 4\pi G\bar{\rho}\delta ,$$

which can be solved and upon neglecting the decaying mode, and we end up with the factorisation solution

$$(D.7) \quad \delta(\mathbf{x}, t) = \delta_0(\mathbf{x})D_+(t) ,$$

where $D_+(t)$ denotes the growing mode. Within this linear solution the spatial contribution to the density contrast is time-constant and so the peculiar velocity \mathbf{u} has a constant direction which is moreover collinear to the direction of the peculiar gravitational acceleration $\mathbf{u}(\mathbf{x}) \sim \int \mathbf{g}(\mathbf{x}, t) dt$. As measured today the peculiar velocity field can be expressed by its acceleration field via

$$(D.8) \quad \mathbf{u}(\mathbf{x}) = \frac{2}{3H_0\Omega_m} f(\Omega_m) \mathbf{g}(\mathbf{x}).$$

For the function $f(\Omega_m) \equiv (a/D_+)dD_+/da$ one finds phenomenologically $f(\Omega_m) \simeq \Omega_m^{0.6}$ which remains a good fit even when Λ is switched on in addition. Eliminating \mathbf{g} with the help of Poisson's equation and letting \mathbf{u} evolve within linear theory one obtains in the end [Sch06]

$$(D.9) \quad \mathbf{u}(\mathbf{x}, t) = \frac{\Omega_m^{0.6}}{4\pi} aH(a) \int \delta(\mathbf{y}, t) \frac{\mathbf{y} - \mathbf{x}}{|\mathbf{y} - \mathbf{x}|^3} d^3y.$$

This result gives a principal possibility to obtain Ω_m by observation of the peculiar velocity field as well as the according density contrast.

D.2. Statistical Properties of the Density Field

The growing mode solution (D.7) is a central result of the linear theory applied above. We see that the spatial shape of the density fluctuations is frozen when followed in the comoving frame and solely its amplitude is growing. The growth factor $D_+(t)$ can be computed for an arbitrary composition of cosmological density parameters through

$$(D.10) \quad D_+(a) \propto \frac{H(t)}{H_0} \int_0^a \frac{da'}{[\Omega_m a'^{-1} + \Omega_\Lambda a'^2 - (\Omega_m + \Omega_\Lambda - 1)]^{3/2}}.$$

The factor of proportionality is fixed by the normalisation given by $D_+(t_0) = 1$ and thus $\delta_0(\mathbf{x})$ would be the density distribution as observable today if the evolution was linear all the time. However, we know of vast structures today like for instance the Shapley Concentration **SEC** for which the density contrast is of the order of ~ 1 such that the linear perturbation analysis becomes invalid.

Taking as an example the Einstein-de Sitter model with $\Omega_\Lambda = 0$, $\Omega_m = 1$ and scaling $a(t) = (t/t_0)^{2/3}$ for the Hubble function and mean density it is

$$(D.11) \quad H(t) = \frac{2}{3} \frac{1}{t} \quad \text{and} \quad \bar{\rho}(t) = a^{-3} \rho_{\text{crit}} = \frac{3H_0^2}{8\pi G} \left(\frac{t_0}{t}\right)^2.$$

With an ansatz $D \propto t^n$ we readily solve (D.6). We skip the decaying mode and keep the growing mode which is

$$(D.12) \quad D_+(t) = \left(\frac{t}{t_0}\right)^{2/3} = a(t),$$

and thus the growth factor is equal to the scale factor in the special case of an Einstein-de Sitter solution.

In order to describe the actually observed density field today by physical means, usually two concepts are used: the two-point correlation function and the power spectrum which we have introduced in sec. 1.2.1. The statistical nature of the description means that we are looking for a physical means that can be attributed to an observed density distribution so that we consider models (universes) with equal such statistical properties as equivalent. In other words one can imagine a whole statistical ensemble of Universes to be describable through a statistical quantity where, of course, the details of $\delta(\mathbf{x})$ may be different in all those Universes.

First, the two-point correlation function $\xi(\mathbf{x}, \mathbf{y})$ of a density field is defined through

$$(D.13) \quad \langle \rho(\mathbf{x})\rho(\mathbf{y}) \rangle = \bar{\rho}^2 \langle [1 + \delta(\mathbf{x})][1 + \delta(\mathbf{y})] \rangle = \bar{\rho}^2 [1 + \langle \delta(\mathbf{x})\delta(\mathbf{y}) \rangle] \equiv \bar{\rho}^2 [1 + \xi(\mathbf{x}, \mathbf{y})],$$

where $\langle \cdot \rangle$ is an ensemble average and the expectation value $\langle \delta(\mathbf{x}) \rangle = 0$ at all locations \mathbf{x} . The standard model assumption of large-scale homogeneity implies that ξ only depends on $\mathbf{x} - \mathbf{y}$ and

not on \mathbf{x} or \mathbf{y} individually. The standard requirement of isotropy also removes any orientational dependence of ξ such that the two-point correlation will be a function of only $r = |\mathbf{x} - \mathbf{y}|$ when regarded in the standard cosmological model. Because of ergodicity, we can replace the ensemble average by the spatial average, that is due to (D.13) one can measure the two-point correlation function by collecting many products of densities for all pairs of points at a distance r . This has been done for example for the luminous red galaxy catalogue ($z \sim 0.3$) of the SDSS [HEB⁺05], confirming the large-scale homogeneity of the Universe. When analysing such galaxy catalogues the luminosity distribution is a crucial quantity. A quite general approximation for galaxy luminosities is given by the Press-Schechter law [PS74]

$$(D.14) \quad f(L) = \frac{f^*}{L^*} \left(\frac{L}{L^*} \right)^\alpha e^{-L/L^*},$$

wherein f^* is responsible for the normalisation, α controls the slope of the function at small L and L^* is a special value beyond which the luminosity distribution undergoes the exponential decrease. Now, among galaxies that have luminosities of the order of L^* , the following approximate relation for the two-point correlation function can be found from galaxy surveys: $\xi(r) = (r/r_0)^{-\gamma}$. With this relation being a good approximation within $2 \text{ Mpc} \lesssim r \lesssim 30 \text{ Mpc}$, the correlation length is found to be roughly $r_0 \simeq 5 \text{ Mpc}$ and the slope is $\gamma \simeq 1.8$. Principally one can proceed in writing down higher correlations up to the n point correlation function, but these are much harder to access observationally.

Besides the two-point correlation one can utilise the *power spectrum* $P(k)$ in order to describe a density field statistically. We can expand a given density field in terms of Fourier modes as $\delta(\mathbf{x}) = \sum A_k \cos(\mathbf{x} \cdot \mathbf{k})$ with amplitudes A_k . The power spectrum now describes the distribution of amplitudes with a common wavenumber k . Two point correlation function and power spectrum are Fourier transforms of each other

$$(D.15) \quad P(k) = 2\pi \int_0^\infty \xi(r) r^2 \frac{\sin(kr)}{kr} dr.$$

The factorisation (D.7) implies the following for the time evolution of the power spectrum

$$(D.16) \quad P(k, t) = D_+^2(t) P(k, t_0) \equiv D_+^2(t) P_0(k),$$

and k is the wavenumber in comoving coordinates. As mentioned in sec. 1.3.3 the initial conditions for $P(k)$ are provided by the used underlying inflationary model and yield a nearly scale-invariant Harrison-Zel'dovich spectrum with a random Gaussian initial density field. Furthermore, because we neglected pressure terms and only considered matter domination there have to be corrections included for the power spectrum bringing it to its final form (1.29). These corrections are encoded in the transfer function $T(k)$ which reflects the parameters of the underlying cosmological model as well as the temperature of the used Dark Matter. In case of Hot Dark Matter (HDM) the dark constituents are relativistic, therefore do not remain bound in the potential well of a gravitative perturbation but rather do free-stream and thus tend to smooth out any initial density perturbations on small scales. In such a scenario the power spectrum will be strongly suppressed at large k and as a consequence the very largest structures are formed first, producing then smaller structures – like galaxies – only later through fragmentation. This is in contradiction with observations that indicate the existence of galaxies already at extreme redshifts of ~ 6 . Therefore Cold Dark Matter (CDM) is the prevailing concept from the perspective of structure formation.

D.3. Silk Damping and Hierarchy

We now consider small imperfections in the tightly coupled baryon-photon fluid of the early Universe before decoupling. Albeit strong, the coupling of matter and radiation is not exact and photons will have some finite mean free path. Therefore, on small scales, where the radiation is able to resort without scatter, the pressure support, that constitutes the restoring force of the adiabatic matter oscillations, would vanish. Hence, oscillations on such small scales are

effectively damped out by the photon dissipation; this is referred to as *Silk damping* [Sil68]. The Silk damping occurs for the same reasons as the damping of sound waves in an imperfect gas: namely because of the finite shear viscosity and heat conductivity that are present in the fluid. A full treatment of the photon transport problem with the according coefficients of thermal conduction and shear viscosity has been given by Weinberg [Wei72].

We are interested in an estimate that may express the order of magnitude of the Silk damping; we follow the treatment by Longair [Lon98]. The main process for the photon scattering in the primeval plasma is Thomson scattering by the free electrons. We can obtain an estimate by performing a rough transport calculation with the Thomson scattering of radiation. Generally, for Thomson scattering, the mean free path of the photons is given by

$$(D.17) \quad \lambda = \frac{1}{n_e \sigma_T},$$

where $\sigma_T \simeq 6.665 \times 10^{-29} \text{m}^2$ is the Thomson cross section and n_e the number density of electrons. The photons and electrons are in tight thermal contact before decoupling. And because the plasma is fully ionised, the electrons are also in tight electromagnetic interaction with the protons (Coulomb scattering), so that the photons are in close contact to the protons as well. We want to determine how far the photons can diffuse within a certain cosmic time t under the given free mean path. This can be quantified by means of the according diffusivity D , given by $D = \lambda c/3$. The radial distance that photons can cover by diffusion is therefore

$$(D.18) \quad r_D \simeq (Dt)^{1/2} = \left(\frac{\lambda ct}{3} \right)^{1/2}.$$

Next we should compute the corresponding baryonic mass $M_D \equiv (4\pi/3)r_D^3 \rho_b$ within a ball of a radius that equals the discussion radius.

First, long before decoupling ($z > 2.4 \times 10^4 \Omega h^2$), radiation is dominant in the Universe and the relation between cosmic time and redshift is given by

$$(D.19) \quad t = \left(\frac{3c^2}{32\pi G \rho} \right)^{1/2} = \left(\frac{3c^2}{32\pi G \chi a_{\text{SB}} T^4} \right)^{1/2} \frac{1}{(1+z)^2} \simeq \frac{2.4 \times 10^{19}}{(1+z)^2} \text{ s},$$

with $a_{\text{SB}} = 4k_{\text{SB}}/c$ and the Stefan-Boltzmann constant $k_{\text{SB}} = 5.670 \times 10^{-8} \text{JK}^{-4} \text{m}^{-2} \text{s}^{-1}$, $\rho = \chi(T) a_{\text{SB}} T^4$ being the total energy density and $\chi(T) \simeq 1.68$ being a parameter that encodes the sum over the statistical weights g_i of the involved (standard model) particles. For T_0 we insert the presently measured CMB monopole temperature of $T_0 \simeq 2.725 \text{K}$. Further, the number density of electrons n_e varies with redshift as

$$(D.20) \quad n_e = \frac{\Omega_b \rho_{\text{crit}}}{m_p} (1+z)^3 \simeq 11 \Omega_b h^2 (1+z)^3 \text{ m}^{-3},$$

and so we are ready to compute the resulting damping mass or Silk mass, which amounts to

$$(D.21) \quad M_D = \frac{4\pi}{3} r_D^3 \rho_b \simeq 2.4 \times 10^{26} (\Omega_b h^2)^{-1/2} (1+z)^{-9/2} M_\odot.$$

This was so far for the times before matter-radiation equality. Within the matter-dominated epoch, the redshift behaviour of cosmic time can be expressed as

$$(D.22) \quad t = \frac{2}{3H_0 \Omega^{1/2}} (1+z)^{-3/2} \simeq \frac{2.06 \times 10^{17}}{3H_0 \Omega^{1/2} (1+z)^{3/2}} \text{ s}.$$

This leads to a Silk mass of

$$(D.23) \quad M_D \simeq 2.0 \times 10^{23} (\Omega_b h^2)^{-5/4} (1+z)^{-15/4} M_\odot.$$

The evolution of damping mass M_D , Jeans mass M_J and horizon mass M_H are plotted in fig. D.1. Silk damping continues until recombination and upon the last scattering surface ($z \simeq 1088$) the damping mass reaches a value of up to $M_D \simeq 10^{12} (\Omega_b h^2)^{-5/4} (1+z)^{-15/4} M_\odot$. Taking big bang nucleosynthesis into account, a bound of around $\Omega_b h^2 < 0.036$ can be given, and it follows that perturbations with masses smaller than roughly $10^{14} M_\odot$ are damped out by the Silk mechanism.

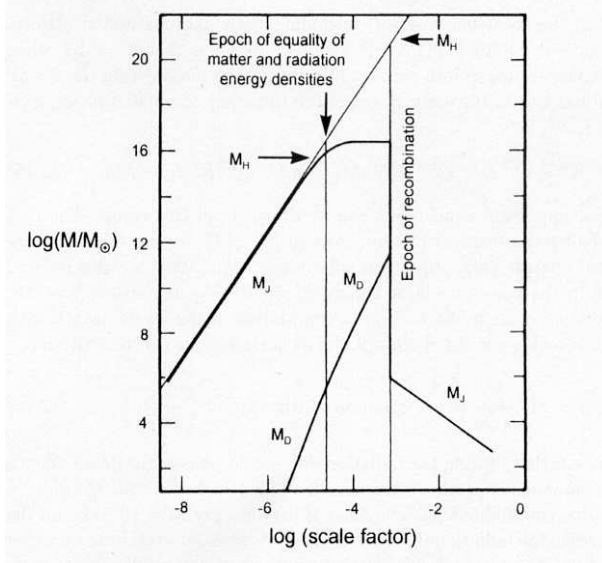


FIGURE D.1. Schematic evolution of scales and their associated masses that are relevant for structure formation within the theory of purely baryonic (no Dark Matter) acoustic fluctuations. The *Jeans scale* is characterised by the wavelength $\lambda_J \equiv c_s \sqrt{\pi/(G\rho)}$; which is the maximal scale for stable oscillations at any epoch. This is a result from non-linear Newtonian perturbation theory; it means that any density perturbations with wavelengths larger than the Jeans wavelength represent unstable modes. The Jeans mass can be defined as the mass contained in a ball of diameter λ_J , thus $M_J \equiv (\pi\lambda_J^3/6)\rho_b$. The mass contained in the particle horizon is around $M_H \simeq 3.0 \times 10^{22}(\Omega_b h^2)^{-1/2} a^{3/2} M_\odot$. The scale behaviour of the Jeans mass at early times can be estimated by $M_J \simeq 8.5 \times 10^{28} a^3 \Omega_b h^2 M_\odot$ and by $M_J \simeq 3.75 \times 10^{15} (\Omega_b h^2)^{-2} M_\odot$ after equality. The development of the Silk damping scale – which occurs because of photon dissipation and ends at decoupling – is traced by M_D ; c.f. (D.21) and (D.23). The picture is taken from [Lon98].

Summarising the result of the above diffusion estimate, we can conclude that all masses smaller than roughly $10^{12} M_\odot$ are effectively suppressed by the photon dissipation. From this we can learn an important lesson for the hierarchy of structure formation in the framework of purely baryonic – i.e. neglecting Dark Matter – acoustic perturbations: only those perturbations with masses of a very heavy galaxy and larger could have passed through to the post-recombination epoch. Those perturbations with smaller associated masses – like stars, star clusters or normal galaxies – are suppressed exponentially to very small amplitudes. Hence, in this framework, the formation of structure is anti-hierarchical (bottom-down), large structures formed first and then have fragmented to the smaller observed structures. Let us emphasise that this result is valid under the assumption of *adiabatic baryonic perturbations*, where adiabaticity is defined by the thermodynamic relation

$$(D.24) \quad \frac{\delta p}{p} = \gamma \frac{\delta \rho}{\rho},$$

and γ being the ratio of specific heats: $\gamma = 4/3$ for a relativistic gas and $\gamma = 5/3$ for a monoatomic non-relativistic gas.

A competing framework is the theory of *isothermal perturbations*. Here, isothermal means that the perturbations do not induce perturbations in the background radiation temperature at the times of radiation domination. The intrinsic temperature of the isothermal perturbations equals that of the uniform radiation background and so the isothermal perturbations are frozen into the radiation-dominated background. As a consequence, there is no Silk damping in this picture. Therefore in the isothermal scenario, structure growth is hierarchical (bottom-up):

small structures would form first, then larger structures are attained by clustering processes. The big advantage of the bottom-up scenario is that it allows structures of the mass of globular clusters to have formed first and indeed, globular clusters are among the oldest objects known in our Milky Way.

However, as we discuss in chap. 2 there is overwhelming evidence – within the scope of standard cosmology – for the existence of Dark Matter, such that the above two versions of pure baryonic structure formation are falsified. When transported into the framework of Dark Matter, the competition between hierarchical and anti-hierarchical structure formation is mapped onto the CDM (bottom-up) and HDM (bottom-down) scenarios respectively. In the CDM picture, hierarchical processes lead to the formation of Dark Matter halos of galaxy clusters and galaxies. Then, the baryons would fall into these potential wells and subsequently can lose energy by dissipative processes; then eventually gas clouds and stars are formed. In the HDM scenario, vast structures, like galaxy clusters, are formed first and an asymmetric decay of these progenitors then leads to pancake-like structure, into which the baryonic matter then collapses. Both of these models have been plugged into extensive computer simulations trying to reconstruct the growth of structure. Being consistent with the conclusions of the preceding sec. D.1, a main result of the simulations is that HDM – albeit (too) good in producing filament structure – produces galaxies only at too late times. Moreover, as it was mentioned already above, the CDM ansatz is successful in reproducing the measured two-point correlation function of galaxies on a considerably wide range of scales.

APPENDIX E

Thermal History in a Nutshell

According to the Big Bang picture, the Universe was increasingly hotter when going further backwards in time, $T(z) = T_0(1 + z)$. Because of the very high temperatures, e.g. $3 \times 10^9\text{K}$ at $z = 10^9$, and high pressure in the very early Universe which are ‘even’ higher than in the interior of stars, one can expect a lot of interesting high-energy processes like nuclear fusion to happen during the early epochs. Here we want to give a concise overview of the basic steps that lead to nucleosynthesis, following the treatment in [Sch06].

E.1. Neutrino Decoupling

An assumption of utmost importance is underlying all the standard theory of the evolution of particle processes in the early Universe: we assume that all the cross sections and other fundamental constants and all the details of nuclear and particle physics we take from the current standard model of high energy physics have been exactly the same also fourteen billion years ago. Having that in mind, we can jump into the evolution of the very early Universe at temperatures of around $\sim 10^{12}\text{K}$ or roughly 100MeV . To see what the basic setup may yield we can compare this initial energy scale with the rest masses of common standard model particles,

$$(E.1) \quad m_n \simeq 939.6\text{MeV}, \quad m_p \simeq 938.3\text{MeV}, \quad m_\mu \simeq 140\text{MeV}, \quad m_e \simeq 511\text{keV}.$$

The baryons are too heavy to be possibly produced at the considered temperature, and so at this epoch the baryons must have existed already. Further, pairs of muons can in principle be produced via $\gamma + \gamma \rightarrow \mu^+ + \mu^-$ down to temperatures $\sim m_\mu/3$. But, as is known, existing muons are unstable (lifetime $2.2 \times 10^{-6}\text{s}$) and decay into electrons (positrons) and neutrinos as well as antineutrinos. Thus at the given temperature of around 100MeV there are the following *relativistic* particles in the Universe: photons as well as electrons and neutrinos and their antiparticles. We are within radiation domination and only these particles are contributing to the radiation energy density ρ_r at the moment. Although the exact mass of neutrinos has not yet been measured, one can give a bound of $m_{\nu_e} < 2\text{eV}$ from tritium decay. From cosmology – if one accepts numerous implicit assumptions – one can infer a bound of $m_{\nu_e} < 1\text{eV}$ from measurements probing the effect of HDM on the small-scale power spectrum of density fluctuations in the Universe.

Because of these mass constraints, we can safely regard the neutrinos as massless (relativistic) in our discussion. Besides the relativistic particles there are also some non-relativistic particles: protons, neutrons and the hypothetical WIMPs. Because of their absence in the accelerator experiments carried out by now, we know that the WIMP rest mass must be higher than around 100GeV . All constituents apart from the WIMPs are in equilibrium through particle reactions. The baryon reactions are discussed later, and so we can note the following relevant reactions of the relativistic particles

$$(E.2) \quad e^\pm + \gamma \leftrightarrow e^\pm + \gamma, \quad e^+ + e^- \leftrightarrow \gamma + \gamma, \quad \nu + \bar{\nu} \leftrightarrow e^+ + e^-, \quad \nu + e^\pm \leftrightarrow \nu + e^\pm.$$

We consider radiation domination, and so the total energy density is that of the radiation,

$$(E.3) \quad \rho = \rho_r = 10.75 \frac{\pi^2 (k_B T)^4}{30 \hbar c^3} \quad \text{at} \quad t \simeq \left(\frac{T}{1\text{MeV}} \right)^{-2} 0.3\text{s}.$$

The cosmic time was computed with the solution $t = (32\pi G\rho/3)^{-1/2}$, valid at the epoch of radiation domination.

Equilibrium can only be attained by the particle bath if the rate of the above reactions is high. However, the environment temperature in which the particles are trying to equilibrate is continuously changing, and so the particle equilibrium is also continuously readjusting. Under these circumstances, an equilibrium can only be upheld if the time between two particle reactions is much smaller than the time scale of global temperature change. The rate of change in temperature is dictated by the cosmic expansion and so we can note the following constraint for equilibrium: the rate of particle reactions Γ has to be higher than the expansion rate.

The rate of particle reactions is $\Gamma \propto n\sigma$, i.e. it is proportional to the number density of the respective particle species and to the interaction cross section. The reactions involving neutrinos belong to the weak interactions. Both of the components of the rate are decreasing with cosmic time. The number density of particles is diluted as $n \propto a^{-3} \propto t^{-3/2}$ because of global expansion. On the other hand, the weak cross sections are energy dependent and scale roughly as $\sigma \propto E^2 \propto T^2 \propto a^{-2}$. Thus, the reaction and expansion rate respectively scale as

$$(E.4) \quad \Gamma \propto n\sigma \propto a^{-5} \propto t^{-5/2} \quad \text{versus} \quad H \propto t^{-1}.$$

Thus, equilibrium can be realised at early times, when the reaction rates are higher than the expansion rate. At later times, the equilibrium will be broken because the speed of the reactions eventually falls behind the expansion rate: this is called a *freeze-out*. The weak interaction freeze-out occurs at

$$(E.5) \quad \frac{\Gamma}{H} \simeq \left(\frac{T}{1.6 \times 10^{10}\text{K}} \right)^3,$$

so that the neutrinos become decoupled from the equilibrium with other particle species at temperatures $T \lesssim 10^{10}\text{K}$. When the neutrinos froze out, they had a thermal distribution with the same temperature as the other particles. From their decoupling at around $T \sim 10^{10}\text{K}$ on, the neutrinos will keep this distribution, only their temperature is continuously redshifted according to $T \propto a^{-1}$.

This is a prediction. It says that there should exist a primordial neutrino background, similar to the CMB which is a primordial photon background. It is estimated that the neutrino abundance per flavour is 113cm^{-3} today, and the cosmic neutrino temperature amounts to around 1.9K . Because of the very small interaction cross section and the fact that the momentum of the primordial neutrinos is also very low, there is little hope to observe the relic neutrino background.

E.2. Electron-Positron Annihilation

We further follow the cooling of the early Universe. At temperatures of around $\sim 5 \times 10^9\text{K}$ (500keV) there are not enough photons in the distribution, with energies above the pair production threshold of 511keV , that could maintain pair production at a high rate. Therefore the efficient production of electron-positron pairs will fade out at this point. At the same time, the annihilation reaction $e^+ + e^- \rightarrow \gamma + \gamma$ is proceeding undisturbedly, and because of its large cross section the number of present electron-positron pairs will drop rather rapidly.

Through this mechanism, there will be an effect on the photon distribution. The non-equilibrium annihilation will induce additional energy to the photon bath. Since the form of the spectrum remains (Planck spectrum), the main effect is an increase in temperature of the photons. This increase is fed by the energy which was initially present in form of electron and positron rest mass as well as kinetic energy. When annihilation happens, the neutrinos are already frozen out and so the gain in temperature has no effect on them. Therefore the photon temperature will be ahead of the neutrino temperature after the effect of pair annihilation; in fact one can show that $T_{\text{aft. annih.}} \simeq 1.4 T_{\text{bef. annih.}} = 1.4 T_\nu$. This ratio of photon to neutrino temperature is frozen and valid up to today, and thus we see now the reason for the prediction of 1.9K for the neutrino background temperature made above.

After annihilation the number of relativistic particle species is reduced and so this in turn leads to a change the expansion law in (E.1) to $t = 0.55s(T/1\text{MeV})^{-2}$. Moreover, through annihilation the ratio of baryons to photons approaches a constant value

$$(E.6) \quad \eta \equiv \frac{n_b}{n_\gamma} \simeq 2.73 \times 10^{-8} (\Omega_b h^2).$$

From this we can get also an estimate on the electron to photon ratio n_e/n_γ . Before annihilation the ratio of electrons (and positrons) to photons was roughly one, but during annihilation most of the electrons disappear. However, not all of the electrons disappear; it turns out that there remains a small excess of electrons over positrons. But there is of course another particle that carries a charge: the proton. Because the Universe appears to be electrically neutral (bound on free charges $\lesssim 10^{-27}$ [Pad02]), the electron excess is just compensated by the number of protons. Therefore the electron to photon ratio should roughly equal η . Now – since the neutrons are also to be counted – one has more precisely $n_e/n_\gamma \simeq 0.8\eta$.

E.3. Nucleosynthesis

If the environment implies a high enough pressure and temperature, nuclear fusion can take place, like it does happen within stars. That is, protons and neutrons can combine to form nuclei, and in fact the primordial formation of light elements is finished already after the first few minutes.

E.3.1. Baryon Equilibrium. As discussed, the baryons play no significant role for the dynamics of the very early Universe. However, protons and neutrons are in thermal equilibrium via weak interaction processes. Their equilibrium reactions are

$$(E.7) \quad p + e^- \leftrightarrow n + \nu, \quad p + \bar{\nu} \leftrightarrow n + e^+, \quad n \leftrightarrow p + e^- + \bar{\nu},$$

the last of which is the beta decay of the neutron with a lifetime of $\tau_n \simeq 887\text{s}$. In order to not freeze out, the reactions have to be quicker than the global expansion. The ratio of proton to neutron number densities is given by the Boltzmann factor

$$(E.8) \quad \frac{n_n}{n_p} = e^{-\Delta mc^2/(k_B T)},$$

which is governed by the mass difference $\Delta m \equiv m_n - m_p$ (neglecting their chemical potentials). This distribution is only valid up to neutrino decoupling. At the moment of neutrino decoupling, the ratio of neutrons to protons is around $n_n/n_p \simeq 1/3$, and after the neutrino freeze-out the equilibrium is broken and becomes dominated by the decay of the free neutron. A number of neutrons has to become bound into nuclei rather quickly, so that a fraction of neutrons can survive up to today.

E.3.2. Deuterium Production. The simplest nucleus is deuterium, made from just a proton and a neutron. It is produced via

$$(E.9) \quad p + n \rightarrow D + \gamma.$$

The binding energy of deuterium is $\chi_D \simeq 2.2\text{MeV}$, the mass difference is $\Delta m \simeq 1.3\text{MeV}$ and the electron rest mass is 511keV ; so all of these mass scales are of the same order of magnitude. The reaction (E.9) belongs to the strong interactions and is therefore running at a high efficiency.

But there is a catch. During neutrino decoupling and pair annihilation the temperature of the Universe becomes less than the binding energy χ_D , but not much less. And since there are much more photons than baryons, c.f. (E.6), there will be enough photons in the high energy tail of the Planck spectrum to break up the freshly formed deuterium. From the explicit balance equations one can infer that the formation rate of deuterium can exceed its photo-dissociation rate only at temperatures around $T_D \simeq 8 \times 10^8\text{K}$. This happens only at a cosmic time of around three minutes – the decay of the neutrons has gone on in the meantime – and so the neutron to proton ratio would have decreased to $n_n/n_p \simeq 1/7$. Once the obstacle of photo-dissociation is left behind, the production of deuterium proceeds very quickly (strong interaction). All available

neutrons become bound into deuterium and as soon as there is a significant abundance of it, the deuterium can start to form ${}^4\text{He}$. Now, the helium has already a sizeable binding energy of $\chi_{{}^4\text{He}} \simeq 28\text{MeV}$ and is thus not vulnerable to photo-dissociation anymore. Apart from a small rest fraction, nearly all the deuterium is processed into ${}^4\text{He}$. Therefore, in order to efficiently produce helium, the Universe has to overcome the ‘bottleneck’ of the deuterium stage with its low binding energy.

E.3.3. Helium Abundance. As we have seen by now, almost all of the neutrons in the Universe become bound into helium nuclei after around three minutes. Therefore it should be possible to predict the helium abundance. Every helium has two neutrons and so the number density of four-helium will be $n_{{}^4\text{He}} = n_n/2$. The number of protons, when helium formation is over, amounts to $n_{\text{H}} = n_p - n_n$ because ${}^4\text{He}$ is symmetric in protons and neutrons. Finally, this gives us the mass fraction of ${}^4\text{He}$ with respect to the full baryon density at T_{D} as

$$(E.10) \quad Y \equiv \frac{4n_{{}^4\text{He}}}{4n_{{}^4\text{He}} + n_{\text{H}}} = \frac{2n_n}{n_p + n_n} = \frac{2(n_n/n_p)}{1 + (n_n/n_p)} \simeq \frac{1}{4}.$$

This is a simple but robust prediction of BBN: a fraction of about one fourth of the baryonic matter in the Universe is bound into ${}^4\text{He}$. This prediction refers of course to the primordial mass fraction. Through fusion processes within stars, metals can be formed and the helium mass fraction is modified. However, it is possible to experimentally observe metal-poor regions in the Universe – regions, where little processing of baryonic matter has taken place – and indeed a helium mass fraction of $Y \simeq 0.25$ is measured. Of course, a full quantitative computation of light element abundances takes into account all the possible balance and rate equations and what we sketched here is only a back-of-the-envelope estimate that should introduce the basic steps. In fig. E.1 we show the result of a more detailed BBN calculation for the mass fraction.

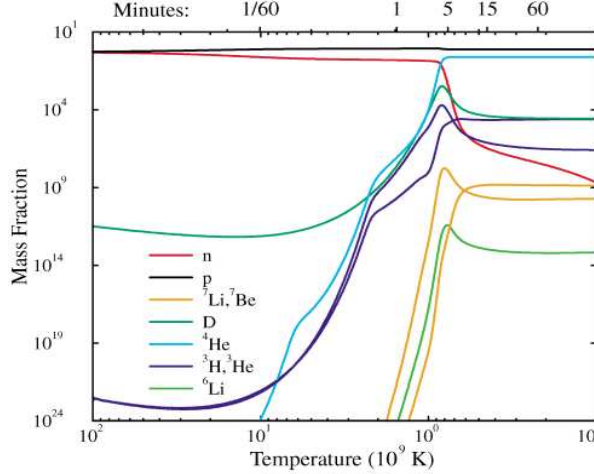


FIGURE E.1. Temperature/cosmic time evolution of the BBN abundances of light elements. Due to beta decay of the free neutrons there is a decrease in the neutron abundance within the first $\simeq 3\text{min}$. Parallel to the neutron decrease, the deuterium abundance rises steeply until it passes the dissociation bottleneck, and subsequently helium can be formed efficiently. Only a very little fraction ($\sim 10^{-5}$) of deuterium is not processed. There are also subdominant fractions of ${}^3\text{He}$, ${}^7\text{Li}$ and other elements produced during BBN. Picture is taken from [HES].

Since the abundances of the light elements are directly sensitive to the baryon to photon ratio η , one can use measured abundances of the light elements to constrain η [Y⁺06],

$$(E.11) \quad 3.4 \times 10^{-10} < \eta < 6.9 \times 10^{-10} \quad \text{and} \quad \Omega_b \simeq 3.66 \times 10^7 \eta h^{-2}.$$

APPENDIX F

Additional Plots and Results

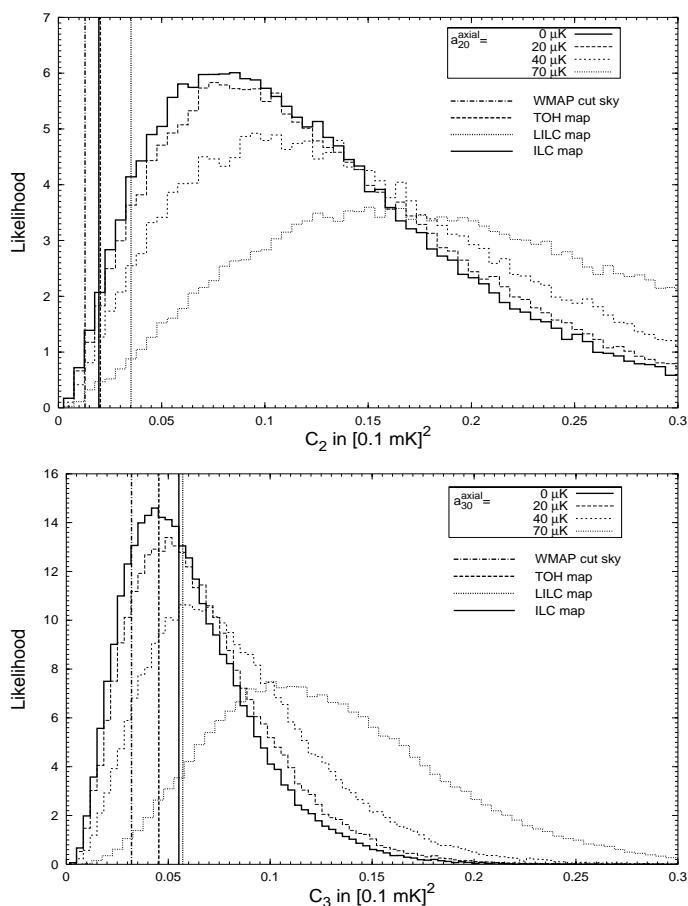


FIGURE F.1. The angular power anomaly with respect to WMAP(1yr) data. The likelihood of quadrupole and octopole power with increasing axial contamination, due to e.g. a local Rees-Sciama effect, is compared to WMAP(1yr) data. Vertical lines indicate the measured values as given in tab. 4.3. See sec. 4.3.1 for a discussion of the cleaned maps. From the WMAP cut-sky analysis, adding *any* multipole power to the quadrupole is already excluded at $> 99\% \text{C.L.}$, whereas it is possible to add up to $80 \mu\text{K}$ to the octopole until reaching the same exclusion level. Adding $50 \mu\text{K}$ ($100 \mu\text{K}$) to the quadrupole leads to an exclusion of $99.6\% \text{C.L.}$ ($99.9\% \text{C.L.}$).

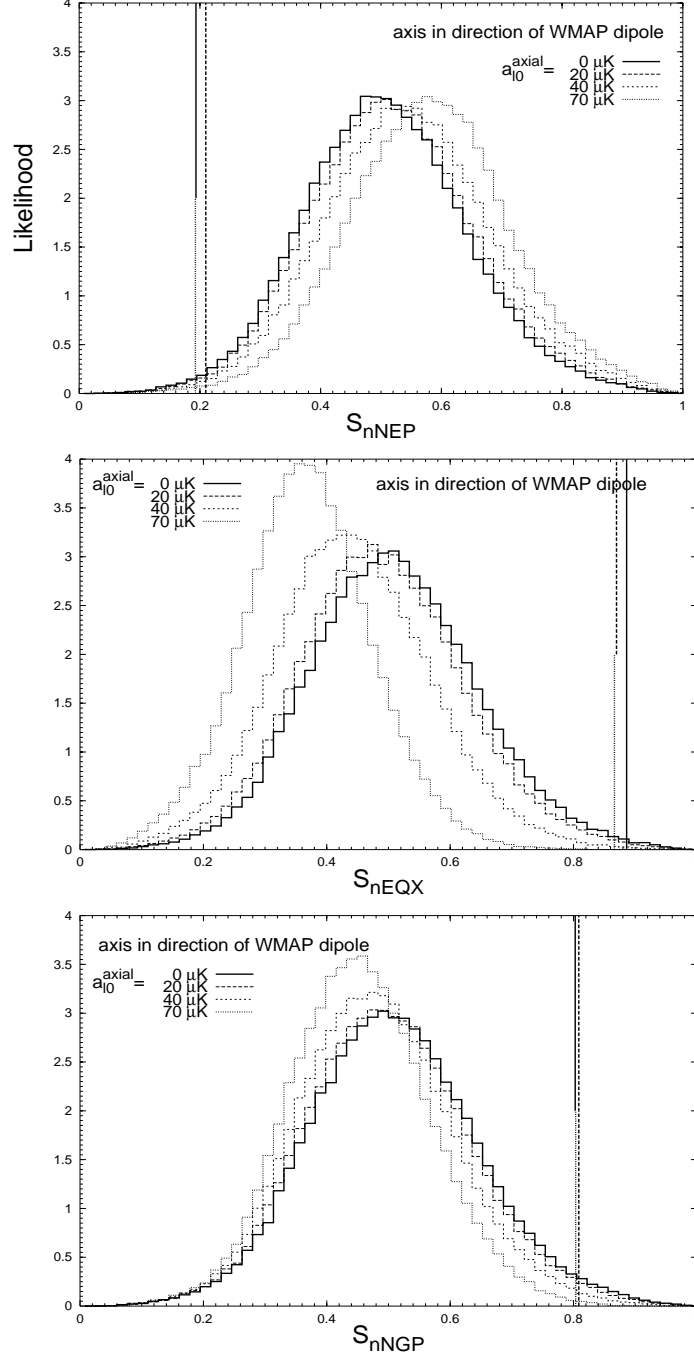


FIGURE F.2. Alignment statistic (4.7) for quadrupole and octopole normals. The preferred axis \hat{z} of the model points in all three cases to the direction of the WMAP dipole. Shown are the likelihoods of the S -statistic for statistically isotropic Gaussian skies (thick solid lines), corresponding to the Λ CDM prediction, as well as different magnitudes of axial contamination of the CMB. Vertical lines represent the measured S -values from the TOH (solid line), LILC (dotted line) and ILC (dashed line) maps, c.f. tab. 4.3. Introducing a preferred axis induces correlations. For the axis pointing in the direction of the dipole these correlations make the discrepancy between the measured S -values and model even bigger. For the alignment test with the north galactic pole, a contribution $a_{l0}^{axial} = 60\mu\text{K}$ ($70\mu\text{K}$) leads to an exclusion of 99.7% C.L. (99.8% C.L.).

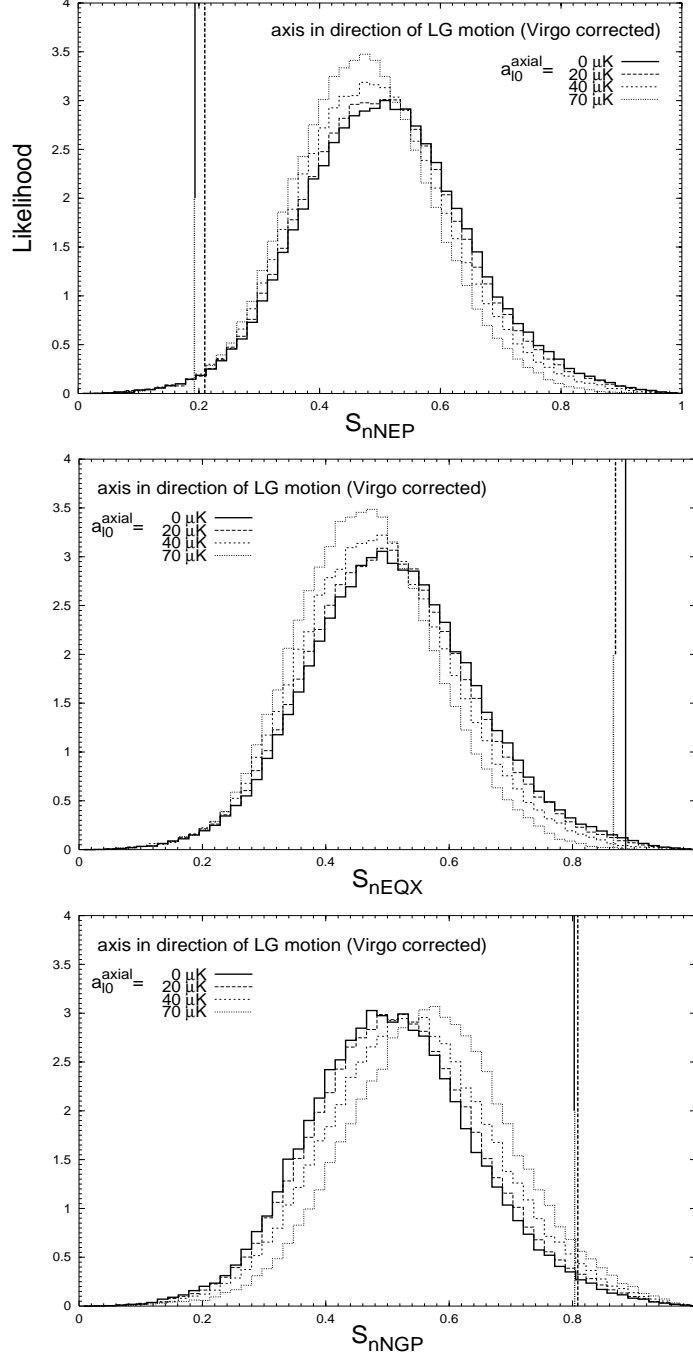


FIGURE F.3. Similar to fig. F.2, here the preferred axis \hat{z} of the model points to the direction of motion of the local group after correction for the Virgo infall. For this axis direction and the test directions NEP and EQX, the induced correlations make the discrepancy between the measured S -values and model bigger, similar to the case of the dipole fig. F.2. For the alignment test with the equinox, already a contribution of $a_{l0}^{\text{axial}} = 60 \mu\text{K}$ leads to an exclusion of 99.9% C.L. On the other hand, in case of $\hat{x} = \text{NGP}$, the anomaly is decreased in that the exclusion drops from 98% C.L. with $a_{l0}^{\text{axial}} = 0 \mu\text{K}$ to 96% C.L. with $a_{l0}^{\text{axial}} = 70 \mu\text{K}$.

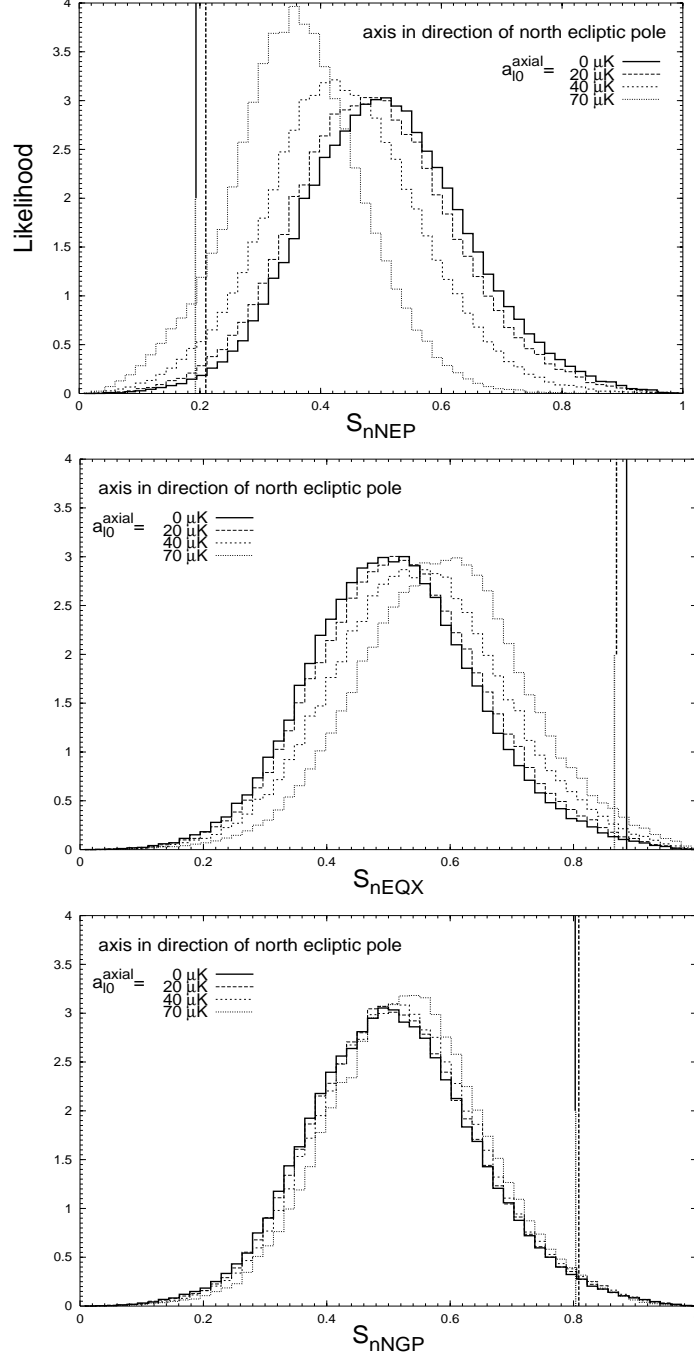


FIGURE F.4. Similar to fig. F.2, here the preferred axis \hat{z} of the model points to the direction of the north ecliptic pole. Evidently, a Solar system effect is preferred by the data. For instance the first figure ($\hat{x} = \text{NEP}$) shows that the exclusion level can be weakened from 99% C.L. with $a_{\ell 0}^{\text{axial}} = 0 \mu\text{K}$ to 96% C.L. (92% C.L.) with $a_{\ell 0}^{\text{axial}} = 40 \mu\text{K}$ ($a_{\ell 0}^{\text{axial}} = 70 \mu\text{K}$) by axial contributions. For the alignment test with the equinox, the exclusion drops from 99.5% C.L. with $a_{\ell 0}^{\text{axial}} = 0 \mu\text{K}$ to around 98% C.L. with $a_{\ell 0}^{\text{axial}} = 70 \mu\text{K}$.

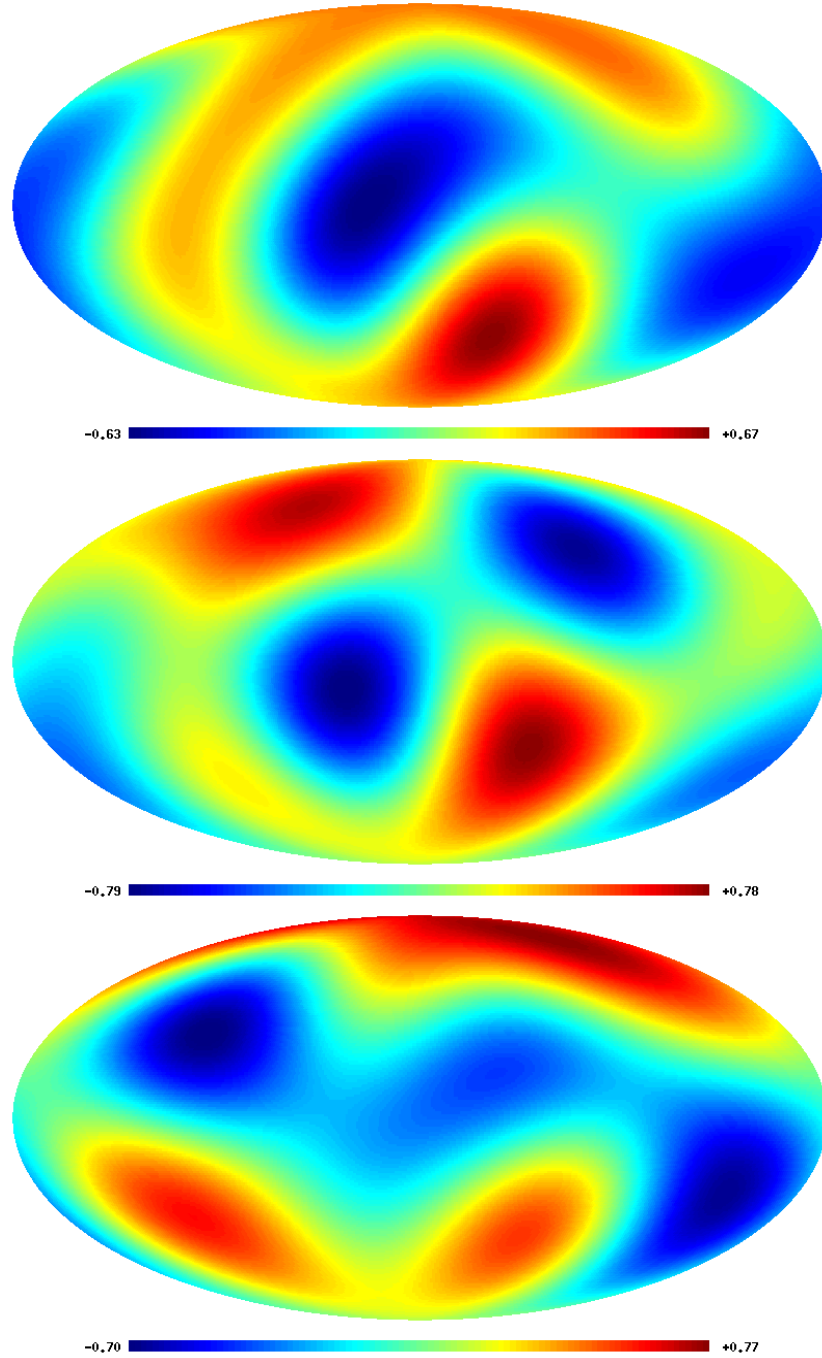


FIGURE F.5. $\ell = 2+3$ Mollweide maps showing the effect of additional axial contributions. Upper map: a random realisation of an statistically isotropic and Gaussian superimposed quadrupole and octopole. Middle map: adding an axial contribution of $a_{20}^{\text{axial}} = a_{30}^{\text{axial}} = 70\mu\text{K}$ to the random map, with the preferred axis of the model \hat{z} pointing in the direction of the dipole. Lower map: adding the same contribution, now with the preferred axis being in direction of the north ecliptic pole. For further explanation see the caption of fig. 4.8. The colour legends are in units of 0.1mK.

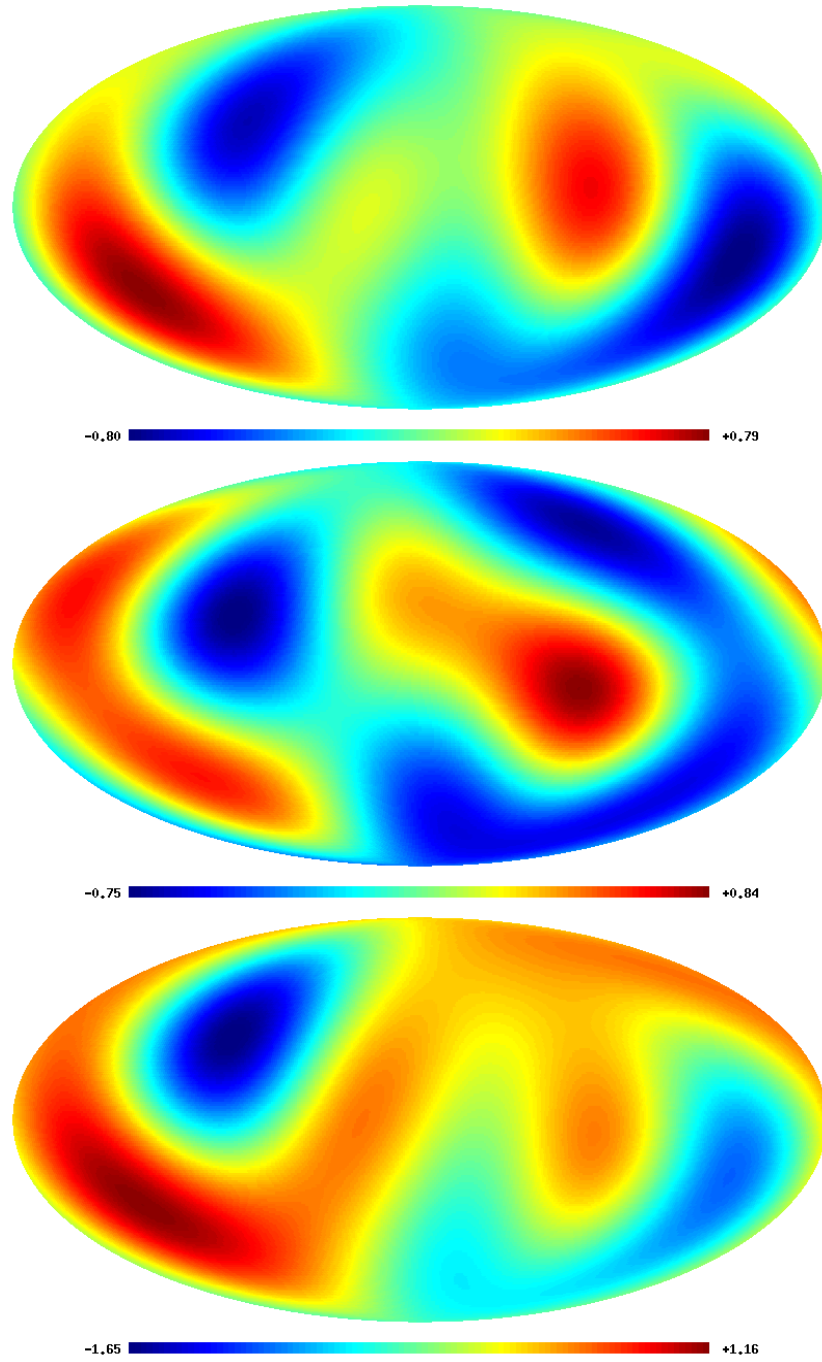


FIGURE F.6. Same procedure as in fig. F.5, now with a different initial random realisation (upper map); for explanation see caption of fig. F.5. The colour legends are in units of 0.1mK.

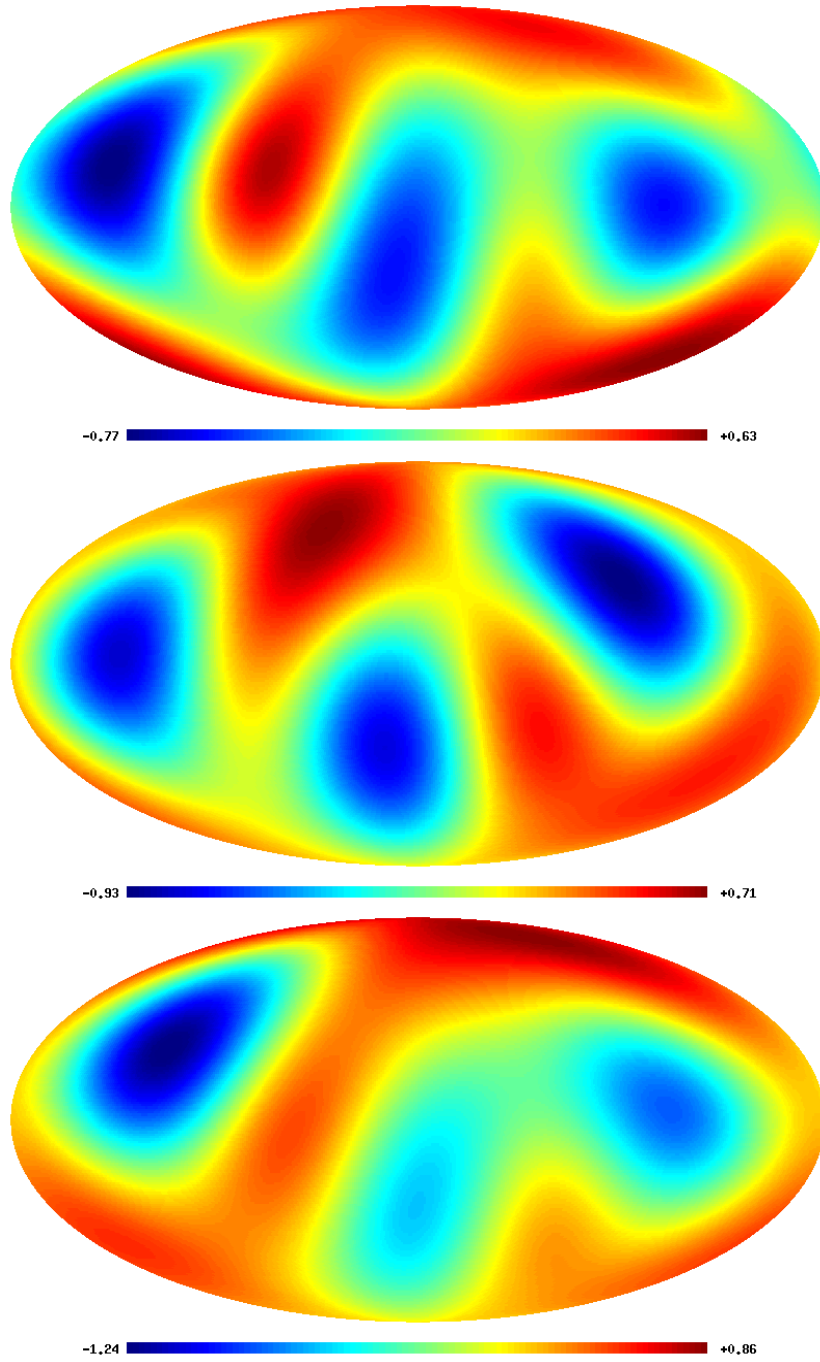


FIGURE F.7. Same procedure as in fig. F.5, now with a different initial random realisation (upper map); for explanation see caption of fig. F.5. The colour legends are in units of 0.1mK.

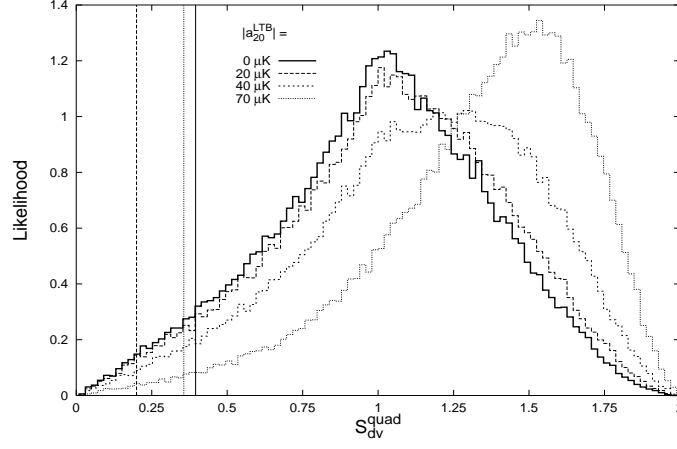


FIGURE F.8. Besides oriented areas, it is also possible to study the alignment of the multipole vectors themselves. Here, we probe the alignment of the quadrupole vectors themselves with the z direction. The test is defined as $S_{\hat{d}v}^{\text{quad}} \equiv \sum |\hat{d} \cdot \hat{v}^{(\ell,i)}|$. Axial contributions are added up to $70\mu\text{K}$. After some threshold behaviour ($\sim 40\mu\text{K}$), the $S_{\hat{d}v}^{\text{quad}}$ alignment becomes very sensitive on axial contaminations. The horizontal lines indicate WMAP one-year data: solid (ILC), dashed (TOH) and dotted (LILC) maps. For more detail on the various cleaned one-year maps see sec. 4.3.1.

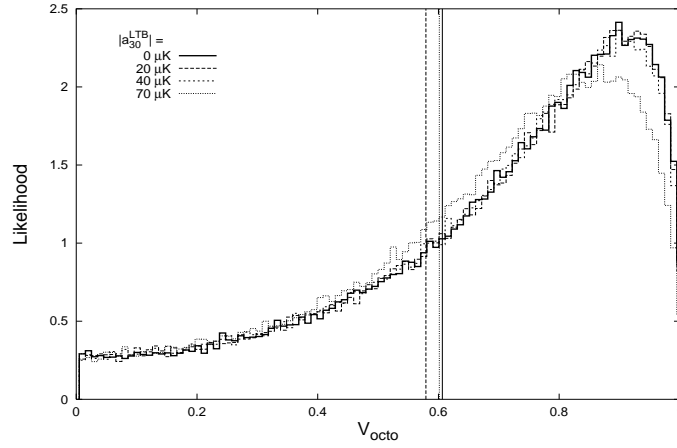


FIGURE F.9. Histogram showing the (anomalous) planarity of the octopole. The absolute value of the parallelepipedial product represents a volume and is an invariant when concerning three spatial vectors $\hat{v}^{(3,i)}$. Therefore we can test for planarity by using the parallelepipedial product as a suitable statistic, $V_{\text{octo}} \equiv |(\hat{v}^{(3,1)} \times \hat{v}^{(3,2)}) \cdot \hat{v}^{(3,3)}|$. The vertical data lines are due to the same maps as in fig. F.8. The parallelepipedial product is rather insensitive to axial contributions.

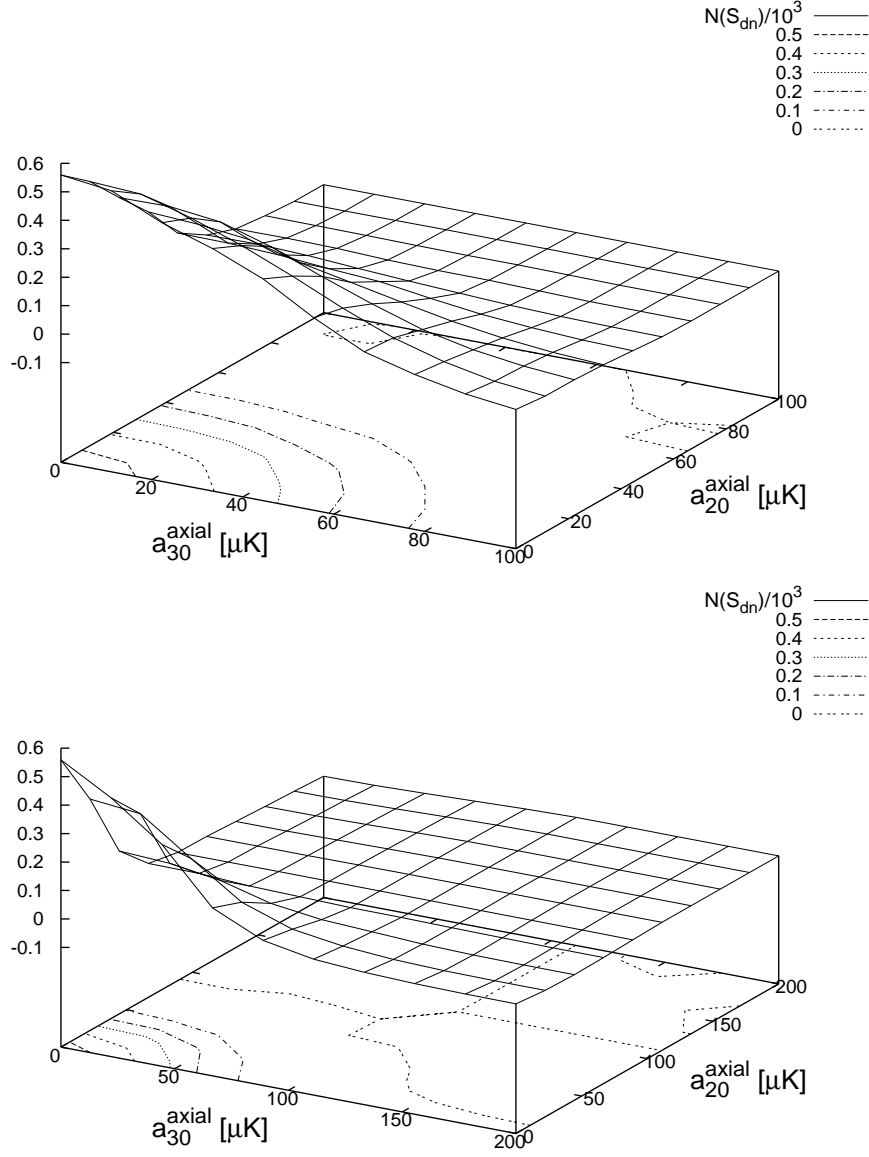


FIGURE F.10. Probing the effect on the alignment statistic $S_{\hat{a}_n} \equiv \sum |n^{(\ell;i,j)} \cdot \mathbf{d}|$ when adding asymmetric values of quadrupole and octopole axial contributions. Here $\hat{\mathbf{d}}$ is matched with the z axis and therefore the statistic measures alignment of quadrupole and octopole normals with the z direction. Plotted is, the arbitrarily scaled ($\times 10^{-3}$) number of Monte Carlos that are, for given values of $a_{\ell 0}^{\text{axial}}$, consistent with an experimental value of $S_{\hat{a}_n} \simeq 3.47$. That is, for instance a contour of 0.5 in the figure means that below this contour there are $\gtrsim 500$ hits consistent with data – but never more than ~ 600 , as can be seen from the figures. The experimental value is an average of $S_{\hat{a}_n}$ for the ILC, TOH and LILC maps of WMAP(1yr). The total number of Monte Carlos here is 10^5 . The upper figure and the lower figure show the same test, only in the lower figure the simulated range is larger by a factor of two. We can conclude that for this test only small and *symmetric* axial contributions to the quadrupole and octopole have the chance to be consistent with data.

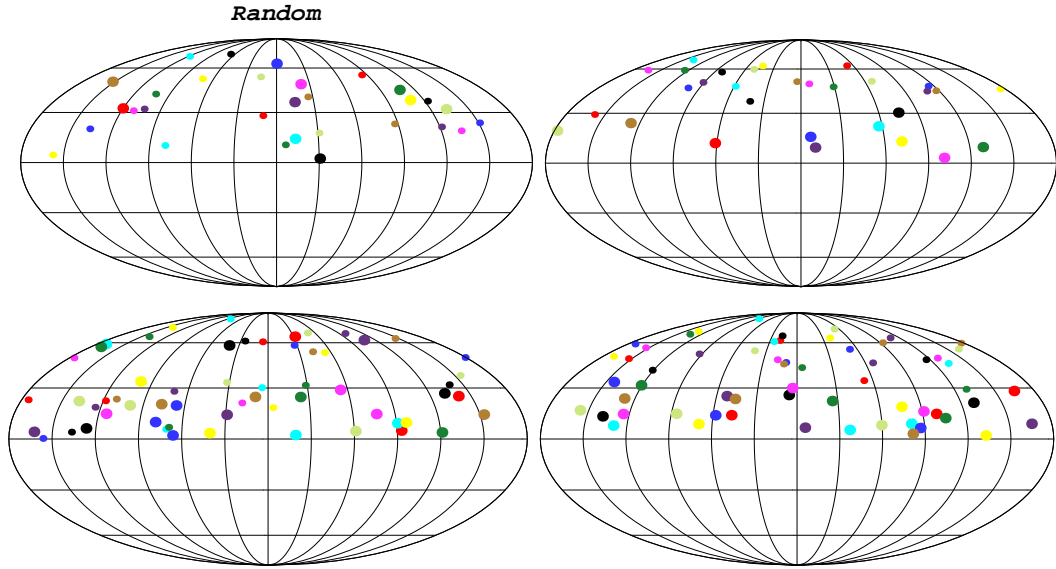


FIGURE F.11. Figure similar to fig. 5.2, here we added a smaller contribution of $a_{\ell 0} = 100 \mu K$ to the multipoles, such that we can observe the onset of the separation process of the vectors. Mollweide projection of the sky with quadrupole (upper row) and octopole (lower row) multipole vectors [equation (5.5)]. The mesh consists of steps in 30° . Displayed are ten pairs of quadrupole vectors (small dots) and their area vectors [equation (5.6)] (big dots) as well as ten triples of octopole vectors (small dots) and their area vectors (big dots); togetherness is indicated by colour. The arbitrary sign of the vectors has been used to gauge them all to the northern hemisphere. The statistically isotropic and Gaussian case (left column) is broken by the imprint of a moderate axial effect $a_{\ell 0} = 100 \mu K$ (right column) whereupon multipole vectors start to move to the pole and area vectors start to move to the equatorial plane. The full separation can be observed when adding strong contributions $a_{\ell 0} \sim 1000 \mu K$, c.f. fig. 5.2.

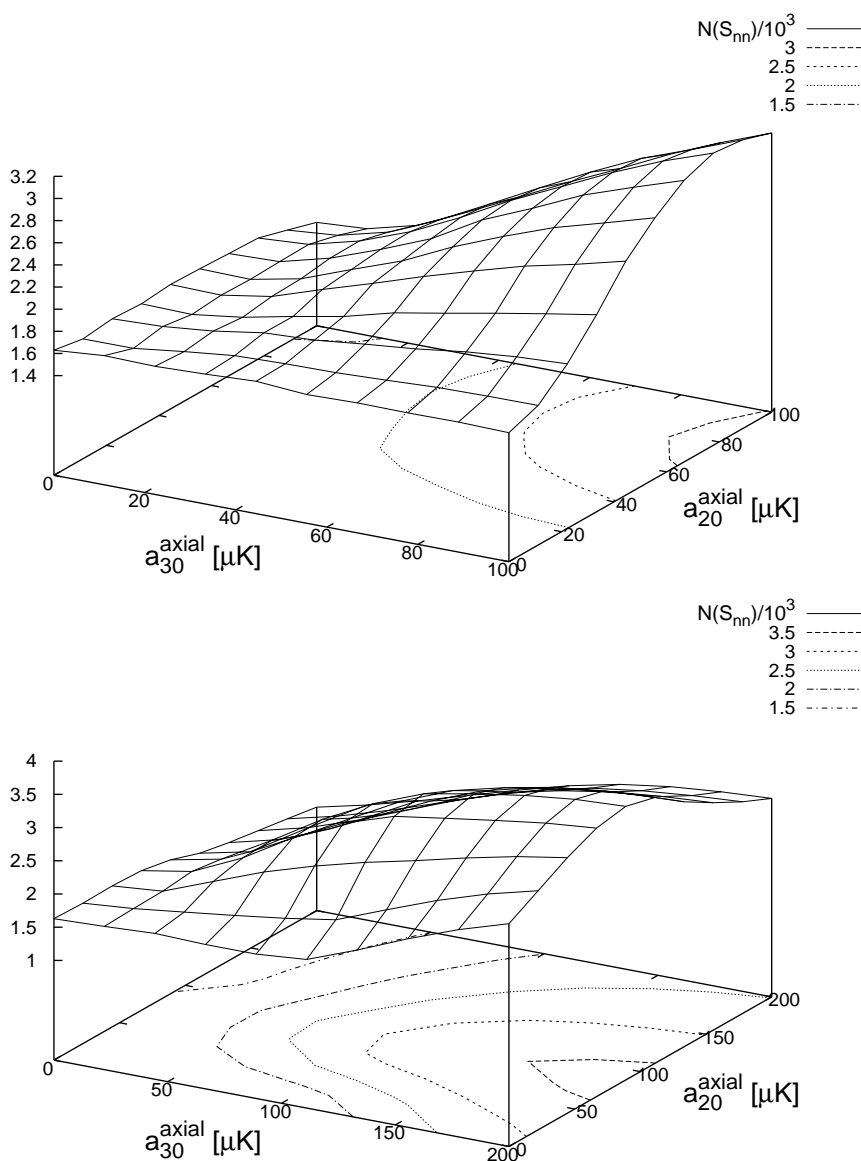


FIGURE F.12. Testing the effect of asymmetric additive contributions $a_{\ell 0}^{\text{axial}}$ on the intrinsic cross alignment of quadrupole and octopole. Here, the cross alignment test is defined as $S_{nn} \equiv \sum |\hat{n}^{(2;1,2)} \cdot \hat{n}^{(3;i,j)}|$; note the different pre-factor as compared to (5.8). Like in fig. F.10, we have plotted the arbitrarily scaled ($\times 10^{-3}$) number of Monte Carlos that are, for given values of $a_{\ell 0}^{\text{axial}}$, consistent with an experimental value of $S_{nn} \simeq 2.62$, that has been obtained from WMAP(1yr) cleaned maps. The total number of Monte Carlos is again 10^5 . The upper and lower figure show the same test, only with a different range of simulations. From the upper figure, we see that indeed, intrinsic alignments are apparently cured by adding axial contributions up to $\sim 100\mu\text{K}$. In the lower figure we see that, when increasing $a_{\ell 0}^{\text{axial}}$ further, this is only a local maximum. This is perfectly consistent with our findings fig. 5.3.

Bibliography

- [AA06] Havard Alnes and Morad Amarzguoui, *CMB Anisotropies Seen by an off-Center Observer in a Spherically Symmetric Inhomogeneous Universe*, Phys. Rev. **D74** (2006), 103520, astro-ph/0607334.
- [AA07] ———, *The Supernova Hubble Diagram for off-Center Observers in a Spherically Symmetric Inhomogeneous Universe*, Phys. Rev. **D75** (2007), 023506, astro-ph/0610331.
- [ACW07] Lotty Ackerman, Sean M. Carroll, and Mark B. Wise, *Imprints of a Primordial Preferred Direction on the Microwave Background*, Phys. Rev. **D75** (2007), 083502, astro-ph/0701357.
- [AFMS93] J. V. Arnau, M. J. Fullana, L. Monreal, and D. Saez, *On the Microwave Background Anisotropies Produced by Nonlinear Voids*, Astrophys. J. **402** (1993), 359–368.
- [AFZ06] Garry W. Angus, Benoit Famaey, and HongSheng Zhao, *Can MOND Take a Bullet? Analytical Comparisons of Three Versions of MOND Beyond Spherical Symmetry*, Mon. Not. Roy. Astron. Soc. **371** (2006), 138, astro-ph/0606216.
- [AJW06] L. Raul Abramo, Laerte Sodre Jr., and Carlos Alexandre Wuensche, *Anomalies in the low CMB Multipoles and Extended Foregrounds*, Phys. Rev. **D74** (2006), 083515, astro-ph/0605269.
- [Akh02] Evgeny K. Akhmedov, *Vacuum Energy and Relativistic Invariance*, 2002, hep-th/0204048.
- [Ale06] Stephon H. S. Alexander, *Is Cosmic Parity Violation Responsible for the Anomalies in the WMAP Data?*, 2006, hep-th/0601034.
- [ALST07] Ralf Aurich, S. Lustig, F. Steiner, and H. Then, *CMB Alignment in Multi-Connected Universes*, Class. Quant. Grav. **24** (2007), 1879–1894, astro-ph/0612308.
- [APO] Team APOD, *The official NASA site ‘Astronomy Picture of the Day’ at <http://apod.nasa.gov/apod/lib/aptree.html>*.
- [Arn62] Arnowitt, D., Deser, S. and Misner C. W., *in Gravitation: An Introduction to Current Research*, New York: Wiley, edited by Witten, Louis, 1962.
- [AS72] Milton Abramowitz and Irene A. Stegun, *Handbook of Mathematical Functions*, Dover Publications Inc., New York, 1972.
- [AS03] Luis Raul Abramo and Jr. Sodre, Laerte, *Can the Local Supercluster Explain the low CMB Multipoles?*, 2003, astro-ph/0312124.
- [Ast] Think Astronomy, *Homepage of the Think Astronomy community at <http://www.thinkastronomy.com>*.
- [B⁺03a] C. Bennett et al., *First Year Wilkinson Microwave Anisotropy Probe (WMAP) Observations: Foreground Emission*, Astrophys. J. Suppl. **148** (2003), 97, astro-ph/0302208.
- [B⁺03b] C. L. Bennett et al., *First Year Wilkinson Microwave Anisotropy Probe (WMAP) Observations: Preliminary Maps and Basic Results*, Astrophys. J. Suppl. **148** (2003), 1, astro-ph/0302207.
- [B⁺06a] James Bock et al., *Task Force on Cosmic Microwave Background Research*, 2006, astro-ph/0604101.
- [B⁺06b] Maruša Bradač et al., *Strong and Weak Lensing United III: Measuring the Mass Distribution of the Merging Galaxy Cluster 1E0657-56*, Astrophys. J. **652** (2006), 937–947, astro-ph/0608408.
- [BBS91] K. G. Begeman, A. H. Broeils, and R. H. Sanders, *Extended Rotation Curves of Spiral Galaxies - Dark haloes and Modified Dynamics*, Mon. Not. Roy. Astron. Soc. **249** (1991), 523.
- [BBS07] Daniel Babich, Cullen H. Blake, and Charles Steinhardt, *What Can the Cosmic Microwave Background Tell Us About the Outer Solar System?*, 2007, arXiv:0705.0986 [astro-ph].
- [BdVS06] D. Boyanovsky, Hector J. de Vega, and N. G. Sanchez, *CMB Quadrupole Suppression. I: Initial Conditions of Inflationary Perturbations*, Phys. Rev. **D74** (2006), 123006, astro-ph/0607508.
- [Beh03] Juliane Behrend, *On the Averaging Problem in General Relativity. Diplom thesis, University of Heidelberg*, 2003, Available e.g. at <http://www.thphys.uni-heidelberg.de/~behrend/>.
- [Bek04] Jacob D. Bekenstein, *Relativistic Gravitation Theory for the MOND Paradigm*, Phys. Rev. **D70** (2004), 083509, astro-ph/0403694.
- [BG83] M. Birkinshaw and S. F. Gull, *A Test for Transverse Motions of Clusters of Galaxies*, Nature **302** (1983), 315–317.
- [BG06] H. Balasin and Daniel Grumiller, *Significant Reduction of Galactic Dark Matter by General Relativity*, 2006, astro-ph/0602519.

- [BKH05] Krzysztof Bolejko, Andrzej Krasiński, and Charles Hellaby, *Formation of Voids in the Universe within the Lemaitre-Tolman Model*, Mon. Not. Roy. Astron. Soc. **362** (2005), 213.
- [BL93] J. Bicak and T. Ledvinka, *Relativistic Disks as sources of the Kerr metric*, Phys. Rev. Lett. **71** (1993), 1669–1672.
- [BM06] Richard A. Battye and Adam Moss, *Anisotropic Perturbations Due to Dark Energy*, Phys. Rev. **D74** (2006), 041301, astro-ph/0602377.
- [BM07] J. R. Brownstein and J. W. Moffat, *The Bullet Cluster 1E0657-558 Evidence Shows Modified Gravity in the Absence of Dark Matter*, 2007, astro-ph/0702146.
- [BMN06] Tirthabir Biswas, Reza Mansouri, and Alessio Notari, *Nonlinear Structure Formation and Apparent Acceleration: an Investigation*, 2006, astro-ph/0606703.
- [BN07] Tirthabir Biswas and Alessio Notari, *Swiss-Cheese Inhomogeneous Cosmology & the Dark Energy Problem*, 2007, astro-ph/0702555.
- [Bol05] Krzysztof Bolejko, *Supernovae Ia Observations in the Lemaitre-Tolman Model*, 2005, astro-ph/0512103.
- [Bol07] ———, *Evolution of Cosmic Structures in Different Environments in the Quasispherical Szekeres Model*, Phys. Rev. **D75** (2007), 043508, astro-ph/0610292.
- [Bon47] H. Bondi, *Spherically Symmetric Models in General Relativity*, Mon. Not. Roy. Astron. Soc. **107** (1947), 410, reprinted with historical comments in Gen. Rel. Grav. **31** (1999), 1777.
- [Bon77] W. B. Bonnor, *A Rotating Dust Cloud in General Relativity*, J. Phys. A: Math. Gen. **10** (1977), 1673–1677.
- [Bon80] ———, *The Rigidly Rotating Relativistic Dust Cylinder*, J. Phys. A: Math. Gen. **13** (1980), 2121–2132.
- [BT94] James Binney and Scott Tremaine, *Galactic Dynamics*, Princeton University Press, Princeton New Jersey, 1994.
- [BTT07a] Nikolaos Brouzakis, Nikolaos Tetradis, and Eleftheria Tzavara, *Light Propagation and Large-Scale Inhomogeneities*, 2007, astro-ph/0703586.
- [BTT07b] ———, *The Effect of Large-Scale Inhomogeneities on the Luminosity Distance*, JCAP **0702** (2007), 013, astro-ph/0612179.
- [BTV07] Armando Bernui, Constantino Tsallis, and Thyrso Villela, *Deviation from Gaussianity in the Cosmic Microwave Background Temperature Fluctuations*, Europhys. Lett. **78** (2007), 19001, astro-ph/0703708.
- [Buc01] Thomas Buchert, *On Average Properties of Inhomogeneous Fluids in General Relativity: Perfect Fluid Cosmologies*, Gen. Rel. Grav. **33** (2001), 1381–1405, gr-qc/0102049.
- [Buc07] ———, *Dark Energy from Structure - A Status Report*, 2007, arXiv:0707.2153 [gr-qc].
- [C00] M. N. Célérier, *Do we Really See a Cosmological Constant in the Supernovae Data?*, Astron. Astrophys. **353** (2000), 63–71, astro-ph/9907206.
- [C+06a] Douglas Clowe et al., *A Direct Empirical Proof of the Existence of Dark Matter*, 2006, astro-ph/0608407.
- [C+06b] Andres Curto et al., *Testing Gaussianity on Archeops Data*, 2006, astro-ph/0612148.
- [Car69] Brandon Carter, *Killing Horizons and Orthogonally Transitive Groups in Space-Time*, J. Math. Phys. **10** (1969), 70.
- [CCT06] Luigi Campanelli, P. Cea, and L. Tedesco, *Ellipsoidal Universe Can Solve The CMB Quadrupole Problem*, Phys. Rev. Lett. **97** (2006), 131302, astro-ph/0606266.
- [Chr84] D. Christodoulou, *Violation of Cosmic Censorship in the Gravitational Collapse of a Dust Cloud*, Communications in Mathematical Physics **93** (1984), 171–195.
- [CHR02] J. E. Carlstrom, G. P. Holder, and E. D. Reese, *Cosmology with the Sunyaev-Zel'dovich Effect*, Ann. Rev. Astron. Astrophys. **40** (2002), 643–680, astro-ph/0208192.
- [CHS04] Craig J. Copi, Dragan Huterer, and Glenn D. Starkman, *Multipole Vectors - A New Representation of the CMB Sky and Evidence for Statistical Anisotropy or Non-Gaussianity at $2 \leq \ell \leq 8$* , Phys. Rev. **D70** (2004), 043515, astro-ph/0310511.
- [CHSS06] Craig J. Copi, D. Huterer, D. J. Schwarz, and G. D. Starkman, *On the Large-Angle Anomalies of the Microwave Sky*, Mon. Not. Roy. Astron. Soc. **367** (2006), 79–102, astro-ph/0508047.
- [CHSS07] Craig Copi, Dragan Huterer, Dominik Schwarz, and Glenn Starkman, *The Uncorrelated Universe: Statistical Anisotropy and the Vanishing Angular Correlation Function in WMAP Years 1-3*, Phys. Rev. **D75** (2007), 023507, astro-ph/0605135.
- [Cle85] D. P. Clemens, *Massachusetts-Stony Brook Galactic Plane CO Survey - The Galactic Disk Rotation Curve*, Astrophys. J. **295** (1985), 422–428.
- [CMB] CMBFAST, *Uroš Seljak and Matias Zaldarriaga, homepage of CMBFAST at <http://cfa-www.harvard.edu/~mzaldarr/CMBFAST/cmbfast.html> or <http://www.cmbfast.org/>*.
- [CPKL03] Carlo R. Contaldi, Marco Peloso, Lev Kofman, and Andrei Linde, *Suppressing the lower Multipoles in the CMB Anisotropies*, JCAP **0307** (2003), 002, astro-ph/0303636.
- [Cro06] Daniel J. Cross, *Comments on the Cooperstock-Tieu Galaxy Model*, 2006, astro-ph/0601191.

- [CS98] M. N. C el erier and J. Schneider, *A Solution to the Horizon Problem: a Delayed Big Bang Singularity*, Phys. Lett. **A249** (1998), 37.
- [CS02] M. N. C el erier and P. Szekeres, *Timelike and Null Focussing Singularities in Spherical Symmetry: A Solution to the Cosmological Horizon Problem and a Challenge to the Cosmic Censorship Hypothesis*, Phys. Rev. **D65** (2002), 123516.
- [CS05] Asantha Cooray and Naoki Seto, *Did WMAP see Moving Local Structures?*, JCAP **0512** (2005), 004, astro-ph/0510137.
- [CT05a] Fred I. Cooperstock and S. Tieu, *General Relativity Resolves Galactic Rotation Without Exotic Dark Matter*, 2005, astro-ph/0507619.
- [CT05b] ———, *Perspectives on Galactic Dynamics via General Relativity*, 2005, astro-ph/0512048.
- [CT06] ———, *Galactic Dynamics via General Relativity and the Exotic Dark Matter Enigma*, Mod. Phys. Lett. **A21** (2006), 2133–2142.
- [D⁺03] A. G. Doroshkevich et al., *Gauss-Legendre Sky Pixelization (GLESP) for CMB Maps*, 2003, astro-ph/0305537.
- [D⁺07] Tamara M. Davis et al., *Scrutinizing Exotic Cosmological Models Using ESSENCE Supernova Data Combined with Other Cosmological Probes*, 2007, astro-ph/0701510.
- [DL03] Tamara M. Davis and Charles H. Lineweaver, *Expanding Confusion: Common Misconceptions of Cosmological Horizons and the Superluminal Expansion of the Universe*, 2003, astro-ph/0310808.
- [dOCT06] Angelica de Oliveira-Costa and Max Tegmark, *CMB Multipole Measurements in the Presence of Foregrounds*, Phys. Rev. **D74** (2006), 023005, astro-ph/0603369.
- [dOCTZH04] Angelica de Oliveira-Costa, Max Tegmark, Matias Zaldarriaga, and Andrew Hamilton, *The Significance of the Largest Scale CMB Fluctuations in WMAP*, Phys. Rev. **D69** (2004), 063516, astro-ph/0307282.
- [DPS⁺07] V. Dikarev, O. Preu , S. Solanki, H. Kr ger, and A. Krivov, *The Microwave Anisotropy Probe Mission*, Earth Moon and Planets (2007), 47.
- [Dre88] A. Dressler, *The Supergalactic Plane Redshift Survey - A Candidate for the Great Attractor*, Astrophys. J. **329** (1988), 519–526.
- [DS02] Scott Dodelson and Ewan Stewart, *Scale dependent spectral index in slow roll inflation*, Phys. Rev. **D65** (2002), 101301.
- [DZS78] A. G. Doroshkevich, I. B. Zeldovich, and R. A. SiuniaeV, *Fluctuations of the Microwave Background Radiation in the Adiabatic and Entropic Theories of Galaxy Formation*, Astronomicheskii Zhurnal **55** (1978), 913–921.
- [EBGL04] Hans Kristian Eriksen, A. J. Banday, K. M. Gorski, and P. B. Lilje, *Foreground Removal by an Internal Linear Combination Method: Limitations and Implications*, Astrophys. J. **612** (2004), 633–646, astro-ph/0403098.
- [EHB⁺04] H. K. Eriksen, F. K. Hansen, A. J. Banday, K. M. G rski, and P. B. Lilje, *Asymmetries in the Cosmic Microwave Background Anisotropy Field*, Astrophys. J. **605** (2004), 14–20.
- [Ein17] Albert Einstein, *Kosmologische Betrachtungen zur Allgemeinen Relativit tstheorie*, Sitzungsber. Preuss. Akad. Wiss. Berlin (Math. Phys.) **1917** (1917), 142–152.
- [EM07] Kari Enqvist and Teppo Mattsson, *The Effect of Inhomogeneous Expansion on the Supernova Observations*, JCAP **0702** (2007), 019, astro-ph/0609120.
- [Enq07] Kari Enqvist, *Lema tre-Tolman-Bondi Model and Accelerating Expansion*, 2007, arXiv:0709.2044 [astro-ph].
- [ER02] Roberto Emparan and Harvey S. Reall, *Generalized Weyl Solutions*, Phys. Rev. **D65** (2002), 084025, hep-th/0110258.
- [ES79] D. M. Eardley and L. Smarr, *Time functions in Numerical Relativity: Marginally Bound Dust Collapse*, Phys. Rev. **D19** (1979), 2239–2259.
- [ETJ⁺97] M. Einasto, E. Tago, J. Jaaniste, J. Einasto, and H. Andernach, *The Supercluster-Void Network I. The Supercluster Catalogue and Large-Scale Distribution*, Astron. Astrophys. Suppl. Ser. **123** (1997), 119–133, astro-ph/9610088.
- [EvE98] George F. R. Ellis and Henk van Elst, *Cosmological models - Cargese Lectures 1998*, 1998, gr-qc/9812046.
- [EvEM01] George F. R. Ellis, Henk van Elst, and Roy Maartens, *General Relativistic Analysis of Peculiar Velocities*, Class. Quant. Grav. **18** (2001), 5115–5124, gr-qc/0105083.
- [FBNP⁺06] Yasushi Fukazawa, J. G. Betoya-Nonesca, J. Pu, A. Ohto, and N. Kawano, *Scaling Mass Profiles Around Elliptical Galaxies Observed with Chandra and XMM-Newton*, Astrophys. J. **636** (2006), 698, astro-ph/0509521.
- [FGM⁺06] Peter E. Freeman, C. R. Genovese, C. J. Miller, R. C. Nichol, and L. Wasserman, *Examining the Effect of the Map-Making Algorithm on Observed Power Asymmetry in WMAP Data*, Astrophys. J. **638** (2006), 1, astro-ph/0510406.
- [FI86] J. E. Felten and R. Isaacman, *Scale Factors $R(t)$ and Critical Values of the Cosmological Constant Λ in Friedmann Universes*, Reviews of Modern Physics **58** (1986), 689–698.

- [Fis07] André Fischer, *Untersuchung der kosmischen Mikrowellenstrahlung mit Hilfe Maxwellscher Multipolvektoren. Diplom thesis, Bielefeld University*, 2007, Available e.g. at <http://www.physik.uni-bielefeld.de/cosmology/theses.html>.
- [Fri05] Priscilla C. Frisch, *Tentative Identification of Interstellar Dust in Heliosphere Nose*, *Astrophys. J.* **632** (2005), L143–L146, astro-ph/0506293.
- [FRV04] Francesc Ferrer, Syksy Rasanen, and Jussi Valiviita, *Correlated Isocurvature Perturbations from Mixed Inflation-Curvature Decay*, *JCAP* **0410** (2004), 010, astro-ph/0407300.
- [FS07] J. R. Fergusson and Edward P. S. Shellard, *Primordial non-Gaussianity and the CMB Bispectrum*, *Phys. Rev.* **D76** (2007), 083523, astro-ph/0612713.
- [FSA94] M. J. Fullana, D. Saez, and J. V. Arnau, *On the Microwave Background Anisotropy Produced by Great Attractor-like Structures*, *Astrophys. J. Suppl.* **94** (1994), 1–16.
- [FSSB01] P. Fouqué, J. M. Solanes, T. Sanchis, and C. Balkowski, *Structure, Mass and Distance of the Virgo Cluster from a Tolman-Bondi Model*, *Astron. Astrophys.* **375** (2001), 770–780, astro-ph/0106261.
- [G+05] J. Richard III Gott et al., *A Map of the Universe*, *Astrophys. J.* **624** (2005), 463, astro-ph/0310571.
- [Gar06a] David Garfinkle, *Inhomogeneous Spacetimes as a Dark Energy Model*, *Class. Quant. Grav.* **23** (2006), 4811–4818, gr-qc/0605088.
- [Gar06b] ———, *The Need for Dark Matter in Galaxies*, *Class. Quant. Grav.* **23** (2006), 1391, gr-qc/0511082.
- [GCP06] A. E. Gumrukcuoglu, Carlo R. Contaldi, and Marco Peloso, *CMB Anomalies from Relic Anisotropy*, 2006, astro-ph/0608405.
- [Gfr] Gfroerer, *Timothy H., personal homepage of at http://webphysics.davidson.edu/faculty/thg/, Copyright due to Brooks/Cole - Thomson*.
- [GH04] Christopher Gordon and Wayne Hu, *A Low CMB Quadrupole from Dark Energy Isocurvature Perturbations*, *Phys. Rev.* **D70** (2004), 083003, astro-ph/0406496.
- [GHHC05] Christopher Gordon, Wayne Hu, Dragan Huterer, and Thomas M. Crawford, *Spontaneous Isotropy Breaking: A Mechanism for CMB Multipole Alignments*, *Phys. Rev.* **D72** (2005), 103002, astro-ph/0509301.
- [GHS07] Tuhin Ghosh, Amir Hajian, and Tarun Souradeep, *Unveiling Hidden Patterns in CMB Anisotropy Maps*, *Phys. Rev.* **D75** (2007), 083007, astro-ph/0604279.
- [GHW90] H. P. Gush, M. Halpern, and E. H. Wishnow, *Rocket Measurement of the Cosmic-Background-Radiation mm-Wave Spectrum*, *Phys. Rev. Lett.* **65** (1990), 537–540.
- [H+03] G. Hinshaw et al., *First Year Wilkinson Microwave Anisotropy Probe (WMAP) Observations: Angular Power Spectrum*, *Astrophys. J. Suppl.* **148** (2003), 135, astro-ph/0302217.
- [H+07] ———, *Three-Year Wilkinson Microwave Anisotropy Probe (WMAP) Observations: Temperature Analysis*, *Astrophys. J. Suppl.* **170** (2007), 288, astro-ph/0603451.
- [Haj07] Amir Hajian, *Analysis of the Apparent Lack of Power in the Cosmic Microwave Background Anisotropy at Large Angular Scales*, 2007, astro-ph/0702723.
- [HBB+96] G. Hinshaw, A. J. Branday, C. L. Bennett, K. M. Gorski, A. Kogut, C. H. Lineweaver, G. F. Smoot, and E. L. Wright, *Two-Point Correlations in the COBE DMR Four-Year Anisotropy Maps*, *Astrophys. J. Lett.* **464** (1996), L25, astro-ph/9601061.
- [HBM+05] Frode K. Hansen, E. Branchini, P. Mazzotta, P. Cabella, and K. Dolag, *A Full-Sky Prediction of the SZ Effect from Diffuse Hot Gas in the Local Universe and the upper Limit from the WMAP Data*, *Mon. Not. Roy. Astron. Soc.* **361** (2005), 753–762, astro-ph/0502227.
- [HEB+05] David W. Hogg, Daniel J. Eisenstein, Michael R. Blanton, Neta A. Bahcall, J. Brinkmann, James E. Gunn, and Donald P. Schneider, *Cosmic Homogeneity Demonstrated with Luminous Red Galaxies*, *Astrophys. J.* **624** (2005), 54–58.
- [HES] Team HESE, *Official site of the High Energy Space Environment Branch* <http://heseweb.nrl.navy.mil/gamma/>.
- [HMM97] Neil P. Humphreys, Roy Maartens, and David R. Matravers, *Anisotropic Observations in Universes with Nonlinear Inhomogeneity*, *Astrophys. J.* **477** (1997), 47, astro-ph/9602033.
- [HN99] Jai-chan Hwang and Hyerim Noh, *The Sachs-Wolfe Effect: Gauge Independence and a General Expression*, *Phys. Rev.* **D59** (1999), 067302, astro-ph/9812007.
- [Hog00] David W. Hogg, *Distance Measures in Cosmology*, 2000, astro-ph/9905116.
- [HPLN02] J. Hwang, T. Padmanabhan, O. Lahav, and H. Noh, *On the 1/3 Factor in the CMB Sachs-Wolfe Effect*, *Phys. Rev.* **D65** (2002), 043005, astro-ph/0107307.
- [HS95] Wayne Hu and Naoshi Sugiyama, *Toward Understanding CMB Anisotropies and Their Implications*, *Phys. Rev.* **D51** (1995), 2599–2630, astro-ph/9411008.
- [HS04] Paul Hunt and Subir Sarkar, *Multiple Inflation and the WMAP ‘Glitches’*, *Phys. Rev.* **D70** (2004), 103518, astro-ph/0408138.
- [HS07] ———, *Multiple Inflation and the WMAP ‘Glitches’ II. Data Analysis and Cosmological Parameter Extraction*, 2007, arXiv:0706.2443 [astro-ph].

- [HSLB04] Michael J. Hudson, Russell J. Smith, John R. Lucey, and Enzo Branchini, *Streaming Motions of Galaxy Clusters Within 12000 km/s - V. The Peculiar Velocity Field*, Mon. Not. Roy. Astron. Soc. **352** (2004), 61, astro-ph/0404386.
- [HST] Team HST, *Official site of the Hubble Space Telescope at <http://hubblesite.org/>*.
- [HTET01] M. O. Hanski, G. Theureau, T. Ekholm, and P. Teerikorpi, *Kinematics of the Local Universe. IX. The Perseus-Pisces Supercluster and the Tolman-Bondi Model*, Astron. Astrophys. **378** (2001), 345–360, astro-ph/0109080.
- [Hub29] Edwin Hubble, *A Relation Between Distance and Radial Velocity Among Extra-Galactic Nebulae*, Proc. Nat. Acad. Sci. **15** (1929), 168–173.
- [HW04] Stefan Hofmann and Oliver Winkler, *The Spectrum of Fluctuations in Inflationary Quantum Cosmology*, 2004, astro-ph/0411124.
- [IAB+03] E. Iodice, M. Arnaboldi, F. Bournaud, F. Combes, L. S. Sparke, W. van Driel, and M. Capaccioli, *Polar Ring Galaxies and the Tully Fisher Relation: Implications for the Dark Halo Shape*, Astrophys. J. **585** (2003), 730.
- [INN02] H. Iguchi, T. Nakamura, and K. Nakao, *Is Dark Energy the Only Solution to the Apparent Acceleration of the Present Universe?*, Prog. Theor. Phys. **108** (2002), 809–818, astro-ph/0112419.
- [IRWG07] Mustapha Ishak, James Richardson, Delilah Whittington, and David Garred, *Dark Energy or Apparent Acceleration Due to a Relativistic Cosmological Model More Complex than FLRW?*, 2007, arXiv:0708.2943 [astro-ph].
- [IS06] Kaiki Taro Inoue and Joseph Silk, *Local Voids as the Origin of Large-angle Cosmic Microwave Background Anomalies*, Astrophys. J. **648** (2006), 23–30, astro-ph/0602478.
- [IS07] ———, *Local Voids as the Origin of Large-angle Cosmic Microwave Background Anomalies: The Effect of a Cosmological Constant*, Astrophys. J. **664** (2007), 650–659, astro-ph/0612347.
- [Isl85] Jamal N. Islam, *Rotating Fields in General Relativity*, Cambridge University Press, Cambridge, 1985.
- [J+07a] N. Jarosik et al., *Three-Year Wilkinson Microwave Anisotropy Probe (WMAP) Observations: Beam Profiles, Data Processing, Radiometer Characterization and Systematic Error Limits*, Astrophys. J. Suppl. **170** (2007), 263, astro-ph/0603452.
- [J+07b] Myungkook James Jee et al., *Discovery of a Ringlike Dark Matter Structure in the Core of the Galaxy Cluster Cl 0024+17*, 2007, arXiv:0705.2171 [astro-ph].
- [JBE+06] T. R. Jaffe, A. J. Banday, H. K. Eriksen, K. M. Gorski, and F. K. Hansen, *Bianchi Type VII_h Models and the WMAP 3-year Data*, 2006, astro-ph/0606046.
- [JW85] B. J. T. Jones and R. F. G. Wyse, *The Ionisation of the Primeval Plasma at the Time of Recombination*, Astr. Astrophys. **149** (1985), 144–150.
- [Kan69] R. Kantowski, *The Coma Cluster as a Spherical Inhomogeneity in Relativistic Dust*, Astrophys. J. **155** (1969), 1023.
- [KE06] Dale D. Kocevski and Harald Ebeling, *On The Origin of the Local Group's Peculiar Velocity*, Astrophys. J. **645** (2006), 1043–1053, astro-ph/0510106.
- [Ker63] G. D. Kerr, *Gravitational Field of a Spinning Mass as an Example of Algebraically Special Metrics*, Phys. Rev. Lett. **11** (1963), 237.
- [KH02] Andrzej Krasinski and Charles Hellaby, *Structure Formation in the Lemaitre-Tolman Model*, Phys. Rev. **D65** (2002), 023501.
- [KH04a] ———, *Formation of a Galaxy with a Central Black Hole in the Lemaitre-Tolman Model*, Phys. Rev. **D69** (2004), 043502.
- [KH04b] ———, *More Examples of Structure Formation in the Lemaitre-Tolman Model*, Phys. Rev. **D69** (2004), 023502.
- [KH05] ———, *Structure Formation in the Lemaitre-Tolman Cosmological Model (A Non-Perturbative Approach)*, in: *Topics in Mathematical Physics, General Relativity and Cosmology. Proceedings of a Symposium on the Occasion of the 75th Birthday of Plebański, Mexico*, 2005.
- [KH06] ———, *Alternative Methods of Describing Structure Formation in the Lemaitre-Tolman Model*, Phys. Rev. **D73** (2006), 023518.
- [KKN+07] Tomohiro Kai, Hiroshi Kozaki, Ken-ichi Nakao, Yasusada Nambu, and Chul-Moon Yoo, *Can Inhomogeneities Accelerate the Cosmic Volume Expansion?*, Prog. Theor. Phys. **117** (2007), 229–240, gr-qc/0605120.
- [KKZ97] Hans-Volker Klapdor-Kleingrothaus and Kai Zuber, *Teilchenastrophysik*, B. G. Teubner, Stuttgart, 1997.
- [KLS+93] A. Kogut, C. Lineweaver, G. F. Smoot, C. L. Bennett, A. Banday, N. W. Boggess, E. S. Cheng, G. de Amici, D. J. Fixsen, G. Hinshaw, P. D. Jackson, P. Janssen, M. and Keegstra, K. Loewenstein, P. Lubin, J. C. Mather, L. Tenorio, R. Weiss, D. T. Wilkinson, and E. L. Wright, *Dipole Anisotropy in the COBE Differential Microwave Radiometers First-Year Sky Maps*, Astrophys. J. **419** (1993), 1, astro-ph/9312056.
- [KM06] Tomi Koivisto and David F. Mota, *Dark Energy Anisotropic Stress and Large Scale Structure Formation*, Phys. Rev. **D73** (2006), 083502, astro-ph/0512135.

- [KME04] Dale D. Kocevski, Christopher R. Mullis, and Harald Ebeling, *The Dipole Anisotropy of the First All-Sky X-ray Cluster Sample*, *Astrophys. J.* **608** (2004), 721–730, astro-ph/0403275.
- [Kom58] Arthur Komar, *Covariant Conservation Laws in General Relativity*, *Phys. Rev.* **113** (1958), no. 3, 934.
- [Kor05] Mikolaj Korzynski, *Singular Disk of Matter in the Cooperstock and Tieu Galaxy Model*, 2005, astro-ph/0508377.
- [Kra97] Andrzej Krasinski, *Inhomogeneous Cosmological Models*, Cambridge University Press, Cambridge, 1997.
- [KS07] Masahiro Kawasaki and Toyokazu Sekiguchi, *Cosmological Constraints on Isocurvature and Tensor Perturbations*, 2007, arXiv:0705.2853 [astro-ph].
- [Lem33] A. G. Lemaître, *L’Univers en Expansion*, *Ann. Soc. Sci. Bruxelles* **A53** (1933), 51, reprinted in English with historical comments in *Gen. Rel. Grav.* **29** (1997), 637.
- [Les04] Julien Lesgourgues, *An Overview of Cosmology*, 2004, Lecture Notes for the Summer Students Program of CERN (2002-2004), astro-ph/0409426.
- [Lew32] T. Lewis, *Some Special Solutions of the Equations of Axially Symmetric Gravitational Fields*, *Proc. Roy. Soc. Lond.* **A136** (1932), 176.
- [LFB⁺88] D. Lynden-Bell, S. M. Faber, D. Burstein, R. L. Davies, A. Dressler, R. J. Terlevich, and G. Wegner, *Spectroscopy and Photometry of Elliptical Galaxies. V - Galaxy Streaming toward the new Supergalactic Center*, *Astrophys. J.* **326** (1988), 19–49.
- [Lid04] Chris Lidman, *Observing Distant Type Ia Supernovae with the ESO VLT*, *The European Organisation for Astronomical Research in the Southern Hemisphere Messenger* **118** (2004), 24.
- [LM05] Kate Land and Joao Magueijo, *The Axis of Evil*, *Phys. Rev. Lett.* **95** (2005), 071301, astro-ph/0502237.
- [LM07] ———, *The Axis of Evil Revisited*, *Mon. Not. Roy. Astron. Soc.* **378** (2007), 153–158, astro-ph/0611518.
- [Lon98] Malcom S. Longair, *Galaxy Formation*, *Astronomy and Astrophysics Library*, Springer, Berlin Heidelberg New York, 1998.
- [Lon07] Michael J. Longo, *Does the Universe Have a Handedness*, 2007, astro-ph/0703325.
- [LP96] David Langlois and Tsvi Piran, *Dipole Anisotropy from an Entropy Gradient*, *Phys. Rev.* **D53** (1996), 2908–2919, astro-ph/9507094.
- [LRSH04] John Lucey, David Radburn-Smith, and Mike Hudson, *Beta, Local SNIa Data and the Great Attractor*, 2004, Appearing in the Proceedings of the Meeting on Nearby Large Scale Structures and the Zone of Avoidance, Cape Town, South Africa, 28 Mar - 2 Apr 2004, astro-ph/0412329.
- [LS07] Nan Li and Dominik J. Schwarz, *On the Onset of Cosmological Backreaction*, *Phys. Rev.* **D76** (2007), 083011, gr-qc/0702043.
- [LSS] Team LSST, *Site of the proposed Large Synoptic Survey Telescope at http://www.lsst.org/lstst_home.shtml*.
- [LWR⁺03] J. P. Luminet, J. Weeks, A. Riazuelo, R. Lehoucq, and J. P. Uzan, *Dodecahedral Space Topology as an Explanation for Weak Wide-Angle Correlations in the Cosmic Microwave Background*, *Nature*. **425** (2003), 593, astro-ph/0310253.
- [M91] Attila Mészáros, *On Shell Crossing in the Tolman Metric*, *Mon. Not. Roy. Astron. Soc.* **253** (1991), 619–624.
- [M⁺04] Maxim Markevitch et al., *Direct Constraints on the Dark Matter Self-Interaction Cross-Section from the Merging Cluster 1E0657-56*, *Astrophys. J.* **606** (2004), 819–824, astro-ph/0309303.
- [Maa98] Roy Maartens, *Covariant Velocity and Density Perturbations in Quasi-Newtonian Cosmologies*, *Phys. Rev.* **D58** (1998), 124006, astro-ph/9808235.
- [Man05] Reza Mansouri, *Structured FRW Universe leads to Acceleration: A Non-Perturbative Approach*, 2005, astro-ph/0512605.
- [Mas05] Karen L. Masters, *Cosmology in the Very Local Universe - Why Flow Models Matter*, 2005, Appearing in the Proceedings of the 22nd Texas Symposium on Relativistic Astrophysics at Stanford University, Stanford, California, 13-17 Dec 2004, astro-ph/0503271.
- [Max79] James C. Maxwell, *A Treatise on Electricity and Magnetism - Volume I*, Dover Publications Inc., New York, 1979.
- [MCC⁺94] J. C. Mather, E. S. Cheng, D. A. Cottingham, R. E. Eplee, Jr., D. J. Fixsen, T. Hewagama, R. B. Isaacman, K. A. Jensen, S. S. Meyer, P. D. Noerdlinger, S. M. Read, L. P. Rosen, R. A. Shafer, E. L. Wright, C. L. Bennett, N. W. Boggess, M. G. Hauser, T. Kelsall, S. H. Moseley, Jr., R. F. Silverberg, G. F. Smoot, R. Weiss, and D. T. Wilkinson, *Measurement of the Cosmic Microwave Background Spectrum by the COBE FIRAS Instrument*, *Astrophys. J.* **420** (1994), 439–444.
- [MDW⁺07] M. Maturi, K. Dolag, A. Waelkens, V. Springel, and T. Ensslin, *The Actual Rees-Sciama Effect from the Local Universe*, 2007, arXiv:0708.1881 [astro-ph].
- [Mes63] Leon Mestel, *On the Galactic Law of Rotation*, *Mon. Not. Roy. Astron. Soc.* **126** (1963), 553.

- [MFB92] V. F. Mukhanov, H. A. Feldman, and R. H. Brandenberger, *Theory of Cosmological Perturbations. Part 1. Classical Perturbations. Part 2. Quantum Theory of Perturbations. Part 3. Extensions*, Phys. Rept. **215** (1992), 203.
- [MH07] M. L. McClure and Charles Hellaby, *The Metric of the Cosmos II: Accuracy, Stability, and Consistency*, 2007, arXiv:0709.0875 [gr-qc].
- [Mil83] M. Milgrom, *A Modification of the Newtonian Dynamics as a Possible Alternative to the Hidden Mass Hypothesis*, Astrophys. J. **270** (1983), 365–370.
- [MKMR07] Valerio Marra, Edward W. Kolb, Sabino Matarrese, and Antonio Riotto, *On Cosmological Observables in a Swiss-Cheese Universe*, 2007, arXiv:0708.3622 [astro-ph].
- [Mof05] John W. Moffat, *Cosmic Microwave Background, Accelerating Universe and Inhomogeneous Cosmology*, JCAP **0510** (2005), 012, astro-ph/0502110.
- [MS90] E. Martinez-Gonzalez and J. L. Sanz, *CMB Anisotropies Generated by Cosmic Voids and Great Attractors*, Mon. Not. Roy. Astron. Soc. **247** (1990), 473–478.
- [MS98] Jérôme Martin and Dominik J. Schwarz, *Predictions of Inflation for the CMB*, 1998, Private Communication.
- [MS07] Joao Magueijo and Rafael D. Sorkin, *Occam's Razor meets WMAP*, Mon. Not. Roy. Astron. Soc. Lett. **377** (2007), L39–L43, astro-ph/0604410.
- [MTW73] Charles W. Misner, Kip S. Thorne, and John A. Wheeler, *Gravitation*, San Francisco: W.H. Freeman and Co., 1973.
- [Nar02] Jayant Vishnu Narlikar, *An Introduction to Cosmology*, Cambridge University Press, Cambridge, 2002.
- [NEFM05] Fabrizio Nicastro, Martin Elvis, Fabrizio Fiore, and Smita Mathur, *Measured Cosmological Mass Density in the WHIM: the Solution to the 'Missing Baryons Problem'*, 2005, astro-ph/0501126, and refs. therein.
- [NM95] G. Neugebauer and R. Meinel, *General Relativistic Gravitational Field of a Rigidly Rotating Disk of Dust: Solution in Terms of Ultraelliptic Functions*, Phys. Rev. Lett. **75** (1995), 3046.
- [Org] Astronomy Online Org, *Homepage of Astronomy Online Org at <http://astronomyonline.org/default.asp?Cate=Home>*.
- [P+98] S. Perlmutter et al., *Discovery of a Supernova Explosion at Half the Age of the Universe and its Cosmological Implications*, Nature **391** (1998), 51–54.
- [P+99] ———, *Measurements of Omega and Lambda from 42 High-Redshift Supernovae*, Astrophys. J. **517** (1999), 565–586, astro-ph/9812133.
- [P+07] L. Page et al., *Three Year Wilkinson Microwave Anisotropy Probe (WMAP) Observations: Polarization Analysis*, Astrophys. J. Suppl. **170** (2007), 335, astro-ph/0603450.
- [Pad02] Thanu Padmanabhan, *Theoretical Astrophysics, Volume III: Galaxies and Cosmology*, Cambridge University Press, Cambridge, 2002.
- [Pan92] M. Panek, *Cosmic Background Radiation Anisotropies from Cosmic Structures - Models Based on the Tolman Solution*, Astrophys. J. **388** (1992), 225–233.
- [Pap53] Achille Papapetrou, *Eine Rotationssymmetrische Lösung in der Allgemeinen Relativitätstheorie*, Annalen der Physik **12** (1953), 309.
- [Pap66] ———, *Champs Gravitationelles Stationnaires à Symétrie Axiale*, Ann. Inst. H. Poincaré **A4** (1966), 83.
- [Par07] Aseem Paranjape, *A Covariant Road to Spatial Averaging in Cosmology : Scalar Corrections to the Cosmological Equations*, 2007, arXiv:0705.2380 [gr-qc].
- [Pea99] John A. Peacock, *Cosmological Physics*, Cambridge University Press, Cambridge, 1999.
- [Pee93] Phillip James Edwin Peebles, *Principles of Physical Cosmology*, Princeton University Press, Princeton New Jersey, 1993.
- [PK98] M. Plionis and V. Kolokotronis, *The X-Ray Cluster Dipole*, Astrophys. J. **500** (1998), 1, astro-ph/9707147.
- [PK06] Jerzy Plebański and Andrzej Krasinski, *An Introduction to General Relativity and Cosmology*, Cambridge University Press, Cambridge, 2006.
- [PM84] H. H. Partovi and B. Mashhoon, *Toward Verification of Large-Scale Homogeneity in Cosmology*, Astrophys. J. **276** (1984), 4.
- [PP90] B. Paczynski and T. Piran, *A Dipole Moment of the Microwave Background as a Cosmological Effect*, Astrophys. J. **364** (1990), 341–348.
- [PQC+06] D. Proust, H. Quintana, E. R. Carrasco, A. Reisenegger, E. Slezak, H. Muriel, R. Dünner, L. Sodré, Jr., M. J. Drinkwater, Q. A. Parker, and C. J. Ragone, *Structure and Dynamics of the Shapley Supercluster. Velocity Catalogue, General Morphology and Mass*, Astron. Astrophys. **447** (2006), 133–144.
- [PR03] P. J. E. Peebles and Bharat Ratra, *The Cosmological Constant and Dark Energy*, Rev. Mod. Phys. **75** (2003), 559–606, astro-ph/0207347, and refs. therein.

- [PRFJ07] N. Prause, D. Reimers, C. Fechner, and E. Janknecht, *The Baryon Density at $z=0.9-1.9$ - Tracing the Warm-Hot Intergalactic Medium with Broad Lyman-Alpha Absorption*, 2007, arXiv:0705.1633 [astro-ph].
- [PS74] William H. Press and Paul Schechter, *Formation of Galaxies and Clusters of Galaxies by Self-similar Gravitational Condensation*, *Astrophys. J.* **187** (1974), 425–438.
- [PW65] A. A. Penzias and R. W. Wilson, *A Measurement of Excess Antenna Temperature at 4080 Mc/s*, *Astrophys. J.* **142** (1965), 419–421.
- [R⁺98] Adam G. Riess et al., *Observational Evidence from Supernovae for an Accelerating Universe and a Cosmological Constant*, *Astron. J.* **116** (1998), 1009–1038, astro-ph/9805201.
- [R⁺06] ———, *New Hubble Space Telescope Discoveries of Type Ia Supernovae at $z > 1$: Narrowing Constraints on the Early Behavior of Dark Energy*, 2006, astro-ph/0611572.
- [Ref03] Alexandre Refregier, *Weak Gravitational Lensing by Large-Scale Structure*, *Ann. Rev. Astron. Astrophys.* **41** (2003), 645–668, astro-ph/0307212.
- [RLLA07] Anais Rassat, Kate Land, Ofer Lahav, and Filipe B. Abdalla, *Cross-Correlation of 2MASS and WMAP3: Implications for the Integrated Sachs-Wolfe Effect*, *Mon. Not. Roy. Astron. Soc.* **377** (2007), 1085–1094, astro-ph/0610911.
- [RM95] K. C. Roth and D. M. Meyer, *Cyanogen Excitation in Diffuse Interstellar Clouds*, *Astrophys. J.* **441** (1995), 129–143.
- [RRS06a] Aleksandar Rakić, Syksy Rasanen, and Dominik J. Schwarz, *Can Extragalactic Foregrounds Explain the Large-Angle CMB Anomalies?*, 2006, astro-ph/0609188.
- [RRS06b] ———, *Microwave Sky and the Local Rees-Sciama Effect*, *Mon. Not. Roy. Astron. Soc.* **369** (2006), L27–L31, astro-ph/0601445.
- [RS68] M. J. Rees and D. W. Sciama, *Larger Scale Density Inhomogeneities in the Universe*, *Nature* **217** (1968), 511.
- [RT81] D. J. Raine and E. G. Thomas, *Large-Scale Inhomogeneity in the Universe and the Anisotropy of the Microwave Background*, *Mon. Not. Roy. Astron. Soc.* **195** (1981), 649–660.
- [S⁺03] D. N. Spergel et al., *First Year Wilkinson Microwave Anisotropy Probe (WMAP) Observations: Determination of Cosmological Parameters*, *Astrophys. J. Suppl.* **148** (2003), 175, astro-ph/0302209.
- [S⁺07] ———, *Wilkinson Microwave Anisotropy Probe (WMAP) Three Year Results: Implications for cosmology*, *Astrophys. J. Suppl.* **170** (2007), 377, astro-ph/0603449.
- [SBL91] G. Sironi, G. Bonelli, and M. Limon, *The Brightness Temperature of the South Celestial Pole and the Temperature of the Cosmic Background Radiation Measured at 36.6 and 12 Centimeter Wavelength*, *Astrophys. J.* **378** (1991), 550–556.
- [Sch85] Bernard F. Schutz, *A First Course in General Relativity*, Cambridge, 1985.
- [Sch03] Peter Schneider, *Gravitational Lensing as a Probe of Structure*, 2003, astro-ph/0306465.
- [Sch06] ———, *Einführung in die Extragalaktische Astronomie und Kosmologie*, Springer-Verlag, Berlin Heidelberg New York, 2006.
- [SDS] Team SDSS, *Official site of the Sloan Digital Sky Survey at <http://www.sdss.org/>*.
- [Sel96] U. Seljak, *Rees-Sciama Effect in a Cold Dark Matter Universe*, *Astrophys. J.* **460** (1996), 549, astro-ph/9506048.
- [Sen34] N. R. Sen, *On the Stability of Cosmological Models*, *Z. Astrophysik* **9** (1934), 215, reprinted with historical comments in *Gen. Rel. Grav.* **29** (1997), 1473.
- [Sil68] J. Silk, *Cosmic Black-Body Radiation and Galaxy Formation*, *Astrophys. J.* **151** (1968), 459.
- [SJWW95] S. T. Staggs, N. C. Jarosik, D. T. Wilkinson, and E. J. Wollack, *A Measurement of the Cosmic Background Spectrum at 1.4 GHz*, *Astrophys. Lett. Comm.* **32** (1995), 3.
- [SKCSS07] Joey Shapiro Key, Neil J. Cornish, David N. Spergel, and Glenn D. Starkman, *Extending the WMAP Bound on the Size of the Universe*, *Phys. Rev.* **D75** (2007), 084034, astro-ph/0604616.
- [SKM⁺03] H. Stephani, D. Kramer, M. MacCallum, C. Hoenselaers, and E. Herlt, *Exact solutions of Einstein's field equations*, Cambridge University Press, Cambridge, 2003.
- [Smo97] George F. Smoot, *The Cosmic Microwave Background Spectrum*, 1997, Published in Erice 1996, Current Topics in Astrodynamical Physics 407-440, astro-ph/9705101.
- [SSHC04] Dominik J. Schwarz, Glenn D. Starkman, Dragan Huterer, and Craig J. Copi, *Is the Low- l Microwave Background Cosmic?*, *Phys. Rev. Lett.* **93** (2004), 221301, astro-ph/0403353.
- [STT⁺98] Y. Sofue, A. Tomita, Y. Tutui, M. Honma, and Y. Takeda, *Nuclear-to-Disk Rotation Curves of Galaxies in the H α and [N(II)] Emission Lines*, *PASJ* **50** (1998), 427.
- [SW67] R. K. Sachs and A. M. Wolfe, *Perturbations of a Cosmological Model and Angular Variations of the Microwave Background*, *Astrophys. J.* **147** (1967), 73.
- [SW07] Dominik J. Schwarz and Bastian Weinhorst, *(An)isotropy of the Hubble Diagram: Comparing Hemispheres*, 2007, arXiv:0706.0165 [astro-ph].
- [SZ70] R. A. Sunyaev and Y. B. Zeldovich, *Small-Scale Fluctuations of Relic Radiation*, *Astrophysics and Space Science* **7** (1970), 3–19.

- [SZ96] Uroš Seljak and Matias Zaldarriaga, *A Line of Sight Approach to Cosmic Microwave Background Anisotropies*, *Astrophys. J.* **469** (1996), 437–444, astro-ph/9603033.
- [Sza04] László B. Szabados, *Quasi-Local Energy-Momentum and Angular Momentum in GR: A Review Article*, *Living Reviews in Relativity* **7** (2004), 4.
- [Sze75] Peter Szekeres, *A Class of Inhomogeneous Cosmological Models*, *Commun. Math. Phys.* **41** (1975), 55–64.
- [T⁺05] Matthieu Tristram et al., *The CMB Temperature Power Spectrum from an Improved Analysis of the ARCHEOPS Data*, *Astron. Astrophys.* **436** (2005), 785–797, astro-ph/0411633.
- [T⁺07] R. Brent Tully et al., *Our Peculiar Motion Away from the Local Void*, 2007, arXiv:0705.4139 [astro-ph].
- [TdOCH03] Max Tegmark, Angelica de Oliveira-Costa, and Andrew Hamilton, *A High Resolution Foreground Cleaned CMB Map from WMAP*, *Phys. Rev.* **D68** (2003), 123523, astro-ph/0302496.
- [TL95] R. Tuluie and P. Laguna, *The Imprint of Proper Motion of Nonlinear Structures on the Cosmic Microwave Background*, *Astrophys. J. Lett.* **445** (1995), L73–L76, astro-ph/9501059.
- [TN07] Masayuki Tanimoto and Yasusada Nambu, *Luminosity Distance-Redshift Relation for the LTB Solution Near the Center*, *Class. Quant. Grav.* **24** (2007), 3843–3857, gr-qc/0703012.
- [Tol34] R. C. Tolman, *Effect of Inhomogeneity on Cosmological Models*, *Proc. Nat. Acad. Sci. USA* **20** (1934), 169, reprinted with historical comments in *Gen. Rel. Grav.* **29** (1997), 935.
- [Tom01] Kenji Tomita, *Analyses of Type Ia Supernova Data in Cosmological Models with a Local Void*, *Prog. Theor. Phys.* **106** (2001), 929–939, astro-ph/0104141.
- [Tom05a] K. Tomita, *Second-Order Gravitational Effects of Local Inhomogeneities on CMB Anisotropies and Non-Gaussian Signatures*, *Phys. Rev.* **72** (2005), no. 10, 103506, astro-ph/0509518.
- [Tom05b] ———, *Second-Order Gravitational Effects of Local Inhomogeneities on CMB Anisotropies in Nonzero- Λ Flat Cosmological Models*, *Phys. Rev.* **72** (2005), no. 4, 043526, astro-ph/0505157.
- [Tro07] Roberto Trotta, *The Isocurvature Fraction after WMAP 3-Year Data*, *Mon. Not. Roy. Astron. Soc. Lett.* **375** (2007), L26–L30, astro-ph/0608116.
- [TS72] A. Tomimatsu and H. Sato, *New Exact Solution for the Gravitational Field of a Splitting Mass*, *Phys. Rev. Lett.* **29** (1972), 1344.
- [TSM04] Shinji Tsujikawa, Parampreet Singh, and Roy Maartens, *Loop Quantum Gravity Effects on Inflation and the CMB*, *Class. Quant. Grav.* **21** (2004), 5767–5775, astro-ph/0311015.
- [TSVZ92] R. B. Tully, R. Scaramella, G. Vettolani, and G. Zamorani, *Possible Geometric Patterns in 0.1c Scale Structure*, *Astrophys. J.* **388** (1992), 9–16.
- [Tul88] R. Brent Tully, *Distances to galaxies in the field*, 1988, Large-Scale Motions in the Universe: A Vatican study Week, pp. 169–177.
- [Tul07] ———, *The Local Velocity Anomaly*, 2007, arXiv:0708.2449 [astro-ph].
- [Tur52] Herbert W. Turnbull, *Theory of Equations*, University Mathematical Texts, Oliver and Boyd, Edinburgh London New York, 1952.
- [Val05] Chris Vale, *Local Pancake Defeats Axis of Evil*, 2005, astro-ph/0509039.
- [VL05] D. Vogt and Patricio S. Letelier, *Presence of Exotic Matter in the Cooperstock and Tieu Galaxy Model*, 2005, astro-ph/0510750.
- [vS37] W. J. van Stockum, *The Gravitational Field of a Distribution of Particles Rotating About an Axis of Symmetry*, *Proc. Roy. Soc. Edinburgh* **A57** (1937), 135.
- [VW77] C. V. Vishveshwara and J. Winicour, *Relativistically Rotating Dust Cylinders*, *J. Math. Phys.* **18** (1977), 1280.
- [Wal84] Robert M. Wald, *General Relativity*, The University of Chicago Press, Chicago London, 1984.
- [Wee04] Jeffrey R. Weeks, *Maxwell's Multipole Vectors and the CMB*, 2004, astro-ph/0412231.
- [Wei72] Steven Weinberg, *Gravitation and Cosmology: Principles and Applications of the General Theory of Relativity*, Wiley, Weinheim Berlin New York, 1972.
- [Wey17] Hermann Weyl, *Zur Gravitationstheorie*, *Annalen der Physik* **54** (1917), 117.
- [WMAa] Team WMAP, *Data products at <http://lambda.gsfc.nasa.gov/>*.
- [WMAb] ———, *Official website of the Wilkinson Microwave Anisotropy Probe at <http://map.gsfc.nasa.gov/index.html>*.
- [WNL⁺07] Chun-Hsien Wu, Kin-Wang Ng, Wolung Lee, Da-Shin Lee, and Yeo-Yie Charng, *Quantum Noise and a low Cosmic Microwave Background Quadrupole*, *JCAP* **0702** (2007), 006, astro-ph/0604292.
- [Y⁺06] W. M. Yao et al., *Review of Particle Physics*, *J. Phys.* **G33** (2006), 1–1232.
- [Yor79] York, J. W. jr., in *Sources of Gravitational Radiation; Proceedings of the Workshop, Seattle, Wash., July 24-August 4, 1978*, Cambridge University Press, edited by Smarr, L. L., 1979.
- [Zal93] Roustam Zalaletdinov, *Towards a Theory of Macroscopic Gravity*, *Gen. Rel. Grav.* **25** (1993), 673–695.
- [Zal04] ———, *Space-Time Averages of Classical Physical Fields*, 2004, gr-qc/0411004.
- [Zwi33] F. Zwicky, *Die Rotverschiebung von extragalaktischen Nebeln*, *Helvetica Physica Acta* **6** (1933), 110.